2014-11-12

Computational Insights into the Mechanisms and Structures of Peptide Bond Cleaving Metalloenzymes and Their Synthetic Analogues

Tingting Zhang
University of Miami, zhangttgre@163.com

UNIVERSITY OF MIAMI

COMPUTATIONAL INSIGHTS INTO THE MECHANISMS AND STRUCTURES OF PEPTIDE BOND CLEAVING METALLOENZYMES AND THEIR SYNTHETIC ANALOGUES

By

Tingting Zhang

A DISSERTATION

Submitted to the Faculty
of the University of Miami
in partial fulfillment of the requirements for
the degree of Doctor of Philosophy

Coral Gables, Florida

December 2014

UNIVERSITY OF MIAMI

A dissertation submitted in partial fulfillment of
the requirements for the degree of
Doctor of Philosophy

COMPUTATIONAL INSIGHTS INTO THE MECHANISMS AND STRUCTURES OF PEPTIDE BOND CLEAVING METALLOENZYMES AND THEIR SYNTHETIC ANALOGUES

Tingting Zhang

Approved:

_____

Rajeev Prabhakar, Ph.D.
Professor of Chemistry

_____

Françisco M. Raymo, Ph.D.
Professor of Chemistry

_____

Jamie D. Walls, Ph.D.
Professor of Chemistry

_____

M. Brian Blake, Ph.D.
Dean of the Graduate School

_____

Akira Chiba, Ph.D.
Professor of Biology

ZHANG, TINGTING (Ph.D., Chemistry)
Computational Insights into the Mechanisms and Structures of Peptide Bond Cleaving Metalloenzymes and Their Synthetic Analogues (December 2014)

Abstract of a dissertation at the University of Miami.

Dissertation supervised by Professor Rajeev Prabhakar.
No. of pages in text. (188)

The selective hydrolysis of peptide or amide bond is required in a wide range of biological, biotechnological and industrial applications. There are significant kinetic barriers to these reactions since peptide bonds are extremely stable and possess a half-life for hydrolysis of 350–600 years at room temperature and pH 4–8. Therefore, nature has devised enzymes to rapidly and selectively cleave these bonds under physiological conditions that are known as peptidases. Specifically, metallopeptidases, generate a scaffold capable of binding one or two metal ions to hydrolyze peptide bonds. The studies on metallopeptidases are important to understand the functions of these enzymes and to design their synthetic analogues.

In this thesis, state-of-the-art theoretical and computational chemistry techniques including quantum mechanics (QM), hybrid quantum mechanics/molecular mechanics (QM/MM ONIOM), and molecular dynamics (MD) simulations have been utilized to investigate the mechanisms and structures of mononuclear and binuclear metallopeptidases and their synthetic analogues. In particular, the catalytic mechanisms of four different synthetic complexes of mononuclear metallopeptidases and three natural enzymes and their synthetic analogues of binuclear metallopeptidases have been elucidated. These studies have provided the information regarding the conformation of

the reactants, ligand environment, and the role of the metal ions. In addition, the structural properties and interactions between amyloid β peptides (Aβ40/Aβ42) and insulin degrading enzyme (IDE) mutants have been explored using MD simulations.

Dedicated to My Parents

ACKNOWLEDGEMENTS

I am so thankful for all the help and support that I received at the University of Miami. First of all, I would like to express my sincere gratitude to my advisor, Dr. Rajeev Prabhakar, for leading me into such an exciting field of chemistry. I was given the opportunity to study complex chemical and biochemical systems which is amazing and interesting. He always encouraged me when I faced a problem and taught me how to think independently to solve it. He patiently helped me when I made mistakes. He reminded me often to have a positive attitude towards anything and his kindness, freedom of thought, and consistent support made my entire graduate life very smooth. I feel very lucky to have had him as my mentor.

I would also like to thank Dr. Françisco Raymo, Dr. Jamie Walls, and Dr. Akira Chiba for being my committee members and providing invaluable insight into my research. I wish to express my sincere appreciation to Dr. V. Ramamurthy, Dr. Carl Hoff, Dr. Burjor Captain and Dr. Norito Takenaka for sharing their extraordinary expertise. I also would like to convey my gratitude to Dr. Roger Leblanc for his encouragement and concern. I would like to thank Dr. Tegan Eve for his excellent training and coordination during my teaching assistantship which greatly improved my teaching skills. I also would like to thank the chemistry department staff members Lydia, Marlene, Susana, and Sara for all their support.

I am grateful to all my wonderful and lovely lab mates Arghya, Xiaoxia, Mehmet, Shanghao, Ram, and TJ for making the lab enjoyable and feeling like a home. Arghya,

Xiaoxia, and Mehmet shared their experience and helped me a lot from the very beginning of my research. Special thanks to TJ for his valuable suggestions and corrections during the preparation of this thesis.

I would like to thank all my friends Dianting, Anhui, Cai, Zhili, Sheba, Barnali, Xiaowen, Sanem, Anjaneyulu, Pradeep, Jeet, Hossein, Song, Yanhua, Revathy, Sumit, Shampa, Veeranna, Rajib, Jyothi, Zhenghua, Beijun, Yang, Xu, Subu, and Ali at UM for their great friendship that will never be forgotten.

Finally, I am forever indebted to my parents and my fiancé who give me love, support, and encouragement. They are the driving force for me to move on. Having them in my life is the greatest blessing for me.

“The way to get good ideas is to get lots of ideas and throw the bad ones away.”

- Linus Pauling

TABLE OF CONTENTS

Page

LIST OF FIGURES

LIST OF TABLES

Chapter 1 Introduction

The hydrolytic cleavage of peptide bonds occurs in multiple steps during metabolic and signaling biochemical pathways. For instance, rigorous control of concentrations within a cell requires the rapid degradation of numerous important regulatory proteins. This process is essential for living organisms since they are involved in functional and regulatory roles in the control of the cell cycle, transcription, signal transduction and cell death.[1,2] It also plays important roles in a wide range of biotechnological and industrial applications.[3] There are significant kinetic barriers to these reactions since peptide bonds are extremely stable and possess a half-life for hydrolysis of 350–600 years at room temperature and pH 4–8.[4,5] Therefore, nature has devised enzymes to rapidly and selectively cleave these bonds under physiological conditions that are known as peptidases. The peptidases catalyze the hydrolysis of peptide bonds of proteins through the following overall reaction:

$$\text{R-(O=)C-NH-R'} + \text{H}_2\text{O} \rightarrow \text{R-COOH} + \text{NH}_2\text{-R'} \qquad (1)$$

These peptidases are divided into four different types: the first type (serine proteases) utilizes a Ser as a nucleophile to attack the carbonyl carbon, leading to the generation of an intermediate acyl-enzyme that is subsequently attacked by water. The second type (cysteine proteases) functions in a similar manner to the first, but Ser is replaced by Cys. The third type (aspartic proteases) utilizes the general acid-base mechanism to cleave the

peptide bond by containing two catalytic carboxylate functional groups. The fourth type known as metallopeptidases uses one or two metal ions to selectively hydrolyze the peptide bonds. The metal ions can increase the electrophilicity of the substrates and /or enhance the nucleophilicity of water by positioning a hydroxide next to the substrate.[6] Hence, various kinds of structures, functional groups, and chemical mechanisms of the above peptidases have been used to accelerate hydrolysis reactions.[7-9]

Although the existing natural proteases/peptidases are highly efficient, they also possess certain disadvantages.[10,11] Most of them exhibit broad specificities and tend to cleave themselves producing small fragments.[12] They are expensive and function under narrow temperature and pH conditions.[13] Therefore, the design and synthesis of efficient artificial proteases/peptidases that can imitate the natural catalytic processes utilized by natural enzymes is needed. These synthetic analogues of peptidases can offer the following advantages over enzymes: (1) they are inexpensive and may be recyclable[14], (2) they impose little or no steric constraints because of their smaller size, (3) they can cleave proteins either terminally or internally, and (4) their properties can be tuned for specific applications.

Moving towards this goal, amide hydrolysis by organic functional groups,[15,16] metal ions,[17] and metal ion-organic group complexes[18] has been studied in the last few decades. A number of transition metal (Pd, Pt, Zn, Cu, Co, Fe, Ni, etc.) containing complexes for peptide hydrolysis have been synthesized.[17,19-27] These metallopeptidases generate a scaffold capable of binding one or two metal ions.[28] The metal centers of the mononuclear metallopeptidases (bound with one metal ion) can catalyze the reaction by

playing multiple roles,[29] including providing sites for substrate binding, activating the nucleophile, and stabilizing the transition state.[28] On the other hand, the binuclear metallopeptidases are bound to two metal ions. It was indicated that only one single metal ion is essential for catalysis, but in some instances, both metal ions are required for full activity.[28]

In comparison to natural metallopeptidases, the hydrolytic reactions employed by existing synthetic analogues have low efficiency and catalytic turnover. More knowledge about the mechanisms of the reaction, the role of metal ions, ligand effects, and the function of the second shell residues of both natural and synthetic metallopeptidases is required to design better synthetic analogues with higher catalytic activities. Since many natural metallopeptidases are Zn containing enzymes, the spectroscopy facilities cannot detect the metal center due to its diamagnetic d^{10} configuration. The adoption of experimental techniques cannot follow the catalytic steps of those enzymes due to the rapid reaction rate and unstable intermediates. Therefore, the detailed structural and mechanistic information regarding natural and synthetic metallopeptidases cannot be obtained by experiments alone. In this regard, computational chemistry methodologies are being utilized to elucidate these critical issues.

Furthermore, there is growing interest in understanding the properties and functioning of proteases/peptidases due to their involvement in various life threatening diseases such as AIDS, Malaria, and Alzheimer's disease (AD).[30] AD is a neurodegenerative disorder characterized by the deposition of extracellular senile plaques and intracellular neurofibrillary tangles in the brain.[31-33] Genetic, animal modeling, and biochemical

studies indicates that the major components of these senile plaques are 40/42 amino acid residues containing amyloid β (Aβ) peptide.[34-36] Aβ peptides are naturally generated through the sequential cleavage of amyloid precursor protein (APP) by β-secretase (BACE) and γ-secretase enzymes.[37-41] The Aβ peptides aggregating to form amyloid fibrils those accumulate at the center of senile plaques resulting in neurotoxicity.[42-48] Currently, there are three potential therapeutic strategies available for the treatment of AD. The first method inhibits BACE and γ-secretase enzymes that produce Aβ peptides. The second method is to prevent the aggregation of Aβ to form amyloid fibrils by inhibitors. Since the Aβ peptides are degraded by metallopeptidases such as Insulin degrading enzyme (IDE) and Neprilysin (NEP). The third strategy is to degrade the monomeric/oligomeric forms of Aβ by natural or synthetic metallopeptidases.[49,50] However, there are still many unsolved issues due to the rapid aggregation of Aβ peptides, lack of substrate bound enzyme complexes, elusive mechanistic pathway, and short lived transition states.

Computational chemistry is a rapidly developing field benefiting from the tremendous progress of computing facilities in the last few decades. It is an indispensable tool to study the atomic and molecular properties and reaction paths for chemical reactions in chemistry and biochemistry. Quantum mechanics and molecular mechanics are the two main theories used in computational chemistry. The history of quantum chemistry traces back to the early 20th century when Erwin Schrödinger formulated the Schrödinger equation. This mathematical model could describe how the quantum state of a physical system changes in time but can only be solved for a two particle system. Therefore, a

range of approximate solutions are applied for the studying of larger systems. Quantum chemistry is a field that focuses on the application of quantum mechanics. The development of the density functional theory (DFT) led to a remarkable revolution in quantum chemistry.[51] The foundation of DFT was laid by Hohenberg and Kohn. The basic is that the total energy of a system is a unique functional of the electron density. Since DFT is very accurate and has low computational cost, it is widely used to calculate the properties of a system with up to 200 atoms. In order to study large molecular systems without quantum mechanical calculations, molecular mechanics (MM) is employed. In MM, each atom is treated as a single particle by ignoring the electrons. The motions of nuclei are studied by utilizing classical mechanics equations which are known as force fields. Force fields which are derived from both experimental data and quantum mechanical calculations describe the covalent and noncovalent interactions of the molecular system. One of the main applications of MM is energy minimization, which aims to gain the lowest energy conformation of the molecule after optimization the structure. MM can be applied to study small molecules and biological systems with total atoms from thousands to millions. Therefore, MM is widely used in molecular dynamics (MD) simulations to investigate the geometry conformational and thermodynamic properties of large systems.

In this thesis, DFT and MM based methods have been employed to study the mechanistic and structural aspects of mononuclear and binuclear metallopeptidases and their synthetic analogues. It is organized in the following manner: Chapter 2 briefly describes the theoretical background and computational methodologies which are utilized

in the investigation. Chapter 3 discusses the catalytic mechanism of the mononuclear metal-cyclen complexes using DFT calculations.[52] These studies include the conformation of the reactants, pendant functioning on the energetics, ligand environment, and the role of the metal ions. The hydrolysis of the peptide bond by a set of Zr(IV) complexes are also illustrated in this chapter. The mechanism of a host-guest complex formed by a hydrophobic environment of *β*-cyclodextrin (CD) conjugated to a mononuclear Pd(II) catalyst have been investigated using QM/MM methods.[53] Finally, the methanolysis of synthetic mononuclear Pb(II) and Zn(II) analogues will be discussed. In Chapter 4, the peptide cleavage mechanism of binuclear metallopeptidases has been proposed. It includes three natural enzymes (leucine aminopeptidase (LeuAP), D-aminopeptidase (DppA), and human renal dipeptidase (hrDP)) and three synthetic analogues. Chapter 5 will focus on the structural properties and interactions between the amyloid β peptides (Aβ40/Aβ42) and insulin degrading enzyme (IDE) mutants using MD simulations.

Chapter 2 Theoretical Background and Computational Methods

In this chapter, quantum chemical and molecular mechanics based methods will be discussed shortly. These methods have been employed to determine reaction mechanisms and the structural properties of the chemical/biochemical systems discussed in this thesis.

2.1 Quantum Chemical Methods

Quantum chemical treatment of electrons, which doesn`t obey classical behavior is necessary in order to understand the electronic nature of molecular systems. This starts with the well-known time-independent Schrödinger equation:

$$\hat{\mathrm{H}}\psi = E\psi \tag{1}$$

Where, $\hat{\mathrm{H}}$ is the Hamiltonian operator, ψ is the wave function, and E is the energy of the system. Wave function describes the wave character, position and the behavior, of an electron. Although wave function is a mathematical term and has no physical meaning, ψ^2 (square of the wave function) describes the probability of finding an electron defined with the corresponding wave function at a given point and time. $\hat{\mathrm{H}}$, on the other hand, is comprised of the kinetic energy of electrons (T_e), the kinetic energy of the nuclei (T_N), the electron-electron repulsion (V_{ee}), the nuclear-nuclear repulsion (V_{NN}), and the attraction of the electrons to the nuclei (V_{Ne}):

$$\hat{\mathrm{H}} = T_e + T_N + V_{ee} + V_{NN} + V_{Ne} \tag{2}$$

Schrödinger equation can only be solved for one electron systems, such as hydrogen atom or H_2^+. Thus, many approximations were introduced to make it possible to solve this equation for many electron systems. The most fundamental approximation is the Born-Oppenheimer approximation,[54] which states that due to the large difference in mass of electrons and nuclei, electrons can be assumed to move in a field of fixed nuclei. This leads to the approximation that the kinetic energy of nuclei can be neglected allowing the separation of the electronic and nuclear part of Schrödinger equation.

$$\psi_{BO}(\vec{r}, \vec{R}) = \psi_{el}(\vec{r})\psi_{nuc}(\vec{R}) \tag{3}$$

2.1.1 Hartree-Fock (HF) Theory

Quantum chemistry focuses on solving the electronic Schrödinger equation, and the first solution was introduced by famous Hartree-Fock (HF) method in 1930. HF describes the complex multi-electron wave function as an anti-symmetrized product of molecular orbitals or spin-orbitals, $\psi_i(r_i,s_i)$ where r is the vector variable and s is the spin variable. The anti-symmetry principle introduced by Fock in 1930 introduces the Pauli Exclusion Principle into the definition and N-electron wave function is constructed as an anti-symmetric product of N one-electron wave functions, which is known as Slater determinant Φ_{SD}:

$$\Phi_{SD} = \frac{1}{\sqrt{N!}} \begin{vmatrix} \psi_1(r_1, s_1) & \dots & \psi_N(r_1, s_1) \\ \vdots & \ddots & \vdots \\ \psi_1(r_N, s_N) & \dots & \psi_N(r_N, s_N) \end{vmatrix} \tag{4}$$

Minimization of the HF energy and application of the variational principle[55] produces the HF equations:

$$\widehat{F}_i\,\psi_i(r_i, s_i) = \epsilon_i\,\psi_i(r_i, s_i) \tag{5}$$

This equations are eigenvalue equations where $\widehat{F}_i$ is the Fock operator and the Lagrangian multiplier ϵ_i are the eigen values. The Fock operator is single-electron Hamiltonian for each individual electron in the system:

$$\widehat{F}_i = -\frac{1}{2}\nabla_i^2 - \sum_{\mathrm{A}}^{\mathrm{M}} \frac{\mathrm{Z_A}}{\mathrm{r}_{i\mathrm{A}}} + \mathrm{V_{HF}}(i) \tag{6}$$

First two terms are kinetic and potential energies, and the third is the Hartree-Fock potential. HF potential defines the average repulsive potential that each electron experiences due to the remaining of electrons. $\mathrm{V_{HF}}(i)$ is defined as:

$$V_{HF}(r_1, s_1) = \sum_{J}^{N} (\hat{\mathrm{J}}_{\mathrm{j}}(r_1, s_1) - \widehat{K}_{\mathrm{j}}(r_1, s_1)) \tag{7}$$

$\hat{\mathrm{J}}_{\mathrm{j}}$ is the Coulomb operator, which defines the electronic repulsion between two electrons, and $\widehat{K}_{\mathrm{j}}$ is the exchange operator, which is related to the fact that electrons with the same spin state must be far away from each other.

The HF equations can only be solved by the iterative self consistent field (SCF) theory.[56,57] At the beginning of the SCF cycle, the set of atomic coefficients are assigned and atomic orbitals are calculated. After the calculation of the Coulomb and exchange operators, HF energy is calculated. The variational method minimizes the energy and the second cycle starts. In this cycle previously calculated coefficients are iterated and new set of coefficients are calculated, which help to caculate the new HF energy. These cycles continue until there is no significant change in the energy observed from the last cycle. At this step the structure is called to be converged.

2.1.2 Density Functional Theory (DFT)

Wave function methods discussed previously are proved to be very successful in the study of small molecules. However, they become very expensive computationally to study bigger molecules as they rely on finding the wave function, which depends on 3N coordinates. Hohenberg-Kohn theorem,[58] which density functional theory (DFT)[59,60] is built on suggests that for a non-degenerate ground state the energy, E[ρ], can be given by unique functional of the electron density ρ of the system. Thus, there is no need for the determination of many electron wave functions. The density can be defined as:

$$\rho(\vec{r}) = \sum_{i=1}^{occ} |\phi_i(\vec{r})|^2 \quad (8)$$

Where ϕ_i are the one-electron orbitals. The general DFT energy functional can be expressed as:

$$E_{DFT} = T_s[\rho] + E_{ne}[\rho] + J[\rho] + E_{xc}[\rho] \quad (9)$$

$T_s[\rho]$ is the kinetic energy calculated from a Slater determinant, $E_{ne}[\rho]$ is the attraction between the nuclei and electrons, $J[\rho]$ is the Coulombic interaction between electrons, and $E_{xc}[\rho]$ is the exchange-correlation energy which is given by:

$$E_{xc}[\rho] = (T[\rho] - T_s[\rho]) + (E_{ee}[\rho] - J[\rho]) \quad (10)$$

$E_{ee}[\rho]$ is the electron-electron repulsion term. The first term in the equation can be considered as the kinetic correlation energy and the second term is both exchange and correlation energy. The ultimate challenge of DFT is to obtain $E_{xc}[\rho]$ correctly. Several density functionals use different approximations to calculate the exchange energy. The simplest approximation is the Local Spin Density Approximation (LSDA), which treats electron density ρ can be treated locally as a uniform electron cloud. Although LSDA provides good results with HF calculations, it is obvious that in real system, the electron density is far from spatially uniform and LSDA fails with the fluctuating electron densities. Generalized Gradient Approximation (GGA) introduces a major improvement to LSDA. In GGA the correlation functional not only depends on the local value of electron density but also on the local change of it, i.e. gradient of the density. The most improved method of modern DFT is the hybrid DFT, which combines functionals of LSDA, improvements of GGA, and also some HF exchange calculated from Kohn-Sham orbitals. The most popular hybrid functional is the B3LYP functional, which has been

used for all the studies in this thesis. B3LYP functional is consisted of the mixture of HF and DFT exchange functionals with the experimentally fitted parameters A, B, C:[61-63]

$$F_{xc}^{B3LYP} = (1-A)F_x^{Slater} + AF_x^{HF} + BF_x^{Becke} + CF_c^{LYP} + (1-C)F_c^{VWN} \quad (11)$$

In this equation, F_x^{Slater} is the Slater (LSDA) exchange functional, F_x^{HF} is the HF exchange functional, F_x^{Becke} is Becke`s gradient correction to LSDA exchange functional, F_c^{LYP} is the correlation function by Lee, Yang, Parr, and F_c^{VWN} is the correlation function by Vosko, Wilk, Nussair. Three parameters A= 0.20, B= 0.72, and C= 0.81 are determined by Becke through fitting to a set of 55 small molecules consisted of first and second row elements.[62] The other hybrid functional, MPWPW91 by Barone and Adamo that has been used in the comparison of B3LYP is the modified Perdew-Wang exchange functional PW91 in combination with the original PW91 correlation function and a mixing ratio of exact and DFT exchange of 0.25:0.75.

2.1.3 Accuracy of DFT Methods

The HF theory was known to calculate molecular properties such as bond lengths, angles, vibrational frequencies and energies with large deviations from experimental values. LDA and GGA methods certainly improved these calculations but still large deviations were found from experimental values. The introduction of hybrid functional methods changed the field of computational chemistry forever. B3LYP is still the most popular hybrid functional method and is widely used.

The accuracy of different DFT methods were tested in two studies by Bauschlicher Jr. and Curtiss, et al. with two different sets of molecules containing first and second row elements.[64,65]

Table 2. 1 Accuracy of DFT methods.

Data Sets	Wave function methods			DFT methods	
	HF	G2	G3	BLYP	B3LYP
G2-1	74.5	-	-	5.0	2.2
G2/97	-	1.50	1.01	5.77	3.31

It was found that B3LYP performs much better than any other DFT methods. On calculating the atomization energies of the G2-1 set B3LYP calculations had a mean absolute error of 2.2 kcal/mol while HF method had a deviation 74.5 kcal/mol (Table 2.1). Other DFT methods, such as BLYP produced a mean absolute error of 5.0 kcal/mol, BP86 a mean deviation of 10.3 kcal/mol. Only Pople`s G2[66] and G3[64] methods were found to be superior than DFT methods on G2-97 set (Table 2.1). G2 and G3 methods calculated the energies with mean absolute errors of 1.50 and 1.01 kcal/mol, respectively while B3LYP deviated by 3.31 kcal/mol. However, these wave function methods are computationally very demanding, but in contrary DFT methods benefit from faster basis set convergence regarding the energy. B3LYP has an excellent performance to cost ratio as these benchmark experiments showed. In addition to the sets of molecules consisted of first and second row elements, there have been studies with transition metals as well.[67,68] Metal-ligand bond strengths in MR^+ complexes (M=first row transition metal and R=H,

CH2, CH3, OH) give typical errors of 3.6-5.5 kcal/mol for B3LYP functional. Additionally, studies on the successive bond strengths of CO in $Fe(CO)_5^+$ and $Ni(CO)_4$, and the M-CO bond energy in $M(CO)_6$ complex (M=Cr, Mo, W) produced an average error of 2.6 kcal/mol. Although, it is extremely hard to treat transition metal complexes because of the degeneracy of 3d orbitals, B3LYP functional handles these calculations with reasonable average errors.

2.1.4 Modeling Chemical Reactions

Given the fact that enzymes are large molecules consisted of thousands of atoms, quantum chemical investigation with the DFT methods employed in the present thesis limits the system of interest to ~200 atoms. Therefore, the real system must be reduced into a model containing only the parts of interest for the given mechanism. This works well for the systems possessing a small part called the active site, in which the catalysis reaction takes place. However, while modeling active sites one has to be careful with the residues to be included in the model. This can be done with the trial of energy calculations with and without the certain residues to check the contribution of that particular residue in the energetics of the catalysis. We have searched the literature and constructed the active site models in the light of previous studies. In addition to selecting the residues for the active site model, it is also important to reduce the residues into small molecules to save computing time. Implementation of this approach is extremely common, and is showed to have only minor effects on the results.[69] In the present thesis the histidine residues are modeled as imidazoles, aspartic/glutamic acids as propionic

acids, and cysteine residues as ethanethiols. The rigidity imposed on the active site imposed by the rest of the enzyme is modeled by constraining the atom leading to the backbone of the residue during the geometry optimization. In some cases, additional water molecules are added to the model in order to mimic the hydrogen bonding contributions. Charges and the multiplicities of the systems are carefully calculated depending on the active site model.

2.1.5 Localization of Transition States

Computational chemistry proves itself to be a valuable tool in studying enzyme catalyzed reactions and constructing a potential energy surface (PES) for the whole reaction path. It is constructed by calculating the relative energies of all steps in the reaction. The saddle points called the transition states are the highest energy points between two consecutive minima. Upon construction of PES, reaction rates can be calculated by the help of transition state theory (TST). According to TST the transition state is in equilibrium with all reactant molecules and the rate of the reaction can be calculated by using the following equation:

$$k = \frac{k_B T}{h} e^{-\frac{\Delta G^{\ddagger}}{RT}} \tag{12}$$

where k_B is Boltzmann`s constant, $h$ is Planck`s constant, and $\Delta G^{\ddagger}$ is the difference in Gibbs free energies of the reactant and the transition state. At temperature T = 298.15 K, the change of every 1.4 kcal/mol in the barrier ($\Delta G^{\ddagger}$) rate of the reaction changes by one order of magnitude. However, determination of the transition state is not easy and

requires a chemical intuition. Thus, having the structures of both reactant and product is very important, which leads to an accurate guess of transition state structure. Moreover, depending on the reaction is exothermic or endothermic; the transition state will look more like the reactant or the product, respectively. The first step for determining the transition state is to get a maximum energy structure on PES. In the next step, a Hessian is calculated for this point. After that, a full transition state optimization is performed using the Hessian calculated in the last step. Once the optimization is completed, a new Hessian is calculated for this optimized structure and the validity of the transition state is confirmed with one imaginary frequency associated with the reaction coordinate.[62]

2.1.6 Solvent Effects

In this thesis all calculations were performed in gas phase. Thus, interactions between the model complex and surrounding environment were totally missing in the optimizations. However, in reality systems studied here work in solvent medium. Therefore, steric contributions from the protein environment and the effect of the solvent molecules that surrounds the protein must be taken into the account. The first method to accomplish that is called QM/MM method, in which the active site model is treated with quantum mechanics, and the rest of the protein is treated with molecular mechanics. The second approach, which was implemented throughout this thesis to treat the contribution from the medium surrounding the protein, utilizes continuous dielectric medium to count for the solvent around the system. Here, solvent perturbs the gas behavior of the system as the system is subjected to the electrostatic potential by the continuous solvent. The

dielectric permittivity constant (ε) has a low value (ε=4) for protein environments, and high value (ε=80) for the aqueous organic reactions. There are several different methods available to calculate the solvent effects. The method used in this thesis was called the self consistent reaction field (SCRF) with the polarizable continuum model (PCM) using the integral equation formalism version (IEFPCM).[70] In SCRF method Poisson-Boltzmann equation is solved and the solvent charge distribution is added to the SCF procedure. This procedure is repeated until self-consistency is reached. IEFPCM model creates the solute cavity via a set of overlapping spheres around the atoms.

2.1.7 Hybrid QM/MM (ONIOM)

Hybrid QM/MM methods are among the best molecular modeling approaches to quantitatively study the enzymatic reactions. In such methods both quantum mechanics and molecular mechanics methods are merged together. The portions of the system which involve the modification of chemical bonds are treated with the quantum mechanical methods. On the other hand, the rest of the system which may contribute the electrostatic, hydrogen bonding interactions and also the steric effects are treated with molecular mechanics based methods. The Hamiltonian equation for hybrid QM/MM methods is as follows:

$$\mathrm{H}_{complete} = \mathrm{H}_{QM} + \mathrm{H}_{MM} + \mathrm{H}_{QM/MM} \tag{13}$$

Where H_{QM} is the interaction between atoms present in the QM section, H_{MM} describes the interaction between the atoms in MM section, and $H_{QM/MM}$ defines the atomic interactions between the QM and MM section.

In ONIOM[71-77] calculations, instead of having discrete QM and MM sections, the whole system is divided into 'real system' (all atoms) and a subset of the real system called 'model system'. The 'model system' consists of a small number of atoms that take part in the chemical reactions. In two-layer ONIOM calculations, molecular mechanics calculations are performed on the 'real system' as well as on the 'model system' and then the energy of the 'model system' is subtracted from that of the 'real system'.

$$E_{ONIOM} = E_{MM,real} + E_{QM,model} - E_{MM,model} \quad (14)$$

The partial charges from the "real - model" system may then be incorporated into the Hamiltonian for the 'model system'. This effectively accounts for the electrostatic interactions between the QM and MM systems. This leads to the polarization of the QM wave function by the point charge from the MM system.

2.1.8 Computational Methods for QM and QM/MM Calculations

In this thesis all the calculations were performed by using Gaussian03/09 program.[78,79] Geometries of reactants, transition states, intermediates, and products were optimized without any symmetry constraints by using B3LYP functional and Lanl2dz basis set.[61-63,80] All degrees of freedom were optimized and the transition states obtained were confirmed to have one imaginary frequency corresponding to the reaction coordinate. The

final energies of the fully optimized structures were further improved by performing single point calculations using the triple zeta quality basis set, 6-311+G(d,p). Contributions of zero-point energy and thermal corrections were calculated at the level of the optimization (B3LYP) and added to the final functional/6-311+G(d,p) energies, because it is extremely unfeasible to calculate these contributions by using the big basis set (6-311+G(d,p)). The solvent effects from the surrounding environment were included in the energies by using the dielectric constant (ε) either four for enzymatic catalysis in the protein environment or eight for those in aqueous environment, utilizing the self-consistent reaction field IEFPCM method at the level used for the optimization of the geometries. Throughout the thesis the energies obtained at the functional used/(6-311+G(d,p)) + zero-point energy (unscaled) and thermal corrections (at 298.15 K and 1 atm) + solvent effects will be discussed.

In the QM/MM study, the "model" part is treated at the B3LYP level using the all-electron 6-31G(d) basis set and the "real" system was treated at the MM level utilizing the AMBER force field. QM/MM boundaries were treated with "Link Atom" approach. All transition states were confirmed to have a single imaginary frequency corresponds to the reaction coordinate. The final energetics of the optimized structures were improved by including the single point energy from the triple zeta quality of basis set (6-311+G(d,p)), unscaled zero-point energy and thermal correction (at 298.15 K and 1 atm) estimated at the B3LYP/6-31G(d) level from the QM model study.

2.2 Molecular Mechanics Methods

In molecular mechanics method, motions of the electrons are neglected and they along with nuclei are lumped into atom like particles. Moreover, the energy of the system is calculated based on the nuclear positions only. Since the total energy calculations are based on the function of position of these particles, calculations are much simpler and computationally less expensive than quantum mechanical calculations. Molecular mechanics can be applied to a variety of systems comprised of thousands of atoms such as proteins, DNA, vacuum, implicit or explicit solvent mediums. Molecular mechanics deals with the simple models of interactions in the system such as bond stretching, angle bending and rotation of a functional group around a particular bond. These interactions are determined by implementing pre-determined force field, which contains parameters for these interactions of each atom type depending on the surrounding environment of the atoms (e.g. polar H, non-polar H, and aromatic H). Although molecular mechanics calculations are fast and can be performed on large systems, it is impossible to study the bond breaking and bond forming phenomena in a chemical reaction, which is just opposite of the quantum mechanical calculations. Moreover, it is not possible to obtain chemical property of a system that solely depends on electronic distribution by molecular mechanics methods. Nevertheless, molecular mechanics based methods are extremely useful and commonly applied in the calculation of the conformational flexibility of the proteins, ligand-protein interactions, hydrogen bonding and explicit treatment of a solvent.

2.2.1 Force Fields

As the smallest units in molecular mechanics are atoms, interactions between atoms must be provided explicitly rather than being calculated by solving Schrodinger equation. Thus, force fields define the bonded and non-bonded interactions among atoms present in the system. There are numerous force fields available: AMBER, CHARMM, OPLS, GROMOS, COMPASS etc.[81] All these and other force fields are comprised of following four components:

$$E_{FF} = \sum_{bonds} f(r) + \sum_{angles} f(\theta) + \sum_{torsions} f(\phi) + \sum_{non-bond}(R_{ij}) \quad (15)$$

Bonding energy is described with bond stretching model which can be considered with simple harmonic approximation using Hooke`s law:

$$E_{FF}(r) = \sum_{bonds} k_b(r - r_0)^2 \quad (16)$$

Here k_b is half the force constant and r_0 is the equilibrium bond length. Similarly bond angles are described in this way:

$$E_{FF}(\theta) = \sum_{angles} k_\theta(\theta - \theta_0)^2 \quad (17)$$

The bond length and angles are the most stable parameters in the total force field energy term and they do not deviate from their reference or equilibrium value due to their large force constants. Larger contributions in molecular structure and energy come from the torsional and non-bonded interactions. The torsion term is associated with rotation around the middle bond in three-bond system, also known as the dihedral. It is expressed as a

cosine series expansion, which describes the energy barrier for the rotation around the chemical bond:

$$E_{FF}(\phi) = \sum_{torsions} \frac{Vn}{2}[1 + \cos(n\tau - \phi)] \quad (18)$$

Where *n* describes a rotation that is periodic by 360˚, i.e. n=1 defines a periodicity by 360˚, n=2 defines 180˚, n=3 defines 120˚. Vn is a constant that determines the size of the barrier for rotation around the particular bond, and ϕ is the phase factor, which determines the minimum value of dihedral angle. Second big contributor to force field energy is the non-bonded energy. This term contains two types of interactions: van der Waals and electrostatics. Van der Waals forces are treated with Lennard-Jones 6-12 potential:

$$E_{FF}(\mathrm{R}_{ij}) = \sum_{i<j}^{atoms} \frac{A_{ij}}{R_{ij}^{12}} - \frac{B_{ij}}{R_{ij}^{6}} \quad (19)$$

R_{ij} is the distance between two atoms, A and B are constants relating to repulsive (exchange) and attractive (dispersive London) forces, respectively. The R^{12} term treats the repulsive forces and R^6 term treats the attractive forces. On the other hand, electrostatic interactions are derived from the assigned partial charges of the atoms, the energy is calculated by applying Coulomb`s law:

$$E_{FF}(\mathrm{R}_{ij}) = \sum_{i<j}^{atoms} \frac{q_i q_j}{\varepsilon R_{ij}} \quad (20)$$

In this equation, q_i and q_j are the partial charges of individual atoms, R_{ij} is the distance between the atoms, and ε is the dielectric constant. Parameters for force fields are determined from experimental data, *ab initio*, or semi-empirical quantum calculations. Molecular mechanics is the basis of molecular dynamics and molecular docking methods, which study time dependent behavior of large systems and ligand macromolecule interactions, respectively.

2.2.2 Molecular Dynamics

Molecular dynamics studies the time-dependent behavior of a large system by solving the Newton`s second law of motion:

$$F = ma \qquad \text{or} \qquad -\frac{d\mathrm{V}}{d\mathrm{r}} = m\frac{d^2\mathrm{r}}{dt^2} \tag{21}$$

In these equations, F is the force acting on the atom, m is the mass of the atom, a is the acceleration of the atom, V is the potential energy of the atom at position r. Initially every atom in the system is assigned velocities, and forces are calculated for new nuclear positions. At each time step the aceleration is evaulated from the forces by utilization of various algorithms that solves Newton`s equation numerically, and atomic positions are propogated in time, which constructs the trajectory. Molecular dynamics employs force fields to explore the time evolution of the system.

2.2.3 Solvation Models and Periodic Boundary Condition

An important requisite of computational chemistry is to evaulate the effect of environment on the system. Thus, inclusion of the solvent is necessary while studying the biological systems. This allows not only to examine the effect of protein-solvent interactions, but also disables the long range protein-protein interactions. There are mainly two solvent models: explicit and implicit models. In explicit models the solvent molecules physically placed into the system where in implicit model there is no solvent molecules present but they are treated with the continuum model (by dielectric constant). In this thesis, explicit solvent model was used to treat aqueous environment of systems. There are number of water molecule models available. 3-site simple point charge (SPC) water model[82] was utilized throughout this thesis. Three-site models have three interaction sites, and each atom gets assigned a point charge, oxygen atom also getting the Lennard-Jones parameters. The 3-site models are widely used in molecular dynamics simulations because of their simplicity and computational efficiency.

In order to solvate the protein there is a need of infinite number of water molecules to mimic the bulk solvent effect present in biological systems. This is ensured by periodic boundary conditions (PBC). In PBC, protein and water molecules are enclosed in a defined box (usually cubic box), which is duplicated in all directions. When a solvent molecule leaves the central box from one side of the wall, its image enters from the other side of central box. Thus, protein always interacts with the same number of water molecules, supplied with an infinite number of water molecules by PBC. Size of the

central box is chosen according to the size of protein. The box should be large enough to prevent protein seing its mirror image in the neighboring box, but too large box will increase the computational cost as the number of water molecules to fill the box will increase. In this thesis, proteins were placed inside a cubic box comprised of SPC water molecules and a size of 100x100x100 Å. This size of the box prevented proteins to interact with the mirror images of PBC . Longe range interactions and Van der Waals interactions were treated with Particle Mesh Ewald method[83,84] with the cut-off distance of 12 Å. The temperature was set to 300K.

2.2.4 Computational Methods Used in Molecular Dynamics Simulations

In this thesis all molecular dynamics (MD) simulations were performed using the GROMACS software package[85] utilizing GROMOS96 5A36 force field.[86] Proteins were placed into a cubic box filled with explicit water molecules as described in the previous section. Some water molecules were replaced by sodium and chloride ions to neutralize systems. Simulations were carried out with a NPT ensemble (fixed number of atoms, fixed pressure, fixed temperature, respectively). SETTLE algorithm[87] was implemented to constrain the bond legths and angles of water molecules, and LINCS algorithm[88] was used to constrain the peptide bond length. Long range interactions were calculated by PME method as mentioned in the previous section. Constant pressure of 1.0 bar was applied with a coupling constant of 1.0 ps, whereas protein, water molecules, and ions were coupled seperately to a bath at 300K by using v-rescale thermostat with a coupling constant of 0.1 ps. Equations of motion were integrated in every 2 fs.

Chapter 3 Peptide Cleavage Mechanism of Mononuclear Complexes

3.1 Background

Metallopeptidases catalyze the hydrolytic cleavage of amide bonds of peptides and proteins. This process involved in the control of cell cycle, transcription, signal transduction, antigen processing and apoptosis.[1] The metallopeptidases utilize conserved amino acid residues like histidine (His), aspartate (Asp), glutamate (Glu), and cysteine (Cys) to generate a scaffold capable of binding one or two metal ions, typically Zn(II), at the active sites.[28,89-98] These mononuclear or dinuclear metal centers adjust catalysis including binding and positioning the substrate, activating the nucleophile of the reaction, and stabilizing the transition state to control the activity of the enzymes.[99] In this chapter, several mononuclear metallopeptidases and their analogues with different properties will be discussed.

In nature, many mononuclear metallopeptidases possess zinc, some have cobalt, in their active sites (the critical port of enzymes where a reaction occurs).[94,96,97,100-102] The reason why nature prefers zine is owing to its unique chemical properties. Zinc is a good Lewis acid and redox stable (no reactive radicals). The coordination number of catalytic zinc sites in the enzymes can change from four to six because of its flexible geometry. Zinc can bind to the suitable sites strongly and exchange its ligand rapidly. Moreover, zinc exhibits hard-soft character which can polarize different ligands.[91]

In fact, a range of attempts to replace Zinc metal center by utilizing other alternative metals, such as cobalt, Copper, nickel, and cadmium, were successful. It was found that the enzymes with replacements presented activity or was even showing hyperactive property.[103] In the recent years, Suh and his coworkers reported that mononuclear Co(III)- and Cu(II)-containing complexes of 1,4,7,10-tetraazacyclododecane (cyclen) and 1-oxa-4,7,10-triazacyclododecane (oxacyclen) can selectively cleavage the peptide bonds in of a variety of biomolecules (Scheme 1).[104-113] In addition, Grant, K.'s lab studied the hydrolysis of a series of zirconium (a metal center also exhibits high Lewis acidity) complexes with a total of 17 different ligands.[114] Pd(II) ion containing metal complex ($[Pd(H_2O)_4]^{2+}$) conjugated with a hydrophobic environment of β-cyclodextrin (CD) was synthesized to catalyze the cleavage of a peptide bond.[115-117] Moreover, Berreau's lab proposed that mononuclear Pb(II)- and Zn(II)-complexes can methanolyze amide bond under mild conditions.[118,119] However, the structure, function, and mechanism of the these metallopeptidases and analogues that can mimic the aspects of zinc enzymes are still elusive and more knowledge are required.[120] In this regard, all the aforementioned complexes will be discussed in this chapter.

Scheme 1

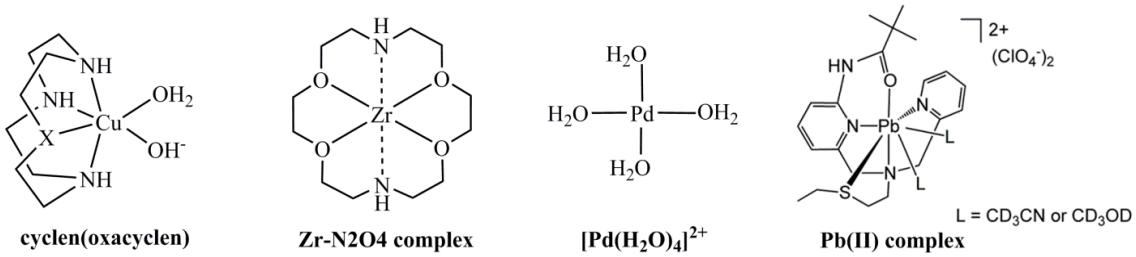

3.2 Peptide Hydrolysis by Metal-Cyclen Complexes and Their Analogues

It has been reported that Co(III)- and Cu(II)-containing complexes of 1,4,7,10-tetraazacyclododecane (cyclen) and 1-oxa-4,7,10-triazacyclododecane (oxacyclen) (**I_{MC}** and **I_{MOC}** respectively in Figure 3.1) can perform the selective proteolytic cleavage of a variety of critical biomolecules such as albumin, myoglobin, lysozyme, amyloid beta (Aβ) peptide and human islet amyloid polypeptide (h-IAPP).[104-113] In order to provide specificity to these complexes, a pendant (an organic group or an aromatic chain) was attached (**I_{CoC}** in Figure 3.1).[107,111,113] Depending on its chemical nature, the pendant functioned as a recognition site and interacted with either a specific group or region of the substrate. Furthermore, the pendant made the scissile peptide bond accessible to the peptide bond cleaving metal center. For instance, an **I_{CoC}** type of molecule was observed to hydrolyze the Phe20-Ala21 and Ala21-Glu22 peptide bonds of Alzheimer Aβ oligomers.[106,121,122]

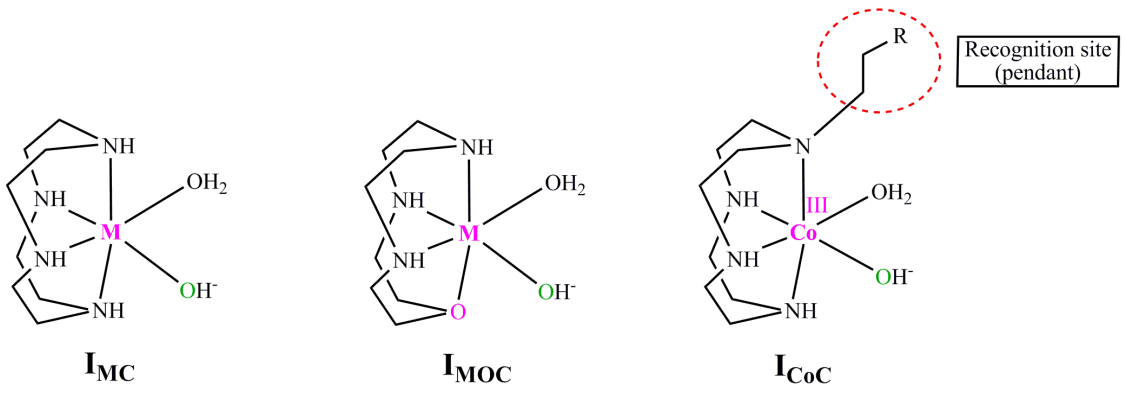

I_{MC} **I_{MOC}** **I_{CoC}**

Figure 3. 1 Structures of metal-cyclen (**I_{MC}**), metal-oxacyclen (**I_{MOC}**) and Co(III)-cyclen including pendant (**I_{CoC}**)

3.2.1 Experimentally Proposed Mechanism

$\mathbf{I_{MC}}$ and $\mathbf{I_{MOC}}$ complexes have been proposed to utilize one of the three following mechanisms generally proposed for ester and amide hydrolysis (Figure 3.2): (**A**) the electrophilic activation of the carbonyl moiety by the metal center through the formation of a single bond between the metal ion and carbonyl oxygen atom; (**B**) provision of a hydroxyl nucleophile by the metal center from a water molecule at neutral pH; and (**C**) A dual activation mechanism which is a combination of the first two and provides a way to simultaneously activate the carbonyl bond and to generate the hydroxyl nucleophile.[108,123,124] The first two mechanisms (**A** and **B**) are kinetically indistinguishable and have been a subject of much debate for several decades. Using X-ray crystallography, Lipscomb et al. demonstrated that peptide bond cleaving metalloenzymes utilize the dual activation mechanism (**C**).[91,125] This mechanism is likely more efficient and has been proposed for the Co(III)-cyclen ($\mathbf{I_{CoC}}$) complex.[108,123] According to this mechanism, at the starting point of the reaction the $\mathbf{I_{CoC}}$ complex is coordinated to a water molecule and hydroxyl ion. In the first step, the water molecule is substituted by the substrate through the formation of a bond between its carbonyl oxygen atom and the metal ion **($\mathbf{II_{CoC}}$)**. The formation of this bond polarizes the scissile peptide bond (-C-N-). In the next step, the metal bound hydroxyl nucleophile attacks the peptide bond and creates a tetrahedral intermediate **($\mathbf{III_{CoC}}$)** containing a four-membered ring. The catalytic rate of this reaction was proposed to depend on the stability of the rate-determining transition state which is affected by the Lewis acidity of the Co(III) ion and the geometry of the complex formed between the metal ion and the chelating ligand.[108] In the final step, the collapse of $\mathbf{III_{CoC}}$ through a proton transfer to the amine group leads to

the cleavage of the peptide bond (-C-N-) and the formation of separated amine ($-NH_2$) and carboxyl (-COO) termini (**IV$_{CoC}$**).

The measured rate constants (k_{cat}) is 0.07 (h^{-1}) for the cleavage of myoglobin by Co(III)-containing complexes of cyclen without pendant (**I$_{CoC-P}$**) at pH 9.0 and 50°C correspond to barriers of 25.9 kcal/mol. On the other hand, the rate constants (k_{cat}) is 0.3 (h^{-1}) for Co(III)-oxacylen (**I$_{CoOC-P}$**) under the same conditions.[105] The measured k_{cat} values were converted into barriers using the Arrhenius equation ($k = Ae^{-Ea/RT}$, where A is the pre-exponential factor, Ea is the activation energy, R is the gas constant and T is the temperature). **I$_{CoOC-P}$** exhibited four times greater activity than **I$_{CoC-P}$** for this substrate. In **I$_{CoOC-P}$** the pK_a values for the Co(III)-bound water molecules revealed a higher Lewis acidity for the Co(III) center (pK_{a1} = 3.33 and pK_{a2} = 6.96) compared to **I$_{CoC-P}$** (pK_{a1} = 5.66 and pK_{a2} = 8.14).[105] This is because the oxygen of oxacyclen in the N_3O ligand environment is less basic than the nitrogen of cyclen in the N_4 environment. Thus, the observed improvement in the activity of the oxacyclen analogue (**I$_{CoOC-P}$**) is likely to be due to the increased Lewis acidity of the metal center and steric effects in the transition state corresponding to the **III$_{CoC}$** intermediate. On the other hand, a pendant containing complex of Co(III)-oxacyclen (**I$_{CoOC}$**) was reported to cleave the myoglobin substrate with a barrier of 24.7 kcal/mol at pH = 8.0 and 50 °C.[126]

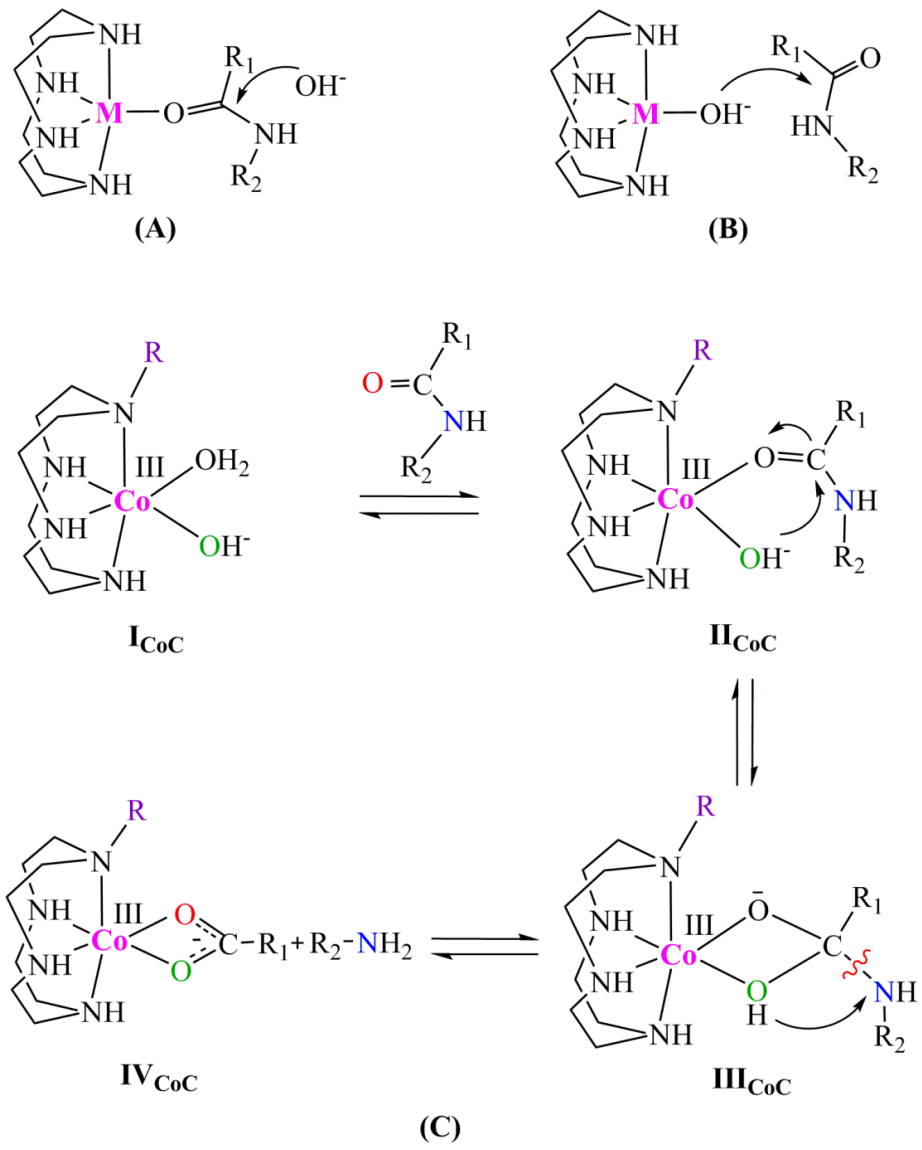

Figure 3. 2 The experimentally proposed mechanism of peptide hydrolysis.

The measured kinetics regarding the functioning of a Cu(II)-cyclen complex without a pendant are not available. But for a pendant containing Cu(II)-cyclen complex ($\mathbf{I_{CuC}}$) the measured k_{cat} values of 0.58, 0.75, and 1.4 (h^{-1}) for the cleavage of myoglobin, lysozyme, and γ-globulin respectively at pH 9.0 and 50°C.[109] The corresponding barriers is 24.5,

24.3, and 23.9 kcal/mol. Whereas, the Cu(II)-oxacyclen complexes without and with pendant ($\mathbf{I_{CuOC\text{-}P}}$ and $\mathbf{I_{CuOC}}$) cleave myoglobin with a barrier of 25.7 kcal/mol and ~25.0 kcal/mol respectively under the similar conditions.[104,126]

Despite the availability of the aforementioned experimental information, there are several unresolved issues regarding the mechanisms, structures, roles of the metal ion, ligand environment, and pendant functioning on the energetics of this reaction. For instance, based on the orientation of the hydrogen atoms attached to nitrogen atoms, the reactant can exist in the following four conformations: (1) *anti-anti* (N^4H and $N^{10}H$ hydrogen atoms are on the opposite sides of the metal), (2) *syn-syn* (N^4H and $N^{10}H$ hydrogen atoms are on the same sides of the metal), (3) *syn-anti* (N^4H is on the same and $N^{10}H$ is on the opposite side of the metal) and (4) *anti-syn* (N^4H is on the opposite and $N^{10}H$ is on the same side of the metal), Figure 3.3. The conformations of the reactants for these complexes are not known experimentally. The exact mechanism of the reaction is also not well understood. The binding site (1, 4, 7 or 10 position of the cyclen ring) of the pendant on this complex and its effect on the energetics of the reaction also remain unknown. Furthermore, the influence of different metals on the energetics of this reaction using the same substrate is not available.

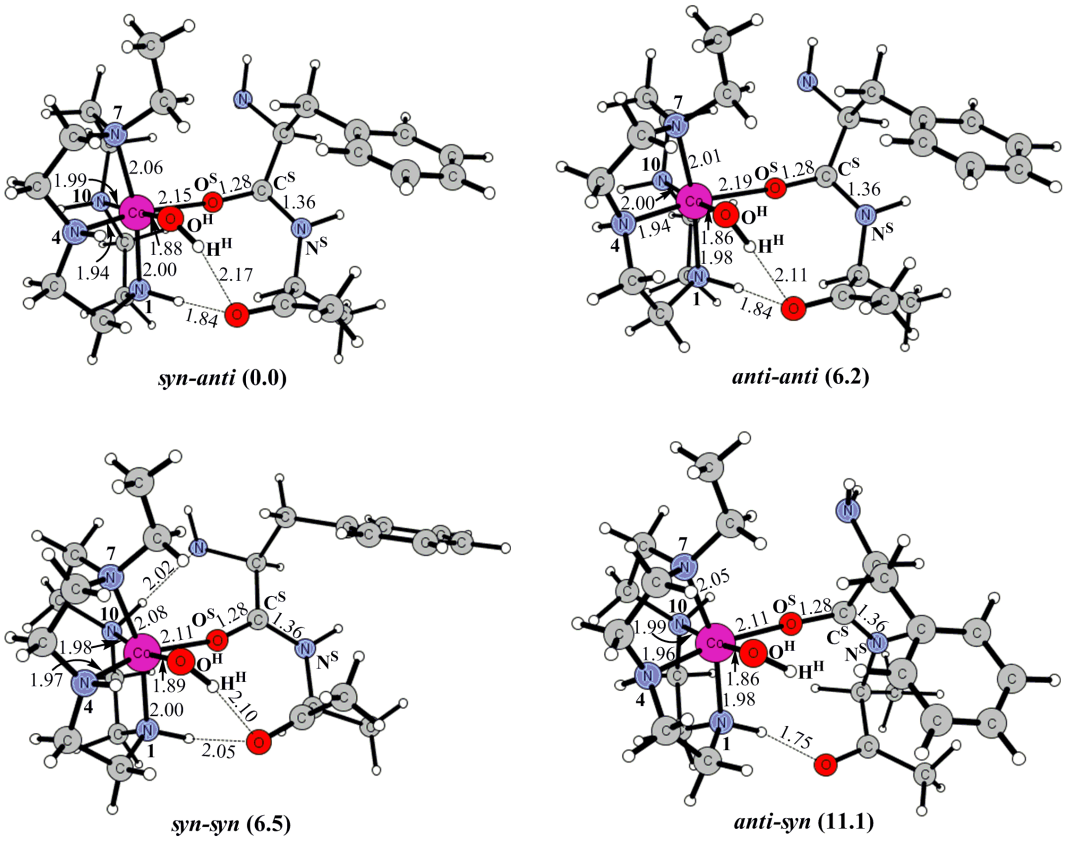

Figure 3. 3 Optimized structures of the reactants of the Co(III)-cyclen complex (in kcal/mol).

In this study, we have addressed all these issues through investigation of the hydrolysis of the Phe-Ala peptide bond of a amyloid beta (Aβ42) peptide by cyclen and oxacyclen complexes containing different metals using density functional theory (DFT) calculations. The available experimental information has been fully utilized in these studies. The results gleaned from our calculations will elucidate the roles of the metal, ligand environment and pendant on the energetics of this critical reaction. They will also

provide structures of short-lived intermediates and transition states that cannot be observed through experimental techniques. Our studies will also help to develop the next generation of synthetic analogues for efficient peptide hydrolysis.

3.2.2 Computational Methods

All calculations were performed using the Gaussian 03 program package.[79] The geometry optimizations of reactants, intermediates, transition states and products were performed at the B3LYP/Lanl2dz level without any geometrical constraint using the corresponding Hay-Wadt effective core potential (ECP) for the metal ion.[62,127,128] The final energies of the optimized structures were further improved by performing single point calculations including additional d and p polarization functions for O (α=0.96), N (α=0.74), C (α=0.59) and H (α=0.36) atoms, respectively (taken from the EMSL's Gaussian basis set library) in the basis set used for optimizations. Hessians were calculated at the same level of theory as the optimizations to confirm the nature of the stationary points along the reaction coordinate. The transition states were confirmed to have only one negative eigenvalue corresponding to the reaction coordinates. The dielectric constant of 78.39 corresponding to water was used to estimate the effect of the solvent[129] utilizing the self-consistent reaction field IEFPCM method[130] at the B3LYP/Lanl2dz level. Throughout the manuscript, the energies obtained at the B3LYP/{Lanl2dz + d(O, N and C) + p(H)}[123,131] level including thermal corrections and solvent effects in water are discussed.

To test the accuracy of the B3LYP method, the barrier of the reaction computed using this functional was compared with calculations performed using the M06-L functional[132]

for the $\mathbf{I_{CuC}}$ complex. It was found that, in comparison to the B3LYP functional, the application of the M06-L functional increased the barrier by 2.5 kcal/mol.

3.2.3 Computational Models

In the models, the metal ion was coordinated either to the 1,4,7,10-tetraazacyclododecane (cyclen) or 1-oxa-4,7,10-triazacyclododecane (oxacyclen) macrocycle. The organic pendant was modeled as the ethyl group ($-C_2H_5$) and attached to the N^7 atom of the macrocycle. This site was found to be the most energetically stable location for the pendant. Based on experimental information, a dipeptide consisting of the Phe20-Ala21 peptide bond taken from Aβ42 was used as the substrate. To study the roles of different metals on the energetics of the reaction, the Cu(II) ion was substituted by other divalent metals like Ni(II), Pd(II), Zn(II) and Cd(II). The reactants of the Co(III), Pd(II), Zn(II) and Cd(II) existed in the singlet state. The Cu(II)-cyclen complex existed in the doublet spin state, which the Ni(II) preferred the high spin triplet state. The overall charge was +2 for the Co(III) complex and was +1 for all other metal ions.

3.2.4 Results and Discussion

First, the mechanisms of the peptide bond (Phe-Ala) hydrolysis by the Co(III)- and Cu(II)-cyclen complexes have been discussed. In addition, the activities of the oxacyclen analogues of Co(III) and Cu(II) have been explored. Finally, the effects of the metal substitution (Ni(II), Pd(II), Zn(II) and Cd(II)) on the energetics of the reaction have been discussed.

3.2.4.1 Mechanisms of the Co(III)- and Cu(II)-Cyclen Complexes ($\mathbf{I_{CoC}}$ and $\mathbf{I_{CuC}}$).

In all the metal-cyclen (M-Cyc) complexes, the metal ion is coordinated to the cyclen macrocycle, a hydroxyl ion and one water molecule. In the first step of the mechanism, the dipeptide (Phe-Ala) substrate substitutes the metal bound water molecule and interacts with the M-Cyc complex. The formation of this bond polarizes the scissile peptide bond (C^S-N^S). Depending on the orientations of the protons bound to the N^4 and N^{10} atoms, the reactant can exist in the following four conformations: *syn-anti*, *anti-anti*, *syn-syn* or *anti-syn* (Figure 3.3).[133,134] In the *syn* conformation, protons bound to the N^4 or N^{10} atoms face the substrate, while in the *anti* conformation they are located on the opposite side of the substrate.

The optimization of the reactant ($\mathbf{II_{CoC}}$) for the Co(III)-cyclen complex predict the *syn-anti* conformer as the most stable structure followed by *anti-anti*, *syn-syn*, and *anti-syn* that are 6.2, 6.5, and 11.1 kcal/mol higher in energy, respectively. This result is supported by the NMR data and X-ray structures of other Co-cyclen complexes. The measured NMR data of $[Co(cyclen)Cl_2]^+$ and the X-ray structure of $[Co(cyclen)(NO_2)_2]^+$ showed that they existed in the *syn-anti* conformation.[135,136] The X-ray structures of both $[Co(cyclen)(NH_3)_2]^{3+}$ and $[Co(cyclen)(diamine)]^{3+}$ (diamine = $H_2N(CH_2)_2NH_2$, $H_2N(CH_2)_3NH_2$) complexes were also crystallized in the *syn-anti* conformation.[137] In $\mathbf{II_{CoC}}$, the sum of all four angles (N^1-Co-N^4, N^1-Co-N^{10}, N^4-Co-N^7 and N^{10}-Co-N^7) is 342.91°. The barriers for the inter-conversion of different isomers e.g. *syn-syn* → *anti-syn* is prohibitively high.

However, in the Cu(II)-cyclen case the reactant ($\mathbf{II_{CuC}}$) exists in the *syn-syn* conformation (Figure 3.4). This structure is also supported by the experimentally measured structural data of the Cu(cyclen)$(NO_3)_2$ and Cu(cyclen)Br_2 complexes that showed both favored the *syn-syn* conformation.[138] The *anti-syn*, *syn-anti* and *anti-anti* structures are 1.1, 3.3 and 4.8 kcal/mol higher in energy than the *syn-syn* isomer, respectively. For divalent metal ions, these energy differences are due to alterations in the N^1-Cu-N^7 and N^4-Cu-N^{10} angles (Figure 3.4). These angles determine the strain of the cyclen ring and the stability of the reactants. The sum of these angles is different in all four conformors (281.06° for *syn-syn*, 256.17° for *anti-syn*, 266.58° for *syn-anti* and 241.84° for *anti-anti*).

3.2.4.1.1 Stepwise Mechanism

As discussed above, the reactant **($\mathbf{II_{CoC}}$)** of the Co(III)-cyclen complex exists in the *syn-anti* conformation (Figure 3.5). In $\mathbf{II_{CoC}}$, the hydroxyl nucleophile ($-O^HH^H$) is coordinated to the Co(III) ion and the Co-O^S bond polarizes the scissile C^S-N^S peptide bond (Co-O^H = 1.88 Å, Co-O^S = 2.15 Å and O^S-C^S = 1.28 Å). In the first step of the mechanism, from $\mathbf{II_{CoC}}$ the Co(III) bound hydroxyl ion ($-O^HH^H$) makes a nucleophilic attack on the C^S atom of the scissile peptide bond (C^S-N^S). The optimized transition state ($\mathbf{TS1_{CoC\text{-}SW}}$) for this process is shown in Figure 3.5. In comparison, the Co-O^H and C^S-O^S bond distances increased by 0.08 and 0.03 Å respectively and the Co-O^S bond decreased by 0.2 Å in $\mathbf{TS1_{CoC\text{-}SW}}$ (Co-O^1 = 1.96 Å, C^S-O^S = 1.31 Å, and O^H-C^S = 1.76 Å). It is noteworthy that the C^S-N^S bond is significantly elongated by 0.08 Å in this transition

state (C^S-N^S = 1.44 Å). The barrier for this step is 24.1 kcal/mol and it leads to the formation of a tetrahedral intermediate (**III$_{CoC-SW}$**). In **III$_{CoC-SW}$**, the hydroxyl group (-O^HH^H) attached to the C^S and the C^S-N^S peptide bond is significantly activated (C^S-N^S = 1.48 Å) and perfectly set up for cleavage in the next step. The generation of **III$_{CoC-SW}$** is endothermic by 22.5 kcal/mol from **II$_{CoC}$**.

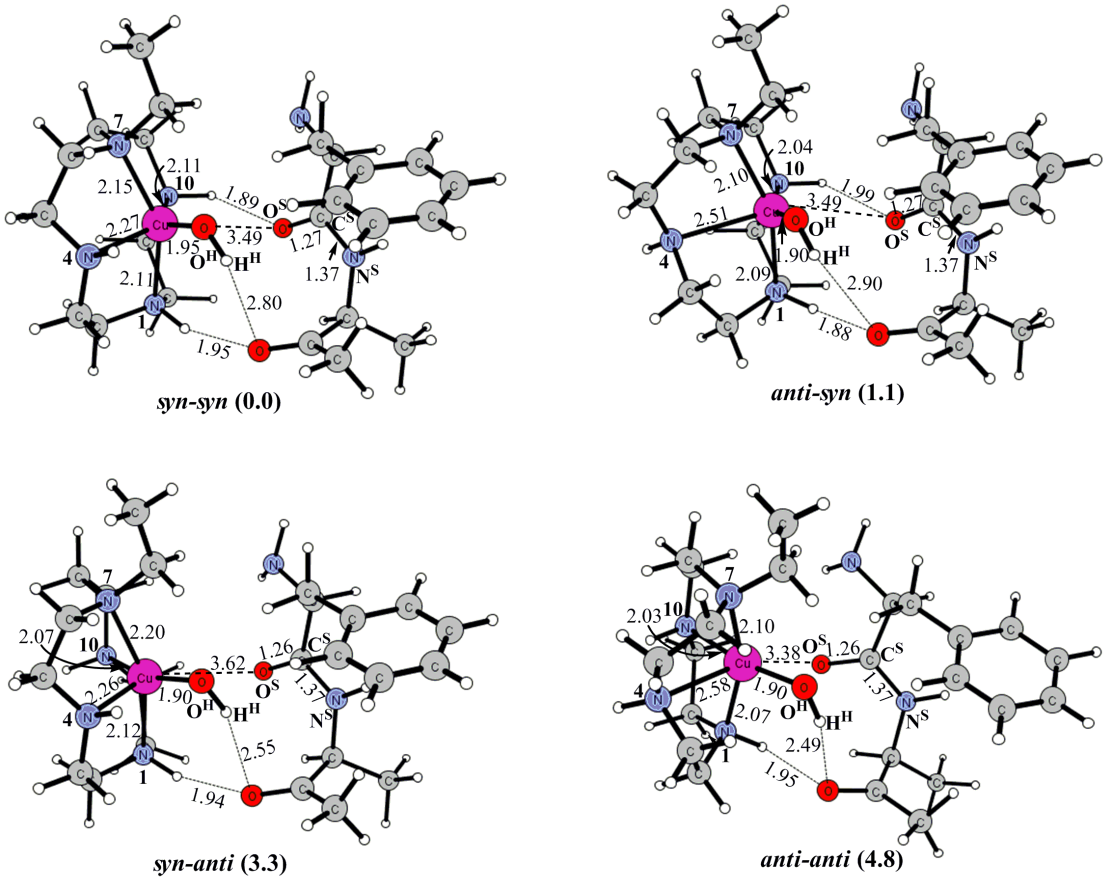

Figure 3. 4 Optimized structures of the reactants of the Cu(II)-cyclen complex (in kcal/mol).

In the next step, from **III$_{CoC-SW}$** the H^H proton from the C^S bound hydroxyl group (-O^HH^H) is transferred to the N^S atom of the peptide bond. This transfer occurs concomitantly with the cleavage of the C^S-N^S peptide bond. The barrier for this

synchronous process is 19.5 kcal/mol from $\mathbf{III_{CoC\text{-}SW}}$. Since this step follows a step that is endothermic by 22.5 kcal/mol, the overall barrier from $\mathbf{II_{CoC}}$ becomes 42.0 kcal/mol. This step is the rate-limiting step of the entire mechanism. All the corresponding distances in the optimized transition state for this process ($\mathbf{TS2_{CoC\text{-}SW}}$) indicate that this process is concerted (O^H-H^H = 1.27 Å, H^H-N^S = 1.29 Å and N^S-C^S = 1.59 Å). The computed barrier is similar to those (38-40 kcal/mol) computed for the hydrolysis of the *Gly-Pro-Met, Gly-Pro-His, Gly-Sar-Met* and *Gly-Gly-Met* peptide bonds by $[Pd(H_2O)_4]^{2+}$.[139] This process creates the product ($\mathbf{IV_{CoC}}$) in which the N- terminal is separated, but the C- terminal is still bound to the metal center. The formation of $\mathbf{IV_{CoC}}$ is exothermic by 13.3 kcal/mol from $\mathbf{II_{CoC}}$.

However, in the Cu(II)-cyclen complex, in contrast to its Co(III) counterpart, the reactant ($\mathbf{II_{CuC}}$) exists in the *syn-syn* conformation and in the absence of the metal-O^S bond, the polarization of the peptide bond is missing. The reason for these structural changes is the difference in the coordination number of the Cu(II) and Co(III) ions that is 5 for the former and 6 for the latter. Furthermore, the overall charge of the Co(III)-cyclen complex is one unit greater than the Cu(II)-cyclen complex. In $\mathbf{II_{CuC}}$, all the metal-ligand bond distances are longer compared to $\mathbf{II_{CoC}}$. For instance, the Cu-N^1, Cu-N^4, Cu-N^7 and Cu-N^{10} bond distances in the cycle macrocycle are longer by 0.11, 0.33, 0.09 and 0.12 Å respectively and the Cu-O^H bond length is elongated by 0.07 Å (Cu-N^1 = 2.11 Å, Cu-N^4 = 2.27 Å, Cu-N^7 =2.15 Å, Cu-N^{10} = 2.11 Å and Cu-O^H = 1.95 Å), Figure 3.6. Furthermore, even the scissile peptide bond (C^S-N^S) is 0.01 Å longer than the one found for the Co(III)-cyclen complex (C^S-N^S = 1.37 Å). From $\mathbf{II_{CuC}}$, the creation of the tetrahedral intermediate ($\mathbf{III_{CuC\text{-}SW}}$) occurs with a barrier of 19.8 kcal/mol and the optimized

transition state (**TS1$_{CuC-SW}$**) for this process is shown in Figure 3.6 (Cu-O^H = 2.35 Å, Cu-O^S = 2.26 Å and O^S-C^S = 1.35 Å). Similar to the Co(III)-cyclen case, in **TS1$_{CuC-SW}$** the C^S-N^S bond is significantly activated by 0.09 Å (C^S-N^S = 1.46 Å). The creation of **III$_{CuC-SW}$** in this process is endothermic by 14.7 kcal/mol. The barrier of this step is 7.8 kcal/mol lower than the computed value for the Co(III)-cyclen complex. This is rather surprising considering the absence of the polarization of the peptide bond by **II$_{CuC}$**. However, there are several factors that contribute to the differences in the calculated energetics of these complexes. The geometries of the cyclen macrocycle are different in both complexes. **II$_{CuC}$** contains one less ligand than **II$_{CoC}$**. The charge on the Cu(II) ion in **II$_{CuC}$** is 0.18e greater than the Co(III) ion in **II$_{CoC}$**. The charge on the O^H atom of the metal bound hydroxyl in **II$_{CuC}$** is also 0.11e more negative than the charge on the corresponding atom in **II$_{CoC}$**. As a result, the Cu-O^H bond distance is also 0.07 Å longer than the Co-O^H bond distance. All these differences indicate that, in comparison to **II$_{CoC}$**, the hydroxyl ion in **II$_{CuC}$** is a better nucleophile. In the next step, as discussed in the Co(III)-cyclen case, a proton transfer from the C^S bound hydroxyl group (-O^HH^H) to the N^S atom leads to the cleavage of the peptide bond. From **III$_{CuC-SW}$**, the barrier and exothermicity of this process are 19.0 and 30.3 kcal/mol respectively. Since this step follows a step that is endothermic by 14.7 kcal/mol, the overall barrier from **II$_{CuC}$** becomes 33.7 kcal/mol. Similar to the Co(III)-cyclen complex, this step is the rate-limiting step of the entire mechanism. The barrier for this complex is approximately 8.0 kcal/mol higher than the barrier experimentally measured for the cleavage of myoglobin, lysozyme, albumin and γ-globulin substrates by Cu(II)-cyclen complexes.[109] This overestimation could be due to a difference in the substrates, as well as, the measurement of rate constants at a much

higher temperature (50 °C). In comparison, our calculations were performed at room temperature (25 °C). Due to the temperature dependence of the pre-exponential constant in the Arrhenius equation, it is not possible to accurately estimate the measured barrier at 25 °C.

These results explicitly show that only the first step involving the generation of the tetrahederal intermediate contributes to the difference in the energetics of this reaction for $\mathbf{II_{CoC}}$ and $\mathbf{II_{CuC}}$. The overall barrier for the $\mathbf{II_{CuC}}$ complex is 8.3 kcal/mol lower than the barrier computed for the $\mathbf{II_{CoC}}$ complex.

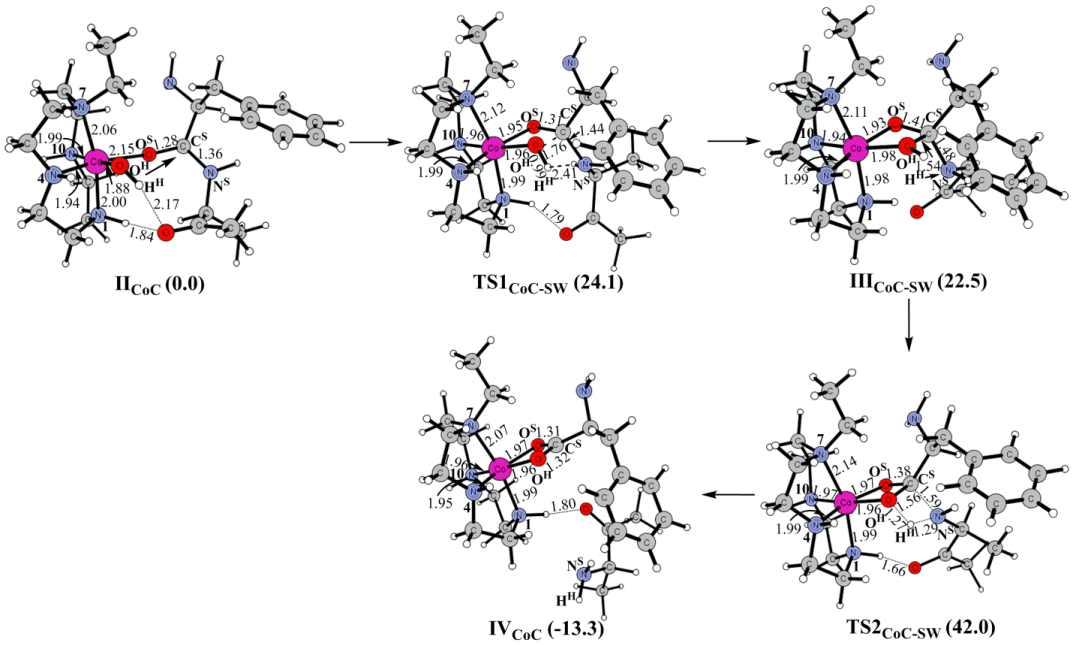

Figure 3. 5 Structures (in Å) and energies (in kcal/mol) of the reactant, transition states, intermediate and product in the stepwise mechanism of the Co(III)-cyclen complex.

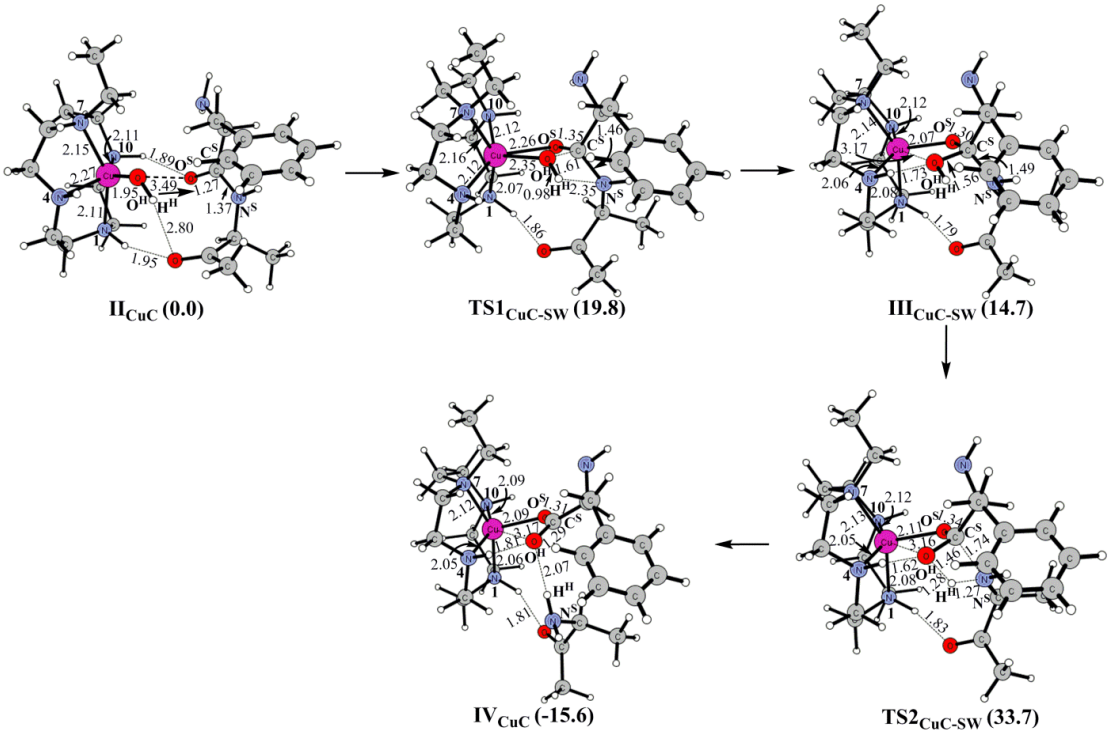

Figure 3. 6 Structures (in Å) and energies (in kcal/mol) of the reactant, transition states, intermediate and product in the stepwise mechanism of the Cu(II)-cyclen complex.

3.2.4.1.2 Concerted Mechanism

In the concerted mechanism for the Co(III)-containing complex, from the *syn-anti* reactant (**II$_{CoC}$**) the hydroxyl group (-O^{H}H^{H}) is transferred to the C^{S} of the peptide bond concomitantly with the dissociation of the -O^{H}H^{H} and transfer of the H^{H} atom to the C^{S} atom of the substrate. This synchronous process cleaves the peptide bond and directly leads to the formation of the product (**IV$_{CoC}$**). The barrier of 39.8 kcal/mol for this mechanism is 2.2 kcal/mol lower than the value (42.0 kcal/mol) computed for the

stepwise mechanism. In the optimized transition state ($\mathbf{TS_{CoC}}$ in Figure 3.7), all the relevant bond distances indicate that this process is concerted (O^H-C^S = 1.59 Å, H^H-N^S = 1.32 Å, O^H-H^H = 1.24 Å, N^S-C^S = 1.59 Å). The removal of the pendant (-C_2H_5 group) in this complex significantly lowers the barrier by 9.3 kcal/mol to 30.5 kcal/mol. This reduction is likely caused by the following changes in the structure of the cyclen ring. The absence of the electron donating –CH_2CH_3 group increases the negative charge on the nitrogen atom (N^7) it was attached to and in turn raises the positive charge on the Co(III) ion. This results in enhanced polarization of the peptide bond and an increase in the nucleophilicity of the hydroxyl nucleophile. The computed barrier for this complex (without pendant) is in good agreement with the measured value of 25.9 kcal/mol for the cleavage of myoglobin by the corresponding Co(III)-cyclen complex ($\mathbf{I_{CoC\text{-}P}}$) at pH 9.0 and 50°C.[105]

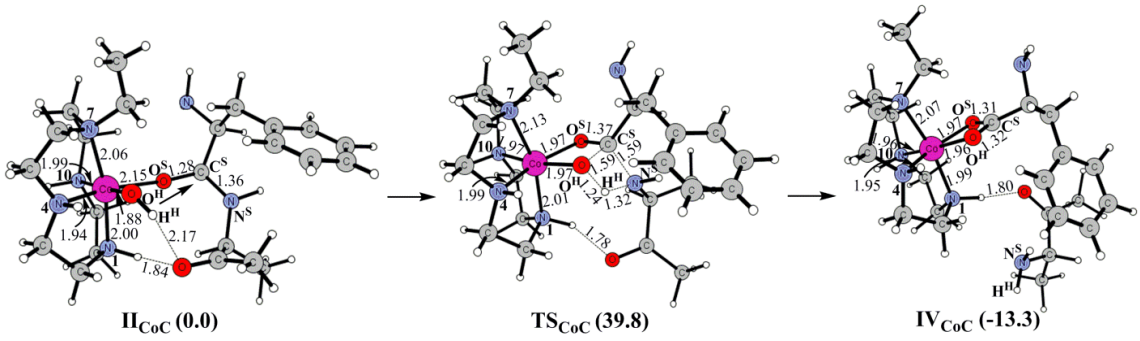

Figure 3. 7 Structures (in Å) and energies (in kcal/mol) of the reactant, transition states, intermediate and product in the concerted mechanism of the Co(III)-cyclen complex.

For the Cu(II)-cyclen complex, the reaction through the concerted mechanism occurs with a barrier of 32.7 kcal/mol from $\mathbf{II_{CuC}}$. Similar to the Co(III) case, this barrier is slightly (1.0 kcal/mol) lower than the barrier computed for the stepwise mechanism. The difference in barrier of 7.1 kcal/mol between the Co(III)- and Cu(II)-cyclen complexes using this mechanism is also similar to 8.3 kcal/mol computed for the stepwise mechanism. In the optimized transition state ($\mathbf{TS_{CuC}}$ in Figure 3.8), all the corresponding distances indicate that this process is concerted (O^H- C^S = 1.51 Å, H^H-N^S = 1.27 Å, O^H-H^H = 1.27 Å and N^S-C^S = 1.69 Å). As observed for the Co(III)-containing complex, due to exactly the same reasons, the removal of the pendant reduces the barrier by 3.0 kcal/mol to 29.7 kcal/mol.

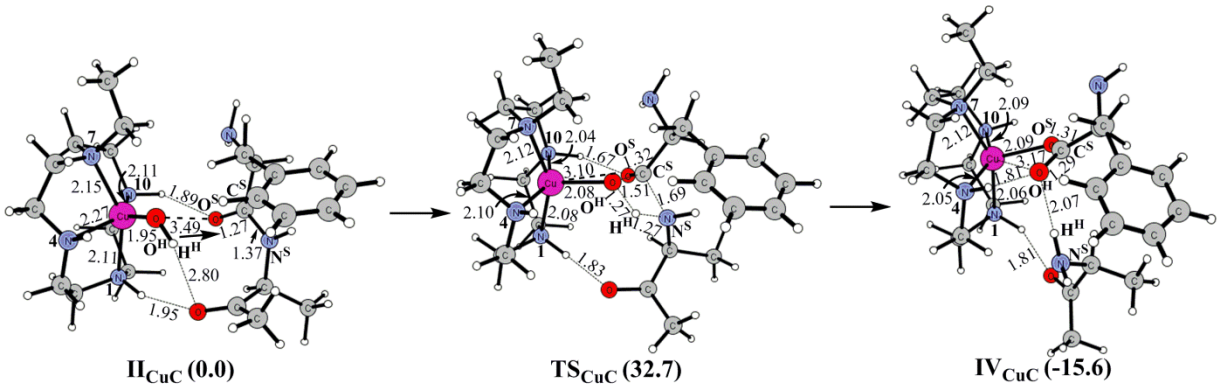

Figure 3. 8 Structures (in Å) and energies (in kcal/mol) of the reactant, transition states, intermediate and product in the concerted mechanism of the Cu(II)-cyclen complex.

These results show that the inclusion of an organic pendant increases the barrier for the reaction. The barrier for the concerted mechanism is also slightly lower than the stepwise mechanism. Therefore, only this mechanism has been utilized in the remaining studies.

3.2.4.2 Mechanisms of the Co(III)- and Cu(II)-Oxacyclen Complexes

In order to improve the peptide bond cleaving activity of metal-cyclen complexes, one of the nitrogen atoms of the cyclen ring (N_4) was substituted with an oxygen atom to develop metal-oxacyclen (N_3O) complexes.[105] Due to the increased Lewis acidity of the metal center and steric effects, both Co(III)- and Cu(II)-oxacyclen complexes without pendant ($\mathbf{I_{CoOC\text{-}P}}$ and $\mathbf{I_{CuOC\text{-}P}}$) were observed to exhibit slightly improved activities.[104,105] However, out of four nitrogen atoms (N^1, N^4, N^7 and N^{10}) which one is exactly replaced by the oxygen atom in these complexes has not been determined.[104,105] Based on the N → O substitution, three different groups (7-alkyl-1-oxa-4,7,10-triazacyclododecane (**I**), 7-alkyl-4-oxa-1,7,10-triazacyclododecane (**II**) and 7-alkyl-10-oxa-1,4,7-triazacyclododecane (**III**)) of Co(III)-oxacyclen can be formed (Figure 3.9). In group **I**, the oxygen atom is located in the trans position to the alkylated N^7 atom at site 1, while in **II** and **III** this atom is positioned at 4 and 10 sites of the cyclen ring respectively. For group **I**, four different isomers (*syn-anti*, *anti-anti*, *anti-syn* and *syn-syn*) are possible depending on the orientation of the two hydrogen atoms on N^4 and N^{10}. In addition, two isomers each (*syn* and *anti*) exist for the **II** and **III** groups. The *syn-anti*, *syn* and *syn* isomers are the energetically most stable in **I**, **II** and **III** respectively. Among these three conformations the *syn* isomer of **III** (*B-syn*) is the most stable and *syn-anti* of **I** and *syn* of **II** (*A-syn*) are 1.1 and 3.8 kcal/mol higher in energy respectively. These results suggest that the oxygen atom should be located at the 10 or 1 position on the oxacyclen ring. Due to small difference in the energies of these complexes, the energetics of the reaction for all has been computed using the "concerted" mechanism.

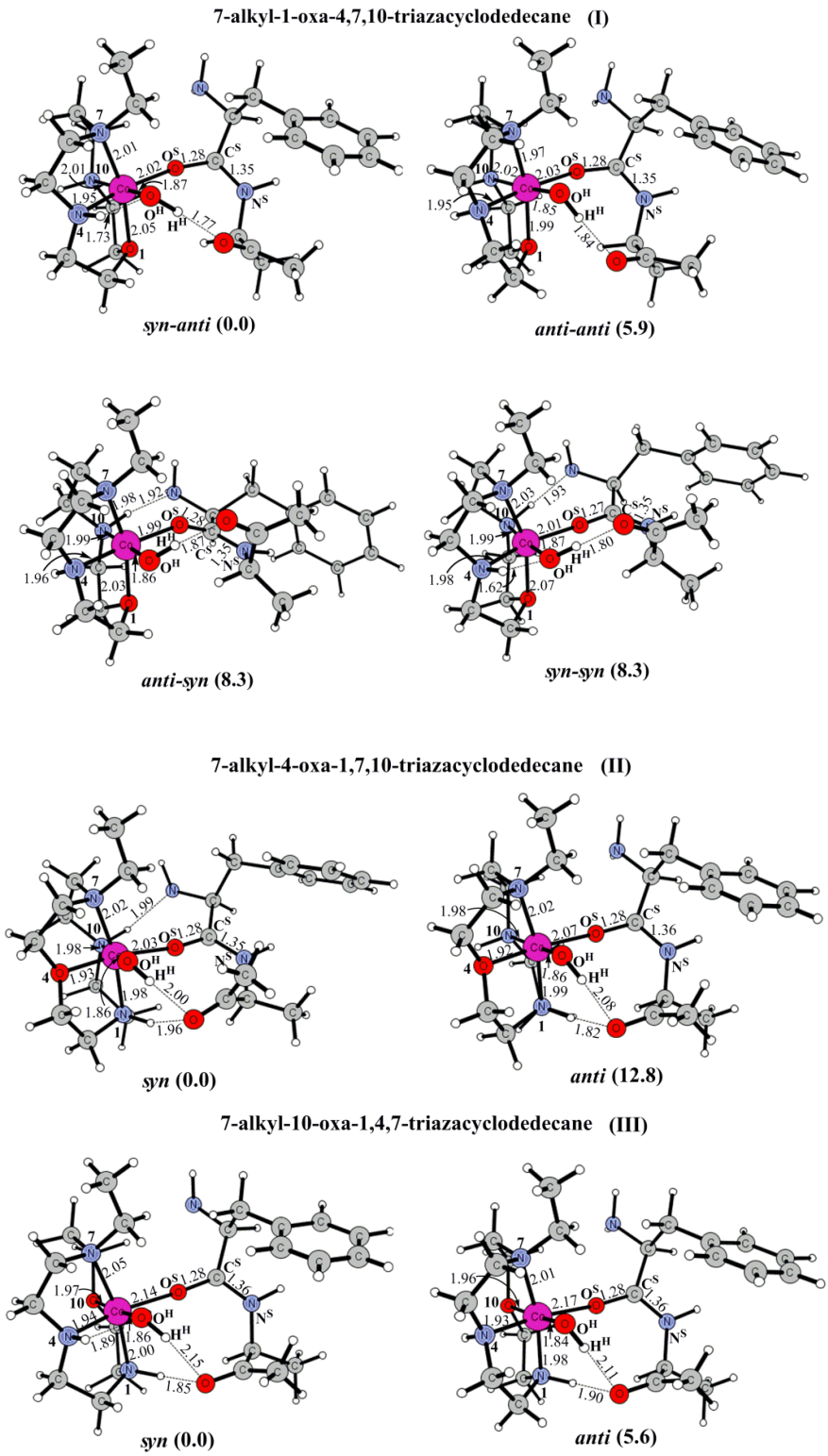

Figure 3. 9 Eight reactant structures of **II_{CoC}-oxacyclen** (in kcal/mol).

A comparison between the reactants of the common conformation (*syn-anti*) for the Co(III)-cyclen and Co(III)-oxacyclen complexes shows that the substitution of the nitrogen with oxygen at 1 position in the macrocycle reduces the Co-N^7 distance by 0.05 Å and increases the Co-N^{10} by 0.02 Å (Figure 3.3 and 3.9). The charge on the Co(III) ion is greater by 0.04e and the Co(III)-O^S bond is significantly stronger (by 0.13 Å) in the oxacyclen case. A comparison of the barriers for this conformation (*syn-anti*) shows that both cleave the peptide bond with similar barriers i.e. 40.1 kcal/mol for Co(III)-oxacyclen and 39.8 kcal/mol for Co(III)-cyclen. The computed barriers are in agreement with the measured kinetics that shows that the oxacyclen complex exhibits only four times greater activity than the cyclen complex.[105] Using transition state theory, this difference corresponds to only a 0.7 kcal/mol difference in the barrier and is too small to compute using theoretical methods. The barriers for the B-syn and A-syn isomers are computed to be 42.7 and 39.5 kcal/mol respectively (Figure 3.10a).

For the Cu(II)-containing complex the *syn-anti*, *A-syn* and *B-syn* isomers are found to be the most stable conformations in the **I**, **II** and **III** groups respectively. Among them the *A-syn* of **II** is the most stable and *B-syn* of **III** and *syn-anti* of **I** are 0.8 and 1.4 kcal/mol higher in energy respectively (Figure 3.11). This indicates that the oxygen atom in the oxacyclen ring should be located at position 4 of the ring for the Cu(II) ion, but the other two positions are also possible. Unlike the Co(III) case, in comparison to the Cu(II)-cyclen, the substitution of the nitrogen with oxygen at position 1 in the Cu(II)-oxacyclen complex increases the Cu-N^7 distance by 0.07 Å and decreases the Cu-N^{10} by 0.07 Å (Figure 3.4 and 3.11). Furthermore, the charge on the Cu(II) ion is greater by 0.09e and the Cu(II)-O^H bond is substantially shorter by 0.09 Å in the oxacyclen case.

From the *syn-anti* conformation, the reaction proceeds with a barrier of 32.5 kcal/mol. As observed in the Co(III) case, this barrier is slightly (0.2 kcal/mol) lower than the computed value (32.7 kcal/mol) for the corresponding cyclen complex. In comparison to the *syn-anti* conformation, the barriers from the other two conformations (*A-syn* and *B-syn*) are higher by 5.5 kcal/mol i.e. (38.0 kcal/mol) (Figure 3.10b). The computed barrier (32.7 kcal/mol) from the *syn-anti* conformation is in agreement with the measured value of ~25.0 kcal/mol at pH 9.0 and 50°C.[126]

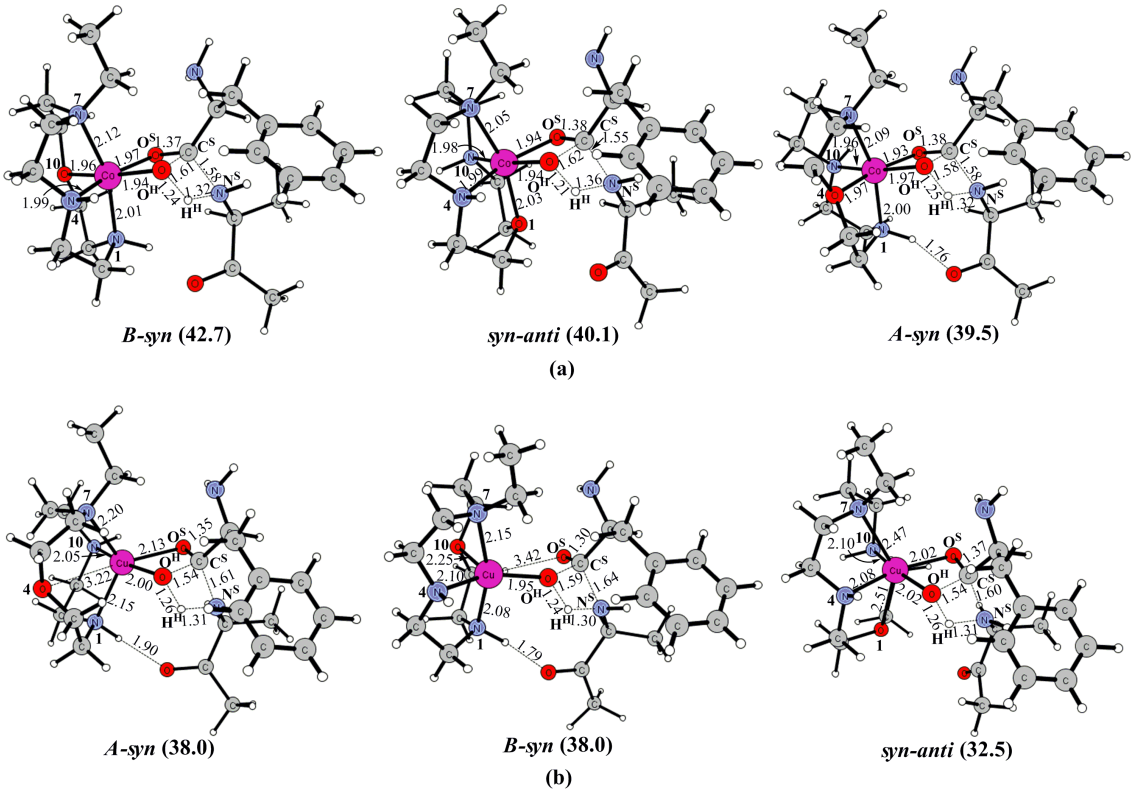

Figure 3. 10 Structures (in Å) and energy barriers (in kcal/mol) of the transition states in the concerted mechanisms of (**a**) Co(III)-oxacyaclen and (**b**) Cu(II)-oxacyaclen

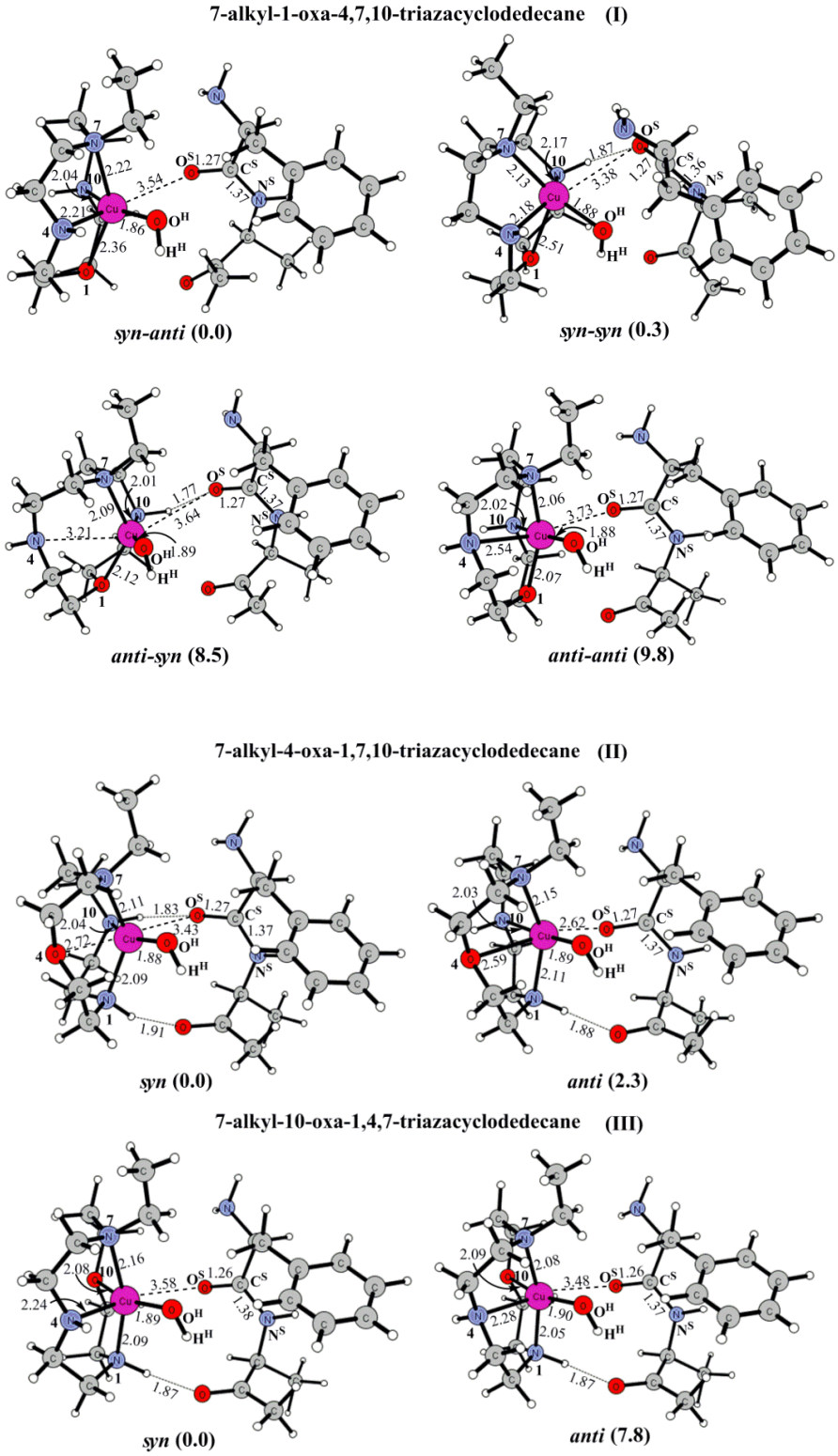

Figure 3. 11 Eight reactant structures of **II$_{CuC}$-oxacyclen** (in kcal/mol).

3.2.4.3 Metal Substitution

In order to elucidate the effect of the metal ion, the energetics of this reaction have been computed by substituting Cu(II) with other divalent metals (Ni(II), Zn(II), Cd(II), and Pd(II)) in the cyclen containing complexes without a pendant. These metals are experimentally known to coordinate to the cyclen macrocycle, but the structures and measured hydrolysis rates of the metal-cyclen complexes are not available.[140] The Ni(II), Zn(II), Cd(II), Pd(II) and Co(III) ions have been reported to form stable complexes with six coordination number.[90] Based on this information, the same hexacoordinated structures of metal-cyclen complexes are used in this study.

In the reactants (**II$_{NiC}$**, **II$_{CuC}$**, **II$_{CdC}$**, **II$_{CoC}$**, **II$_{ZnC}$**, and **II$_{PdC}$**), the metal ion is coordinated to the N^1, N^4, N^7, and N^{10} atoms of the cyclen ring, a hydroxyl ion and the substrate (Figure 3.12). The reactant for the Cu(II)-cyclen complex exists in the doublet spin state. The Ni(II)-cyclen exists in the high spin triplet state, whereas, the Zn(II), Cd(II), and Pd(II) containing complexes exist in the singlet state. The Pd(II)-cyclen complex in the low spin singlet state adopts a square planar geometry and loses coordination to the N^4 atom of the cyclen ring and carbonyl group of the substrate. However, in the triplet state **II$_{PdC}$** exists in the hexacoordinated state adopted by all other complexes. This high spin triplet state is 7.6 kcal/mol higher in energy than the ground singlet state. For all other divalent metal complexes except **II$_{NiC}$**, the *syn-syn* isomer is found to be the most stable. For **II$_{NiC}$** this conformation is slightly (1.7 kcal/mol) higher than the *syn-anti* isomer. The computed barriers for **TS$_{NiC}$**, **TS$_{CuC}$**, **TS$_{CdC}$**, **TS$_{CoC}$**, and **TS$_{ZnC}$** are quite comparable i.e. 27.2, 29.7, 30.5, 30.5, and 31.9 kcal/mol, respectively (Figure 3.13). This is likely due to similar differences in the reaction coordinates (O^H-C^S,

H^H-N^S, O^H-H^H, and N^S-C^S) of the corresponding reactant and transition state of these complexes (Figure 3.12 and 3.13). Among all divalent metals, the highest barrier (41.5 kcal/mol) was computed for the tetra-coordinated $\mathbf{TS_{PdC}}$ in its singlet ground state. This barrier was significantly (11.8 kcal/mol) greater than the barrier for $\mathbf{TS_{CuC}}$. In the reactant of $\mathbf{II_{PdC}}$, the O^H-C^S and H^H-N^S bonds are substantially longer by 0.76 and 1.42 Å than in the reactant of $\mathbf{II_{CuC}}$ (Table 3.1)**.** The charge on the Pd is also 0.17e lower than the charge on the Cu ion. However, in the hexa-coordinated triplet state for $\mathbf{II_{PdC}}$, these coordinates are quite similar to $\mathbf{II_{CuC}}$ and as a result the barrier is lowered by 6.5 kcal/mol. These results suggest that the electronic state of the metal ion and binding mode of the cyclen ring play critical roles in the activities of these complexes.

3.2.5 Summary and Conclusions

In this study, mechanisms of peptide hydrolysis by Co(III)- and Cu(II)-containing complexes of cyclen and oxacyclen have been investigated. In particular, the roles of the ligand environment, pendant and metal ion on the energetics of this reaction have been computed. The Co(III)-cyclen complex was found to exist in the *syn-anti* conformation, while Cu(II)-cyclen exists in the *syn-syn* conformation. These complexes can utilize two different mechanisms, "stepwise" and "concerted." In the stepwise mechanism, the overall barrier of 33.7 kcal/mol for the Cu(II)-cyclen complex ($\mathbf{II_{CuC}}$) was 8.3 kcal/mol lower than the barrier of 42.0 kcal/mol computed for its Co(III)-containing counterpart ($\mathbf{II_{CoC}}$). In the mechanism, the first step involving the generation of the tetrahederal intermediate was found to contribute to the difference in the energetics of $\mathbf{II_{CoC}}$ and

$\mathbf{II_{CuC}}$. The "concerted" mechanism occurs with a slightly lower barrier than the "stepwise" mechanism for both complexes (39.8 kcal/mol for $\mathbf{II_{CoC}}$ and 32.7 kcal/mol for $\mathbf{II_{CuC}}$). The removal of the pendant molecule (-C_2H_5 group) in $\mathbf{II_{CoC}}$ and $\mathbf{II_{CuC}}$ lowered the barrier by 9.3 and 3.0 kcal/mol respectively. The computed barrier of 30.5 kcal/mol in the Co(III) case is in good agreement with the measured value of 25.9 kcal/mol for the cleavage of myoglobin at pH 9.0 and 50°C.[105]

In the Co(III)-oxacyclen complex, the oxygen atom is likely positioned at the 10 or 1 position of the oxacyclen ring. A comparison between the barriers using the common conformation (*syn-anti*) of the Co(III)-cyclen and Co(III)-oxacyclen showed that both complexes hydrolyze the peptide bond with similar barriers i.e. 39.8 kcal/mol for the former and 40.1 kcal/mol for latter. These barriers are in line with the measured k_{cat} values that suggest that the oxacyclen complex exhibits four times greater activity than the cyclen complex. On the other hand, in the Cu(II)-oxacyclen complex the oxygen atom should be located at the 4 position of the oxacyclen ring. Similar to the Co(III) case, here too the barrier is only slightly (0.2 kcal/mol) lower than the computed value of 32.7 kcal/mol for the corresponding cyclen complex. The substitution of Cu(II) with Ni(II), Zn(II), Cd(II) and Pd(II) in the metal-cyclen complexes showed that the electronic state of the metal ion and binding mode of the cyclen ring play important roles in their activities. The mechanistic and structural information in conjunction with the roles of the metal, ligand environment and pendant provided in this study will enhance our understanding of the functioning of the metal-cyclen complexes and their analogues in peptide hydrolysis.

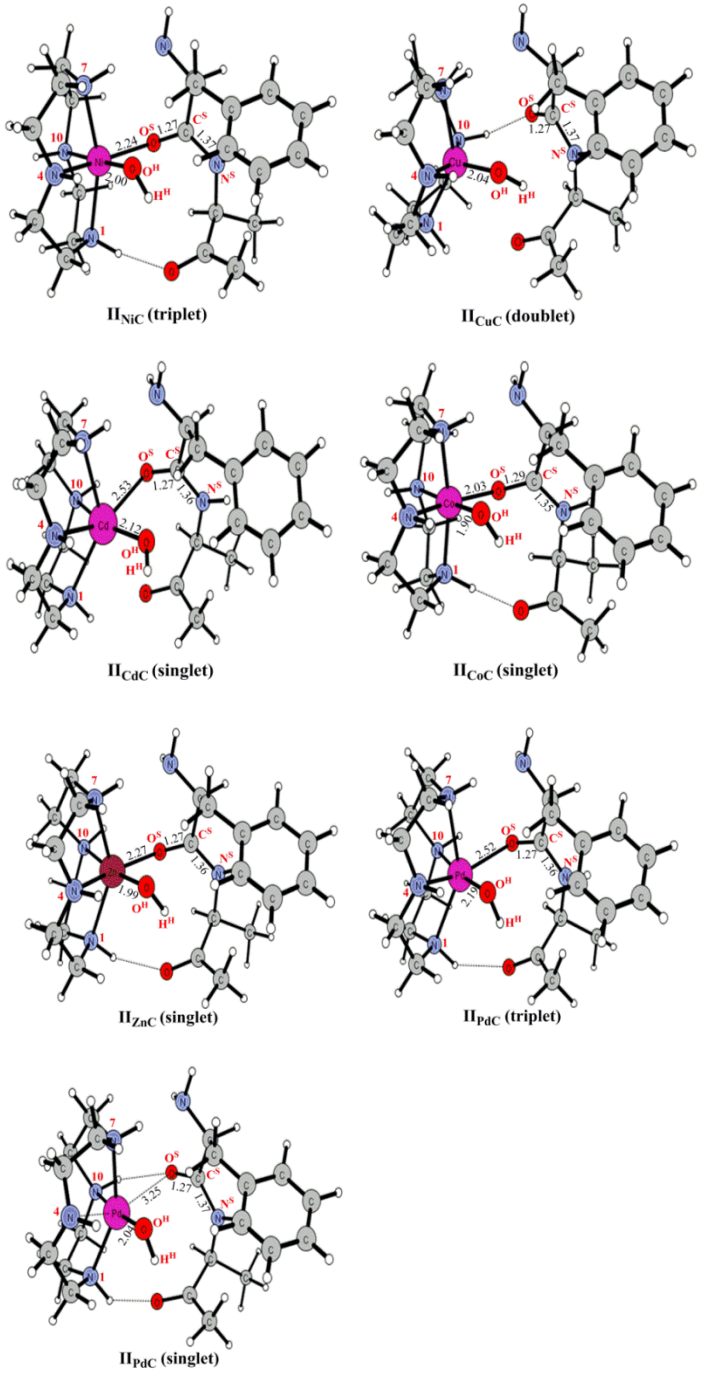

Figure 3. 12 Optimized structures of the reactants of metal-cyclen (without pendant) complexes.

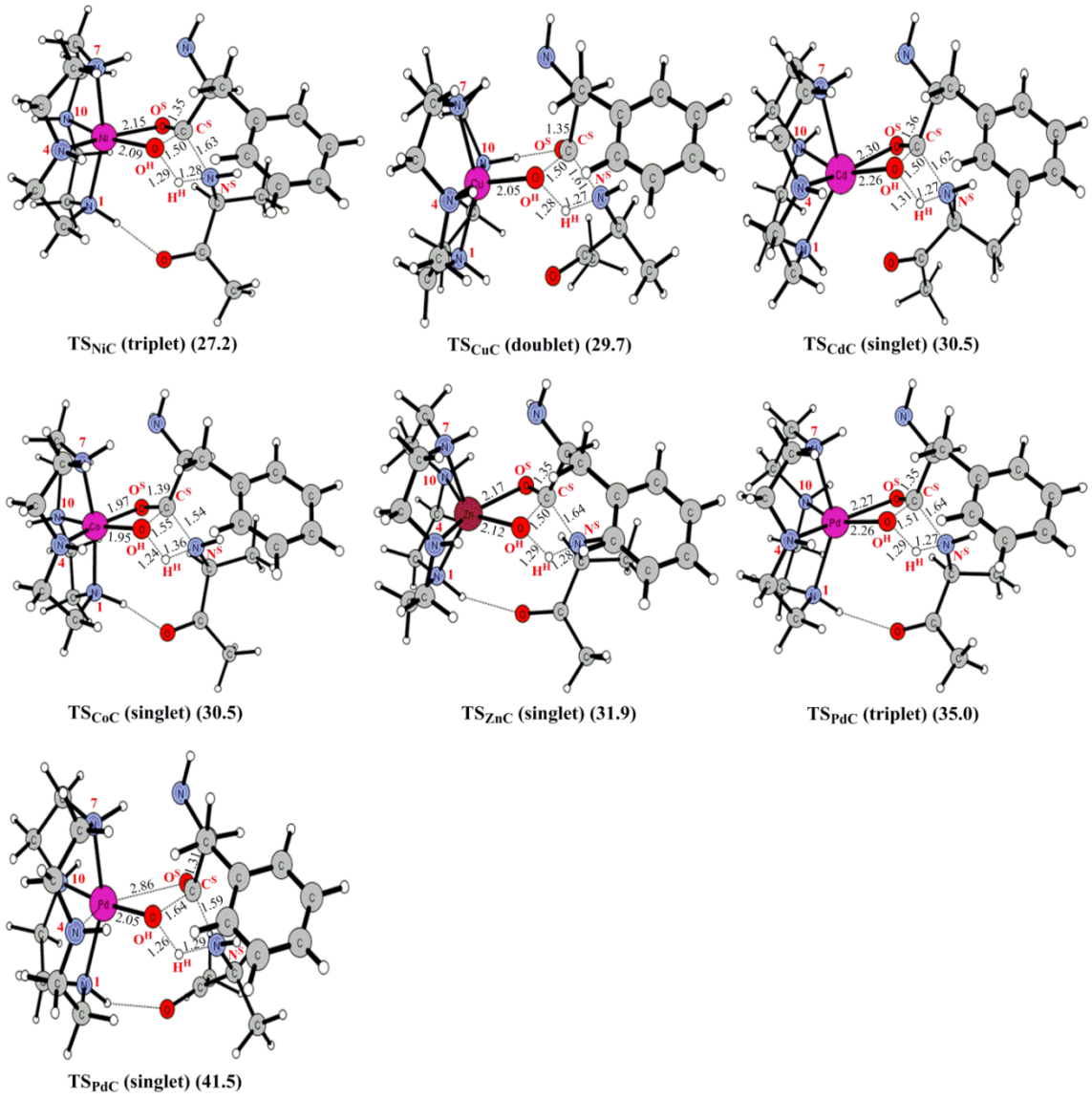

Figure 3. 13 Optimized structures of the transition states of different metal-cyclen complexes (in kcal/mol).

Table 3. 1 Critical bond distances (Å) of the optimized structures of metal cyclen complexes.

Metal-cyclen reactant	O^H-C^S	H^H-N^S	O^H-H^H	N^S-C^S
$\mathbf{II_{NiC}}$ (triplet)	3.04	3.37	0.98	1.37
$\mathbf{II_{CuC}}$ (doublet)	3.28	2.66	0.97	1.37
$\mathbf{II_{CdC}}$ (singlet)	3.08	4.13	0.98	1.36
$\mathbf{II_{CoC}}$ (singlet)	3.04	3.45	0.98	1.35
$\mathbf{II_{ZnC}}$ (singlet)	3.11	3.37	0.98	1.36
$\mathbf{II_{PdC}}$ (triplet)	3.51	3.80	0.98	1.36
$\mathbf{II_{PdC}}$ (singlet)	4.04	4.08	0.98	1.37

Metal-cyclen transition state	O^H-C^S	H^H-N^S	O^H-H^H	N^S-C^S
$\mathbf{TS_{NiC}}$ (triplet)	1.50	1.28	1.29	1.63
$\mathbf{TS_{CuC}}$ (doublet)	1.50	1.27	1.28	1.61
$\mathbf{TS_{CdC}}$ (singlet)	1.50	1.27	1.31	1.62
$\mathbf{TS_{CoC}}$ (singlet)	1.55	1.36	1.24	1.54
$\mathbf{TS_{ZnC}}$ (singlet)	1.50	1.28	1.29	1.64
$\mathbf{TS_{PdC}}$ (triplet)	1.51	1.27	1.29	1.64
$\mathbf{TS_{PdC}}$ (singlet)	1.64	1.29	1.26	1.59

3.3 Mechanism of Zr(IV)-Assisted Peptide Hydrolysis

Zr(IV) displays a significant reactivity towards peptide bond cleavage due to the high Lewis acidity of its stable +4 oxidation state. In addition, Zr(IV) is redox stable, oxophilic, kinetically and steorochemically labile, possesses low cellular toxicity and exhibits fast ligand exchange kinetics which could facilitate the catalytic turnover.[141-143] All the aforementioned advantages make Zr(IV) complexes a promising catalyst for the hydrolysis of peptide bonds.

However, Komiyama and coworkers had reported that Zr(IV) showed very low levels of peptide hydrolysis (~25% conversion of Gly-Phe, pH 7.0, 80 °C, 24 h) in 0.1 M Tris(hydroxymethyl)aminomethane buffer.[144] On the other hand, Grant and coworkers are the first research group to efficiently hydrolyze unactivated peptide amide bonds by utilizing Zr(IV) complexes under near physiological conditions.[145] A series of 16 dipeptides corresponding to the sequences Xaa-Gly and Gly-Xaa were studied in Zr(IV) 4,13-diaza-18-crown-6 **(N2O4)**.[146] Unfavorable electrostatic interactions with positively charged Zr(IV) complex make the positively charged dipeptides displayed low levels of hydrolysis (Lys-Gly dipeptide, pH 7.1, 60 °C, 20 h, yield 17%). The neutral and negatively charged peptides containing Gly and amino acids with oxygen-rich side chains showed efficient hydrolysis under the same conditions (Gly-Gly dipeptide, pH 7.0, 60 °C, 20 h, yield 90%; Gly-Glu dipeptide, pH 7.2, 60 °C, 20 h, yield 97%).[146] In addition, a total of 17 ligands on Zr(IV)-assisted hydrolysis of the unactivated amide bond of dipeptide Gly-Gly had been compared in pH 6.8-7.4 after 4 h and 10 h at 60 °C. In the experiment, three compounds were found to produce the most Gly hydrolysis product

both at t = 4 h, and t = 10 h: 4,13-diaza-18-crown-6 **(N2O4)** ~ 1,4,10-trioxa-7,13-diazacyclopentadecane **(N2O3)** ≥ 2-(2-methoxy)-ethanol **(NO2)** (Scheme 2).[114] It was observed that a ring structure is not required to enhance Zr(IV) reactivity. Moreover, the structural feature "$ROCH_2CH_2OCH_2CH_2NR$" appeared to increase the levels of peptide hydrolysis.[114]

Scheme 2

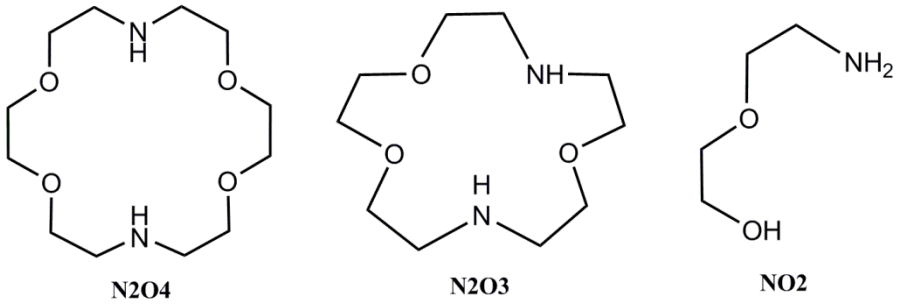

3.3.1 Experimentally Proposed Mechanism

Zr(IV) complexes catalyze the hydrolysis of a Gly-Gly dipeptide bond through the following overall reaction:

$$\text{Gly-C(=O)-NH-Gly} + H_2O \rightarrow \text{Gly-C(=O)OH} + NH_2\text{-Gly} \qquad (1)$$

During the process of peptide cleavage, the Zr(IV) metal center has two functions. First, the Zr(IV) ion polarizes the carbonyl group of the amide bond by binding to the carbonyl oxygen. The preference of Zr(IV) towards oxygen helps avoid the formation of inactive peptide amide nitrogen coordination.[147] Then, the Zr(IV)–bound hydroxide ion (Because the pK_a values of Zr(IV)-bound water molecules are lowered from 15.7 to ≤ 0.6,

Zr-OH readily exists in both acidic and neutral condition.[148]) acts by nucleophilic attack on the carbonyl carbon atom to form a tetrahedral intermediate containing a four-membered ring.

Despite the availability experimental information, several structural and mechanistic questions concerning the Zr(IV)-assisted peptide hydrolysis remain unresolved. For instance, it is unclear whether the hydrolysis process follows a stepwise or concerted mechanism. Second, the protonation states of the ligands (**N2O4**, **N2O3**, and **NO2**) and the effect of the ligand environment on the activities of the Zr(IV) complexes are also unavailable. Moreover, Zr(IV) can form complexes with high coordination numbers and have flexible geometries, as a result, the structures of Zr(IV) binding to the ligands are not known.

In the present DFT study, all the aforementioned aspects have been studied. We performed DFT calculations to investigate hydrolysis of a Gly-Gly peptide bond by Zr(IV)-bound complexes. The mechanistic studies will provide structures of short-lived intermediates and transition states that cannot be easily observed through experimental techniques. These studies will elucidate the mechanisms (stepwise or concerted) of the reactions and determine the nature of the rate-determining step. The protonation states of the ligands have been studied. Our studies will also help to explain the ligand effects of Zr(IV)-bound **N2O4**, **N2O3**, and **NO2** complexes. Moreover, different coordination number models were constructed by utilizing **NO2** as a ligand to gain the favorable structure and geometry of Zr(IV) complex. The results reported in this paper will provide deeper information concerning the functioning of the Zr(IV) complexes and the

predictions will help to optimize the ligand environments to design new Zr(IV)-based metallopetidases.

3.3.2 Computational Methods and Models

All calculations were performed using the Gaussian 03 program package.[79] The geometry optimizations of reactants, intermediates, transition states and products were performed at the B3LYP/Lanl2dz level without any geometrical constraint using corresponding Hay-Wadt effective core potential (ECP) for Zr.[149-151] The final energies of the optimized structures were further improved by performing single point calculations including additional d and p polarization functions for O (α=0.96), N (α=0.74), C (α=0.59) and H (α=0.36) atoms respectively (taken from the EMSL's Gaussian basis set library) in the basis set used for optimizations. Hessians were calculated at the same level of theory as the optimizations to confirm the nature of the stationary points along the reaction coordinate. The transition states were confirmed to have only one negative eigenvalue corresponding to the reaction coordinates. The dielectric constant of 78.39 corresponding to water was used to estimate the effect of the solvent utilizing the self-consistent reaction field IEFPCM method[152] at the B3LYP/Lanl2dz level. Throughout the manuscript, the energies obtained at the B3LYP/ {Lanl2dz + d(O, N and C) + p(H)} including thermal corrections and solvent effects in protein are discussed.

The available experimental information was fully incorporated in building models for the calculations. To obtain target complexes, the Zr(IV)-bound ligand compounds are constructed by using the X-ray crystal structures.[153] In addition, one hydroxyl ion and

Gly-Gly dipeptide are also included in the models by coordinating to a Zr(IV) ion. Gly-Gly dipeptide is modeled as ($NH_2CH_2CONHCH_2COOH$). The Zr(IV)-bound protonated ligands **N2O4** and **N2O3** complexes are denoted as $\mathbf{I_{N2O4}}$ and $\mathbf{I_{N2O3}}$. On the other hand, the deprotonated **N2O4**, **N2O3**, and **NO2** complexes are modeled as $\mathbf{I_{DN2O4}}$, $\mathbf{I_{DN2O3}}$, and $\mathbf{I_{DNO2}}$ respectively by removing the protons from –NH in the ligands.

3.3.3 Results and Discussion

3.3.3.1 Mechanism

The following two different mechanisms were investigated by utilizing the reactants $\mathbf{I_{DN2O4}}$ and $\mathbf{I_{N2O4}}$ for the reaction: (1) stepwise and (2) concerted mechanisms.

Stepwise Mechanism: This mechanism for $\mathbf{I_{DN2O4}}$ and $\mathbf{I_{N2O4}}$ proceeds through the following two steps: (1) formation of the tetrahedral intermediate, and (2) cleavage of the peptide bond.

In the reactant structure $\mathbf{I_{DN2O4}}$, the Gly-Gly dipeptide substrate binds to the Zr(IV) catalyst through Zr-O^S coordination with a distance of 2.25 Å (Figure 3.14). This interaction between the Zr(IV) ion and O^S atom increases the electrophilicity of the C^S and activates it for nucleophilic attack. A hydroxide ion (-O^HH^H) is bound to the Zr(IV) ion. The C^S-N^S peptide bond distance in the reactant is 1.34 Å. Moreover, the O^H-C^S and H^H-N^S distances are 3.22 and 4.09 Å respectively. In $\mathbf{I_{DN2O4}}$, the Zr(IV) ion is in hepta-coordinated form (Zr-O^1 = 2.36 Å, Zr-O^2 = 2.44 Å, Zr-O^3 = 2.49 Å, Zr-O^S = 2.25 Å, Zr-

O^H = 2.04 Å, Zr-N^1 = 2.14 Å, Zr-N^2 = 2.13 Å). The binding of the water molecule to the Zr(IV) ion polarizes this molecule and reduces its pK_a value from 15.7 to ≤ 0.6 to facilitate its activation. In the first step, the hydroxide ion (-O^HH^H) acts as a nucleophile and attacks the C^S atom of the amide bond. After the nucleophilic attack, the peptide bond elongates by 0.06 Å with the C^S-N^S peptide bond distance being 1.40 Å. All the corresponding distances in the fully optimized transition state **TS1$_{DN2O4-SW}$** are shown in Figure 3.14. The first transition state occurs with a barrier of 13.9 kcal/mol from the reactant **I$_{DN2O4}$**. This process leads to the formation of the tetrahedral intermediate **II$_{DN2O4-SW}$**, in which the hydroxyl group (-O^HH^H) is attached to the C^S. In comparison to **I$_{DN2O4}$**, the C^S-N^S peptide bond is already elongated by 0.07 Å (C^S-N^S = 1.41 Å) and perfectly set up for cleavage in the next step. The generation of **II$_{DN2O4-SW}$** is endergonic by 13.6 kcal/mol from **I$_{DN2O4}$**. On the other hand, the computed barrier for the first step of the protonated Zr(IV)-bound ligand complex (**I$_{N2O4}$**) is 41.4 kcal/mol (Figure 3.15), which is 27.5 kcal/mol higher than **TS1$_{DN2O4-SW}$**. The barrier of the generation of protonated intermediate **II$_{N2O4-SW}$** is 41.3 kal/mol from **I$_{N2O4}$**.

In the second step, the H^H dissociates from O^H and donates to the N^S of the peptide bond, which leads to the cleavage of the peptide bond. In **TS2$_{DN2O4-SW}$**, all of the corresponding distances indicate the concerted nature of this process (O^H–H^H = 1.36 Å, H^H–N^S = 1.19 Å, and N^S–C^S = 1.63 Å). The optimized transition state **TS2$_{DN2O4-SW}$** for this process is shown in Figure 3.14 and it crosses over a barrier of 17.0 kcal/mol from **II$_{DN2O4-SW}$**. Since this step follows a step that is endergoic by 13.9 kcal/mol, the overall barrier from **I$_{DN2O4}$** becomes 30.6 kcal/mol (Figure 3.14). This is the rate-limiting step of

the entire mechanism. In the final product **III$_{DN2O4-SW}$**, the separated neutral amine (-NH_2) and charged carboxyl (-COO^-) groups are formed and the latter is bound to the Zr(IV) ion. The formation of **III$_{DN2O4-SW}$** from **I$_{DN2O4}$** is exergonic by 6.3 kcal/mol. In comparison, the barrier for the second step (Figure 3.15) of protonated Zr(IV)-bound ligands **N2O4** (**I$_{N2O4}$**) is 54.6 kcal/mol, which is 24.0 kcal/mol higher than the barrier of **I$_{DN2O4}$**.

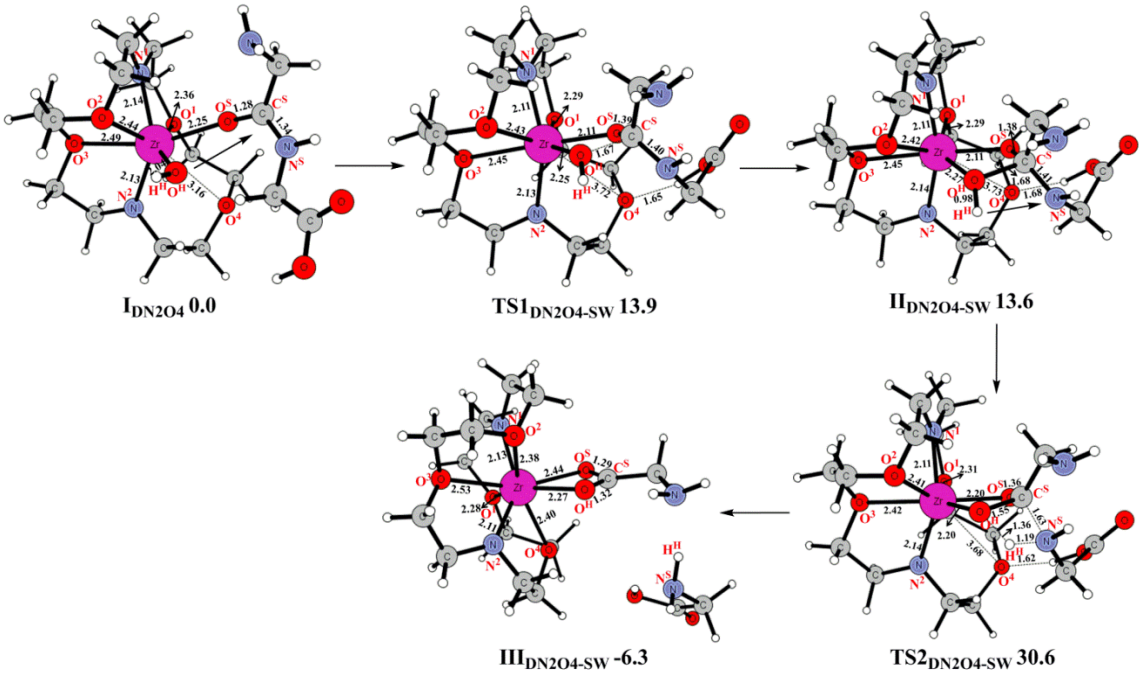

Figure 3. 14 Structures (in Å) and energies (in kcal/mol) of the reactant, transition states (optimized), intermediate, and product for **I$_{DN2O4}$** in the stepwise mechanism.

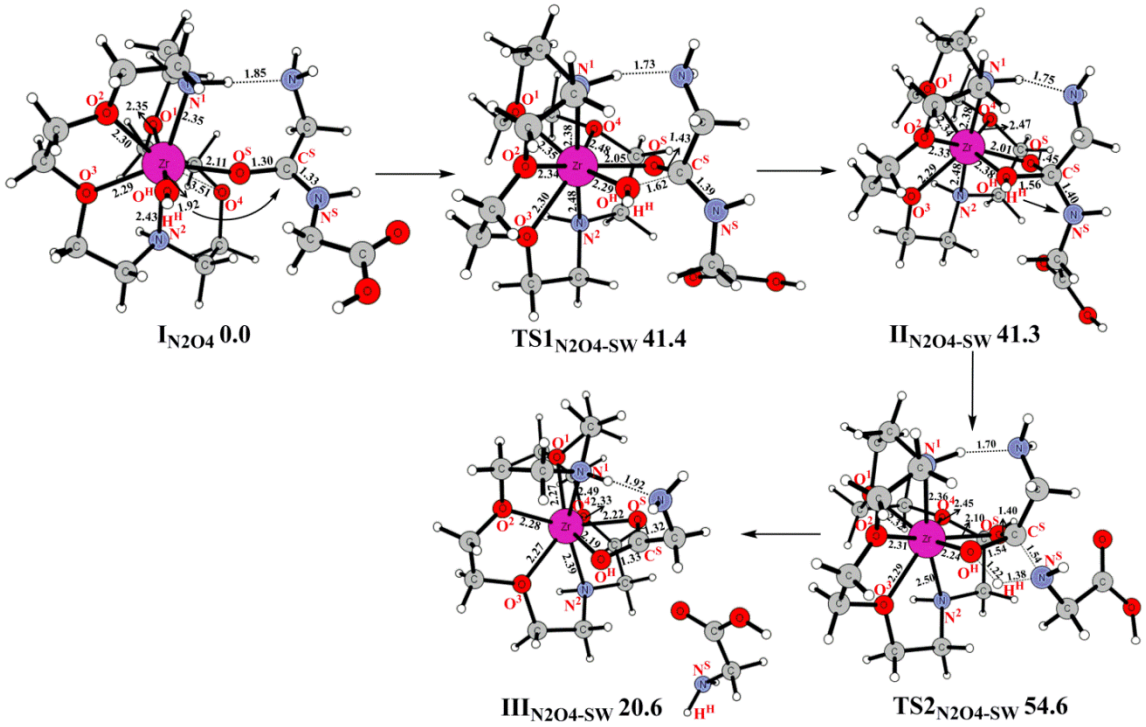

Figure 3. 15 Structures (in Å) and energies (in kcal/mol) of the reactant, transition states (optimized), intermediate, and product for $\mathbf{I_{N2O4}}$ in the stepwise mechanism.

Concerted Mechanism: On the other hand, the peptide bond hydrolysis can also proceed through a concerted mechanism for the same reactants $\mathbf{I_{DN2O4}}$ and $\mathbf{I_{N2O4}}$.

In this mechanism, the hydroxyl group ($-O^HH^H$) is transferred to the C^S of the peptide bond in the transition state ($\mathbf{TS_{DN2O4}}$). This process occurs concomitantly with the dissociation of H^H from O^H and the transfer of the hydrogen atom H^H to the C^S atom, which leads to the cleavage of the peptide bond. The computed barrier for this concerted process was 31.0 kcal/mol. The optimized transition state $\mathbf{TS_{DN2O4}}$ is shown in Figure

3.16. All the relevant bond distances indicate that this process is concerted (O^H-C^S = 1.53 Å, H^H-N^S = 1.36 Å, O^H-H^H = 1.25 Å, N^S-C^S = 1.52 Å). After the cleavage of the peptide bond, it leads to the formation of product $\mathbf{II_{DN2O4}}$ with a negatively charged carboxyl group that forms a four member ring structure with the Zr(IV) center and neutral amine group. This product was found to be 6.3 kcal/mol exergonic from the reactant. On the other hand, the energy barrier from the protonated form $\mathbf{I_{N2O4}}$ to $\mathbf{TS_{N2O4}}$ is 47.1 kcal/mol, which is 16.1 kcal/mol higher than the same process from $\mathbf{I_{DN2O4}}$ (Figure 3.16).

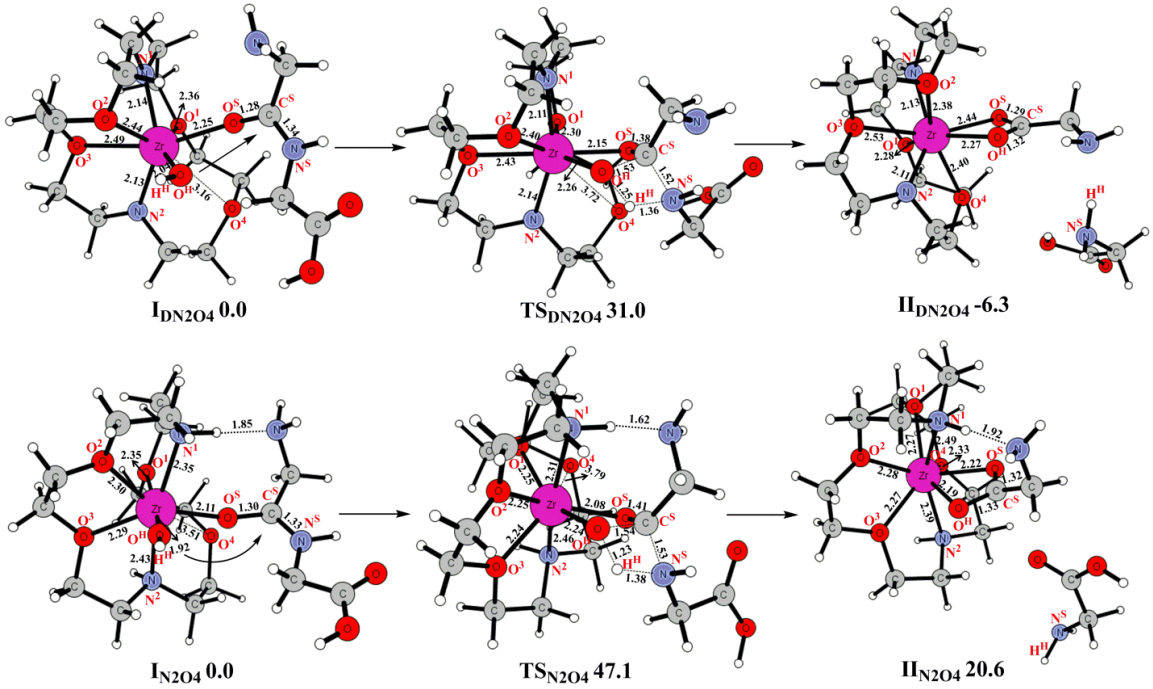

Figure 3. 16 Structures (in Å) and energies (in kcal/mol) of the reactants, transition states, and products for $\mathbf{I_{DN2O4}}$ and $\mathbf{I_{N2O4}}$ in the concerted mechanism.

The barriers for the reactant $\mathbf{I_{DN2O4}}$ in the stepwise and concerted mechanisms are similar. The barriers for the reactant $\mathbf{I_{N2O4}}$ in the stepwise mechanism are much higher than the concerted mechanism. Therefore, the stepwise mechanism can be ruled out. In the next section, all the reactions are investigated by using concerted mechanism.

3.3.3.2 Protonation State

The computed energetics indicate that among the reactants $\mathbf{I_{DN2O4}}$ and $\mathbf{I_{N2O4}}$, $\mathbf{I_{DN2O4}}$ (the deprotonated Zr(IV)-bound ligand **N2O4** complex) is energetically more favorable for the peptide bond cleavage of the dipeptide Gly-Gly. In addition, based on the experimental data, the Gly-Gly dipeptide can be hydrolyzed between pH 4.2-7.4. In addition, the hydrolysis by the Zr(IV)-bound ligand **N2O4** complex is more effective at near neutral pH (pH 7.0, 60 °C, 20 h, yield 90%; pH 4.2, 60 °C, 20 h, yield 65%).[146] It may be expected that the ligand **N2O4** is in the deprotonated state. To elucidate the protonation state of the ligand **N2O4**, four models which include all the possible protonation states have been constructed. The Zr(IV)-bound protonated ligands **N2O4** complex is denoted as $\mathbf{I_{N2O4}}$. The deprotonated **N2O4** complexes are modeled as $\mathbf{I_{DN2O4\text{-}N1}}$, $\mathbf{I_{DN2O4\text{-}N2}}$, and $\mathbf{I_{DN2O4}}$ respectively by removing the protons from $-N^1H$, $-N^2H$, and both $-N^1H$ and $-N^2H$ in the ligands. All the corresponding complexes in the fully optimized structures are shown in Figure 3.16 & 3.17.

In the optimized structures of the reactants, $\mathbf{I_{N2O4}}$ and $\mathbf{I_{DN2O4\text{-}N2}}$ form a hydrogen bond with the N-terminus of Gly because they have the hydrogen in $-N^1H$ (Figure 3.16 & 3.17). $\mathbf{I_{DN2O4}}$, in comparison with all the other reactants, the Zr-O^H bond is longer with a

bond length of 2.04 Å, and the charge on the O^H ion is -1.05e. That is more negative than the O^H ion in all the other reactants (Table 3.2 & 3.3). These differences in the bond distance and charge indicate that the interaction between the Zr(IV) ion with the hydroxyl group ($-O^HH^H$) in $\mathbf{I_{DN2O4}}$ is much stronger. It helps to make $-O^HH^H$ a better nucleophile. The deprotonated **N2O4** ligand increases electron donating ability by adding electron density to the Zr(IV) ion and tend to stabilize the metal center. From reactant $\mathbf{I_{N2O4}}$ to $\mathbf{I_{DN2O4}}$, the Zr-N^1 and Zr-N^2 bond distances are reduced (Zr-N^1 bond is shorter by 0.21 Å, and Zr-N^2 bond is shorter by 0.30 Å) (Table 3.2). As a result, the interaction of the Gly-Gly dipeptide with the Zr(IV) ion is weakened. Those interactions can be rationalized in terms of the charge difference between these atoms. The N^S atom of the Gly-Gly dipeptide in $\mathbf{I_{DN2O4}}$ possesses 0.04e more negative charge than the corresponding atom in $\mathbf{I_{N2O4}}$ (Table 3.3). Furthermore, the charge difference of 2.51e between the Zr(IV) and O^S atoms of $\mathbf{I_{DN2O4}}$ is 0.21e smaller than for $\mathbf{I_{N2O4}}$. The other noticeable differences were found in the interactions of the O^H with carbonyl carbon atom (C^S) of the Gly-Gly dipeptide. Here, the O^H-C^S distance of $\mathbf{I_{DN2O4}}$ is 3.22 Å, which is much shorter than the corresponding distance in all the other reactants.

During the process of hydrolysis of the peptide bond, the charge on the Zr(IV) ion was increased by 0.08e, 0.07e, 0.07e, and 0.03e in the transition state $\mathbf{TS_{N2O4}}$, $\mathbf{TS_{DN2O4\text{-}N1}}$, $\mathbf{TS_{DN2O4\text{-}N2}}$, and $\mathbf{TS_{DN2O4}}$, respectively. Whereas the rate of increase is opposite in the charge on the O^H atom, which is increased by 0.11e, 0.13e, 0.12e, and 0.17e respectively (Table 3.3). In $\mathbf{TS_{DN2O4}}$, the Zr-O^H bond is longer by 0.22 Å from $\mathbf{I_{DN2O4}}$, and the O^H-C^S bond distance is shorter by 1.69 Å (Table 3.2). The elongation and shortening of the Zr-O^H and O^H-C^S bond distances in the $\mathbf{I_{N2O4}} \rightarrow \mathbf{TS_{N2O4}}$ process are greater by 0.10 Å and

0.67 Å, respectively, than in the $\mathbf{I_{DN2O4}} \rightarrow \mathbf{TS_{DN2O4}}$ process. The process has a 47.1 kcal/mol barrier from $\mathbf{I_{N2O4}}$ to $\mathbf{TS_{N2O4}}$. On the other hand, the barriers for the Zr(IV)-bound deprotonated **N2O4** complexes $\mathbf{I_{DN2O4\text{-}N1}}$, $\mathbf{I_{DN2O4\text{-}N2}}$, and $\mathbf{I_{DN2O4}}$ are 40.6, 47.9, and 31.0 kcal/mol, respectively (Figure 3.16 & 3.17). Here, the hydrolysis of the peptide bond of the reactant $\mathbf{I_{DN2O4}}$ is much more energetically feasible than all the other reactants. The reason for the low barrier could be the aforementioned differences in the Zr-O^H and O^H-C^S bond distances.

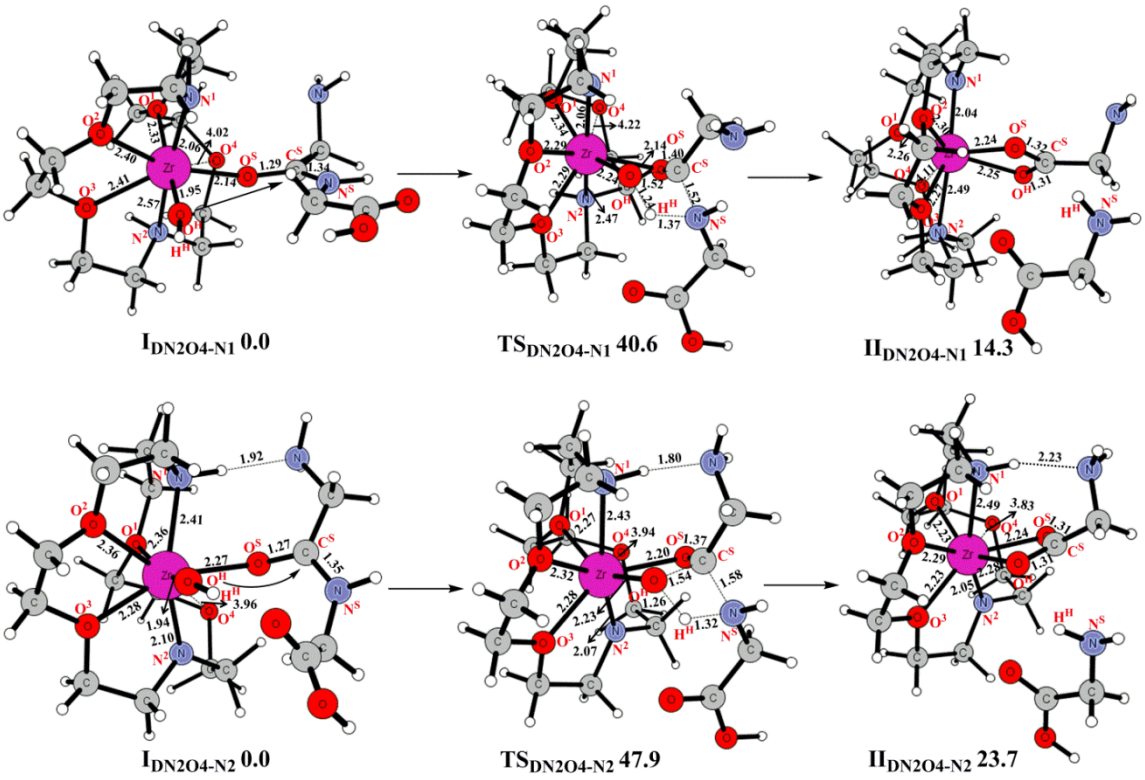

Figure 3. 17 Structures (in Å) and energies (in kcal/mol) of the reactants, transition states, and products for $\mathbf{I_{DN2O4\text{-}N1}}$ and $\mathbf{I_{DN2O4\text{-}N2}}$ in the concerted mechanism.

Table 3. 2 The key geometrical bond distances (Å) of the optimized reactants and transition states for different protonation state complexes ($\mathbf{I_{N2O4}}$, $\mathbf{I_{DN2O4\text{-}N1}}$, $\mathbf{I_{DN2O4\text{-}N2}}$, and $\mathbf{I_{DN2O4}}$)

Reactant	Zr-O^S	O^S-C^S	C^S-N^S	Zr-O^H	O^H-C^S	H^H-N^S	Zr-N^1	Zr-N^2	Zr-O^1	Zr-O^2	Zr-O^3	Zr-O^4
$\mathbf{I_{N2O4}}$	2.11	1.30	1.33	1.92	3.90	4.77	2.35	2.43	2.35	2.30	2.29	3.51
$\mathbf{I_{DN2O4\text{-}N1}}$	2.14	1.29	1.34	1.95	3.92	4.59	2.06	2.57	2.33	2.40	2.41	4.02
$\mathbf{I_{DN2O4\text{-}N2}}$	2.27	1.27	1.35	1.94	3.39	3.52	2.41	2.10	2.36	2.36	2.28	3.96
$\mathbf{I_{DN2O4}}$	2.25	1.28	1.34	2.04	3.22	4.09	2.14	2.13	2.36	2.44	2.49	3.16

Transition state	Zr-O^S	O^S-C^S	C^S-N^S	Zr-O^H	O^H-C^S	H^H-N^S	Zr-N^1	Zr-N^2	Zr-O^1	Zr-O^2	Zr-O^3	Zr-O^4
$\mathbf{TS_{N2O4}}$	2.08	1.41	1.53	2.24	1.54	1.38	2.31	2.46	2.25	2.25	2.24	3.79
$\mathbf{TS_{DN2O4\text{-}N1}}$	2.14	1.40	1.52	2.24	1.52	1.37	2.06	2.47	2.34	2.29	2.29	4.22
$\mathbf{TS_{DN2O4\text{-}N2}}$	2.20	1.37	1.58	2.23	1.54	1.32	2.43	2.07	2.27	2.32	2.28	3.94
$\mathbf{TS_{DN2O4}}$	2.15	1.38	1.52	2.26	1.53	1.36	2.11	2.14	2.30	2.40	2.42	3.72

Table 3. 3 The atomic charges on the key atoms of the optimized reactants and transition states for different protonation state complexes ($\mathbf{I_{N2O4}}$, $\mathbf{I_{DN2O4\text{-}N1}}$, $\mathbf{I_{DN2O4\text{-}N2}}$, and $\mathbf{I_{DN2O4}}$)

Reactant	Zr	O^S	C^S	N^S	O^H	H^H	N^1	N^2	O^1	O^2	O^3	O^4
$\mathbf{I_{N2O4}}$	1.97	-0.75	0.77	-0.58	-0.99	0.56	-0.79	-0.76	-0.65	-0.65	-0.66	-0.63
$\mathbf{I_{DN2O4\text{-}N1}}$	1.89	-0.72	0.79	-0.60	-1.02	0.54	-0.82	-0.74	-0.65	-0.63	-0.64	-0.64
$\mathbf{I_{DN2O4\text{-}N2}}$	1.87	-0.68	0.77	-0.62	-1.01	0.55	-0.77	-0.87	-0.63	-0.63	-0.64	-0.63
$\mathbf{I_{DN2O4}}$	1.82	-0.69	0.78	-0.62	-1.05	0.51	-0.88	-0.86	-0.62	-0.62	-0.61	-0.61

Transition state	Zr	O^S	C^S	N^S	O^H	H^H	N^1	N^2	O^1	O^2	O^3	O^4
$\mathbf{TS_{N2O4}}$	2.05	-0.82	0.82	-0.75	-0.88	0.53	-0.83	-0.77	-0.67	-0.66	-0.67	-0.63
$\mathbf{TS_{DN2O4\text{-}N1}}$	1.96	-0.85	0.82	-0.78	-0.89	0.53	-0.85	-0.76	-0.65	-0.65	-0.64	-0.62
$\mathbf{TS_{DN2O4\text{-}N2}}$	1.95	-0.84	0.82	-0.76	-0.89	0.53	-0.79	-0.86	-0.65	-0.64	-0.64	-0.62
$\mathbf{TS_{DN2O4}}$	1.85	-0.83	0.81	-0.77	-0.88	0.52	-0.88	-0.86	-0.63	-0.61	-0.61	-0.64

To confirm these results, the complexes that include protonated and deprotonated ligands **N2O3** have been investigated. The Zr(IV)-bound protonated ligands **N2O3** complex is denoted as $\mathbf{I_{N2O3}}$. The deprotonated **N2O3** complex is modeled as $\mathbf{I_{DN2O3}}$ by removing the protons from both $-N^1H$ and $-N^2H$ in the ligand. The corresponding complexes in the fully optimized structures are shown in Figure 3.18. Similar to $\mathbf{I_{DN2O4}}$, in $\mathbf{I_{DN2O3}}$, the Zr-O^H bond is longer than that in $\mathbf{I_{N2O3}}$, with the bond length 2.04 Å. Moreover, the O^H-C^S distance of $\mathbf{I_{DN2O3}}$ is 3.39 Å, which is much shorter than the corresponding distance in $\mathbf{I_{N2O3}}$, which is 3.86 Å (Table 3.4). These differences in the

bond distance indicate that the hydroxyl group (-$O^{H}H^{H}$) in $\mathbf{I_{DN2O3}}$ is a better nucleophile and it is more prepared to attack the carbonyl carbon (C^{S}) of the Gly-Gly dipeptide. Furthermore, the charge difference of 2.52e between the Zr(IV) and O^{S} atoms of $\mathbf{I_{DN2O3}}$ is 0.63e smaller than for $\mathbf{I_{N2O3}}$ (Table 3.5). Hence, the Gly-Gly dipeptide is more strongly activated with the length of the N^{S}–C^{S} peptide bond of 1.34 Å which is 0.02 Å longer than the corresponding bond length in $\mathbf{I_{N2O3}}$ (Table 3.4). In summary, the $\mathbf{I_{DN2O3}} \rightarrow \mathbf{TS_{DN2O3}}$ process has a 36.6 kcal/mol barrier which is 10.6 kcal/mol lower than that for the reactant $\mathbf{I_{N2O3}}$ (Figure 3.18).

Table 3. 4 The key geometrical bond distances (Å) of the optimized reactants and transition states for different protonation state complexes ($\mathbf{I_{N2O3}}$ and $\mathbf{I_{DN2O3}}$)

Reactant	Zr-O^{S}	O^{S}-C^{S}	C^{S}-N^{S}	Zr-O^{H}	O^{H}-C^{S}	H^{H}-N^{S}	Zr-N^{1}	Zr-N^{2}	Zr-O^{1}	Zr-O^{2}	Zr-O^{3}
$\mathbf{I_{N2O3}}$	2.11	1.31	1.32	1.93	3.86	4.34	2.41	2.42	2.26	2.28	2.25
$\mathbf{I_{DN2O3}}$	2.30	1.28	1.34	2.04	3.39	4.15	2.12	2.14	2.32	2.37	2.39

Transition state	Zr-O^{S}	O^{S}-C^{S}	C^{S}-N^{S}	Zr-O^{H}	O^{H}-C^{S}	H^{H}-N^{S}	Zr-N^{1}	Zr-N^{2}	Zr-O^{1}	Zr-O^{2}	Zr-O^{3}
$\mathbf{TS_{N2O3}}$	2.08	1.40	1.51	2.22	1.56	1.40	2.42	2.39	2.21	2.25	2.25
$\mathbf{TS_{DN2O3}}$	2.24	1.37	1.58	2.24	1.51	1.31	2.12	2.11	2.27	2.36	2.35

Table 3. 5 The atomic charges on the key atoms of the optimized reactants and transition states for different protonation state complexes ($\mathbf{I_{N2O3}}$ and $\mathbf{I_{DN2O3}}$)

Reactant	Zr	O^S	C^S	N^S	O^H	H^H	N^1	N^2	O^1	O^2	O^3
$\mathbf{I_{N2O3}}$	2.33	-0.82	0.78	-0.58	-1.05	0.55	-0.80	-0.80	-0.69	-0.71	-0.69
$\mathbf{I_{DN2O3}}$	1.84	-0.68	0.76	-0.62	-1.05	0.51	-0.85	-0.86	-0.62	-0.63	-0.62

Transition state	Zr	O^S	C^S	N^S	O^H	H^H	N^1	N^2	O^1	O^2	O^3
$\mathbf{TS_{N2O3}}$	2.32	-0.88	0.83	-0.75	-0.94	0.53	-0.80	-0.80	-0.71	-0.71	-0.70
$\mathbf{TS_{DN2O3}}$	1.83	-0.84	0.82	-0.77	-0.88	0.52	-0.85	-0.86	-0.63	-0.62	-0.61

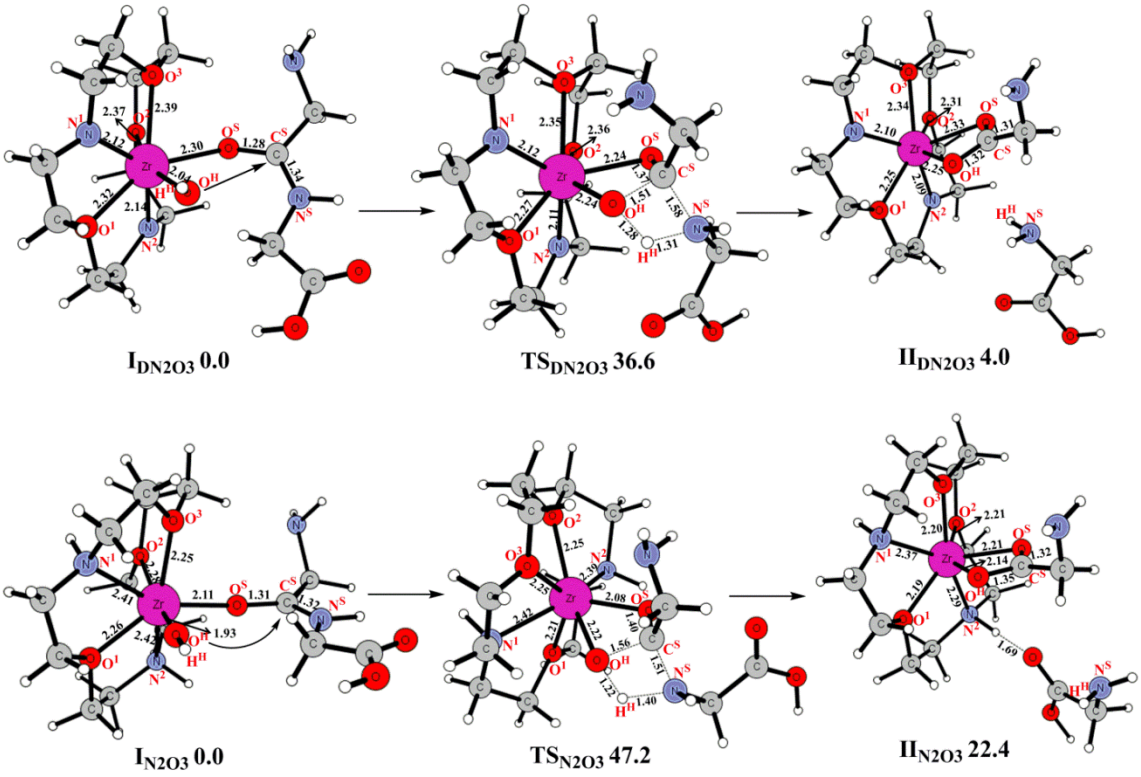

Figure 3. 18 Structures (in Å) and energies (in kcal/mol) of the reactants, transition states, and products for $\mathbf{I_{DN2O3}}$ and $\mathbf{I_{N2O3}}$ in the concerted mechanism.

The results of above study explicitly show that the Zr(IV)-bound ligands **N2O4** and **N2O3** are in the deprotonated form. This could be due to the basicity of the nitrogen atoms decreases from primary to secondary and tertiary amines.[154] As a result, the decreasing basicity of the ligand should increase the Lewis acidity of the metal center.[155]

3.3.3.3 Ligand Effects

According to the experimental data, three Zr(IV)-bound ligand compounds were found to produce the most Gly hydrolysis product both at t = 4 h, and t = 10 h: 4,13-diaza-18-crown-6 **(N2O4)** ~ 1,4,10-trioxa-7,13-diazacyclopentadecane **(N2O3)** ≥ 2-(2-methoxy)-ethanol **(NO2)**.[114] However, the effects of the ligand environment on the activities of the Zr(IV) complexes are unavailable. To shed light on these unresolved issues, we have investigated the hydrolysis of the following three compounds: (1) Zr(IV)-bound deprotonated ligand **N2O4** complex ($\mathbf{I_{DN2O4}}$), (2) Zr(IV)-bound deprotonated ligand **N2O3** complex ($\mathbf{I_{DN2O3}}$), and (3) Zr(IV)-bound deprotonated ligand **NO2** and one water complex ($\mathbf{I_{DNO2\text{-}1W}}$) (The attempt to optimize a Zr(IV)-bound deprotonated ligand **NO2** complex failed). The calculations will provide energetics and structural information for these complexes processes.

In the reactants, $\mathbf{I_{DN2O4}}$ shows weaker binding of the metal center with the ligand at distances of Zr-O^1 = 2.36 Å, Zr-O^2 = 2.44 Å, Zr-O^3 = 2.49 Å. In comparison, the $\mathbf{I_{DN2O3}}$ has the Zr(IV)-ligand bond lengths of Zr-O^1 = 2.32 Å, Zr-O^2 = 2.37 Å, Zr-O^3 = 2.39 Å, while Zr-O^1 = 1.95 Å, Zr-O^2 = 2.29 Å in $\mathbf{I_{DNO2\text{-}1W}}$ (Table 3.6). The optimized structure of $\mathbf{I_{DNO2\text{-}1W}}$ is shown in Figure 3.19. While weak binding of the ligand to the metal center

can enhance the Lewis acidity of the metal center.[155] In addition, the length of the N^S–C^S peptide bond of $\mathbf{I_{DN2O4}}$ and $\mathbf{I_{DN2O3}}$ is 1.34 Å, which is 0.01 Å longer than that in $\mathbf{I_{DNO2\text{-}1W}}$. Moreover, the Zr-$O^H$ bond of $\mathbf{I_{DN2O4}}$ and $\mathbf{I_{DN2O3}}$ is longer with a bond length of 2.04 Å, and the charge on the O^H ion is -1.05e, that is more negative than the O^H ion in $\mathbf{I_{DNO2\text{-}1W}}$ (Table 3.6 & 3.7). These differences in the bond distance and charge make the hydroxyl group (-O^HH^H) in $\mathbf{I_{DN2O4}}$ and $\mathbf{I_{DN2O3}}$ a better nucleophile. Furthermore, the charge difference of 2.51e between the Zr(IV) and O^S atoms of $\mathbf{I_{DN2O4}}$ is 0.25e smaller than for $\mathbf{I_{DNO2\text{-}1W}}$ (i.e. 2.76e) (Table 3.7), and the O^H-C^S distance of $\mathbf{I_{DN2O4}}$ is 3.22 Å, which is much shorter than the corresponding distance in $\mathbf{I_{DN2O3}}$ and $\mathbf{I_{DNO2\text{-}1W}}$ (Table 3.6).

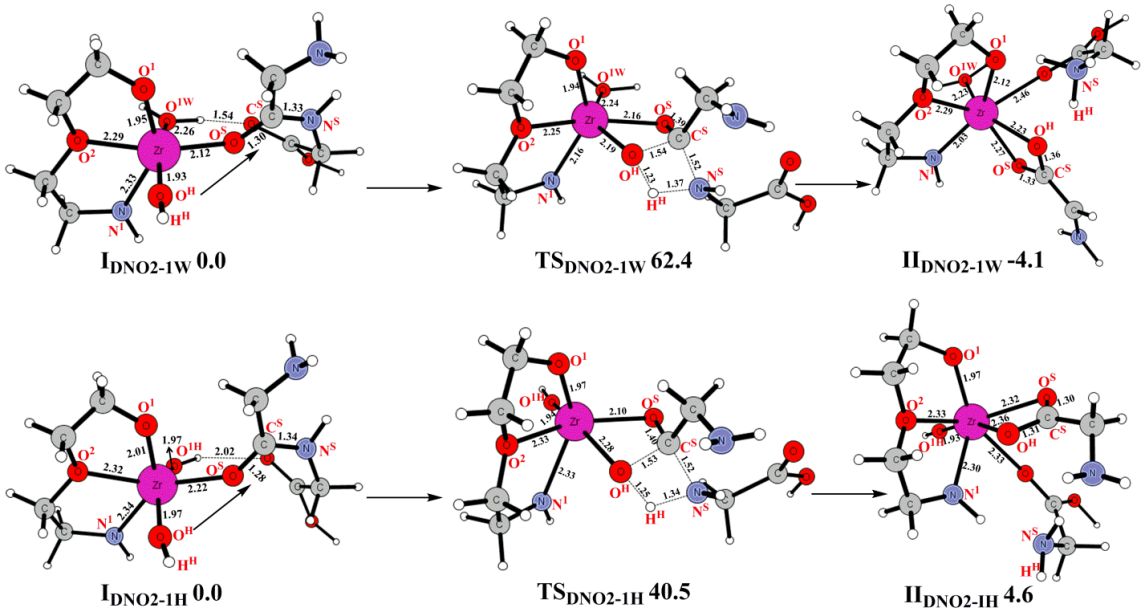

Figure 3. 19 Structures (in Å) and energies (in kcal/mol) of the reactants, transition states, and products for $\mathbf{I_{DNO2\text{-}1W}}$ and $\mathbf{I_{DNO2\text{-}1H}}$ in the concerted mechanism.

Table 3. 6 The key geometrical bond distances (Å) of the optimized reactants and transition states for different ligand complexes ($\mathbf{I_{DN2O4}}$, $\mathbf{I_{DN2O3}}$, and $\mathbf{I_{DNO2\text{-}1W}}$)

Reactant	Zr-O^S	O^S-C^S	C^S-N^S	Zr-O^H	O^H-C^S	H^H-N^S	Zr-N^1	Zr-N^2	Zr-O^1	Zr-O^2	Zr-O^3	Zr-O^4
$\mathbf{I_{DN2O4}}$	2.25	1.28	1.34	2.04	3.22	4.09	2.14	2.13	2.36	2.44	2.49	3.16
$\mathbf{I_{DN2O3}}$	2.30	1.28	1.34	2.04	3.39	4.15	2.12	2.14	2.32	2.37	2.39	--
$\mathbf{I_{DNO2\text{-}1W}}$	2.12	1.30	1.33	1.93	4.10	5.76	2.33	--	1.95	2.29	--	--

Transition state	Zr-O^S	O^S-C^S	C^S-N^S	Zr-O^H	O^H-C^S	H^H-N^S	Zr-N^1	Zr-N^2	Zr-O^1	Zr-O^2	Zr-O^3	Zr-O^4
$\mathbf{TS_{DN2O4}}$	2.15	1.38	1.52	2.26	1.53	1.36	2.11	2.14	2.30	2.40	2.42	3.72
$\mathbf{TS_{DN2O3}}$	2.24	1.37	1.58	2.24	1.51	1.31	2.12	2.11	2.27	2.36	2.35	--
$\mathbf{TS_{DNO2\text{-}1W}}$	2.16	1.39	1.52	2.19	1.54	1.37	2.16	--	1.94	2.25	--	--

Table 3. 7 The atomic charges on the key atoms of the optimized reactants and transition states for different ligand complexes ($\mathbf{I_{DN2O4}}$, $\mathbf{I_{DN2O3}}$, and $\mathbf{I_{DNO2\text{-}1W}}$)

Reactant	Zr	O^S	C^S	N^S	O^H	H^H	N^1	N^2	O^1	O^2	O^3	O^4
$\mathbf{I_{DN2O4}}$	1.82	-0.69	0.78	-0.62	-1.05	0.51	-0.88	-0.86	-0.62	-0.62	-0.61	-0.61
$\mathbf{I_{DN2O3}}$	1.84	-0.68	0.76	-0.62	-1.05	0.51	-0.85	-0.86	-0.62	-0.63	-0.62	--
$\mathbf{I_{DNO2\text{-}1W}}$	2.01	-0.75	0.77	-0.60	-0.98	0.55	-0.49	--	-0.80	-0.66	--	--

Transition state	Zr	O^S	C^S	N^S	O^H	H^H	N^1	N^2	O^1	O^2	O^3	O^4
$\mathbf{TS_{DN2O4}}$	1.85	-0.83	0.81	-0.77	-0.88	0.52	-0.88	-0.86	-0.63	-0.61	-0.61	-0.64
$\mathbf{TS_{DN2O3}}$	1.83	-0.84	0.82	-0.77	-0.88	0.52	-0.85	-0.86	-0.63	-0.62	-0.61	--
$\mathbf{TS_{DNO2\text{-}1W}}$	2.02	-0.85	0.81	-0.76	-0.86	0.53	-0.79	--	-0.79	-0.66	--	--

During the hydrolysis of the peptide bond, the charge on the O^H atom is decreased by 0.17e, 0.17e, and 0.12e in the transition state $\mathbf{TS_{DN2O4}}$, $\mathbf{TS_{DN2O3}}$, and $\mathbf{TS_{DNO2\text{-}1W}}$ respectively (Table 3.7). In $\mathbf{TS_{DN2O4}}$, the O^H-C^S bond distance is shorter by 1.69 Å from $\mathbf{I_{DN2O4}}$ (Table 3.6), the shortening of the O^H-C^S bond distances in the $\mathbf{I_{DN2O3}} \rightarrow \mathbf{TS_{DN2O3}}$ and $\mathbf{I_{DNO2\text{-}1W}} \rightarrow \mathbf{TS_{DNO2\text{-}1W}}$ process are 1.78 Å and 2.56 Å, respectively, which are greater than that in the $\mathbf{I_{DN2O4}} \rightarrow \mathbf{TS_{DN2O4}}$ process. Therefore, the energy barriers for the cleavage of the peptide bond are gradually increased from the reactant $\mathbf{I_{DN2O4}}$ to $\mathbf{I_{DNO2\text{-}1W}}$. The barriers were computed to be 31.0, 36.6, and 62.4 kcal/mol for $\mathbf{I_{DN2O4}}$, $\mathbf{I_{DN2O3}}$, and $\mathbf{I_{DNO2\text{-}1W}}$, respectively. For the case of $\mathbf{I_{DNO2\text{-}1W}} \rightarrow \mathbf{TS_{DNO2\text{-}1W}}$, the barrier is prohibitively high and could be due to the tight binding between the Zr(IV) ion with the ligand. The basicity of the nitrogen atom in the ligand of $\mathbf{I_{DNO2\text{-}1W}}$ is stronger than those in $\mathbf{I_{DN2O4}}$ and $\mathbf{I_{DN2O3}}$ which also affects the energy barrier.

The structural feature "$ROCH_2CH_2OCH_2CH_2NR$" appeared in the ligands of all the three reactants to increase the levels of peptide hydrolysis.[114] The results from this study indicate that a ring structure ligand is better than the non-ring structure ligand to enhance Zr(IV) center reactivity.

3.3.3.4 Coordination Number

Although Zr(IV) can form complexes with flexible geometries with multi-coordination numbers, the formation of high coordination number complexes are preferred.[141] According to the aforementioned computational results, the hydrolysis of the peptide bond of the reactants $\mathbf{I_{DN2O4}}$ and $\mathbf{I_{DN2O3}}$ were much more energetically feasible than $\mathbf{I_{DNO2}}$.

This could be due to the different ligand effects between **N2O4**, **N2O3**, and **NO2** bound to Zr(IV) ion, whereas the coordination number difference may also play a role on it. Both the reactants $\mathbf{I_{DN2O4}}$ and $\mathbf{I_{DN2O3}}$ are in a hepta-coordinated form. However, $\mathbf{I_{DNO2}}$ is a hexa-coordinated complex. In order to gain deeper information concerning the coordination number of the Zr(IV) complexes, a series of models were constructed based on the Zr(IV)-bound deprotonated ligand **NO2** complexes to elucidate these issue. All the complexes are divided into three species according to different coordination number. (1) The hexa-coordinated species: Zr(IV)-bound deprotonated ligand **NO2** and one water complex ($\mathbf{I_{DNO2\text{-}1W}}$), Zr(IV)-bound deprotonated ligand **NO2** and one hydroxyl group (-O^HH^H) complex ($\mathbf{I_{DNO2\text{-}1H}}$); (2) The hepta-coordinated species: Zr(IV)-bound deprotonated ligand **NO2** and two water complex ($\mathbf{I_{DNO2\text{-}2W}}$), Zr(IV)-bound deprotonated ligand **NO2** and two hydroxyl group (-O^HH^H) complex ($\mathbf{I_{DNO2\text{-}2H}}$); and (3) The octa-coordinated specie: Zr(IV)-bound deprotonated ligand **NO2** and three water complex ($\mathbf{I_{DNO2\text{-}3W}}$), the attempts to optimize a Zr(IV)-bound deprotonated ligand **NO2** and three hydroxyl group (-O^HH^H) complex ($\mathbf{I_{DNO2\text{-}3H}}$) are failed.

(1) The hexa-coordinated species:

In the optimized structures of the reactants, the length of the N^S–C^S peptide bond of $\mathbf{I_{DNO2\text{-}1H}}$ is 1.34 Å, which is 0.01 Å longer than that in $\mathbf{I_{DNO2\text{-}1W}}$ (Figure 3.19). In addition, the Zr-O^H bond of $\mathbf{I_{DNO2\text{-}1H}}$ is longer with a bond length of 1.97 Å, and the charge on the O^H ion is -1.02e. This value is more negative than the O^H ion in $\mathbf{I_{DNO2\text{-}1W}}$ (Table 3.8 & 3.9). These differences in the bond distance and charge indicate that the interaction

between the Zr(IV) ion with the hydroxyl group (-$O^{H}H^{H}$) in $\mathbf{I_{DNO2\text{-}1H}}$ is much stronger. Another hydroxyl group (-$O^{1H}H^{H}$) bound to the Zr(IV) ion in $\mathbf{I_{DNO2\text{-}1H}}$ increases electron donating ability by adding electron density to the Zr(IV) ion which stabilizes the metal center. The metal-ligand bond lengths are shown in Table 3.8. In comparison to $\mathbf{I_{DNO2\text{-}1W}}$, the bond lengths of $\mathbf{I_{DNO2\text{-}1H}}$ are longer (Zr-N^{1} = 2.34 Å, Zr-O^{1} = 2.01 Å, Zr-O^{2} = 2.32 Å). Those weak binding interactions will enhance the Zr(IV) center reactivity by decreasing the energy barrier. The N^{S} atom of the Gly-Gly dipeptide in $\mathbf{I_{DNO2\text{-}1H}}$ possesses 0.02e more negative charge than the corresponding atom in $\mathbf{I_{DNO2\text{-}1W}}$ (Table 3.9). The other noticeable differences were found in the interactions of the O^{H} with carbonyl carbon atom (C^{S}) of the Gly-Gly dipeptide. The charge difference of 1.79e between the C^{S} and O^{H} atoms of $\mathbf{I_{DNO2\text{-}1H}}$ is 0.04e larger than that for $\mathbf{I_{DNO2\text{-}1W}}$. This process has a 40.5 kcal/mol barrier from $\mathbf{I_{DNO2\text{-}1H}}$ to $\mathbf{TS_{DNO2\text{-}1H}}$. In comparison, the barrier from $\mathbf{I_{DNO2\text{-}1W}}$ to $\mathbf{TS_{DNO2\text{-}1W}}$ is 62.4 kcal/mol (Figure 3.19). $\mathbf{I_{DNO2\text{-}1H}}$ is much more energetically feasible than $\mathbf{I_{DNO2\text{-}1W}}$. A better nucleophile (-$O^{H}H^{H}$) was created in $\mathbf{I_{DNO2\text{-}1H}}$. In addition, the peptide bond in $\mathbf{I_{DNO2\text{-}1H}}$ was more activated. The differences of structure and electronic nature of $\mathbf{I_{DNO2\text{-}1W}}$ and $\mathbf{I_{DNO2\text{-}1H}}$ may be the reasons for the contribution of the energy difference.

(2) The hepta-coordinated species:

To further investigate the effects of different coordination numbers on the Zr(IV) complexes, two hepta-coordinated species have been created: Zr(IV)-bound deprotonated ligand **NO2** and two water complex ($\mathbf{I_{DNO2\text{-}2W}}$) and Zr(IV)-bound deprotonated ligand **NO2** and two hydroxyl group (-$O^{H}H^{H}$) complex ($\mathbf{I_{DNO2\text{-}2H}}$). In the optimized structures of

the reactants, the length of the N^S–C^S peptide bond of $\mathbf{I_{DNO2\text{-}2H}}$ is 1.36 Å, which is 0.03 Å longer than the same bond in $\mathbf{I_{DNO2\text{-}2W}}$ (Figure 3.20). In addition, the Zr-O^H bond length of $\mathbf{I_{DNO2\text{-}2H}}$ is 2.07 Å which is 0.13 Å longer than that of $\mathbf{I_{DNO2\text{-}2W}}$, and the charge on the O^H ion is -1.04e, which is more negative than the O^H ion in $\mathbf{I_{DNO2\text{-}2W}}$. These differences in the bond distance and charge indicate that the interaction between the Zr(IV) ion with the hydroxyl group (-O^HH^H) in $\mathbf{I_{DNO2\text{-}2H}}$ is much stronger. It helps to make -O^HH^H a better nucleophile. Another two hydroxyl group (-$O^{1H}H^H$ and –$O^{2H}H^H$) bound with Zr(IV) ion in $\mathbf{I_{DNO2\text{-}2H}}$ increases electron donating ability by adding electron density to the Zr(IV) ion and stabilizes the metal center. The metal-ligand bond lengths are shown in Table 3.8. In comparison to $\mathbf{I_{DNO2\text{-}2W}}$, the bond lengths of $\mathbf{I_{DNO2\text{-}2H}}$ are longer (Zr-N^1 = 2.32 Å, Zr-O^1 = 2.17 Å, Zr-O^2 = 2.45 Å). Those weak binding interactions will enhance the Zr(IV) center reactivity by decreasing the energy barrier. The N^S atom of the Gly-Gly dipeptide in $\mathbf{I_{DNO2\text{-}2H}}$ possesses 0.04e more negative charge than the corresponding atom in $\mathbf{I_{DNO2\text{-}2W}}$ (Table 3.9). The other noticeable differences were found in the interactions of the O^H with carbonyl carbon atom (C^S) of the Gly-Gly dipeptide. The charge difference of 1.80e between the C^S and O^H atoms of $\mathbf{I_{DNO2\text{-}2H}}$ is 0.03e larger than that for $\mathbf{I_{DNO2\text{-}2W}}$. The process has a 26.6 kcal/mol barrier from $\mathbf{I_{DNO2\text{-}2H}}$ to $\mathbf{TS_{DNO2\text{-}2H}}$. On the other hand, the barrier for $\mathbf{I_{DNO2\text{-}2W}}$ to $\mathbf{TS_{DNO2\text{-}2W}}$ is 56.0 kcal/mol (Figure 3.20). $\mathbf{I_{DNO2\text{-}2H}}$ is much more energetically feasible than $\mathbf{I_{DNO2\text{-}2W}}$. These results are consistent with the aforementioned results discussed, because the Zr (IV) ion in $\mathbf{I_{DNO2\text{-}2H}}$ is bound to two electron donating groups (-$O^{1H}H^H$ and -$O^{2H}H^H$) instead of two water molecule as shown in $\mathbf{I_{DNO2\text{-}2W}}$.

Table 3. 8 The key geometrical bond distances (Å) of the optimized reactants and transition states for different coordination number complexes ($\mathbf{I_{DNO2\text{-}1W}}$, $\mathbf{I_{DNO2\text{-}1H}}$, $\mathbf{I_{DNO2\text{-}2W}}$, $\mathbf{I_{DNO2\text{-}2H}}$, and $\mathbf{I_{DNO2\text{-}3W}}$)

Reactant	Zr-O^S	O^S-C^S	C^S-N^S	Zr-O^H	O^H-C^S	H^H-N^S	Zr-N^1	Zr-O^1	Zr-O^2	Zr-O^{1W} (O^{1H})	Zr-O^{2W} (O^{2H})	Zr-O^{3W}
The hexa-coordinated species												
$\mathbf{I_{DNO2\text{-}1W}}$	2.12	1.30	1.33	1.93	4.10	5.76	2.33	1.95	2.29	2.26	--	--
$\mathbf{I_{DNO2\text{-}1H}}$	2.22	1.28	1.34	1.97	4.09	5.49	2.34	2.01	2.32	1.97	--	--
The hepta-coordinated species												
$\mathbf{I_{DNO2\text{-}2W}}$	2.21	1.30	1.33	1.94	4.18	6.12	2.35	1.99	2.32	2.25	2.39	--
$\mathbf{I_{DNO2\text{-}2H}}$	2.39	1.27	1.36	2.07	4.03	4.44	2.32	2.17	2.45	2.01	2.01	--
The octa-coordinated specie												
$\mathbf{I_{DNO2\text{-}3W}}$	2.21	1.30	1.33	2.01	4.30	6.18	2.34	2.00	2.41	2.34	2.39	2.44

Transition state	Zr-O^S	O^S-C^S	C^S-N^S	Zr-O^H	O^H-C^S	H^H-N^S	Zr-N^1	Zr-O^1	Zr-O^2	Zr-O^{1W} (O^{1H})	Zr-O^{2W} (O^{2H})	Zr-O^{3W}
The hexa-coordinated species												
$\mathbf{TS_{DNO2\text{-}1W}}$	2.16	1.39	1.52	2.19	1.54	1.37	2.16	1.94	2.25	2.24	--	--
$\mathbf{TS_{DNO2\text{-}1H}}$	2.10	1.40	1.52	2.28	1.53	1.34	2.33	1.97	2.33	1.94	--	--
The hepta-coordinated species												
$\mathbf{TS_{DNO2\text{-}2W}}$	2.12	1.39	1.53	2.21	1.54	1.35	2.35	1.97	2.35	2.32	2.28	--
$\mathbf{TS_{DNO2\text{-}2H}}$	2.09	1.38	1.55	2.56	1.49	1.30	2.29	1.99	2.51	2.08	2.11	--
The octa-coordinated specie												
$\mathbf{TS_{DNO2\text{-}3W}}$	2.17	1.39	1.53	2.32	1.52	1.35	2.37	1.96	2.39	2.22	2.44	2.27

Table 3. 9 The atomic charges on the key atoms of the optimized reactants and transition states for different coordination number complexes ($\mathbf{I_{DNO2\text{-}1W}}$, $\mathbf{I_{DNO2\text{-}1H}}$, $\mathbf{I_{DNO2\text{-}2W}}$, $\mathbf{I_{DNO2\text{-}2H}}$, and $\mathbf{I_{DNO2\text{-}3W}}$)

Reactant	Zr	O^S	C^S	N^S	O^H	H^H	N^1	O^1	O^2	$O^{1W}(O^{1H})$	$O^{2W}(O^{2H})$	O^{3W}
The hexa-coordinated species												
$\mathbf{I_{DNO2\text{-}1W}}$	2.01	-0.75	0.77	-0.60	-0.98	0.55	-0.49	-0.80	-0.66	-0.98	--	--
$\mathbf{I_{DNO2\text{-}1H}}$	1.95	-0.71	0.77	-0.62	-1.02	0.53	-0.49	-0.84	-0.64	-1.01	--	--
The hepta-coordinated species												
$\mathbf{I_{DNO2\text{-}2W}}$	1.91	-0.74	0.78	-0.62	-0.99	0.55	-0.48	-0.83	-0.64	-0.97	-0.94	--
$\mathbf{I_{DNO2\text{-}2H}}$	1.80	-0.66	0.76	-0.66	-1.04	0.48	-0.47	-0.88	-0.60	-1.02	-1.02	--
The octa-coordinated specie												
$\mathbf{I_{DNO2\text{-}3W}}$	1.84	-0.73	0.78	-0.62	-1.02	0.54	-0.48	-0.83	-0.63	-0.97	-0.93	-0.95

Transition state	Zr	O^S	C^S	N^S	O^H	H^H	N^1	O^1	O^2	$O^{1W}(O^{1H})$	$O^{2W}(O^{2H})$	O^{3W}
The hexa-coordinated species												
$\mathbf{TS_{DNO2\text{-}1W}}$	2.02	-0.85	0.81	-0.76	-0.86	0.53	-0.79	-0.79	-0.66	-0.95	--	--
$\mathbf{TS_{DNO2\text{-}1H}}$	1.98	-0.83	0.81	-0.77	-0.90	0.51	-0.49	-0.81	-0.64	-1.00	--	--
The hepta-coordinated species												
$\mathbf{TS_{DNO2\text{-}2W}}$	1.96	-0.83	0.81	-0.78	-0.87	0.52	-0.49	-0.83	-0.64	-0.94	-0.96	--
$\mathbf{TS_{DNO2\text{-}2H}}$	1.89	-0.83	0.81	-0.77	-0.90	0.50	-0.55	-0.81	-0.62	-0.98	-1.07	--
The octa-coordinated specie												
$\mathbf{TS_{DNO2\text{-}3W}}$	1.85	-0.84	0.83	-0.78	-0.90	0.53	-0.48	-0.81	-0.63	-0.96	-0.95	-0.94

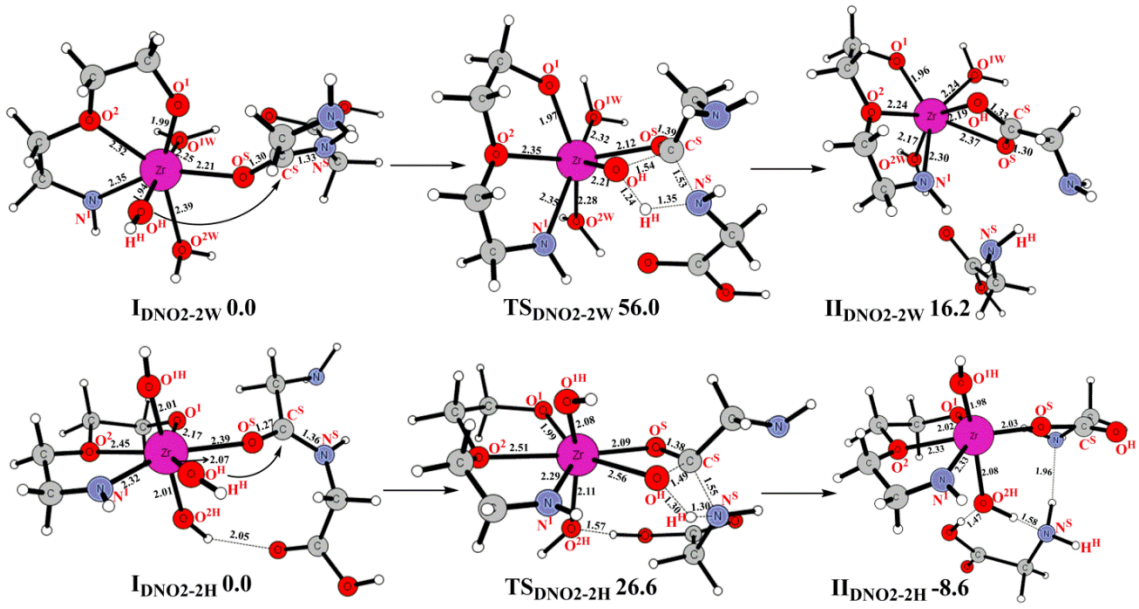

Figure 3. 20 Structures (in Å) and energies (in kcal/mol) of the reactants, transition states, and products for $\mathbf{I_{DNO2\text{-}2W}}$ and $\mathbf{I_{DNO2\text{-}2H}}$ in the concerted mechanism.

(3) The octa-coordinated specie:

The attempts to optimize a Zr(IV)-bound deprotonated ligand **NO2** and three hydroxyl group ($-O^HH^H$) complex ($\mathbf{I_{DNO2\text{-}3H}}$) failed. Therefore, only one octa-coordinated specie Zr(IV)-bound deprotonated ligand **NO2** and three water complex ($\mathbf{I_{DNO2\text{-}3W}}$) has been constructed.

The optimized structures of the reactant and transition state are shown in Figure 3.21. The Zr-O^H bond length of $\mathbf{I_{DNO2\text{-}3W}}$ is 2.01 Å, which is longer than that of both $\mathbf{I_{DNO2\text{-}1W}}$ and $\mathbf{I_{DNO2\text{-}2W}}$. Moreover, the charge on the O^H ion is -1.02e, which is more negative. A coordination number of 8 make the metal-ligand bonds weaker than those in $\mathbf{I_{DNO2\text{-}1W}}$ and

$\mathbf{I_{DNO2\text{-}2W}}$. All the bond lengths of $\mathbf{I_{DNO2\text{-}3W}}$ are shown in Table 3.8 (Zr-N^1 = 2.34 Å, Zr-O^1 = 2.00 Å, Zr-O^2 = 2.41 Å). The computed barrier from $\mathbf{I_{DNO2\text{-}3W}}$ to $\mathbf{TS_{DNO2\text{-}3W}}$ was 49.4 kcal/mol.

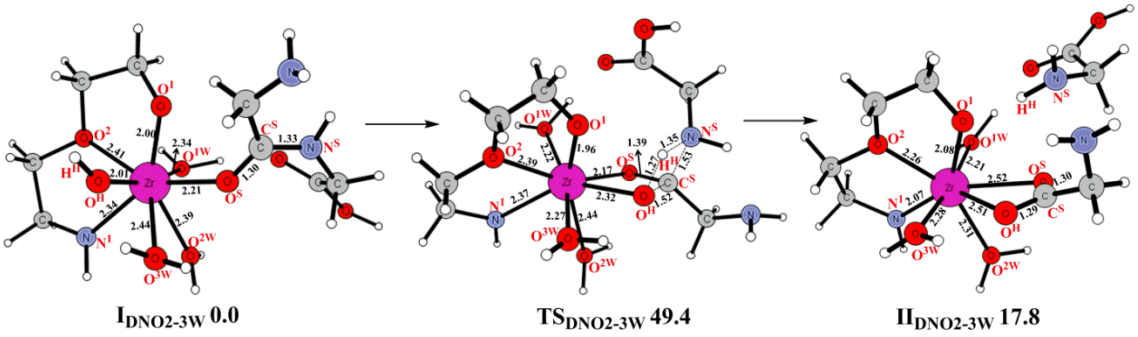

Figure 3. 21 Structures (in Å) and energies (in kcal/mol) of the reactant, transition state, and product for $\mathbf{I_{DNO2\text{-}3W}}$ in the concerted mechanism.

These results reveal that the doubly deprotonated form with 2 hydroxyl groups ($\mathbf{I_{DNO2\text{-}2H}}$) hydrolyzes the reaction with the lowest barrier (26.6 kcal/mol). A seven coordinate complex of Zr(IV) is more effective. This is in excellent agreement with the results of the ligand effects studies. In addition, electron donating groups (–OH) can activate the reactant.

3.3.4 Summary and Conclusions

In the present DFT study, the reaction mechanisms (stepwise and concerted) of the Zr(IV)-assisted peptide hydrolysis has been elucidated. The protonation states of the

ligands and the ligand effects on structures and energetics of the reaction have been investigated. Different coordination number structures of the Zr(IV)-bound complexes have also been studied.

The stepwise mechanism for the deprotonated Zr(IV)-bound ligand **N2O4** ($\mathbf{I_{DN2O4}}$) and the protonated form ($\mathbf{I_{N2O4}}$) proceeds through the following two steps: (1) formation of the tetrahedral intermediate, and (2) cleavage of the peptide bond. The second step is the rate-limiting step of the entire mechanism. The barriers for the second step of $\mathbf{I_{DN2O4}}$ and $\mathbf{I_{N2O4}}$ are 30.6 kcal/mol and 54.6 kcal/mol, respectively. However, in the concerted mechanism, the computed energy barriers for $\mathbf{I_{DN2O4}}$ and $\mathbf{I_{N2O4}}$ are 31.0 kcal/mol and 47.1 kcal/mol, respectively. Since the barriers in the stepwise mechanism are higher in energy, it can be ruled out.

In the studies of the protonation states of the ligands, four models of a **N2O4** ligand which include all the possible protonation states (Zr(IV)-bound protonated **N2O4** complex: $\mathbf{I_{N2O4}}$; singly-deprotonated **N2O4** complexes: $\mathbf{I_{DN2O4\text{-}N1}}$, $\mathbf{I_{DN2O4\text{-}N2}}$; and doubly-deprotonated **N2O4** complex: $\mathbf{I_{DN2O4}}$) have been constructed. The process of hydrolysis of the peptide bond occurs with the barriers of 47.1, 40.6, 47.9, and 31.0 kcal/mol for $\mathbf{I_{N2O4}}$, $\mathbf{I_{DN2O4\text{-}N1}}$, $\mathbf{I_{DN2O4\text{-}N2}}$, and $\mathbf{I_{DN2O4}}$, respectively. By decreasing the basicity of the ligand it could increase the Lewis acidity of the metal center. The results from the Zr(IV)-bound protonated ligand **N2O3** complex ($\mathbf{I_{N2O3}}$) and the deprotonated **N2O3** complex ($\mathbf{I_{DN2O3}}$) confirm this conclusion. Since the $\mathbf{I_{DN2O3}} \rightarrow \mathbf{TS_{DN2O3}}$ process has a 36.6 kcal/mol barrier which is 10.6 kcal/mol lower than that for the reactant $\mathbf{I_{N2O3}}$.

The role of the ligand effects were investigated by comparing the energetics of three Zr(IV)-bound ligand compounds: $\mathbf{I_{DN2O4}}$, $\mathbf{I_{DN2O3}}$, and Zr(IV)-bound deprotonated ligand **NO2** and one water complex $\mathbf{I_{DNO2\text{-}1W}}$ (The attempt to optimize a Zr(IV)-bound deprotonated ligand **NO2** complex failed). The energy barriers for the cleavage of the peptide bond are gradually increased from the reactant $\mathbf{I_{DN2O4}}$ to $\mathbf{I_{DNO2\text{-}1W}}$. The barriers were computed to be 31.0, 36.6, and 62.4 kcal/mol for $\mathbf{I_{DN2O4}}$, $\mathbf{I_{DN2O3}}$, and $\mathbf{I_{DNO2\text{-}1W}}$, respectively.

The coordination numbers of Zr(IV) have been studied in order to gain information on optimal complex structures because Zr(IV) can form complexes with flexible geometries by multi-coordination numbers. Three species complexes (The hexa-coordinated species: $\mathbf{I_{DNO2\text{-}1W}}$ and $\mathbf{I_{DNO2\text{-}1H}}$; the hepta-coordinated species: $\mathbf{I_{DNO2\text{-}2W}}$ and $\mathbf{I_{DNO2\text{-}2H}}$; the octa-coordinated specie: $\mathbf{I_{DNO2\text{-}3W}}$) have been investigated. $\mathbf{I_{DNO2\text{-}2H}}$ is more energetically feasible than all the other reactants in the hydrolysis reaction with the lowest barrier (26.6 kcal/mol). Therefore, seven coordinate complex with hydroxyl groups (–OH) for Zr(IV) is more effective. This information will be useful to understand the catalytic functioning of the Zr(IV) complexes.

3.4 Mechanistic Insights into Metal-Beta Cyclodextrin Catalyzed Peptide Hydrolysis Mechanism

In weakly acidic aqueous solutions, various Pd(II) ion-containing metal complexes are emerging as new metallopeptidases and have been utilized to promote effective and selective hydrolysis of peptides containing methionine (Met) and histidine (His) residues through coordination to the side chains.[156-161] However, most of these Pd(II) complexes are only residue selective.[120,162] Hydrolytic chemistry of a peptide bond has been used with more success in terms of sequence specificity.[25] Due to the hydrophobic and hydrophilic features of cyclodextrin (CD), it has become an extremely attractive component for mimicing an enzyme system. By utilizing the hydrophobic cavity of CD, it can form an inclusion complex (guest and host) with the substrate. Breslow et al. and others have combined bond cleaving capabilities of metal complexes (M) with the hydrophobic environment of *β*-cyclodextrin (CD) to design artificial enzymes (M-CD).[115-117] In M-CD complexes, the hydrophobic cavity of CD binds the substrate and the metal center cleaves the scissile bond. In comparison to the uncatalyzed reaction, they provided substantial rate-accelerations because little entropy and conformational enthalpy were spent in approaching the transition state.[163,164] Recently, for the first time a conjugate of the $[Pd(H_2O)_4]^{2+}$ (**I_{Pd}**) and *β*-cyclodextrin (**I_{Pd}-CD**), 6-S-2-(2-mercaptomethyl)-propane-6-deoxy-β-cyclodextrin diaqua palladium(II), was reported to sequence-specifically cleave the unactivated tertiary Ser-Pro peptide bond in the sequence of Ser-Pro-Phe of bradykinin at pH 7.0 and 60°C (Figure 3.22).[165] The measured rate constant of 0.07 h^{-1} for this reaction corresponds to the barrier of 23.8 kcal/mol using the Arrhenius equation.

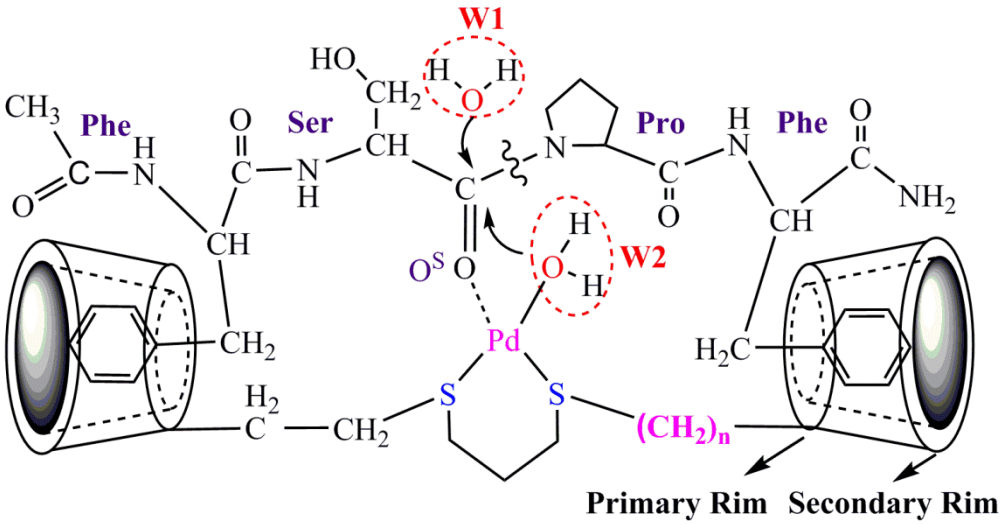

Figure 3. 22 The experimental suggestions for peptide hydrolysis by the **I_{Pd}-CD** complex.

3.4.1 Experimental Proposed Mechanism

I_{Pd}-CD catalyzes the hydrolysis of the Ser-Pro bond through the following overall reaction:

$$\text{Ser-(O=)C-NH-Pro} + H_2O \rightarrow \text{Ser-COOH} + NH_2\text{-Pro} \quad (2)$$

The experimentally proposed mechanisms of the reaction (1) catalyzed by **I_{Pd}-CD** is described in Figure 3.22. First, the aromatic side chain of the Phe residue of the substrate binds to the cavity of CD through weak hydrophobic interactions and positions the Pd^{2+} metal center adjacent to the Ser-Pro peptide bond. The Pd^{2+} ion then coordinates to the carbonyl oxygen atom (O^S) of the substrate and activates the amide group towards

nucleophilic attack by a water molecule.[147,166,167] After the formation of this complex, the peptide bond cleavage can occur through the following two kinetically indistinguishable mechanisms (Figure 3.22): (I) *Cleavage by external attack:* the external solvent water molecule (W1) is activated for hydrolysis and (II) *Cleavage by internal delivery:* the Pd^{2+} bound water molecule (W2) is utilized for hydrolysis. However, the exact reaction mechanism and the information regarding the location of CD (number (n) of $-CH_2$ groups downstream from the S atom of $\mathbf{I_{Pd}}$), conformation of CD (primary or secondary rim of CD facing the substrate), the number of CD (one or two) and optimum metal ion (Pd^{2+}, Zn^{2+} or Co^{2+}) in the $\mathbf{I_{Pd}}$**-CD** complex are currently not available.[165] This information is critical to understand the functioning of this class of artificial enzymes and improving their activities.

The available experimental data provide an ideal platform to address these outstanding issues through state-of-the-art theoretical approaches employed in this study. In the first step, the pure QM approach (DFT: B3LYP) is applied to determine the energetically most feasible mechanism for the hydrolysis of the Ser-Pro peptide bond of the Ser-Pro-Phe substrate by $\mathbf{I_{Pd}}$. In the next step, the hybrid quantum mechanics/molecular mechanics (QM/MM) method ONIOM: B3LYP/Amber has been applied in a systematic manner to perform the following studies (Figure 3.22): (1) the primary rim of CD facing the substrate for n = 1 and 2; (2) the secondary rim of CD facing the substrate; (3) inclusion of the second CD molecule to the left of the metal center with the primary rim facing the substrate for n=2; and (4) the substitution of Pd^{2+} with biological metal ions (Zn^{2+} and Co^{2+}).

3.4.2 Computational Methods and Models

Method: All QM and QM/MM calculations were carried out using the Gaussian 09 program package.[168] The B3LYP/Lanl2dz method was used for the QM only calculations[61,150,151] (With corresponding Hay-Wadt effective core potential (ECP) for Pd, Zn, and Co[61,150,151]). Frequency calculations at the same level were also performed to characterize the nature of all minima and transition states. The final energies of the optimized structures in the QM calculations obtained at the B3LYP/ {Lanl2dz + d(O, N, S and C) + p(H)} energies including thermal corrections.

In our two-layer ONIOM (QM/MM) calculation, the system is divided into two parts. A selected model system (including the Pd(II) catalytic center and cleaving peptide bond) where the chemical reactions occur was treated with quantum mechanism (QM, a high-level method), while the remaining was treated with molecular mechanics (MM, a low-level method). The ONIOM optimization procedure uses macro/microiterations[169] and the electrostatic interactions between the QM and the MM part were treated by mechanical embedding (ME). The present models use charges from ESP (Merz-Kollman) calculations. Charges are calculated for the first stationary point of each model, and the same charges were used in all optimizations with that model.

The geometries of reactants, transition states and products in the QM part were optimized without any symmetry constraints at the B3LYP/Lanl2dz level of theory[61,150,151] (With corresponding Hay- Wadt effective core potential (ECP) for Pd, Zn, and Co[61,150,151]). And the MM part was calculated using Amber force field. The final energies of the optimized structures were further improved by performing single point

calculations including additional d and p polarization functions for O (α=0.96), N (α=0.74), C (α=0.59), S (α=0.50) and H (α=0.36) atoms, respectively (taken from the EMSL's Gaussian basis set library) in the basis set used for optimizations.

Frequency calculations were also carried out at the same (B3LYP/Lanl2dz: Amber) level for the geometry optimizations to obtain Zero-point vibrational (un-scaled), thermal (at 298.15 K and 1 atm.) and entropy corrections (at 298.15 K). While frequency calculations on transition states were employed to confirm the nature of the stationary points, which showed only one negative eigenvalue for transition states.

To test the accuracy of the B3LYP method, the barrier of the reaction computed using this functional was compared with the barrier calculated using the MPW91[170] and M06-L functional[171] for the $\mathbf{I_{Pd}\text{-}CD^{2P}}$ complex. It was found that, in comparison to the B3LYP functional with a barrier of 32.8 kcal/mol, the application of the MPW91 functional slightly (0.1 kcal/mol) increased the barrier, whereas the application of the M06-L functional increased the barrier by 3.4 kcal/mol (36.2 kcal/mol).

Models. The available experimental information was fully incorportated in building models for the calculations. In the QM only study, $\mathbf{I_{Pd}}$ (without β-CD) and substrate, a tripeptide (Ser-Pro-Phe) model, were utilized. While in the ONIOM study, $\mathbf{I_{Pd}}$**-CD** ($\mathbf{I_{Pd}}$ complexed with β-CD) and the tripeptide as the substrate were considered. When β-CD dimer was considered, a tetrapeptide sequence (Phe-Ser-Pro-Phe) was used so as to provide double binding sites. The initial coordinates of β-CD was taken from the three-

dimensional crystal structure.[172] The charge on all the system is zero, and they exist in the singlet spin state.

3.4.3 Results and Discussion

3.4.3.1 External Attack and Internal Delivery Mechanisms

The peptide bonds can be cleaved through the following two mechanisms: (1) the *external water attack* mechanism and (2) *internal water delivery* mechanism. In the *external water attack* mechanism (Figure 3.23a), the Pd(II) complex binds to the substrate through the coordination between the Pd(II) ion and the carbonyl oxygen atom O^S in $\mathbf{I_{Pd\text{-}E}}$. The interaction between the Pd(II) ion and the O^S atom increases the electrophilicity of the C^S [147,173] and activates it for attack by an external water molecule (H_2O^2). In the next step ($\mathbf{TS_{Pd\text{-}E}}$), in a concerted fashion, the N^S atom of the peptide bond abstracts a proton from the external water molecule (H_2O^2), and the hydroxyl group ($-O^2H$) makes a nucleophilic attack on the C^S of the peptide bond. This process leads to the cleavage of C^S-N^S peptide bond with the computed barrier of 51.9 kcal/mol. The optimized transition state $\mathbf{TS_{Pd\text{-}E}}$ is shown in Figure 3.23a. All the relevant bond distances indicate that this process is concerted (O^2- C^S = 1.69 Å, H^3- N^S = 1.33 Å, O^2-H^3 = 1.21 Å, N^S- C^S = 1.58 Å). The DFT calculations suggest that in the *external attack* mechanism the calculated barriers are prohibitively high (> 50.0 kcal/mol) for the cleavage of the peptide bonds, and therefore, this mechanism is ruled out.

In the mechanism of *internal water delivery*, Pd(II) functions as Lewis acid and binds to the carbonyl oxygen atom O^S with a distance of 2.08 Å and activates the C^S atom

(Figure 3.23b, $\mathbf{I_{Pd\text{-}I}}$). Instead of using an external water molecule, a water molecule ($H2O^1$) which is bound to the Pd(II) ion is activated. In the transition state ($\mathbf{TS_{Pd\text{-}I}}$), the O^1- H^1 bond is broken, and the proton H^1 is transferred to the N^S of the peptide bond. This process occurs concomitantly with the transfer of the hydroxyl group ($-O^1H$) to the C^S atom and leads to the cleavage of the peptide bond with energy barrier of 40.2 kcal/mol. It is 11.7 kcal/mol lower than the barrier in the *external attack* mechanism (51.9 kcal/mol). This reduction in barrier is caused by the substantial lowering of the pK_a value of the W2 water molecule due to the binding to the Pd^{2+} ion.

In the presence of CD (at n = 2), the barrier of 39.0 kcal/mol for the *external delivery* mechanism (Figure 3.24) is 6.2 kcal/mol higher than the barrier for the *internal delivery* mechanism (32.8 kcal/mol), Figure 3.25. However, the exact protonation state of the metal-bound water molecule (H_2O of –OH) is not known. A metal bound hydroxyl group ($Pd\text{-}O^1H^1$) will utilize a stepwise mechanism for peptide hydrolysis (Figure 3.26). According to this mechanism, a nucleophilic attack of the $-O^1H^1$ group on the C^S atom of the substrate leads to the creation of a tetrahederal intermediate in which both O^1 and O^S atoms are coordinated to the Pd ion ($\mathbf{II_{Pd}\text{-}CD^{2P}(OH)}$) in Figure 3.26). This process occurs with a barrier of 19.8 kcal/mol and is endothermic by 18.6 kcal/mol. In the next step, a transfer of the H^1 proton to the N^S atom of the $C^S\text{-}N^S$ peptide bond cleaves the bond. From the reactant, this concerted and rate-limiting process takes place with a barrier of 33.5 kcal/mol. The barrier using this mechanism is only slightly higher by 0.7 kcal/mol than the barrier (32.8 kcal/mol) computed for the concerted mechanism. Since the *internal delivery* mechanism is found to be significantly more energetically feasible than the *external attack* mechanism, only this mechanism (in the concerted form) is further

utilized to investigate the effect of CD on the activity of the **I_{Pd}-CD** complex through QM/MM calculations.

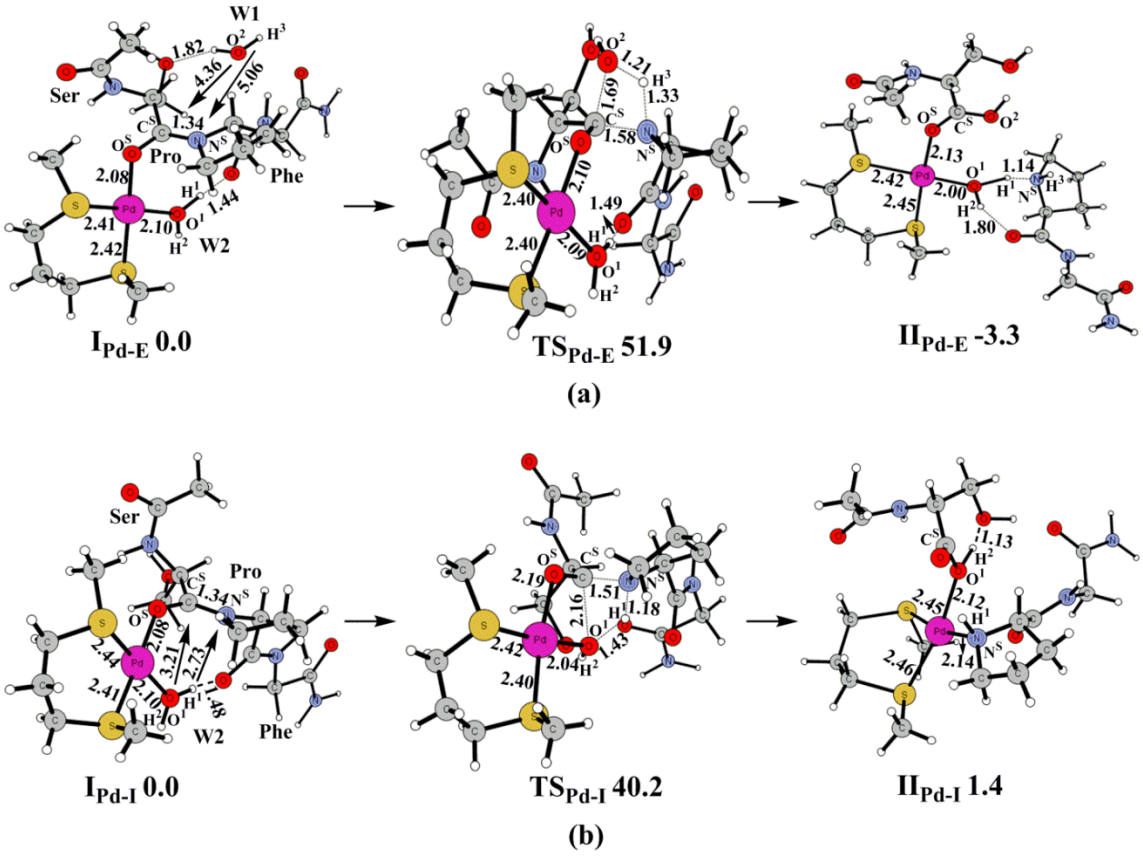

Figure 3. 23 Structures (in Å) and energies (in kcal/mol) of the reactant, transition state (optimized), and product in the QM model for the hydrolysis of Ser-Pro peptide bond in the Ser-Pro-Phe sequence. (a) *external attack* mechanism, (b) *internal delivery* mechanis.

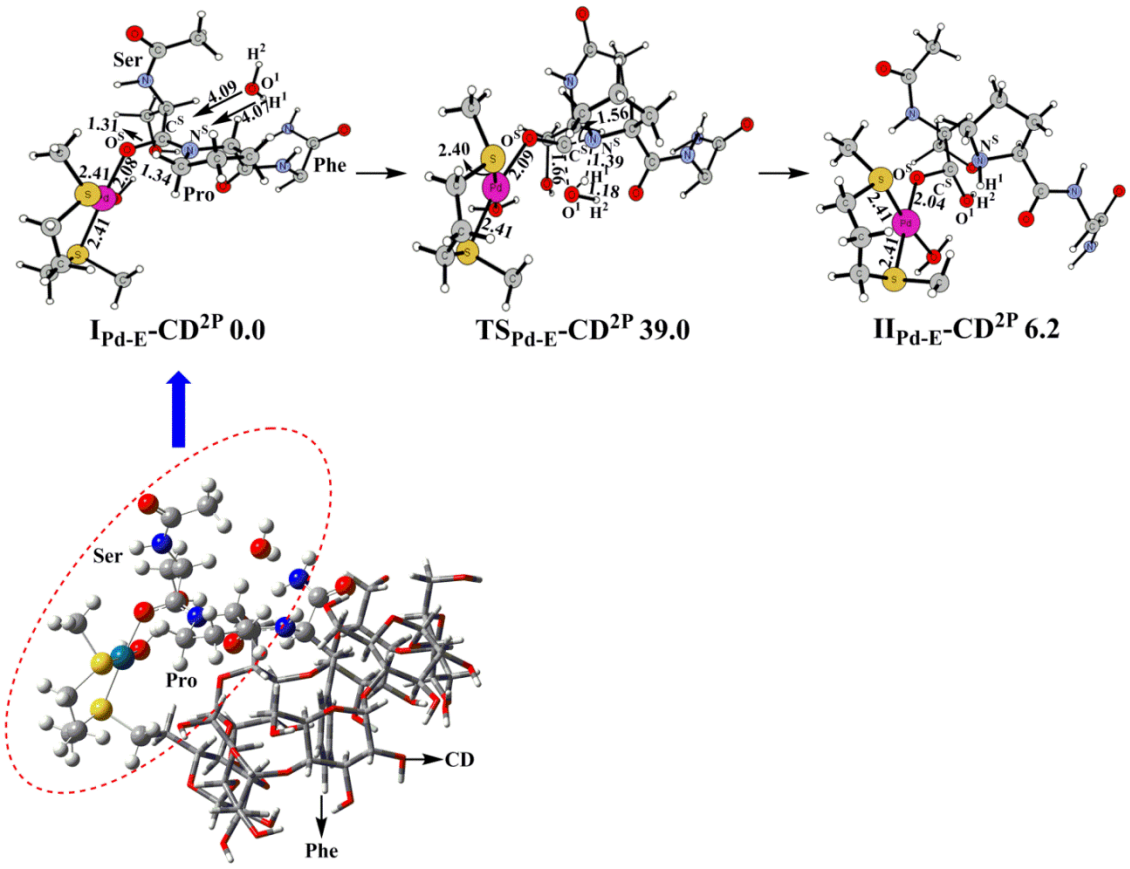

Figure 3. 24 Structures (in Å) and energies (in kcal/mol) of the reactant, transition state (optimized), and product for $\mathbf{I_{Pd\text{-}E}\text{-}CD^{2P}}$.

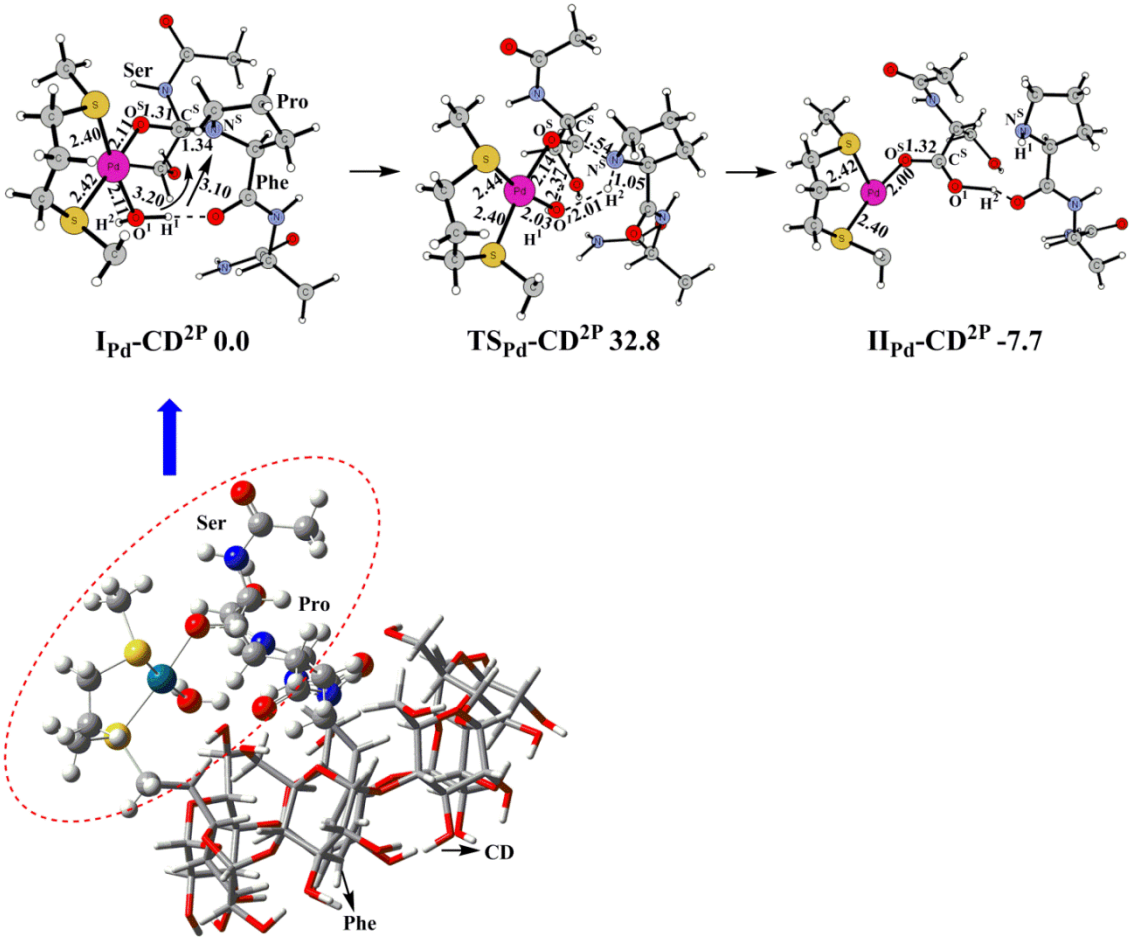

Figure 3. 25 Structures (in Å) and energies (in kcal/mol) of the reactant, transition state (optimized), and product for $\mathbf{I_{Pd}\text{-}CD^{2P}}$.

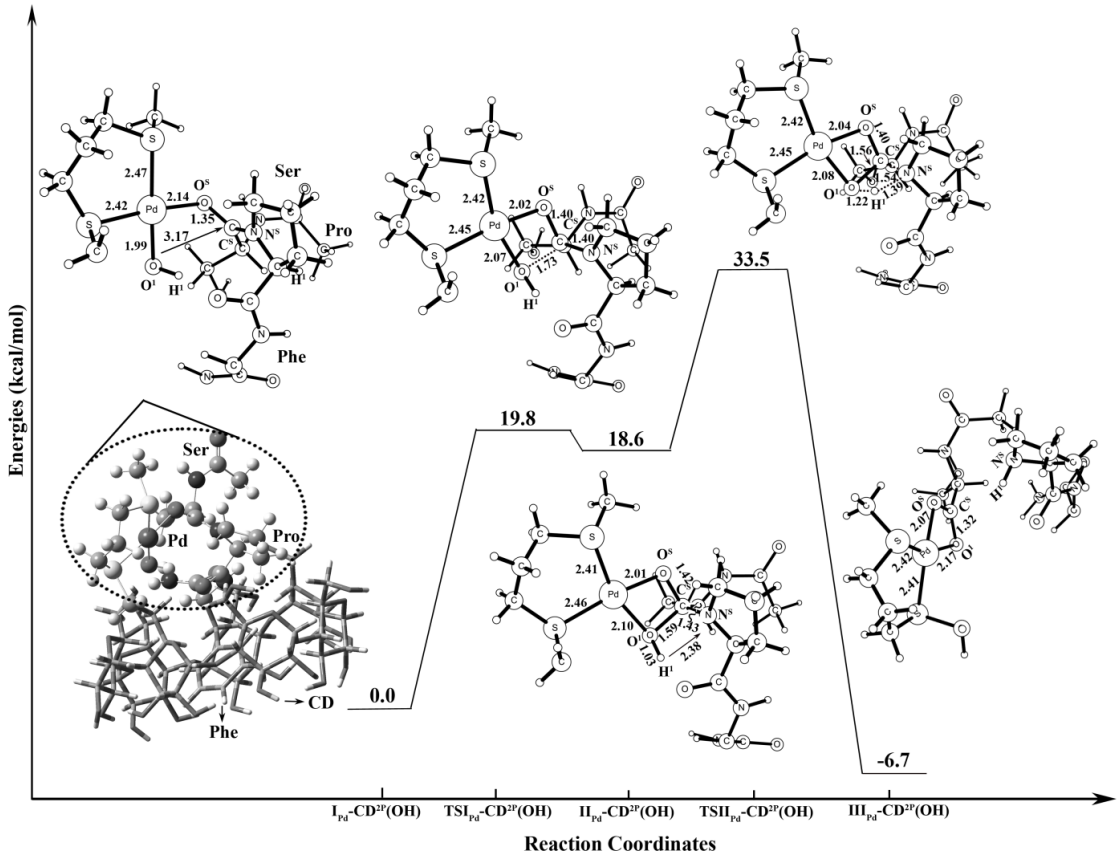

Figure 3. 26 Structures (in Å) and energies (in kcal/mol) of the reactant, transition states (optimized), intermediate and product for **I_{Pd}-CD^{2P}(OH)**.

3.4.3.2 Primary Rim of CD Facing the Substrate for n = 1 and 2

The catalyst (**I_{Pd}-CD)** and substrate (Ser-Pro-Phe) form a host-guest complex through hydrophobic interactions between CD and a Phe residue. In addition, the Pd^{2+} ion coordinates to the carbonyl oxygen (O^S) of the scissile peptide bond (C^S-N^S) (Pd-O^S ~ 2.12 Å), Figure 3.25 & 3.27. From the reactant, the metal bound water molecule

($H^1O^1H^2$) is activated and in a concerted manner the H^1 proton and O^1-H^2 hydroxyl ion are transferred to the N^S and C^S atoms of the scissile peptide bond respectively. This process leads to the cleavage of the peptide bond and separate metal bound carboxyl and amine terminals are created. Between the two possible locations of the CD binding (n = 1 and 2), only n = 2 (**I_{Pd}-CD^{2P}** case) was found to result in a significant reduction in calculation energy compared to the system where the CD is absence.

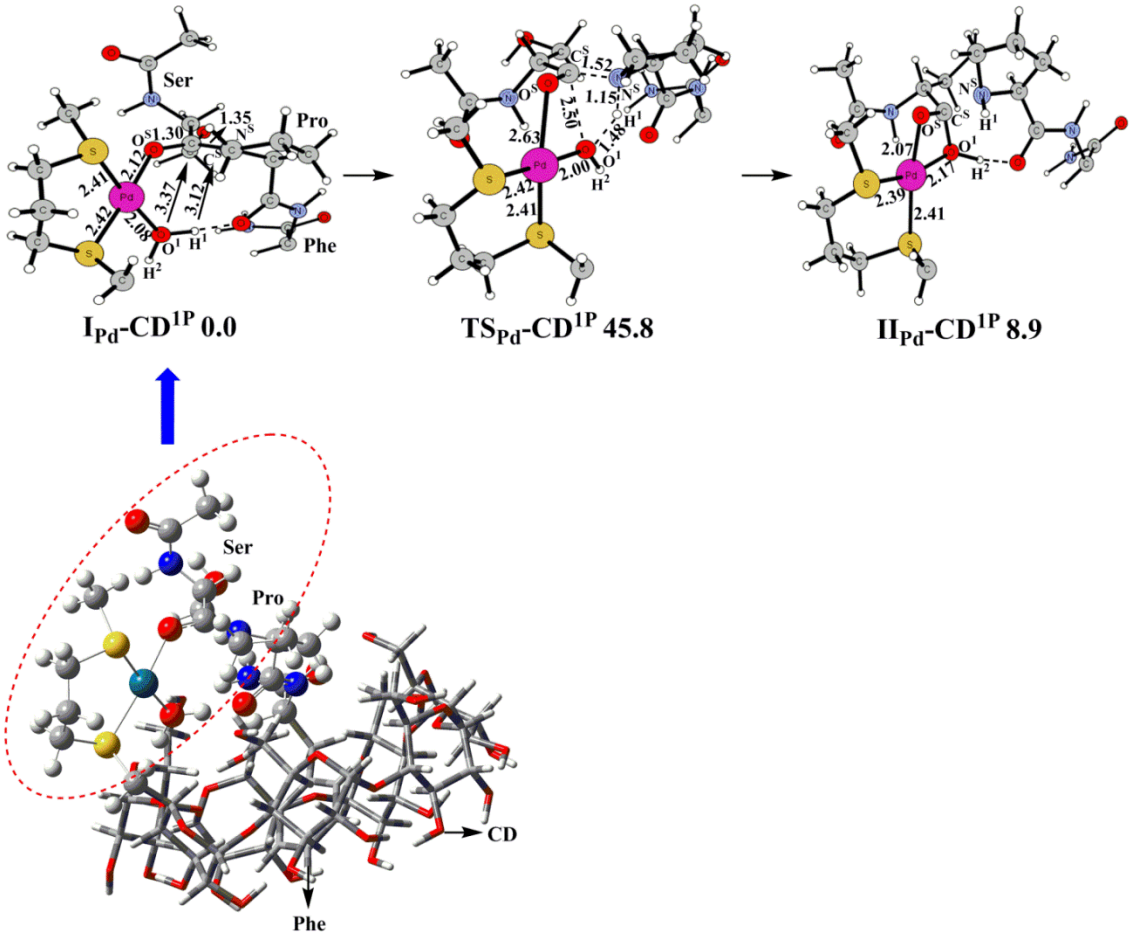

Figure 3. 27 Structures (in Å) and energies (in kcal/mol) of the reactant, transition state (optimized), and product for **I_{Pd}-CD^{1P}**.

In $\mathbf{I_{Pd}\text{-}CD^{2P}}$, the barrier of 32.8 kcal/mol from the reactant is 7.4 kcal/mol lower than the barrier without CD ($\mathbf{I_{Pd\text{-}I}}$), Table 3.10. However, this barrier is 9.0 kcal/mol higher than the measured value.[165] This overestimation could be partially attributed to the measurement of the rate constants at a much higher temperature (60 °C), whereas our calculations were performed at room temperature (25 °C). The binding of CD induces substantial structural changes and increases the Pd-O^S distance by 0.03 Å (Pd-O^S = 2.11 Å) and brings the water nucleophile closer to the scissile peptide bond (C^S-N^S). In $\mathbf{I_{Pd}\text{-}CD^{2P}}$ (Figure 3.25), the electronic charges on the Pd ion and O^S atoms are increased by 0.03 e and 0.02 e, respectively (Pd = 0.45 e and O^S = -0.72 e). These changes enhance the Lewis acidity of the metal center and increase its peptidase activity. In the optimized transition state ($\mathbf{TS_{Pd}\text{-}CD^{2P}}$), all the corresponding distances indicate that this process is concerted (O^1-C^S = 2.37 Å, O^1-H^1 = 2.01 Å, H^1-N^S = 1.05 Å and C^S-N^S = 1.54 Å). The aforementioned structural changes induced by the binding of CD create much better conditions for the cleavage of the peptide bond. The effect of CD on the energetics of the reaction is very surprising because it was previously believed that CD only provides specificity to $\mathbf{I_{Pd}}$.[165]

On the other hand, for n = 1 system ($\mathbf{I_{Pd}\text{-}CD^{1P}}$), the computed barrier of 45.8 kcal/mol for this process is 5.6 kcal/mol higher than the barrier in the absence of CD (40.2 kcal/mol) (Table 3.10). The reason for this increase could be the inclusion of the CD ring at n = 1 shortens the bond distance between the Pd^{2+} ion and water nucleophile (Pd-O^1) and pushes the nucleophile and peptide bond (C^S-N^S) away from each other (Pd-O^1 = 2.08 Å, O^1-C^S = 3.37 Å and H^1-N^S = 3.12 Å), Figure 3.27. In comparison to the QM only model, the Pd-O^1 distance shrinks by 0.02 Å and the O^1-C^S and H^1-N^S distances elongate

by 0.16 and 0.39 Å, respectively (Pd-O^1 = 2.08 Å, O^1-C^S = 3.37 Å and H^1-N^S = 3.12 Å). In addition, the electronic charges on the Pd^{2+} and O^1 atoms are increased by 0.10 and 0.03e (Pd = 0.52 e and O^1 = -0.99 e). All these changes lower the peptidase activity of the complex.

These results suggest that the inclusion of the CD ring at the n = 2 locations can provide 3×10^5 times the acceleration in hydrolytic activity. For the *external attack* (Figure 3.24) and *internal delivery* mechanisms (Figure 3.25) the presence of CD at this position reduces the barriers by 10-12 kcal/mol for the both mechanisms, i.e. 39.0 and 32.8 kcal/mol for the former and latter respectively. Therefore, only this binding location (n = 2) is used in the remaining calculations.

3.4.3.3 Secondary Rim of CD Facing the Substrate ($\mathbf{I_{Pd}}$-$\mathbf{CD^{1S}}$)

The binding of the secondary rim of CD through the C2 atom of the glucose unit of CD with the Pd^{2+} center also forms the host-guest complex with the substrate (**$\mathbf{I_{Pd}}$-$\mathbf{CD^{1S}}$,** Figure 3.28). However, due to the larger cavity of the secondary rim the interactions of the Phe residue of the substrate with CD are much weaker than in **$\mathbf{I_{Pd}}$-$\mathbf{CD^{2P}}$**. Furthermore, in the reactant (**$\mathbf{I_{Pd}}$-$\mathbf{CD^{1S}}$**), the Pd-O^S and O^1-C^S bond distances are decreased and increased by 0.03 and 0.08 Å respectively (Pd-O^S = 2.08 Å and O^1-C^S = 3.28 Å) compared to **$\mathbf{I_{Pd}}$-$\mathbf{CD^{2P}}$**. These structural differences raise the barrier of the reaction by 4.2 kcal/mol than the barrier for the **$\mathbf{I_{Pd}}$-$\mathbf{CD^{2P}}$** system (37.0 kcal/mol from **$\mathbf{I_{Pd}}$-$\mathbf{CD^{1S}}$**), Table 3.10.

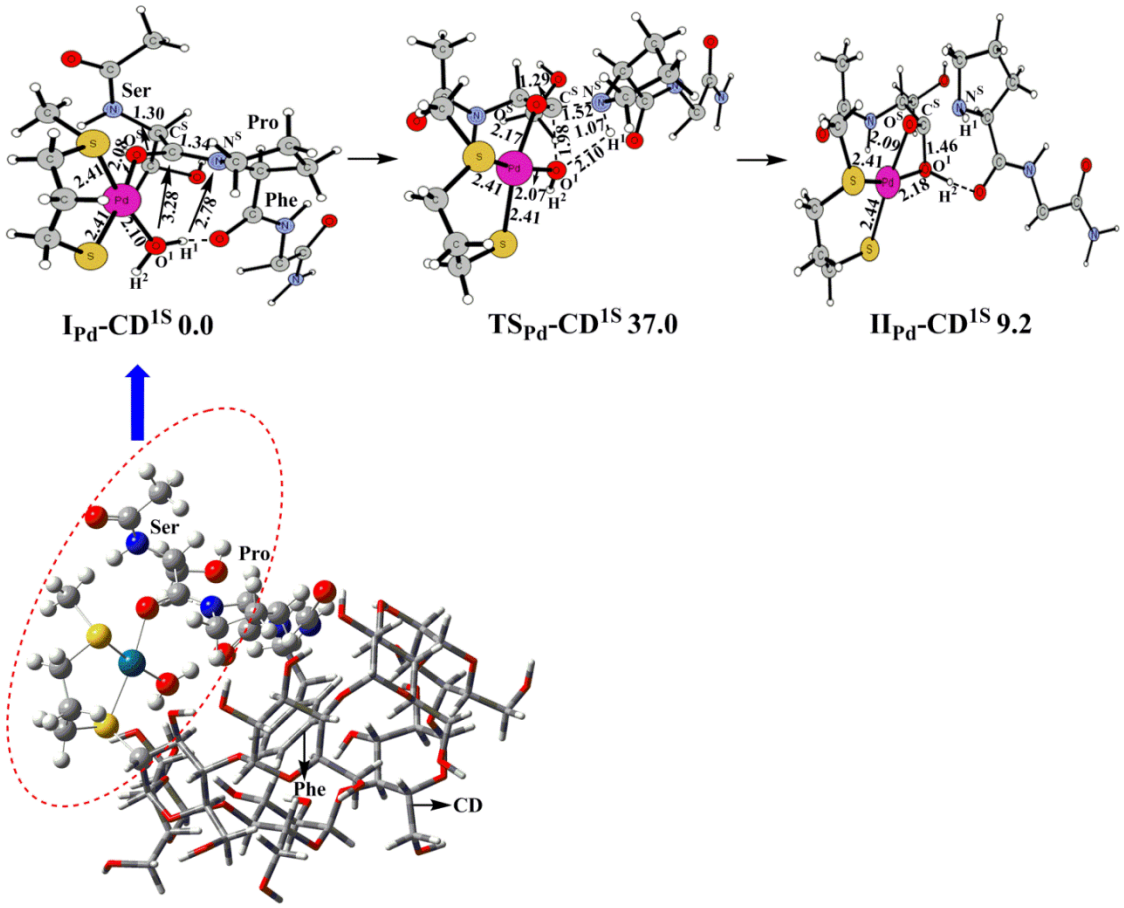

Figure 3. 28 Structures (in Å) and energies (in kcal/mol) of the reactant, transition state (optimized), and product for $\mathbf{I_{Pd}\text{-}CD^{1S}}$.

3.4.3.4 Inclusion of the Second CD Ring at n = 2 ($\mathbf{I_{Pd}\text{-}2CD^{2P}}$)

The effect of the second CD on the energetics of the reaction was investigated by including an additional CD ring to the left of the metal center and a Phe residue in the substrate (Phe-Ser-Pro-Phe sequence) in $\mathbf{I_{Pd}\text{-}CD^{2P}}$. In the reactant ($\mathbf{I_{Pd}\text{-}2CD^{2P}}$, Figure 3.29), both Phe residues interact with the CD rings through hydrophobic interactions. In $\mathbf{I_{Pd}\text{-}2CD^{2P}}$, the Pd-$O^1$ and O^1-C^S distances are 0.04 and 0.16 Å shorter respectively and

the Pd-O^S bond is 0.02 Å longer than the corresponding distances in the reactant (**I_{Pd}-CD^{2P}**) with one CD ring (Pd-O^1 = 2.07 Å, O^1-C^S = 3.04 Å and Pd-O^S = 2.13 Å). Rather interestingly, in comparison to **I_{Pd}-CD^{2P}**, the inclusion of the second CD doesn't provide further rate acceleration and actually increases the barrier slightly by 2.8 kcal/mol i.e. 35.6 kcal/mol from **I_{Pd}-2CD^{2P}**, Table 3.10.

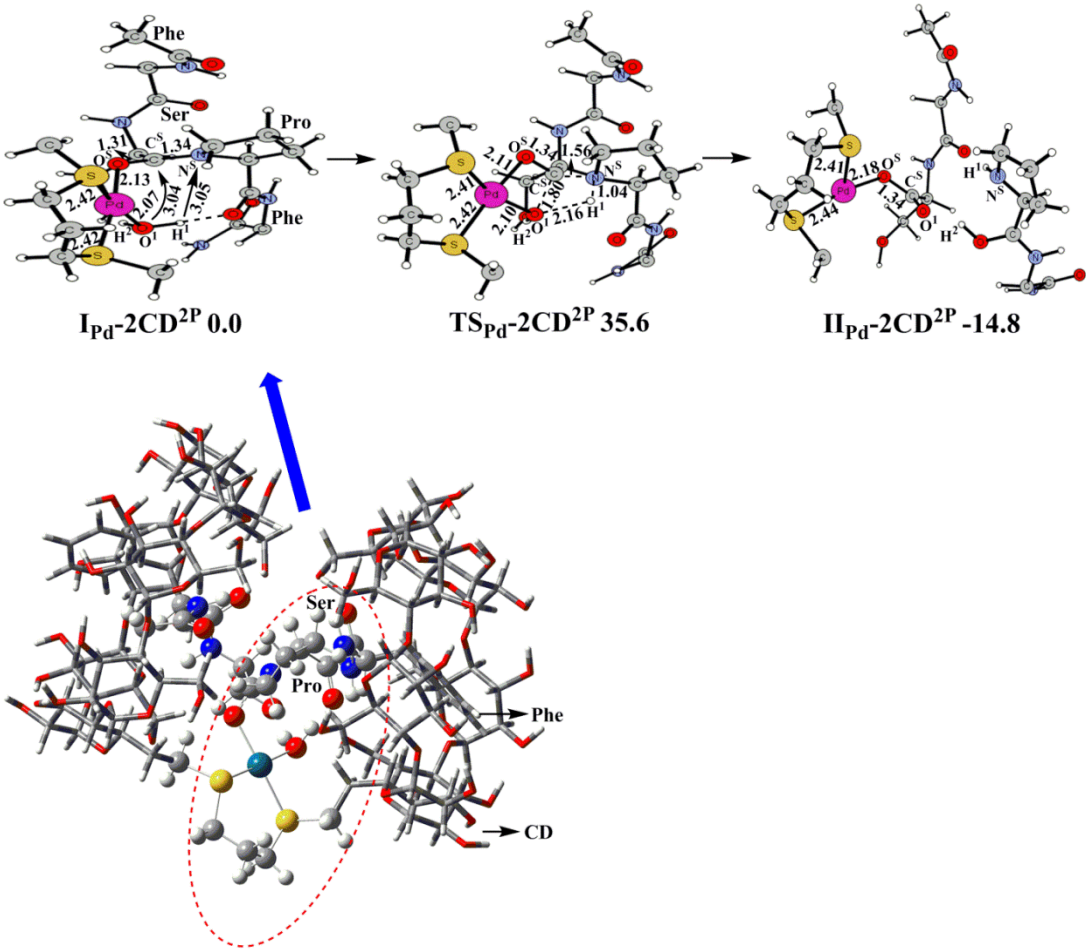

I_{Pd}-2CD^{2P} 0.0 **TS_{Pd}-2CD^{2P} 35.6** **II_{Pd}-2CD^{2P} -14.8**

Figure 3. 29 Structures (in Å) and energies (in kcal/mol) of the reactant, transition state (optimized), and product for **I_{Pd}-2CD^{2P}**.

3.4.3.5 Substitution of Pd with Co and Zn in $\mathbf{I_{Pd}\text{-}CD^{2P}}$

To study the role of the metal ion in the reaction, the nonbiological Pd^{2+} ion in $\mathbf{I_{Pd}\text{-}CD^{2P}}$ was substituted with biological Co^{2+} and Zn^{2+} metals ($\mathbf{I_{Co}\text{-}CD^{2P}}$ and $\mathbf{I_{Zn}\text{-}CD^{2P}}$ respectively). In the reactant of the Co^{2+} variant ($\mathbf{I_{Co}\text{-}CD^{2P}}$, Figure 3.30), all the key distances, Co-O^1, O^1-C^S and Co-O^S are substantially shorter by 0.07, 0.06 and 0.13 Å respectively than the corresponding distances in its Pd^{2+} containing counterpart ($\mathbf{I_{Pd}\text{-}CD^{2P}}$). In comparison to the $\mathbf{I_{Pd}\text{-}CD^{2P}}$ complex (32.8 kcal/mol), the barrier for the reaction was lower by 6.2 kcal/mol i.e. 26.6 kcal/mol for $\mathbf{I_{Co}\text{-}CD^{2P}}$ (Table 3.10). On the other hand, for the Zn^{2+} variant ($\mathbf{I_{Zn}\text{-}CD^{2P}}$), the barrier was increased by 3.1 kcal/mol (35.9 kcal/mol from $\mathbf{I_{Zn}\text{-}CD^{2P}}$, Figure 3.31) than that of $\mathbf{I_{Pd}\text{-}CD^{2P}}$ (Table 3.10).

Table 3. 10 Energetics of peptide hydrolysis for all the cases

Combination	Barrier (kcal/mol)	Exothermicity (kcal/mol)
$\mathbf{I_{Pd\text{-}E}}$	51.9	-3.3
$\mathbf{I_{Pd\text{-}I}}$	40.2	1.4
$\mathbf{I_{Pd\text{-}E}\text{-}CD^{2P}}$	39.0	6.2
$\mathbf{I_{Pd}\text{-}CD^{2P}}$	32.8	-7.7
$\mathbf{I_{Pd}\text{-}CD^{2P}(OH)}$	33.5	-6.7
$\mathbf{I_{Pd}\text{-}CD^{1P}}$	45.8	8.9
$\mathbf{I_{Pd}\text{-}CD^{1S}}$	37.0	9.2
$\mathbf{I_{Pd}\text{-}2CD^{2P}}$	35.6	-14.8
$\mathbf{I_{Zn}\text{-}CD^{2P}}$	35.9	5.8
$\mathbf{I_{Co}\text{-}CD^{2P}}$	26.6	-26.8

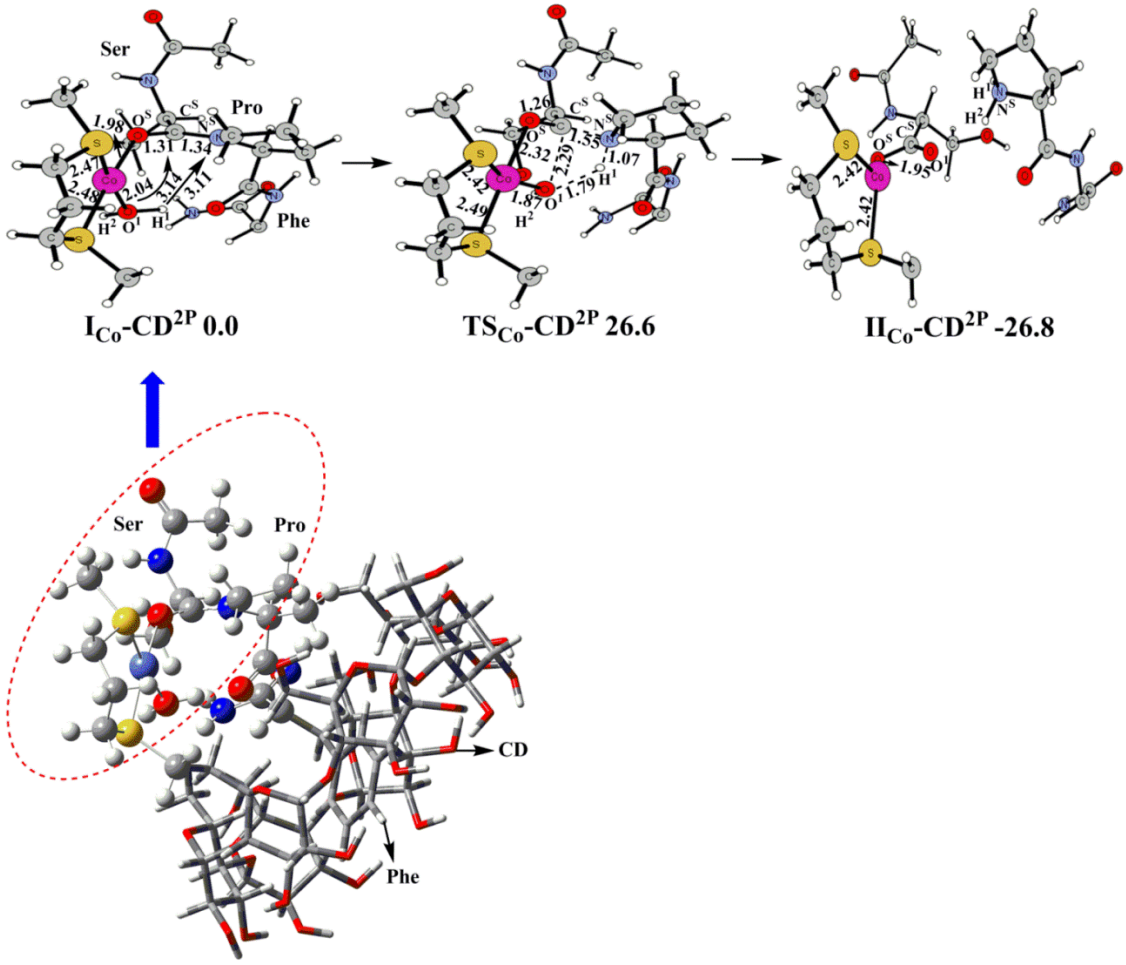

Figure 3. 30 Structures (in Å) and energies (in kcal/mol) of the reactant, transition state (optimized), and product for $\mathbf{I_{Co}}$-$\mathbf{CD^{2P}}$.

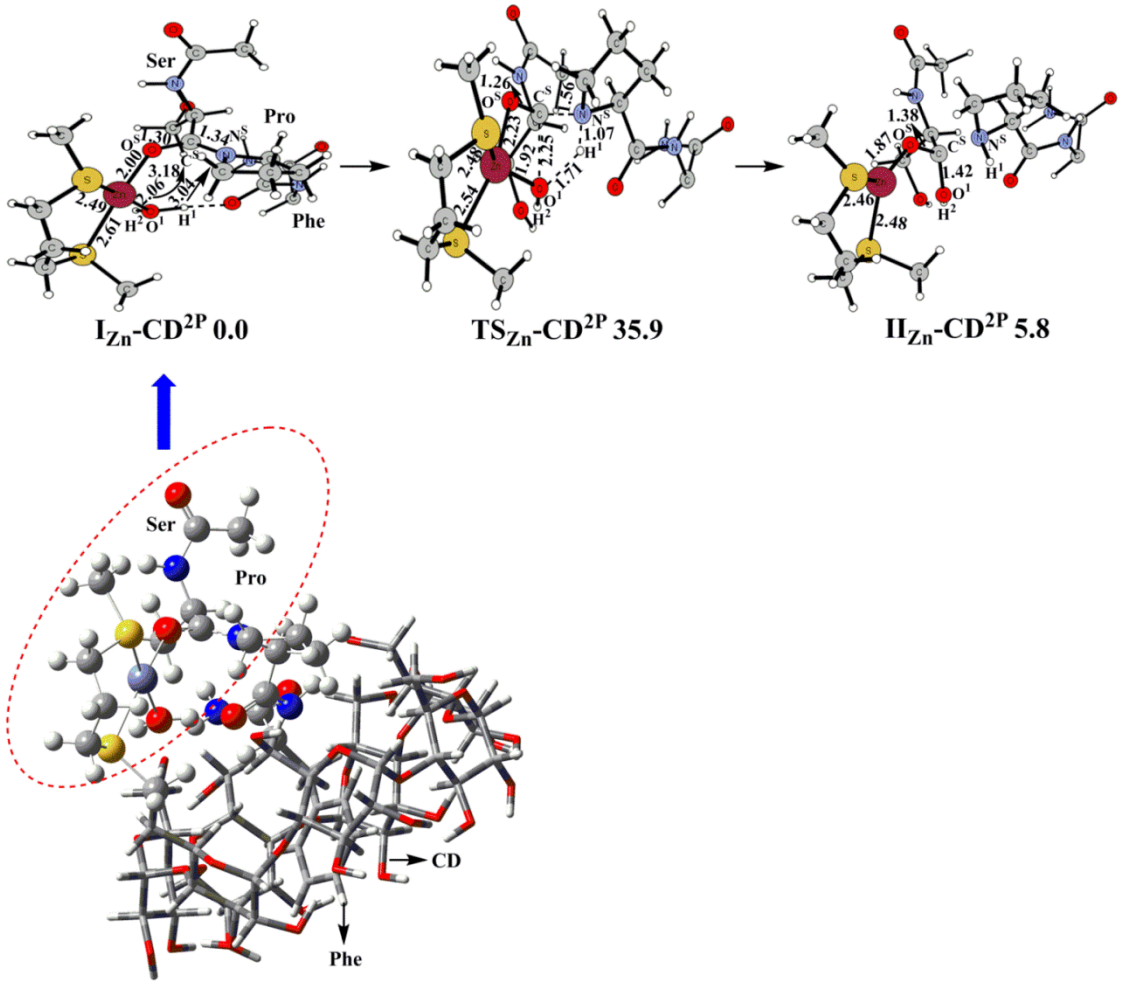

Figure 3. 31 Structures (in Å) and energies (in kcal/mol) of the reactant, transition state (optimized), and product for $\mathbf{I_{Zn}\text{-}CD^{2P}}$.

3.4.4 Summary

In the present QM and QM/MM studies, based on the experimental information, mechanisms for the hydrolysis of the Ser-Pro bond in (Phe)-Ser-Pro-Phe catalyzed by a

Pd(II) complex conjugated with β-CD have been elucidated. Different combinations of how the catalytic center binds to β-CD (n=1 or 2, primary or secondary rim, mono or di β-CD) have been compared to obtain the optimal conformation for hydrolyzing the peptide bond. Moreover, the metal substitution by Co(II) and Zn(II) on structures and energetics of the reaction has been investigated.

The mechanism of the reaction is proposed to follow two mechanisms: (1) the *external water attack* mechanism and (2) *internal water delivery* mechanism. In the *external water attack* mechanism (the QM only model), it utilizes an external water molecule to hydrolyze the peptide bond with a very high barrier of 51.9 kcal/mol. This possibility was ruled out. While for the *internal water delivery* mechanism, by activating the water molecule which coordinates to the Pd(II) ion, the nucleophilic attack goes through a lower barrier of 40.2 kcal/mol. The computed barriers in the presence of CD (at n=2) are also in accordance with the aforementioned results. In addition, both concerted and stepwise pathways proceed through the similar barriers.

It was found that the optimal conformation for the Pd(II) catalytic center conjugated with the β-CD is by connecting the primary rim of β-CD with n=2 ($\mathbf{I_{Pd}\text{-}CD^{2P}}$), with the calculated barrier of 32.8 kcal/mol. Moreover, the reactant ($\mathbf{I_{Pd}\text{-}CD^{1S}}$) formed by the binding of the secondary rim of CD through the C2 atom of the glucose unit with the Pd^{2+} center increased the barrier of the reaction by 4.2 kcal/mol compared to $\mathbf{I_{Pd}\text{-}CD^{2P}}$. The barrier for the Pd(II) metal center connecting a bi-βCD ($\mathbf{I_{Pd}\text{-}2CD^{2P}}$) was calculated to be 35.6 kcal/mol, which is 2.8 kcal/mol higher than the mono-βCD case. The role of the metal ion on the energetics was studied by comparing the energetics of a Pd(II) center

with Co(II) and Zn(II) substituted forms, with computed barriers of 26.6 kcal/mol and 35.9 kcal/mol, respectively. In comparison to $\mathbf{I_{Pd}\text{-}2CD^{2P}}$, the replacement of Pd(II) with Co(II) ($\mathbf{I_{Co}\text{-}CD^{2P}}$) can further provide 3.7×10^4 times the rate enhancement.

The QM and ONIOM results obtained from these studies provide structural (structures of short lived intermediates and transition states), mechanistic (*external* or *internal* water attack), and energetics (activation barriers) information concerning the peptide bond hydrolysis of X-Pro of the X-Pro-Phe sequence. The results indicate that the hydrophobic interactions between catalyst and substrate play an important role in the catalytic hydrolysis. The Pd(II) catalytic center conjugated with β-CD is a promising model for artificial mononuclear peptidases and has potential in the development of an effective model for metalloenzymes. The results reported in this study provide a deeper understanding of the functioning of these artificial enzymes and suggest modifications to improve their activities.

3.5 Pb(II)- and Zn(II)-Promoted Amide Methanolysis

Lead is a toxic environmental pollutant that has dramatic effects in biological systems even in small amounts. Even after the elimination of leaded gasoline, lead poisoning continues to be a problem in the United States, with about 5% of children being affected.[174] While the exact process by which lead poisoning occurs is not completely defined, it is known that lead binds to sulfur rich sites in proteins, often displacing

Zn(II).[175] Recent small molecule and peptide studies have focused on examining the coordination chemistry of Pb(II) in Zn(II)-binding environments.[176-184] Notably, these studies do not include comparisons of biologically-relevant reactivity, which might provide additional insight into the toxic properties of Pb(II).

Studies of zinc-promoted amide cleavage reactions continue to be an active area of research. This is due to the important role that mononuclear zinc centers play in catalyzing amide cleavage reactions that are directly involved in human health and disease[185-187], as well as in reagents for the selective cleavage of peptides.[188-190] Despite the importance of zinc-promoted amide cleavage reactions, few detailed investigations on the kinetics and thermodynamics of such reactions involving a non-activated amide substrate have been reported.[191-193] In this study, we have collaborated with Berreau's lab to investigate amide methanolysis reactions which proceed under mild conditions and involve a reaction pathway with a deprotonated amide intermediate.

The interactions of Pb(II) with amide-containing ligands has been previously investigated.[194-197] However, to our knowledge, no examples of Pb(II)-promoted hydrolysis or alcoholysis of an amide linkage has been previously reported. In the studies outlined herein, Berreau and co-workers have examined amide cleavage reactivity in a system wherein the Zn(II) center can be replaced by Pb(II). It reported amide cleavage studies of [(epppa)Zn]$(ClO_4)_2$ (**3-ClO$_4$**, epppa = *N*-((2-ethylthio)ethyl)-*N*-((6-pivaloylamido-2-pyridyl)methyl)-*N*-((2-pyridyl)methyl)amine; Scheme 3)[118], they first prepared and characterized Pb(II) complexes, [(epppa)Pb$(ClO_4)_2$] (**4-ClO$_4$**) and [(epppa)Pb$(NO_3)_2$] (**4-NO$_3$**), of the same chelate ligand. The kinetics and

thermodynamics of the amide methanolysis reaction of **4-ClO$_4$** was examined and compared to the results obtained for **3-ClO4**. Combined with investigations of possible intermediates in the amide methanolysis reaction pathways, as well as, a computational study of the amide methanolysis reaction pathway as a function of a metal ion, the research presented herein provides the first detailed insight into the influence of Zn(II) versus the toxic heavy metal ion Pb(II) in a biologically relevant reaction. The results of this study reveal how the geometric preferences and larger size of Pb(II) influence an amide cleavage reaction pathway.

Scheme 3

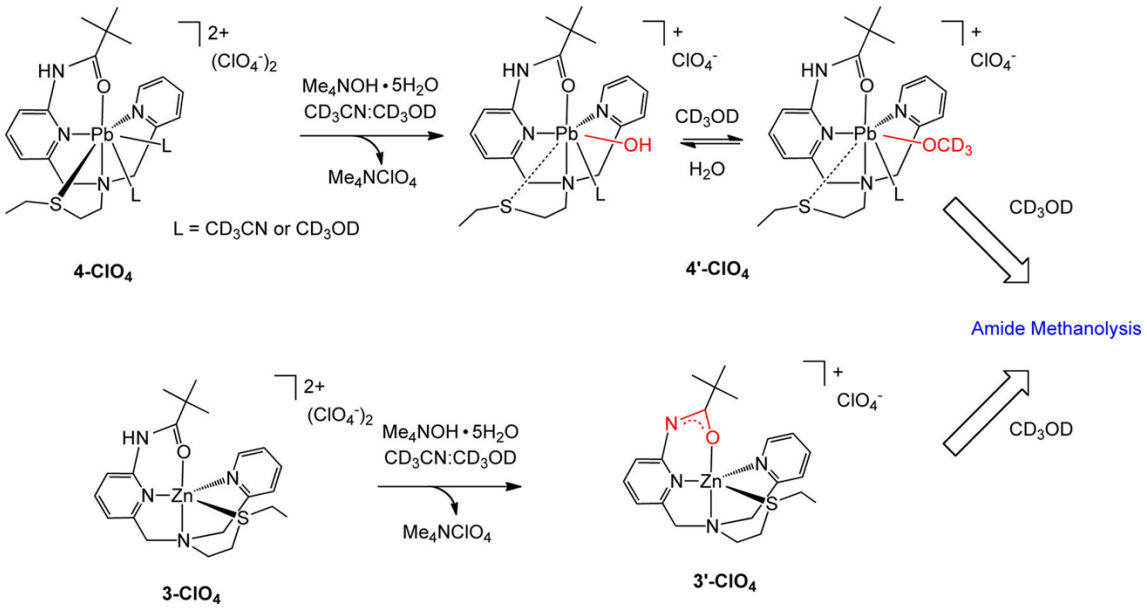

3.5.1 Computational Procedure

Methods: All calculations were performed using the Gaussian 09 program package.[198] The geometries of reactants, intermediates, transition states, and products were optimized in gas phase at the B3LYP/Lanl2dz level of theory without any symmetry constraints using corresponding Hay-Wadt effective core potential (ECP) for Zn and Pb.[61,150,151] The final energies of the optimized structures were further improved by performing single point calculations including additional d and p polarization functions for O ($\alpha = 0.96$), N ($\alpha = 0.74$), C ($\alpha = 0.59$), and H ($\alpha = 0.36$) atoms respectively (taken from the EMSL's Gaussian basis set library) in the basis set used for optimizations. Hessians were calculated at the same level of theory as the optimizations to confirm the nature of the stationary points along the reaction coordinate. The transition states were confirmed to have only one negative eigenvalue corresponding to the reaction coordinates. In this paper, the energies obtained at the B3LYP/{Lanl2dz + d (O, N, and C) + p (H)} including thermal corrections are discussed.

Computational Modeling: The initial structure for calculations of the mononuclear amide-appended zinc complex was taken from the X-ray structure of $[(epppa)Zn](ClO_4)_2$ (**3-ClO_4**). Since the treatment of Zn complex results in the formation of a deprotonated amide complex, the model is the deprotonated N_3O-Ligated Zn complex by removing ClO_4^-, which is shown in Figure 3.32, (**R_{Zn}**). On the other hand, the Pb complex is modeled as a deprotonated N_3O-Ligated Pb complex by replacing two of NO_3^- with acetonitrile from the X-ray structure of $[(epppa)Pb](NO_3)_2$ (**4-NO_3**), which is shown in Figure 3.34, (**R_{Pb}**).

3.5.2 Computational Results

The reaction mechanism is divided into the following three steps: (1) Formation of the amide intermediate, (2) Formation of the tetrahedral intermediate, and (3) Cleavage of the amide bond.

3.5.2.1 Amide Methanolysis by the N_3O-Zinc Complex (R_{Zn})

(1) Formation of the amide intermediate. At the starting point of the mechanism, a free methanol is added to the N_3O-Ligated Zinc complex. In the optimized structure of the reactant (**R_{Zn}**), the methanol interacts with Zn ion to form a covalent bond (Zn-O^M = 2.18 Å), Figure 3.32. In **R_{Zn}**, the Zn ion is in a hexa-coordinated form (Zn-O^1 = 2.01 Å, Zn-N^2 = 2.09 Å, Zn-N^3 = 2.29 Å, Zn-N^4 = 2.14 Å, Zn-S = 3.01 Å). In the first step, the deprotonated N^1 abstracts a proton from the methanol. This process is accompanied by the shortening of the Zn-O^M bond and the elongation of the Zn-S bond, Figure 3.32. For **$TS1_{Zn}$**, with the computed barrier of 22.4 kcal/mol, this step is the rate-limiting step of the entire mechanism. All the corresponding distances in the fully optimized transition state **$TS1_{Zn}$** are shown in Figure 3.32. This step leads to the formation of the amide intermediate **$In1_{Zn}$**. In **$In1_{Zn}$**, the coordination number (6) of the Zn ion remains unchanged and the generation of this intermediate is endergonic by 8.1 kcal/mol from **R_{Zn}**, Figure 3.33.

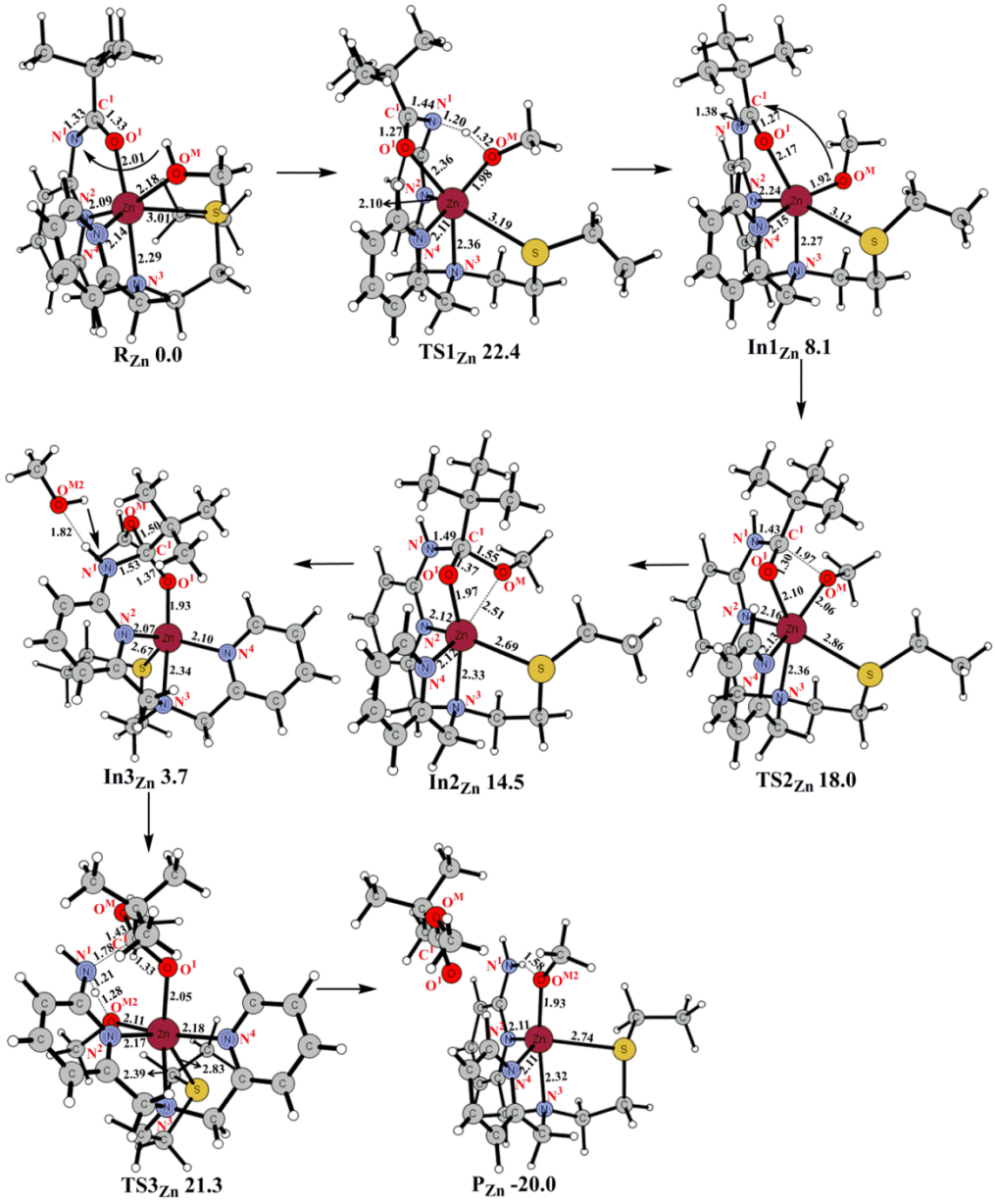

Figure 3. 32 Structures (in Å) and energies (in kcal/mol) of the reactant, intermediates, transition states, and product of the Zn-N3O complex in the stepwise mechanism.

(2) Formation of the tetrahedral intermediate. In this step, from **In1$_{Zn}$**, the deprotonated methanol acts as a nucleophile and attacks the C^1 atom of the amide bond.

This process leads to the creation of a tetrahedral intermediate **In2$_{Zn}$**. The optimized transition state **TS2$_{Zn}$** is shown in Figure 3.32. The process occurs with the barrier of 18.0 kcal/mol. In **In2$_{Zn}$**, in comparison to **In1$_{Zn}$**, the C^1-N^1 amide bond distance is elongated by 0.11 Å (C^1-N^1 = 1.49 Å) and perfectly setup for the cleavage in the next step. This process is endergonic by 14.5 kcal/mol from **R$_{Zn}$**.

(3) Cleavage of the amide bond. In this process, a second molecule of methanol binds to the Zn complex. In the optimized structure of **In3$_{Zn}$**, the methanol interacts with N^1 through a hydrogen bond (O^{M2}-HN^1 = 1.82 Å), Figure 3.32. From **In3$_{Zn}$**, a proton transfer from methanol ($CH_3O^{M2}H$) to the N^1 atom leads to cleavage of the C^1-N^1 amide bond. The optimized transition state **TS3$_{Zn}$** is shown in Figure 3.32 and occurs with a barrier of 17.6 kcal/mol from **In3$_{Zn}$** i.e. the overall barrier of 21.3 kcal/mol from **R$_{Zn}$**, Figure 3.33. In **TS3$_{Zn}$,** all the corresponding distances indicate the concerted nature of this process (O^{M2}-H = 1.28 Å, N^1-H = 1.21 Å, and C^1-N^1 = 1.78 Å distances). In the final product (**P$_{Zn}$**), the separated neutral amine (-NH_2) and carboxyl (-COOR) groups are formed and the latter is releasing from the Zn metal center. From **R$_{Zn}$** the formation of **P$_{Zn}$** is exergonic by 20.0 kcal/mol.

3.5.2.2 Amide Methanolysis by the Pb-N_3O Complex (**R$_{Pb}$**)

(1) Formation of the amide intermediate. In the optimized structure of the reactant (**R$_{Pb}$**), the Pb complex adopted an octa-coordinated geometry. In **R$_{Pb}$**, two solvent

acetonitrile molecules and the methanol substrate interact with the Pb ion (Pb-O^M = 2.05 Å, Pb-N^a = 3.30 Å, Pb-N^{a2} = 3.50 Å) Figure 3.34. In comparison to the reactant of the Zn complex (**R_{Zn}**), the bonds in **R_{Pb}** are much longer (Pb-O^1 = 2.31 Å, Pb-N^2 = 2.48 Å, Pb-N^3 = 2.74 Å, Pb-N^4 = 2.91 Å, Pb-S = 3.11 Å). In the first step, the deprotonated N^1 abstracts a proton from the methanol. This transfer occurs with the barrier of 18.9 kcal/mol which is 3.5 kcal/mol lower than the barrier for the Zn complex. Similar to the Zn case, this is the rate-limiting step for the Pb complex. These computational results are in excellent agreement with the experimental data. All the corresponding distances in the fully optimized transition state **$TS1_{Pb}$** are shown in Figure 3.34. This step leads to the formation of the amide intermediate **$In1_{Pb}$**. In **$In1_{Pb}$**, the coordination number of the Pb ion was reduced by one to seven through the movement of one of the acetonitrile molecule. The generation of **$In1_{Pb}$** is exergonic by 7.2 kcal/mol from **R_{Pb}**.

(2) Formation of the tetrahedral intermediate. This process was started by the nucleophilic attack of the deprotonated methanol to the C^1 atom of the amide bond. This attacks leads to the formation of a tetrahedral intermediate **$In2_{Pb}$**. This process was accompanied by the regeneration of the coordination bond between Pb ion and the solvent acetonitrile molecule. The optimized transition state **$TS2_{Pb}$** is shown in Figure 3.34. Since this step follows a step that is endergonic, the overall barrier for this process becomes 14.7 kcal/mol from **R_{Pb}**. In **$In2_{Pb}$**, the C^1-N^1 amide bond distance is elongated by 0.09 Å (C^1-N^1 = 1.48 Å) compared to **$In1_{Pb}$**. This intermediate is now well prepared

for the cleavage of the amide bond in the next step. This process is endergonic by 10.5 kcal/mol from $\mathbf{R_{Pb}}$, Figure 3.33.

(3) Cleavage of the amide bond. In $\mathbf{In3_{Pb}}$, another free methanol binds to the Pb complex through a hydrogen bond (O^{M2}-HN^1 = 1.90 Å) with the N^1 atom. In the final step, this methanol molecule ($CH_3O^{M2}H$) donates its proton to the nitrogen (N^1) atom of the scissile amide bond (C^1-N^1) and cleaves it. In the optimized transition state $\mathbf{TS3_{Pb}}$, all the key reaction coordinates indicate that this process is concerted (O^{M2}-H = 1.31 Å, N^1-H = 1.20 Å, and C^1-N^1 = 1.77 Å distances), Figure 3.34. In the $\mathbf{In3_{Pb}}$-$\mathbf{TS3_{Pb}}$ transformation, the computed barrier was 11.4 kcal/mol. This process generates a releasing ester product –COOR from the Pb center. The formation of the separated –COOR and $–NH_2$ terminals in the final product $\mathbf{P_{Pb}}$ was 11.7 exergonic from $\mathbf{R_{Pb}}$.

3.5.3 Summary

The DFT studies indicate that both complexes may feasibly undergo amide methanolysis starting from a deprotonated amide species with activation barriers for the rate-determining step that are consistent with experimentally-determined free energies of activation. For example, for the Zn(II)-containing $\mathbf{3\text{-}ClO_4}$, the rate-determining step would involve either protonation of the deprotonated amide or protonation of the amine leaving group, as both steps have similar activation barriers 22.4 and 21.3 kcal/mol, respectively. We note that these activation barriers are also similar to the $\Delta G^{\ddagger}$ values

recently reported for the methanolysis of an internal amide substrate in a Cu(II) complex.[199] The small observed deuterium KIE identified for this reaction is consistent with general acid assistance by the solvent for departure of the leaving group.[199]

On the other hand, the reaction of Pb(II)-containing **4-ClO$_4$** starting from a deprotonated amide species would via rate-limiting amide protonation from a coordinated methanol with a calculated activation barrier of 18.9 kcal/mol. This value is comparable to the experimentally determined free energy of activation (21.3 kcal/mol). However, based on the lack of evidence for the initial formation of a deprotonated amide species in the reaction of **4-ClO$_4$** upon treatment with $Me_4NOH{\cdot}5H_2O$, it is proposed that this reaction proceeds via the direct formation of **Int1$_{Pb}$**, a Pb(II)-OH species, $[(epppa)Pb\text{-}OH(sol)_n]^+$ (sol = CH_3CN or CH_3OH; n = 1-2) that equilibrates with a corresponding Pb(II)-OCH_3 form. The equilibration of these two species is consistent with the observed saturation kinetic data wherein the Pb(II)-OH/Pb(II)-OCH_3 equilibrium precedes nucleophilic attack of the methoxide on the coordinated amide. The calculated activation barrier associated with this nucleophilic attack (**Int1$_{Pb}$** → **TS2$_{Pb}$**, 21.9 kcal/mol) is in good agreement with the experimentally determined activation barrier (21. 3 kcal/mol).

Therefore, we propose that the amide methanolysis reactions of **3-ClO$_4$** and **4-ClO$_4$**, while giving the same products, proceed via different initial reactants that are the result of the differences in the size and coordination preferences of Zn(II) versus Pb(II). That being said, in both cases the metal center is likely playing multiple roles in the amide cleavage reaction. These include electrophilic activation of the carbonyl via coordination of the oxygen atom and stabilization of the nucleophile.[200,201] In terms of Pb(II), our computational studies indicate that the larger Pb(II) ion more effectively stabilizes the

double Lewis activated structure having both amide and nucleophile coordination. The Pb(II) center also stabilizes the tetrahedral intermediate, and substantially lowers the activation barrier for leaving group departure, relative to the Zn(II) analog. These effects may relate to a more flexible metal coordination environment for Pb(II) wherein a greater range of metal-ligand distances may be accessed during the amide cleavage reaction.[202]

Overall, the purpose of this study was to evaluate how the presence of Pb(II) versus Zn(II) would influence an amide cleavage reaction. Our results indicate that Pb(II) may serve as a Lewis acid to promote amide cleavage, and that the differences in the reaction pathway as compared to a Zn(II) analog are due to the inherent chemical properties of this heavy metal ion.

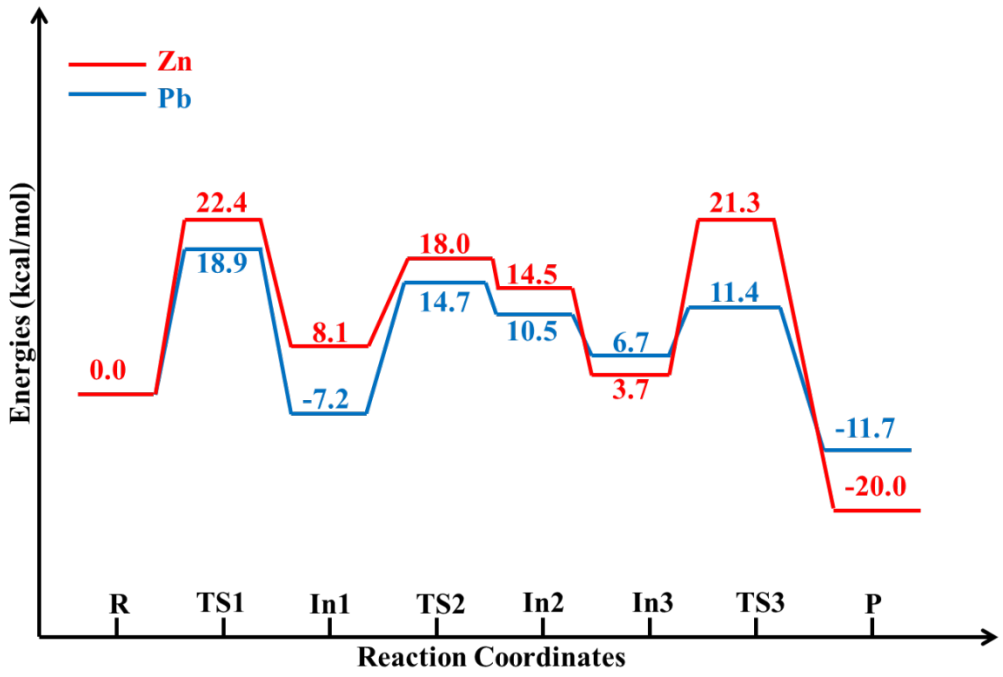

Figure 3. 33 Potential energy diagrams of Zinc and Lead complexes in the stepwise mechanism of methanolysis reaction (in kcal/mol).

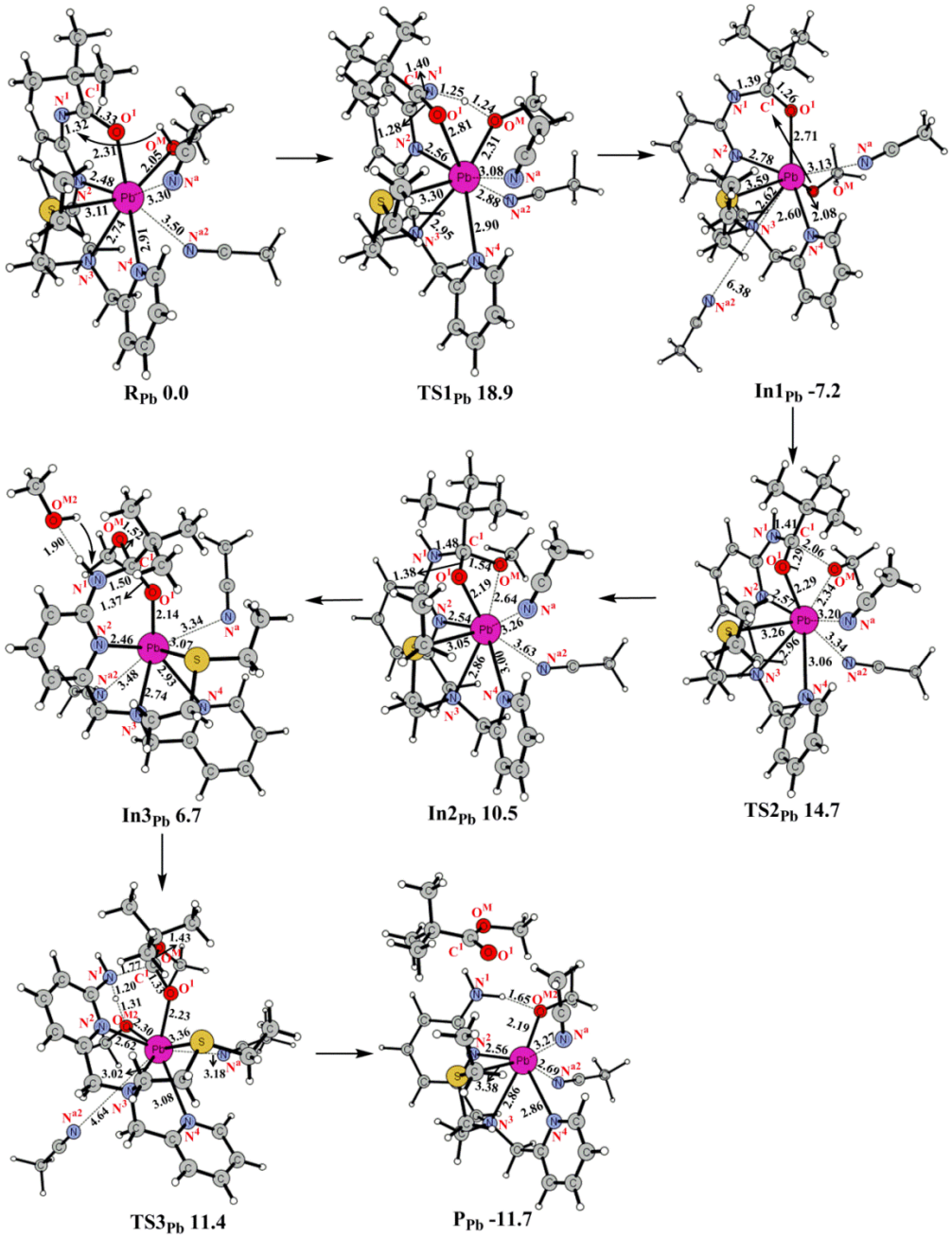

Figure 3. 34 Structures (in Å) and energies (in kcal/mol) of the reactant, intermediates, transition states, and product of the Pb-N3O complex in the stepwise mechanism.

Chapter 4 Peptide Cleavage Mechanism of Binuclear Metallopeptidases and Their Analogues

4.1 Introductory Remarks

In the last chapter, a variety of mononuclear metallopeptidases have been studied. For the dinuclear metal center enzyme, the metal center is denoted as [M1M2], in which M1 and M2 indicate the type of metal ion in site1 and site2.[28] According to the spectroscopic and kinetic data, some enzymes utilize only one metal ion for the catalytic function, whereas other enzymes require that both of the metal ions exhibit activity.[28] In this study, three enzymes of the latter category: leucine aminopeptidase (LeuAP), D-aminopeptidase (DppA), and human renal dipeptidase (hrDP) have been discussed.

Leucine aminopeptidase (LeuAP) constitutes a ubiquitous family of binuclear metallopeptidases that is present in bacteria, plants, animals, and humans.[203-207] This enzyme originally found to cleave the N-terminus Leu of dipeptide or tripeptide substrates as the name implies, although it also hydrolyzes (albeit somewhat more slowly) most of the other amino acids as well.[28] According to the X-ray structures, each monomer of LeuAP is comprised of two domains: the N-terminal (residues 1–150) and the C-terminal (residues 151–482).[208,209] The N-terminus domain interacts among different monomers, whereas the C-terminus domain contains the binuclear active site.[210] The active site contains two Zn(II) ions that occupy different coordination sites that are critical for the catalytic functioning of the enzyme (Figure 4.1).[211-214] Both Zn(II) ions are nonequivalent and co-catalytic.[205] The Zn488 ion (Zn1) coordinates to Asp255, Asp332,

and Glu334 residues with either a carboxyl oxygen or a carbonyl oxygen, and Zn489 (Zn2) are bound to the side chains of Lys250, Asp255, Asp273, and Glu334 (Scheme 4). It has been found that the activity will be enhanced by replacing Zn1 (readily exchangeable site) with Mg(II), Co(II), and Mn(II), whereas the Zn2 (tight binding site) can only be replaced by a Co(II) ion.[212,215-217] LeuAP plays important roles in a wide range of pathophysiological states, including HIV infection,[218] cataracts,[219,220] cancer,[221-223] leukemia, and cystic fibrosis.[224]

Scheme 4

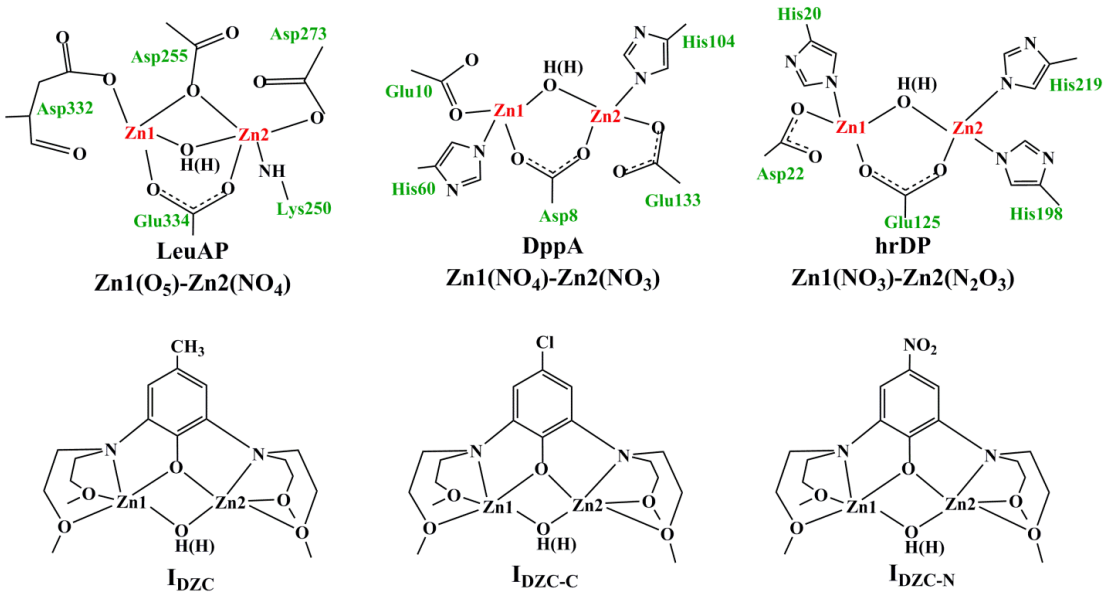

D-aminopeptidase (DppA), identified as a peptidase that hydrolyze N-terminal residues in D-amino acid containing peptides, was isolated from bacillus subtilis recently.[225] It is related to the synthesis and remodeling of peptidoglycan in bacterial cell walls.[226] The X-ray structure reveals that DppA is composed of identical 30 kDa (274 amino acid residues) subunits organized in a decamer. Each monomer of DppA comprises two

separate domains: the N-terminal, forming the core of the monomer, and the C-terminal. The active site containing the binuclear Zn ions center is in the N-terminus domain. In the active site, the Zn1 ion coordinates to residues Asp 8 (OD1), Glu 10 (OE1), and His 60 (ND1), whereas the Zn2 ion is bound to residues Asp 8 (OD2), His 104 (NE2), and Glu 133 (OE1). His 115 forms a hydrogen bond with a water molecule or hydroxide ion which completes both Zn^{2+}-coordination spheres.[227]

Human renal dipeptidase (hrDP) is a membrane-bound glycoprotein that can hydrolyzes dipeptides.[228,229] It plays a critical role in the renal metabolism of glutathione (its conjugates) and some drugs since it is well-known that the dipeptidase is identified as the sole metabolic enzyme for penem and carbapenem β-lactam antibiotics in mammals.[230-232] From the X-ray structure, the hrDP is a homodimer that is composed of 369 amino acid residues (42 kDa) of each subunit. Each subunit contains two nonequivalence Zn ions at the active site, and is located in the C-terminal of the enzyme.[233] In the native structure, Zn1 is liganded by the side chains of Glu125, Asp22, and His20, while Zn2 is liganded to the side chains of Glu125, His198, and His219. Furthermore, His152, uncoordinated to neither of the Zn ions plays an important role in substrate binding through formation of a hydrogen bond.[233]

In our previous studies, possible mechanisms for both forms of the bridging nucleophile (H_2O or -OH), the electronic nature of the substrate and the effects of the replacement of both metal centers on the energetics of the LeuAP-catalyzed reaction have been elucidated.[234] Despite the availability of experimental and computational information, several structural and mechanistic issues concerning three different natural

enzymes aforementioned remain unknown. In the present density functional theory (DFT) study, the effects of the ligand environments of Zn1(O5)-Zn2(NO4) (LeuAP), Zn1(NO4)-Zn2(NO3) (DppA), and Zn1(N2O3)-Zn2(NO3) (hrDP) on the Lewis acidity, p*K*a of water and nucleophilic activation of carbonyl carbon of the scissile bond have been investigated.

In the recent years, Sakiyama et al. have synthesized the Zn1(NO4)-Zn2(NO4) core containing functional analogue (**I$_{DZC}$**) of LeuAP that has four methoxycarbonyl chelating arms. In the crystal structure of **I$_{DZC}$**, both of the Zn ions are bridged by the one phenolic oxygen, and liganded to two oxygens and one nitrogen from methoxycarbonyl. This new dinuclear Zn complex **I$_{DZC}$** was reported as the first dizinc functional model of a aminopeptidase.[235] Furthermore, the analogues of **I$_{DZC-C}$** and **I$_{DZC-N}$**, in which the *p*-methyl group of $-CH_3$ from **I$_{DZC}$** was substituted by –Cl and $-NO_2$ respectively, have been synthesized to improve the activity of the functional model. The second-order rate constants were found to be in accordance with a decreasing order of the electron-withdrawing effect of the *p*-substituents: **I$_{DZC}$** > **I$_{DZC-C}$** > **I$_{DZC-N}$** (250:10:1).[236] However, the mechanism of these synthetic analogues could not be determined from the experiments since no intermediate species have been detected. Therefore, the structure, function, and mechanism of the complexes above have been studied in this manuscript.

4.2 Computational Details

Computational methods

All calculations were performed using the Gaussian 09 program package.[168] The geometry optimizations of reactants, intermediates, transition states, and products were performed at the B3LYP/Lanl2dz level without any geometrical constraint using the corresponding Hay–Wadt effective core potential for Zn.[61,151,237] The final energies of the optimized structures were further improved by performing single-point calculations including additional d and p polarization functions for oxygen (a = 0.96), nitrogen (a = 0.74), carbon (a = 0.59), and hydrogen (a = 0.36) atoms, respectively (taken from the EMSL's Gaussian basis set library), in the basis set used for optimizations. Hessians were calculated at the same level of theory as the optimizations to confirm the nature of the stationary points along the reaction coordinate. The transition states were confirmed to have only one negative eigenvalue corresponding to the reaction coordinates. The dielectric constant of 4.3 corresponding to diethyl ether was used to estimate the effect of the surrounding protein environment utilizing the self-consistent reaction field integral equation formalism polarizable continuum model method[152] at the B3LYP/Lanl2dz level. Throughout this manuscript, the energies obtained at the B3LYP/ {Lanl2dz + d(O, N, and C) + p(H)} level including thermal corrections and solvent effects in the protein are discussed.

Computational Models

The LeuAP model of the active site was constructed using the 1.6 Å X-ray structure of the free enzyme (PDB ID: 1LAM).[208,209] The model contains the binuclear metal center

including all of the first coordination shell residues bound to both Zn1 (Asp255, Asp332, and Glu334) and Zn2 (Lys250, Asp255, Asp273, and Glu334). The important second coordination shell residue such as Leu360 was also included since this residue was experimentally proposed to be involved in the positioning of the substrate at the active site and the subsequent stabilization of transition state(s),[208,238-240] whereas Lys262 was modeled as a water molecule that forms two hydrogen bonds with the side chains of Asp255 and Asp332. In addition, Gly335, Arg336, and Leu337, which interact with the catalytically active bicarbonate ion (HCO_3^-) through hydrogen bonds,[209] were simplified as four water molecules in the model. The Asp255, Asp273, and Glu334 residues were modeled as an acetate ion (CH_3COO^-). The Leu360 residue was also modeled as CH_3COO^-. The L-leucine-*p*-nitroanilide substrate was modeled as $NO_2C_6H_4NHCOCH_2NH_2$ by replacing the $-CH_2CH(CH_3)_2$ chain with a hydrogen atom.

The DppA model of the active site was constructed using the 2.4 Å X-ray structure of the free enzyme (PDB ID: 1HI9).[227] The model contains the binuclear metal center including all of the first coordination shell residues bound to both Zn1 (Asp8, Glu10, and His60) and Zn2 (Asp8, His104, and Glu133). Those residues were simplified as four water molecules which interact with the catalytically active bicarbonate ion (HCO_3^-) through hydrogen bonds in the model. The Asp, Glu, and Leu residues were modeled as an acetate ion (CH_3COO^-). The His residue was also modeled as methylimidazole. The L-leucine-*p*-nitroanilide was used as the substrate. In addition, the hrDP model was constructed followed the same method as LeuAp and DppA. The 2.3 Å crystal structure of the enzyme (PDB ID: 1ITU) was used.[233] The model contains the binuclear Zn ions

including all of the first coordination shell residues bound to both Zn1 (Glu125, His198, and His219) and Zn2 (Glu125, Asp22, and His20).

For the synthetic dinuclear center containing enzymes, the target complex $\mathbf{I_{DZC}}$ was constructed by using the X-ray structure of $[Zn(bomp)(MeCO_2)_2]BPh_4$ (3) [H(bomp): 2,6-bis[bis(2-methoxyethyl)aminomethyl]-4-methylphenol].[235] $\mathbf{I_{DZC\text{-}C}}$ and $\mathbf{I_{DZC\text{-}N}}$ was modeled by replacing the *p*-methyl group of $–CH_3$ from $\mathbf{I_{DZC}}$ to –Cl and $–NO_2$ respectively. The active water molecule was included in the model bound to Zn2 ion. The same substrate L-leucine-*p*-nitroanilide was used. The catalytically active bicarbonate ion (HCO_3^-) including four water molecules which interact with through hydrogen bonds were built in the model.

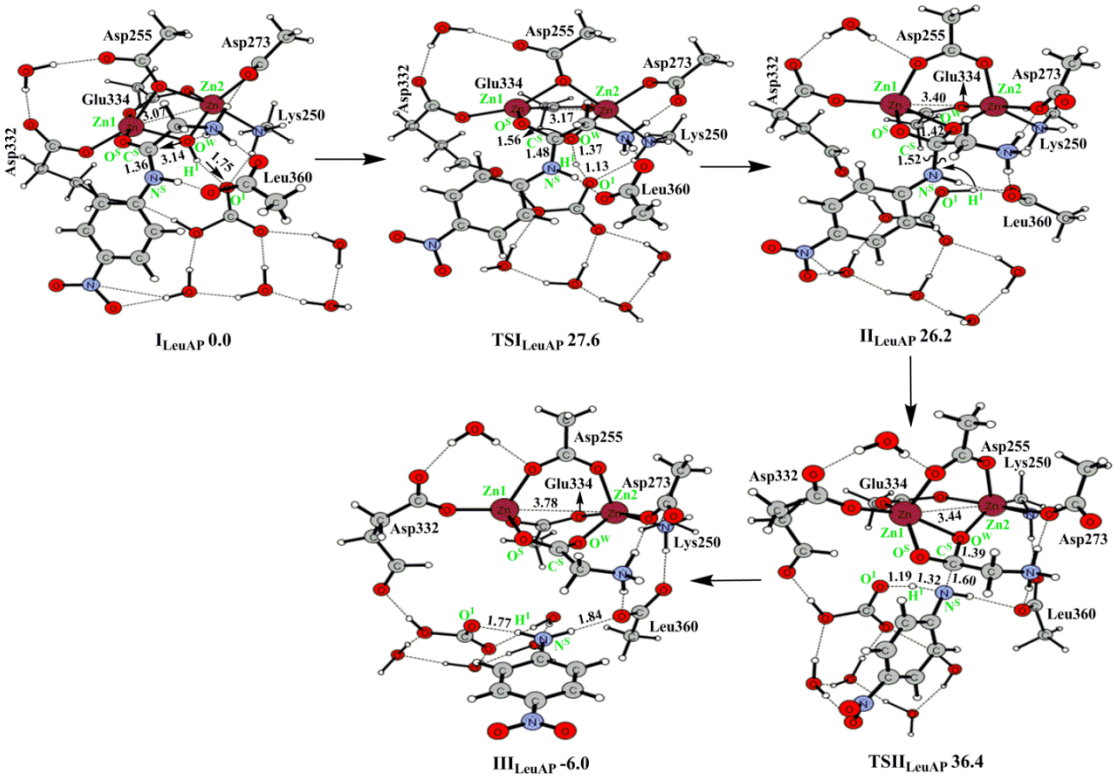

Figure 4. 1 Structures (in Å) and energies (in kcal/mol) of the reactant, transtition states, intermediate, and product of Leucine aminopeptidase (LeuAP).

4.3 Computational Results

4.3.1 Natural Binuclear Peptidases

This mechanism is divided into the following two steps: (1) formation of the gem-diolate intermediate, and (2) cleavage of the peptide bond.

4.3.1.1 Formation of the Gem-Diolate Intermediate

LeuAP Binuclear Peptidase

In the optimized structure of the reactant ($\mathbf{I_{LeuAP}}$), the L-leucine-*p*-nitroanilide substrate, which interacts with the active site through two hydrogen bonds with the second coordination shell residue Leu360, and is bound to the active site of the enzyme (Figure 4.1). The Zn1 (M1 site) ion polarizes the peptide bond through the Zn1–O^S covalent bond (Zn–O^S = 2.22 Å) and orients it towards the nucleophile. The Zn1 ion is pentacoordinated and coordinates to the side chains of Asp255, Asp332, Glu334, and the bridging water ($H^1O^WH^2$) molecule (Zn1–O (Asp255) = 2.07 Å, Zn1–O (Asp332) = 2.00 Å, Zn1–O (Glu334) = 2.15 Å, and Zn1–O^W ($H^1O^WH^2$) = 2.04 Å). The Zn2 (M2 site) ion is also pentacoordinated and ligands to Lys250, Asp255, Asp273, Glu334, and the bridging water molecule (Zn2–N (Lys250) = 2.18 Å, Zn2–O (Asp255) = 2.30 Å, Zn2–O (Asp273) = 2.02 Å, Zn2–O (Glu334) = 2.04 Å, and Zn2–O^W ($H^1O^WH^2$) = 2.04 Å). The Zn1–Zn2 distance in the reactant ($\mathbf{I_{LeuAP}}$) is 3.07 Å. The polarization by both Zn ions is likely to reduce the p*K*a of the bridging water molecule from 14 to almost 7.[241,242] In the first step of the mechanism, the bicarbonate ion functions as a base and abstracts the H^1 proton from the bridging water molecule ($H^1O^WH^2$), accompanied by the nucleophilic attack of

the hydroxyl group ($-O^WH^2$) on the carbon (C^S) atom of the scissile peptide bond (C^S-N^S) (Figure 4.1). The optimized transition state (**TSI_{LeuAP}**) is shown in Figure 4.1 and the computed barrier was 27.6 kcal/mol. O^W-H^1 = 1.37 Å, O^1-H^1 = 1.13 Å, and O^W-C^S = 1.56 Å. This process leads to the formation of the gem-diolate intermediate (**II_{LeuAP}**), in which the bicarbonate ion exists in the neutral form as a carbonic acid. The generation of **II_{LeuAP}** is endothermic by 26.2 kcal/mol from the reactant **I_{LeuAP}**. The C^S-N^S peptide bond is already elongated by 0.16 Å in comparison to **I_{LeuAP}** and well prepared for the cleavage in the next step.

DppA Binuclear Peptidase

In the structure of the reactant (**I_{DppA}**), the L-leucine-*p*-nitroanilide substrate also interacts with the active site through two hydrogen bonds with the second coordination shell residue Leu360 (Figure 4.2). In this case, the coordination number of Zn1 ion is five and it coordinates to the side chains of Asp8, Glu10, His60, and the bridging water ($H^1O^WH^2$) molecule (Zn1–O (Asp8) = 2.14 Å, Zn1–O (Glu10) = 2.01 Å, Zn1–N (His60) = 2.07 Å, and Zn1–O^W ($H^1O^WH^2$) = 2.02 Å). Moreover, the Zn1 ion polarizes the peptide bond through the Zn1–O^S covalent bond (Zn–O^S = 2.30 Å). In comparison to the reactant of **I_{LeuAP}**, the Zn2 ion is tetracoordinated and ligands to Asp8, His104, Glu133, and the bridging water molecule (Zn2–O (Asp8) = 2.01 Å, Zn2–N (His104) = 2.10 Å, Zn2–O (Glu133) = 1.98 Å, and Zn2–O^W ($H^1O^WH^2$) = 2.00 Å). The Zn1–Zn2 distance (Zn1–Zn2 = 3.35 Å) is 0.28 Å longer than that of the reactant (**I_{LeuAP}**). Another noticeable difference was found in the interaction of O^1 with the carbonyl carbon atom (C^S) of the substrate. The bond distance of O^1-C^S of **I_{LeuAP}** is 3.14 Å, which is much shorter than the

corresponding distance in $\mathbf{I_{DppA}}$ (O^1–C^S = 3.27 Å). In addition, the bridging water molecule is activated by binding to both of the Zn ions with an elongated bond distance (H^1–O^W =1.02 Å). In this step, the bicarbonate ion acts as a base by abstracting a proton from the bridging water. The resulting hydroxide ion concomitantly makes a nucleophilic attack on the carbon atom (C^S) of the peptide bond (C^S–N^S) to form a gem-diolate intermediate. All the corresponding distances in the fully optimized transition state ($\mathbf{TSI_{DppA}}$) indicate that this process is concerted (O^W–H^1 = 1.13 Å, O^1–H^1 = 1.31 Å, and O^W–C^S = 1.45 Å) and crosses over a barrier of 29.8 kcal/mol (Figure 4.2). The generation of $\mathbf{II_{DppA}}$ is endothermic by 26.0 kcal/mol from the reactant $\mathbf{I_{DppA}}$.

hrDP Binuclear Peptidase

In comparison to the reactant $\mathbf{I_{LeuAP}}$, the Zn1 ion is pentacoordinated, whereas the Zn2 ion is tetracoordinated in the optimized reactant ($\mathbf{I_{hrDP}}$), which is shown in Figure 4.3. The Zn1 ion forms coordinate bonds with the side chains of Glu125, His198, His219, and the bridging water ($H^1O^WH^2$) molecule (Zn1–O (Glu125) = 2.07 Å, Zn1–N (His198) = 2.14 Å, Zn1–N (His219) = 2.11 Å, and Zn1–O^W ($H^1O^WH^2$) = 1.98 Å). The scissile peptide bond (C^S–N^S) of the substrate is also activated by the interaction of the Zn1 ion with the carbonyl oxygen atom (O^S) (Zn1–O^S = 2.30 Å, C^S–N^S = 1.36 Å). The Zn2 ion coordinates to Glu125, Asp22, and His20, and the bridging water molecule (Zn2–O (Glu125) = 2.01 Å, Zn2–O (Asp22) = 2.02 Å, Zn2–N (His20) = 2.05 Å, and Zn2–O^W ($H^1O^WH^2$) = 2.00 Å). The Zn1–Zn2 distance (Zn1–Zn2 = 3.54 Å) is the longest among all three reactants ($\mathbf{I_{LeuAP}}$, $\mathbf{I_{DppA}}$, and $\mathbf{I_{hrDP}}$). $\mathbf{I_{hrDP}}$ follows the same mechanism as $\mathbf{I_{LeuAP}}$ and

$\mathbf{I_{DppA}}$, the optimized transition state ($\mathbf{TSI_{hrDP}}$) is shown in Figure 4.3 (O^W–H^1 = 1.41 Å, O^1–H^1 = 1.10 Å, and O^W–C^S = 1.55 Å). The computed energy barrier from $\mathbf{I_{hrDP}}$ to $\mathbf{TSI_{hrDP}}$ is 22.1 kcal/mol, which is 5.5 kcal/mol lower than that of the same process of $\mathbf{I_{LeuAP}}$. It may be due to the difference in the interaction of the O^1 with the carbonyl carbon atom (C^S) of the substrate. The bond distance of O^1–C^S of $\mathbf{I_{hrDP}}$ is 3.02 Å, which is much shorter than the corresponding distance in $\mathbf{I_{LeuAP}}$ (O^1–C^S = 3.14 Å). Moreover, the charges on the Zn1 and Zn2 ions of $\mathbf{I_{hrDP}}$ are increased by 0.29e and 0.30e compared to $\mathbf{I_{LeuAP}}$, respectively. Whereas the charge on O^1 is decreased by 0.11e. This helps to make the bridging water molecule ($H^1O^WH^2$) a better nucleophile. All the aforementioned differences could be the reasons for the lowest barrier of the first step for $\mathbf{I_{hrDP}}$ among all three binuclear peptidase. The formation of the intermediate ($\mathbf{II_{hrDP}}$) is 9.4 kcal/mol more exothermic than in the $\mathbf{I_{LeuAP}}$ case, i.e., 16.8 kcal/mol endothermic from the reactant $\mathbf{I_{hrDP}}$.

4.3.1.2 Cleavage of the Peptide Bond

LeuAP Binuclear Peptidase

In the second step, the carbonic acid now functions as an acid and transfers the H^1 proton abstracted in the previous step to the nitrogen (N^S) atom of the C^S–N^S peptide bond, which leads to the cleavage. The computed energy barrier from $\mathbf{II_{LeuAP}}$ to $\mathbf{TSII_{LeuAP}}$ is endothermic by 10.2 kcal/mol. The overall barrier from $\mathbf{I_{LeuAP}}$ becomes 36.4 kcal/mol. This is the rate-limiting step of the entire mechanism. The optimized transition state ($\mathbf{TSII_{LeuAP}}$) for this process is shown in Figure 4.1 and all of the corresponding distances indicate the concerted nature of this process (O^1–H^1 = 1.19 Å, H^1–N^S = 1.32 Å, and N^S–

C^S = 1.60 Å). In the final product (**III_{LeuAP}**), the separated neutral amine ($–NH_2$) and charged carboxyl ($–COO^-$) groups are formed and the latter is bound to Zn1 ion. The formation of **III_{LeuAP}** from **I_{LeuAP}** is exothermic by 6.0 kcal/mol.

DppA Binuclear Peptidase

The cleavages of the peptide bond of the substrate for both the DppA and hrDP binuclear peptidases take place in a similar fashion as for the LeuAP. In the optimized transition state (**$TSII_{DppA}$**), all key reaction coordinates indicate that this process is concerted (O^1–H^1 = 1.08 Å, H^1–N^S = 1.51 Å, and N^S–C^S = 1.57 Å) (Figure 4.2). From **I_{DppA}**, the barrier for this process is 30.2 kcal/mol and this step is the rate-limiting step of the mechanism. It is 6.2 kcal/mol lower than that of the same process of **I_{LeuAP}**. In comparison to the intermediate of **II_{LeuAP}**, the atomic charges on both the Zn ions of **II_{DppA}** are more positive (i.e., +1.72e on Zn1, and +1.72e on Zn2). In addition, the charge on the N^S atom of the scissile peptide bond is -0.66e, which is 0.01e more negative than that of the **II_{LeuAP}**. It is also noteworthy that, in **II_{LeuAP}** the coordination number of both metal ions is 5, whereas the Zn ions are only tetracoordinated in **II_{DppA}**.

hrDP Binuclear Peptidase

For the cleavage of the same substrate by hrDP binuclear peptidase, this process proceeds through the transition state **$TSII_{hrDP}$** and the computed barrier for this step was found to lie higher (8.0 kcal/mol) than the gem-diol intermediate **II_{hrDP}** (i.e., 24.8 kcal/mol from **I_{hrDP}**) (Figure 4.3). It is 11.6 kcal/mol lower than the corresponding barrier of **I_{LeuAP}**. The

low barrier may be due to the differences in structural and electronic states of the gem-diol intermediates. The charges on Zn1 and Zn2 ions of $\mathbf{II_{hrDP}}$ (i.e., +1.71e on Zn1, and +1.72e on Zn2) increased by 0.31e and 0.28e compared to $\mathbf{II_{LeuAP}}$, respectively. Moreover, the charge on the atom of N^S is 0.05e more negative than that of the $\mathbf{II_{LeuAP}}$. The Zn1 and Zn2 ion are pentacoordinated and tetracoordinated respectively in $\mathbf{II_{hrDP}}$, whereas the coordination number of both metal ions is 5 in $\mathbf{II_{LeuAP}}$. The formation of the separated neutral amine ($–NH_2$) and charged carboxyl ($–COO^-$) groups containing the product ($\mathbf{III_{hrDP}}$) is 16.4 exothermic from $\mathbf{I_{hrDP}}$.

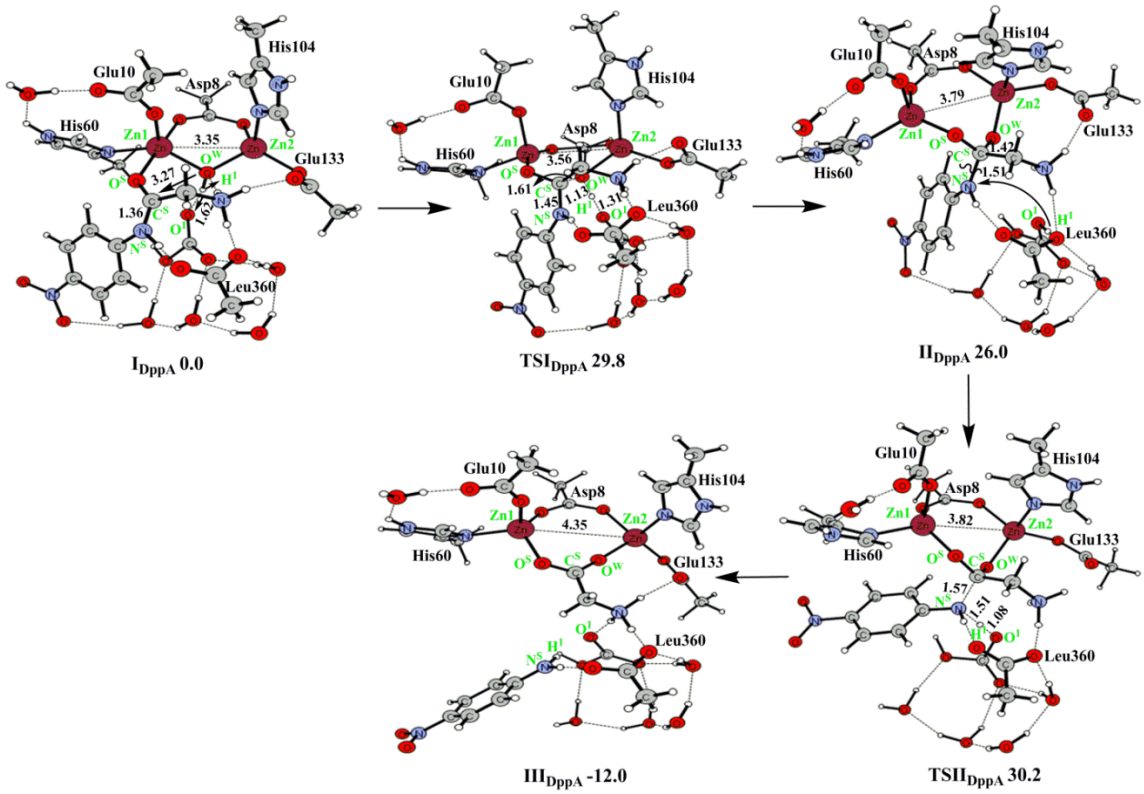

Figure 4. 2 Structures (in Å) and energies (in kcal/mol) of the reactant, transtition states, intermediate, and product of D-aminopeptidase (DppA).

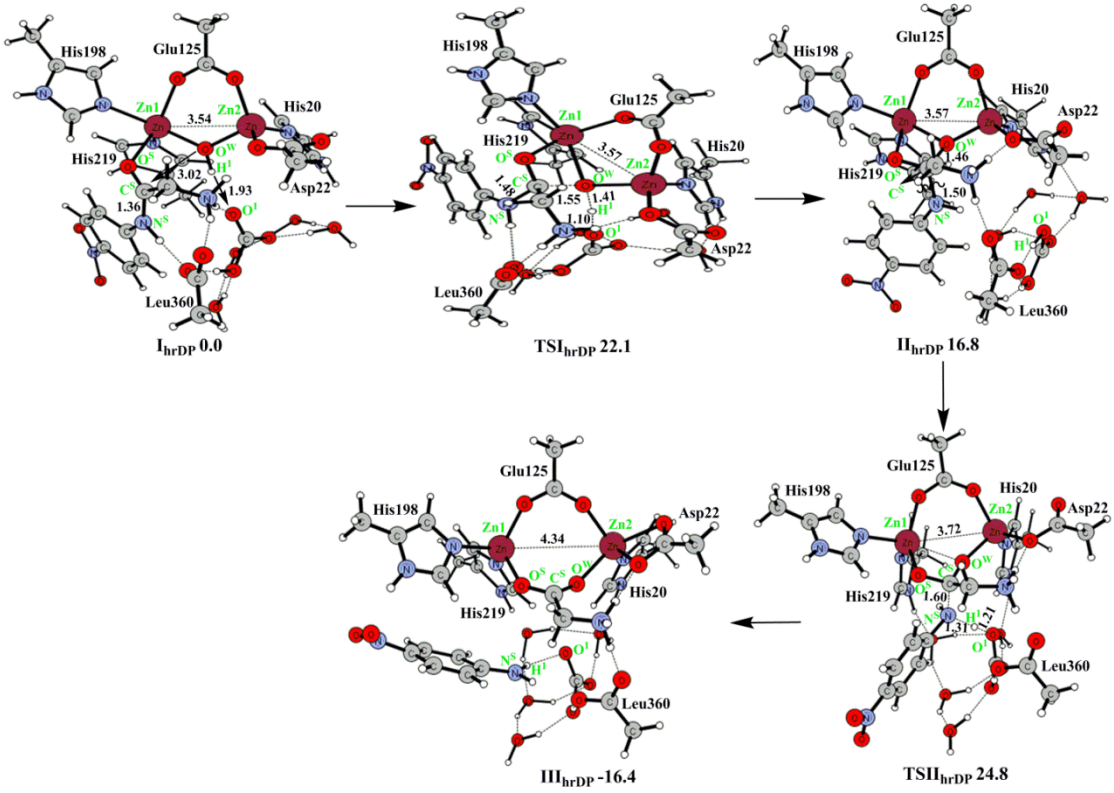

Figure 4. 3 Structures (in Å) and energies (in kcal/mol) of the reactant, transtition states, intermediate, and product of human renal dipeptidase (hrDP).

The computed energetics indicate that Zn1(N2O3)-Zn2(NO3) (**hrDP**) is more energetically favorable than the three natural binuclear peptidases studied. The second step is the rate-limiting step of the entire mechanism.

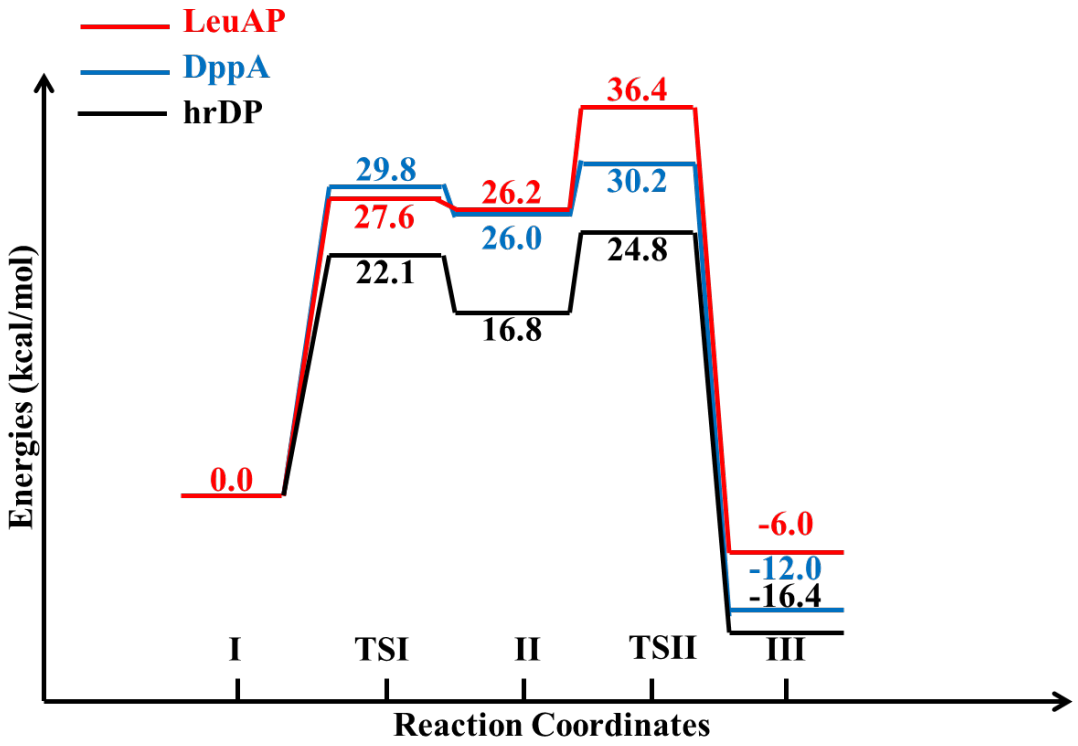

Figure 4. 4 Potential energy diagrams of natural binuclear peptidases (in kcal/mol).

4.3.2 Synthetic Binuclear Peptidases

This mechanism is also divided into the following two steps: (1) formation of the gem-diolate intermediate, and (2) cleavage of the peptide bond.

4.3.2.1 Formation of the Gem-Diolate Intermediate

The L-leucine-*p*-nitroanilide substrate is bound to the Zn1 ion of the enzyme with a carbonyl oxygen atom (O^S) (Figure 4.5, 4.6, & 4.7). The Zn1 ion polarizes the peptide

bond through the Zn1–O^S covalent bond and orients it towards the nucleophile. All the reactants (**I_{DZC}**, **I_{DZC-C}**, and **I_{DZC-N}**) adopt the Zn1(NO4)-Zn2(NO4) motif. Both the Zn ions are pentacoordinated and coordinate to the bridged phenolic oxygen, two oxygens and one nitrogen from methoxycarbonyl. In regards to natural enzymes, this process is different. Only the Zn2 ion is liganded to the water ($H^1O^WH^2$) molecule, which does not coordinate with the Zn1 ion. The Zn1–Zn2 distances in the reactants (**I_{DZC}**, **I_{DZC-C}**, and **I_{DZC-N}**) are in the range of 3.76-3.83 Å which is much longer than the corresponding distances in the natural enzymes (3.07 Å for **I_{LeuAP}**, 3.35 Å for **I_{DppA}**, and 3.54 Å for **I_{hrDP}**). Since the only difference between all the reactants is the *p*-substituent, **I_{DZC}**, the structures of **I_{DZC-C}**, and **I_{DZC-N}** are similar. The strong electron-withdrawing group (*p*-nitro group) of **I_{DZC-N}** removes electron density from the attached π system and makes the π system more electrophilic. It helps to make the Zn metal center a better Lewis acid. The water molecule (H^1O^WH) is more activated with the bond distance of O^W- H^1 = 1.04 Å, whereas the corresponding bond distance is 1.03 Å for the reactants of **I_{DZC}** and **I_{DZC-C}**. Moreover, the distances between H^1 and O^1 are 1.53 Å, 1.51 Å, and 1.49 Å for **I_{DZC}**, **I_{DZC-C}**, and **I_{DZC-N}**, respectively. The H^1 atom is the closest to O^1 in **I_{DZC-N}**. These differences influence the energetics of the creation of the gem-diolate intermediate. The optimized transition states (**TSI_{DZC}**, **TSI_{DZC-C}**, and **TSI_{DZC-N}**) are shown in Figure 4.5, 4.6, & 4.7 and the computed barriers are 25.9, 22.7, and 20.9 kcal/mol, respectively (Figure 8). All key reaction coordinates indicate that this process is concerted. This process leads to the formation of the gem-diolate intermediate (**II_{DZC}**, **II_{DZC-C}**, and **II_{DZC-N}**) which are endothermic by 10.3, 10.1, and 10.8 kcal/mol from their reactants, respectively. The C^S–N^S peptide bonds are elongated and well prepared for the cleavage in the next step.

4.3.2.2 Cleavage of the Peptide Bond

In the second step, the cleavage of the peptide bond for all the synthetic enzymes occurs. The overall computed barriers for this step for $\mathbf{I_{DZC}}$, $\mathbf{I_{DZC\text{-}C}}$, and $\mathbf{I_{DZC\text{-}N}}$ are 29.9, 26.7, and 19.8 kcal/mol, respectively. Similar to the natural enzymes, this process is the rate-limiting step of the entire mechanism. The optimized transition state structures ($\mathbf{TSII_{DZC}}$, $\mathbf{TSII_{DZC\text{-}C}}$, and $\mathbf{TSII_{DZC\text{-}N}}$) are shown in Figure 4.5, 4.6, & 4.7. In the final product ($\mathbf{III_{DZC}}$, $\mathbf{III_{DZC\text{-}C}}$, and $\mathbf{III_{DZC\text{-}N}}$), the separated neutral amine ($–NH_2$) and charged carboxyl ($–COO^-$) groups are formed. The generation of $\mathbf{III_{DZC}}$, $\mathbf{III_{DZC\text{-}C}}$, and $\mathbf{III_{DZC\text{-}N}}$ from $\mathbf{I_{DZC}}$, $\mathbf{I_{DZC\text{-}C}}$, and $\mathbf{I_{DZC\text{-}N}}$ are exothermic by 7.8, 14.6, and 7.5 kcal/mol, respectively.

Of all the synthetic binuclear analogues, the reactant $\mathbf{I_{DZC\text{-}N}}$ is the most energetically feasible. The electron-withdrawing *p*-substituent of $\mathbf{I_{DZC\text{-}N}}$ makes the Zn2-O^WH species a better nucleophile. This may be the reason to enhance the activity of binuclear zinc(II) complexes.

4.4 Summary

In this DFT study, the reaction mechanisms of the Co-catalytic binuclear metal center peptidases have been investigated. Three natural enzymes: leucine aminopeptidase (LeuAP), D-aminopeptidase (DppA), and human renal dipeptidase (hrDP), and three synthetic counterparts: Zn1(NO4)-Zn2(NO4) core containing functional analogues ($\mathbf{I_{DZC}}$, $\mathbf{I_{DZC\text{-}C}}$, and $\mathbf{I_{DZC\text{-}N}}$) have been discussed. The mechanism of the reaction is divided into

the following two steps: (1) formation of the gem-diolate intermediate, and (2) cleavage of the peptide bond.

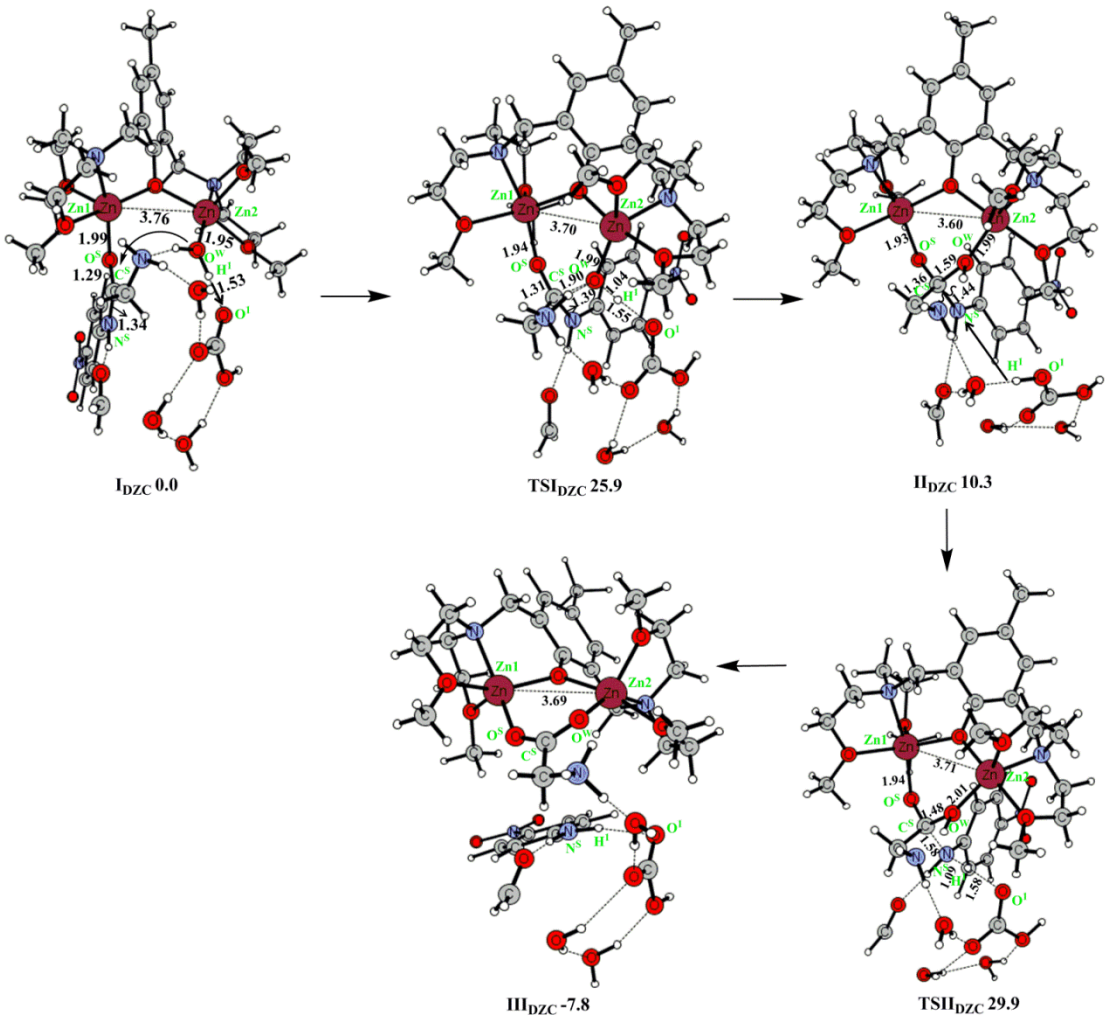

Figure 4. 5 Structures (in Å) and energies (in kcal/mol) of the reactant, transtition states, intermediate, and product of $\mathbf{I_{DZC}}$.

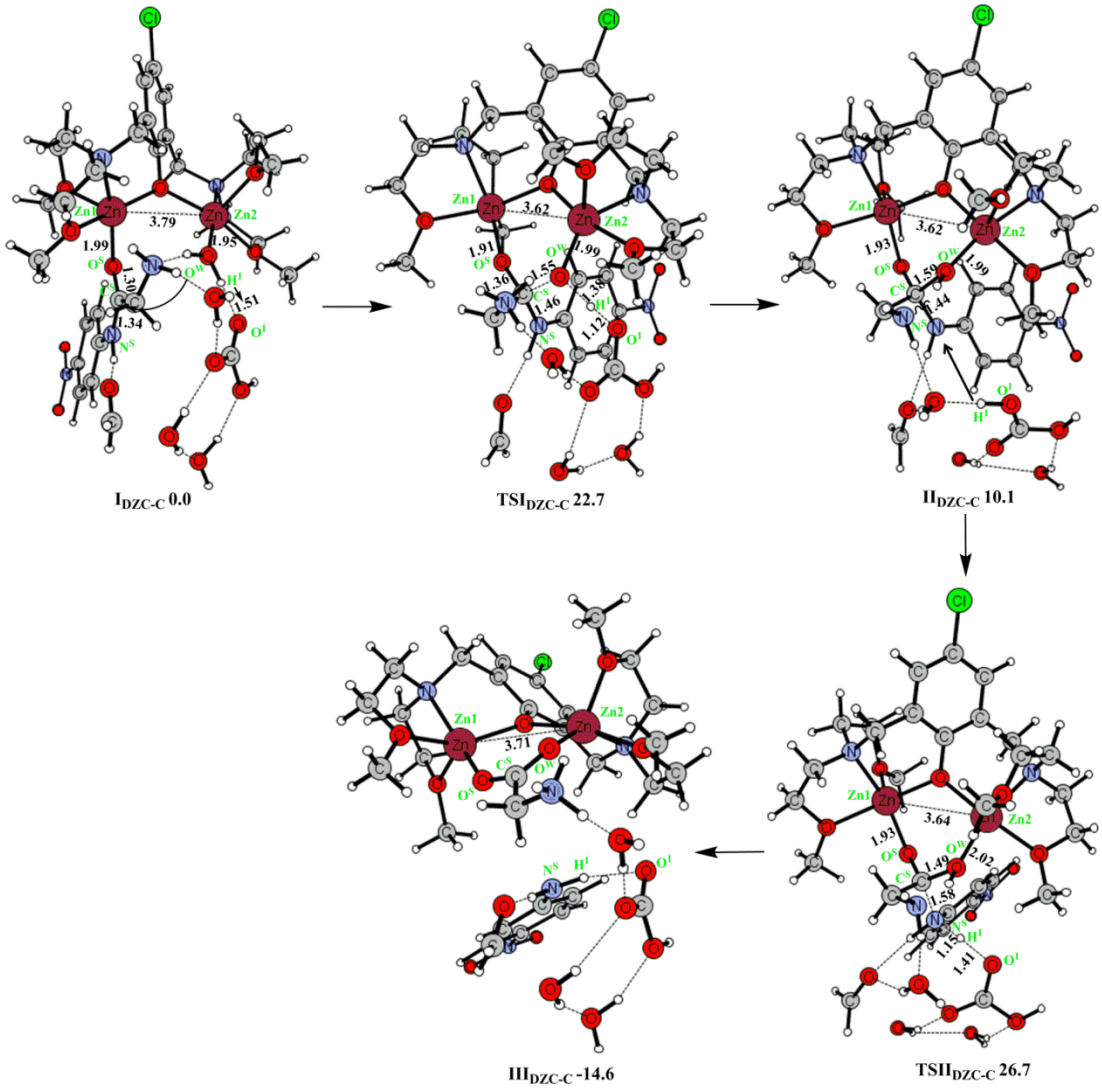

Figure 4. 6 Structures (in Å) and energies (in kcal/mol) of the reactant, transtition states, intermediate, and product of $\mathbf{I_{DZC\text{-}C}}$.

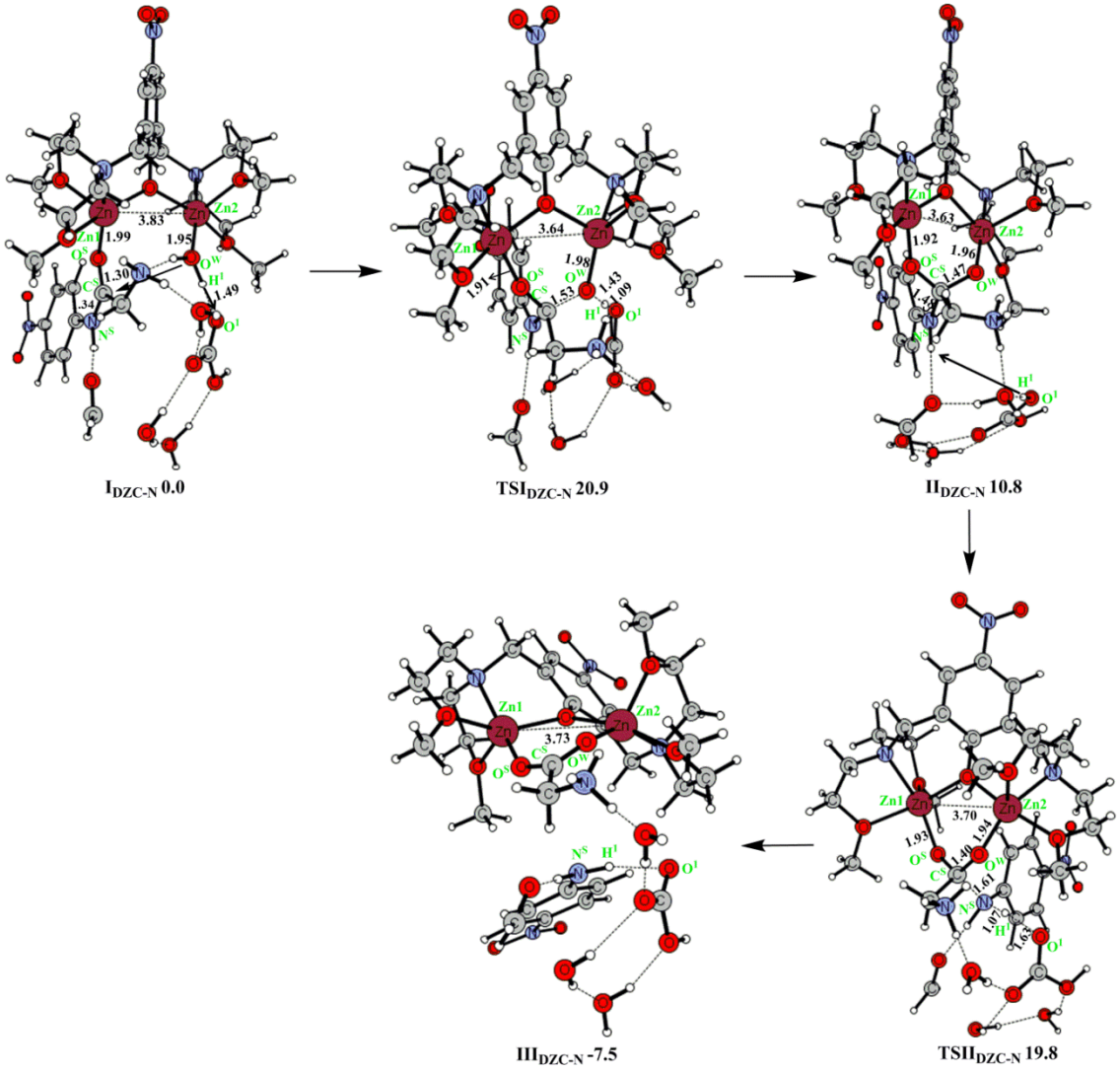

Figure 4. 7 Structures (in Å) and energies (in kcal/mol) of the reactant, transtition states, intermediate, and product of $\mathbf{I_{DZC\text{-}N}}$.

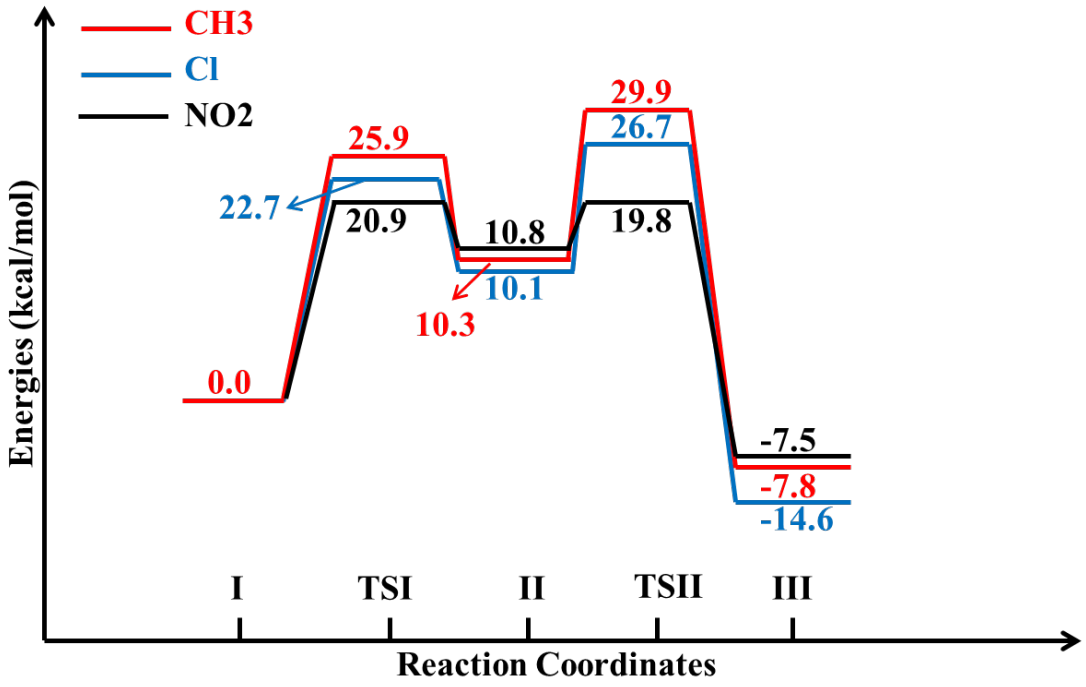

Figure 4. 8 Potential energy diagrams of synthetic analogs (in kcal/mol).

The effects of the ligand environments were studied by comparing the energetics of of Zn1(O5)-Zn2(NO4) (LeuAP), Zn1(NO4)-Zn2(NO3) (DppA), and Zn1(N2O3)-Zn2(NO3) (hrDP). In generation the gem-diolate intermediate, the energy barriers were 27.6, 29.8, and 22.1 kcal/mol for these three natural enzymes, respectively. The cleavage of the peptide bond was found to be the rate-limiting step with the computed barriers of 36.4, 30.2, and 24.8 kcal/mol. The Zn1(NO4)-Zn2(N2O2) (**hrDP**) is more energetically favorable than others of all the three natural binuclear peptidases.

On the other hand, the mechanism of the synthetic analogues was elucidated by $\mathbf{I_{DZC}}$ (modeled by [Zn(bomp)($MeCO_2$)$_2$]BPh_4 (3) [H(bomp): 2,6-bis[bis(2-methoxyethyl)aminomethyl]-4-methylphenol]), including $\mathbf{I_{DZC\text{-}C}}$ and $\mathbf{I_{DZC\text{-}N}}$ (constructed

by replacing the *p*-methyl group of $–CH_3$ from $\mathbf{I_{DZC}}$ to –Cl and $–NO_2$ respectively). $\mathbf{I_{DZC\text{-}N}}$ is the most energetically feasible of all the complexes since the electron-withdrawing *p*-nitro group enhances the Lewis acidity of the Zn metal center which results in the generation of a better nucleophile.

The results in this study have provided the structural and mechanistic information concerning three natural enzymes and three synthetic analogues. The effects of the ligand environments on different enzymes were also discussed. This study provides useful information about binuclear peptidases and will help to design more efficient catalysts.

Chapter 5 Insights into the Effects of the Mutations of Residues Arg824 and Tyr831 from Insulin Degrading Enzyme (IDE) on the Aβ Peptide Hydrolysis

5.1 Background

Alzheimer's disease (AD) is a progressive neurological disease characterized by the extracellular depositions of senile plaques and intracellular neurofibrillar tangles in the brain.[121,243,244] The amyloid-β (Aβ) peptide is reported to be the major constituent of these plaques.[121,245-249] Aβ is naturally produced through the proteolytic cleavage of amyloid precursor protein (APP) by the β- and γ- secretase enzymes.[37,40,41,250-252] The two predominant forms of the Aβ peptides containing 40- and 42-amino acid residues that are produced in vivo are Aβ40 and Aβ42 but only the latter has been observed to be a major contributor (ca. 90%) of the amyloid plaques.[253-257] Insulin-degrading enzyme (IDE) is a Zn^{2+}-metalloprotease that can bind Aβ with high affinity and hydrolyze it into small fragments. Some research demonstrated that the IDE activity is critical in determining the level of Aβ from rodent models and human genetic analysis.[258-261] Therefore, there is growing interest in IDE to provide therapeutic information for the treatment of AD.

IDE is a 113 kDa M16A family enzyme found in becteria, fungi, plants, and animals, which is known to degrade monomeric forms of a wide variety of critical peptides such as insulin, Aβ, amylin, and glucagon.[262-265] An IDE monomer comprises four structurally homologous αβ roll domains (domain1, residues 43-285; domain 2, residues 286-515; domain 3, residues 542-768; domain 4, residues 769-1016), which are 15-24% similar in

sequence [266]. Domain 1 and 2 form N-terminal (IDE-N). Domain 3 and 4 form C-terminal (IDE-C). IDE-N and IDE-C are two roughly equal sized domains that are joined by a 28-amino acid residue loop to form a triangular prism shape enclosed chamber with a volume of ~ 1.3 x 10^4 $Å^3$. This catalytic chamber is large enough to selectively entrap and degrade substrates that are smaller than 6 kDa.[266-271] The selectivity of IDE is influenced by the size, shape, and charge distribution of the internal chamber. IDE-N is largely neutral or negatively charged, whereas IDE-C is positive. IDE-N contains the crucial active site with a Zn^{2+} ion coordinated to two histidine residues (His108 and His112) and one glutamate residue (Glu189). However, IDE-N alone has only 2% of the catalytic activity of wild type IDE (IDE^{WT}).[272] IDE-C plays an important role in facilitating substrate recognition. It was reported that substrates need to undergo conformational change to form β sheets with these two discrete domains of IDE to degrade.[266] In our previous MD simulation structures of IDE^{WT}-Aβ40 and IDE^{WT}-Aβ42, IDE contains an exosite that lies about 30 Å away from the active site. It helps to anchor the N-terminal residues of the substrate and then reorient it facilitating the cleavage at the catalytic site. The N-terminal Asp1-Glu3 residues of both the substrates (Aβ40 and Aβ42) interact through hydrogen bonds with the exosite residues (Gly339, Glu341, Leu359, Gly361, and Gln363) of IDE. These interactions make the substrates form β-sheets with IDE strand β12.[266,267] Several residues of IDE domains 1 and 4 form a polar cavity with patches of hydrophobic and charged regions that interact with the cleavage sites Phe19-Phe20 of the substrates. The hydrophobic residue Phe19 interacts with the aromatic ring of Phe141 of IDE domain 1 through JI-JI interaction. In addition, the carbonyl oxygen atom of Phe19 forms a hydrogen bond with Tyr831 of IDE-C. Whereas, the backbone of Phe20 forms

hydrogen bonds with Ala140 of IDE domain 1 and Arg824 of IDE-C, respectively. These interactions make the Phe19-Phe20 cleavage site accessible to the Zn^{2+} metal center for hydrolysis.[273]

Recently, Shen, Y. et. al found that Arg824 (R824) and Tyr831 (Y831) of domain 4 in IDE play an important role in the catalytic rate of hydrolyzing Aβ. Mutations of these two residues to Ala (A) can substantially reduce the catalytic rate of IDE [266]. For instance, mutation of Tyr831→Ala and Arg824→Ala reduce the catalytic rate of IDE by 6 and 57 times respectively. However, the effects of the mutation on the structures of IDE and enzyme-substrate interactions are not known. In addition, substrate bound crystal structures of IDE mutants are not available to explain the observed decrease in activity. Therefore, in this study, Molecular dynamics (MD) simulation has been utilized to explore the structures and interactions of IDE mutants with two Alzheimer full-length peptides (Aβ40 and Aβ42). We have performed MD simulations on 4 mutants: Aβ40 bound with IDE^{R824A} (IDE^{R824A}-Aβ40), Aβ40 bound with IDE^{Y831A} (IDE^{Y831A}-Aβ40), Aβ42 bound with IDE^{R824A} (IDE^{R824A}-Aβ42) and Aβ42 bound with IDE^{Y831A} (IDE^{Y831A}-Aβ42). The results will provide the structures of substrates bound IDE mutants and help to understand the changes in conformation and interactions of Aβ40 and Aβ42 inside the catalytic chamber of IDE mutants (IDE^{R824A} and IDE^{Y831A}).

5.2 Computational Procedure

5.2.1 MD Simulations

All MD simulations were performed using GROMACS[85,274] with GROMACS force field 53A5.[275] The initial structures of the IDE^{R824A}-Aβ40, IDE^{Y831A}-Aβ40, IDE^{R824A}-Aβ42, and IDE^{Y831A}-Aβ42 complexes were placed in the center of a periodic box with dimensions of 10 nm × 10 nm × 10 nm. These boundaries eliminate unwanted effects from the applied periodic boundary conditions (PBC). In addition, sodium and chloride ions were randomly placed to neutralize the system under study. The enzyme-substrate models contain ca. 10650 atoms that are solvated by approximately 30000 simple point charge (SPC) water molecules.[82] Nonpolar hydrogen atoms in these models are treated implicitly using the united atom approach, where they are collapsed into the connected heavy atom.

The initial structures were further energy minimized with the steepest descent method for 3000 steps by releasing all the constraints. All the 20 ns production phase MD simulations were conducted with a constant number of particles (N), pressure (P), and temperature (T), i.e. NPT ensemble. The SETTLE algorithm was used to constrain the bond length and angle of the water molecules,[87] while the LINCS algorithm was utilized to constrain the bond length of the enzyme.[88] Particle mesh Ewald (PME) was employed to include the contributions of long-range interactions.[83,84] A constant pressure of 1bar was applied with a coupling constant of 1.0 ps; the peptide, water molecules, ions, and the zinc metal ion are coupled separately to a bath at 300 K with a coupling constant of 0.1 ps.

The trajectories are computed for each model with a time step of 2 fs, and the data are saved every 500 steps for analysis. The ionizable residues are set to their normal ionization states at pH 7. The tools available in GROMACS are utilized to analyze the MD trajectories. We used the most representative structures and contact maps for the structural elucidation. The most representative structures are derived from the cluster analysis, where the trajectories are analyzed by grouping structurally similar frames [root-mean-square deviation (rmsd) cutoff of 0.30 nm], and the frame with the largest number of neighbors is denoted as a middle structure that represents that particular cluster. In the contact maps, a contact for a pair of amino acid side chains is considered to be formed when a minimal distance between any pair of their atoms is less than 0.5 nm. YASARA[276] was used for visualization and for the preparation of the structural diagrams presented in this study.

5.2.2 Computational Models

The initial structures of the IDE^{WT}-Aβ40 and IDE^{WT}-Aβ42 complexes were taken from our previous 20ns WT MD simulations [277]. Mutants were performed using the SPDBV program (18), available by download from http://www.expasy.org/spdbv/. Mutagenesis of Arg824 to Ala of IDE^{WT}-Aβ40 and IDE^{WT}-Aβ42 complexes, and Tyr831 to Ala of IDE^{WT}-Aβ40 and IDE^{WT}-Aβ42 complexes were performed, respectively. The Arg824 and Tyr831 sidechains were replaced by the best rotamer of Ala amino acid. The best rotamer is the one that totalize the lowest score according to the formula (score = (4 x NbClash

with backbone N CA and C atoms) + (3 x NbClash with backbone O atoms) + (2 x NbClash with sidechains atoms) - NbHbonds - 4 x Nb SSbonds).

The MD simulations were performed in the following two steps: (1) equilibration of the initial structures for 5 ns by constraining only the catalytic center of the IDE enzyme in a time period called the equilibration phase. The constraints retained the interactions of the substrate with the active site during equilibration; (2) the structures obtained at the end of the 5 ns equilibration phase were subsequently used as the initial structure for the next 20 ns long phase known as the production phase.

5.2.3 Electrostatic Binding Energy Calculation

The solvation energy (ΔG_{sol}) was computed using the following equation.

$$\Delta G_{sol} = \Delta G_{binding}^{ele} + \Delta G_{binding}^{non-polar} \quad (1)$$

Where $\Delta\, G_{binding}^{ele}$ and $\Delta\, G_{binding}^{non-polar}$ represents the electrostatic and non-polar contributions to the solvation energy respectively. In order to compute electrostatic interactions between IDE and Aβ peptide, a continuum electrostatic calculation was performed using the APBS software.[278,279] The relative electrostatic binding energies between IDE (M1) and Aβ peptide (M2) were calculated using the following equation:

$$\Delta G_{binding}^{ele} = \Delta G_{desol\_M1}^{ele} + \Delta G_{desol\_M2}^{ele} + E_{M1-M2}^{ele} \quad (2)$$

Where $\Delta G_{desol\_M1}^{ele}$ describes the desolvation energy of M1 after its binding with M2. Due to the association between M1 and M2, the former loses the electrostatic interactions with

solvent. The following two step procedure was used to calculate this energy: (1) calculation of the electrostatic energy between M1 and the surrounding solvent in the absence of M2 and (2) computation of the electrostatic energy of M1 with the surrounding solvent in the presence of M2 (provided M2 does not carry any partial charge).[280] The difference in energies calculated in these two steps will provide the electrostatic desolvation energy $\Delta G^{ele}_{desol\_M1}$ or $\Delta G^{ele}_{desol\_M2}$. The last term in the equation describing electrostatic interaction (E^{ele}_{M1-M2}) was computed using the electrostatic potential (φ_i) generated by M1 at the position of the atomic charges (q_i) of M2 by solving the following equation.

$$E^{ele}_{M1-M2} = \sum_i^N \varphi i q i \tag{3}$$

The complexation of two monomers (M1 and M2) was computed by solving the Poisson-Boltzmann equation. These calculations were performed at room temperature (298.15 K) using dielectric constants of 2.0 and 78.0 for protein and water environments respectively and the probe sphere of 1.5 Å radius was used for calculating the solute surface. The grid spacing was set to 0.706 Å × 0.750 Å × 0.795 Å and the dielectric boundary was defined as the van der Waals surface. The salt concentration of 50 mM was used for the calculation. For these calculations, all the structures in the PDB format were converted to the PQR format using the PDB2PQR server.[281,282] The non-polar contribution to free energy is computed from the burial of solvent accessible surface area (SASA) of the peptides upon binding using the following equation.

$$\Delta G^{non-polar}_{binding} = \gamma \times \text{SASA} \tag{4}$$

Where SASA values of the IDE mutants and the Aβ peptides are calculated utilizing the YASARA program.[276] The microscopic surface tension co-efficient (γ = 0.00542 kcal/mol $Å^2$) connects the solvent accessible surface area to the free energy of transferring a molecule from alkane to water.[283,284]

5.3 Results and Discussion

In this study, we performed 20 ns simulations of the solvated IDE^{R824A}-Aβ40, IDE^{Y831A}-Aβ40, IDE^{R824A}-Aβ42, and IDE^{Y831A}-Aβ42 to obtain a dynamic picture of the conformational changes that occur in aqueous solution. The objective is to explore the structures and interactions of the full-length Aβ40 and Aβ42 substrates inside the catalytic chamber of IDE mutants at the atomic level, and the difference between mutants and WT complexes.

The rmsd values for all four simulations are depicted in Figure 5.1. They clearly indicate stable conformations after 5 ns of simulation for all IDE^{R824A}-Aβ40, IDE^{Y831A}-Aβ40, IDE^{R824A}-Aβ42, and IDE^{Y831A}-Aβ42 trajectories. In the thermodynamically equilibrated region, these four trajectories do not show any significant changes and the overall rmsd deviations remain below 0.25 nm.

Table 5. 1 RMSDs of the enzyme-substrate complexes vs IDE^{WT}-Aβ40 and IDE^{WT}-Aβ42, respectively. RMSDs of the substrates vs Aβ40 and Aβ42 derived from IDE^{WT}-Aβ40 and IDE^{WT}-Aβ42, respectively.

RMSD (nm)	Enzyme-substrate Complex	Substrate
IDE^{R824A}-Aβ40	2.81	2.34
IDE^{Y831A}-Aβ40	2.80	2.02
IDE^{R824A}-Aβ42	2.97	3.34
IDE^{Y831A}-Aβ42	2.78	3.23

5.3.1 IDE-Aβ40 Mutants

A superposition of the Zn^{2+} metal center derived from IDE^{R824A}-Aβ40 and IDE^{WT}-Aβ40 is shown in Figure 5.2a. In this structure, the residues in the first coordination shell (His108, His112, and Glu189) are bound to the Zn^{2+} ion. It is similar to the superposition structure derived from IDE^{Y831A}-Aβ40 and IDE^{WT}-Aβ40 (Figure 5.2b). However, the rmsd value (2.81 nm) of the enzyme-substrate complex shows significant changes between IDE^{R824A}-Aβ40 and IDE^{WT}-Aβ40. For the substrate only, the rmsd value is 2.34 nm (Table 5.1). In the conformation of Aβ40 derived from the most representative structure of the IDE^{R824A}-Aβ40 and IDE^{WT}-Aβ40, the Asp1-Glu3 segment remains β-sheet conformation. In Aβ40 of IDE^{WT}-Aβ40, the Val18-Phe19 region is in a random coil structure. But this region forms a β-sheet structure in Aβ40 of IDE^{R824A}-Aβ40. Moreover, the Glu15-Lys16 and Asn27-Gly29 region adopt β-sheet structures in Aβ40 of IDE^{WT}-Aβ40. However, in Aβ40 of IDE^{R824A}-Aβ40, they transform into a random coil and loop structure. It is because of the decreasing intramolecular interactions in Aβ40 and the

intermolecular interactions between Aβ40 and IDE domain 1 (Figure 5.3a, b). These interactions are likely to be responsible for the change in secondary structure of Aβ40.

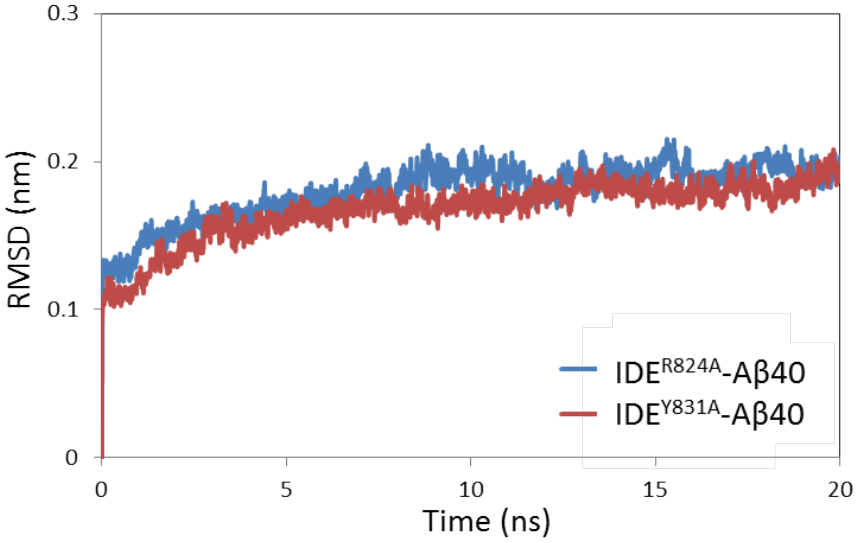

(a)

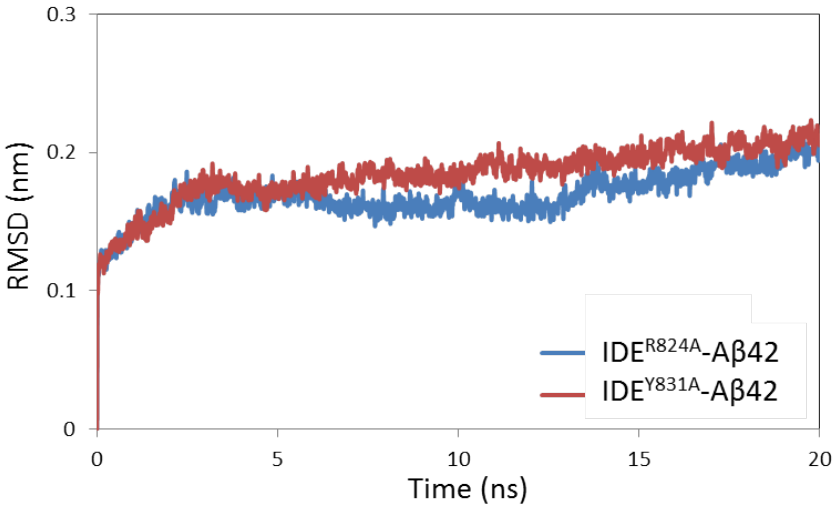

(b)

Figure 5. 1 (a) RMSD of the IDE^{R824A}-Aβ40 and IDE^{Y831A}-Aβ40 trajectories plotted vs time. (b) RMSD of the IDE^{R824A}-Aβ40 and IDE^{Y831A}-Aβ40 trajectories plotted vs time.

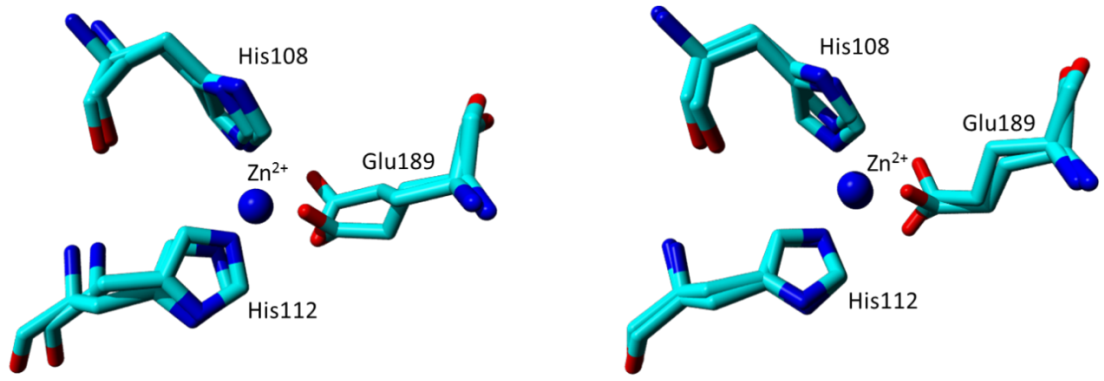

(a) (b)

Figure 5. 2 (a) Superposition of the conformation of the Zn^{2+} metal center derived from the most representative structure of the IDE^{R824A}-Aβ40 and IDE^{WT}-Aβ40 simulation. (b) Superposition of the conformation of the Zn^{2+} metal center derived from the most representative structure of the IDE^{Y831A}-Aβ40 and IDE^{WT}-Aβ40 simulation.

On the other hand, the rmsd values of IDE^{Y831A}-Aβ40 and Aβ40 derived from IDE^{Y831A}-Aβ40 are 2.80 nm and 2.02 nm, respectively (Table 5.1). The Asp1-Glu3 region also retains its β-sheet character in the Aβ40 derived from IDE^{Y831A}-Aβ40 (Figure 5.3c). However, Glu15-Lys16 and Asn27-Gly29 transform into a random coil and loop structure, because they lose the interactions between fragments Gln15-Lys16 and Asn27-Gly29.

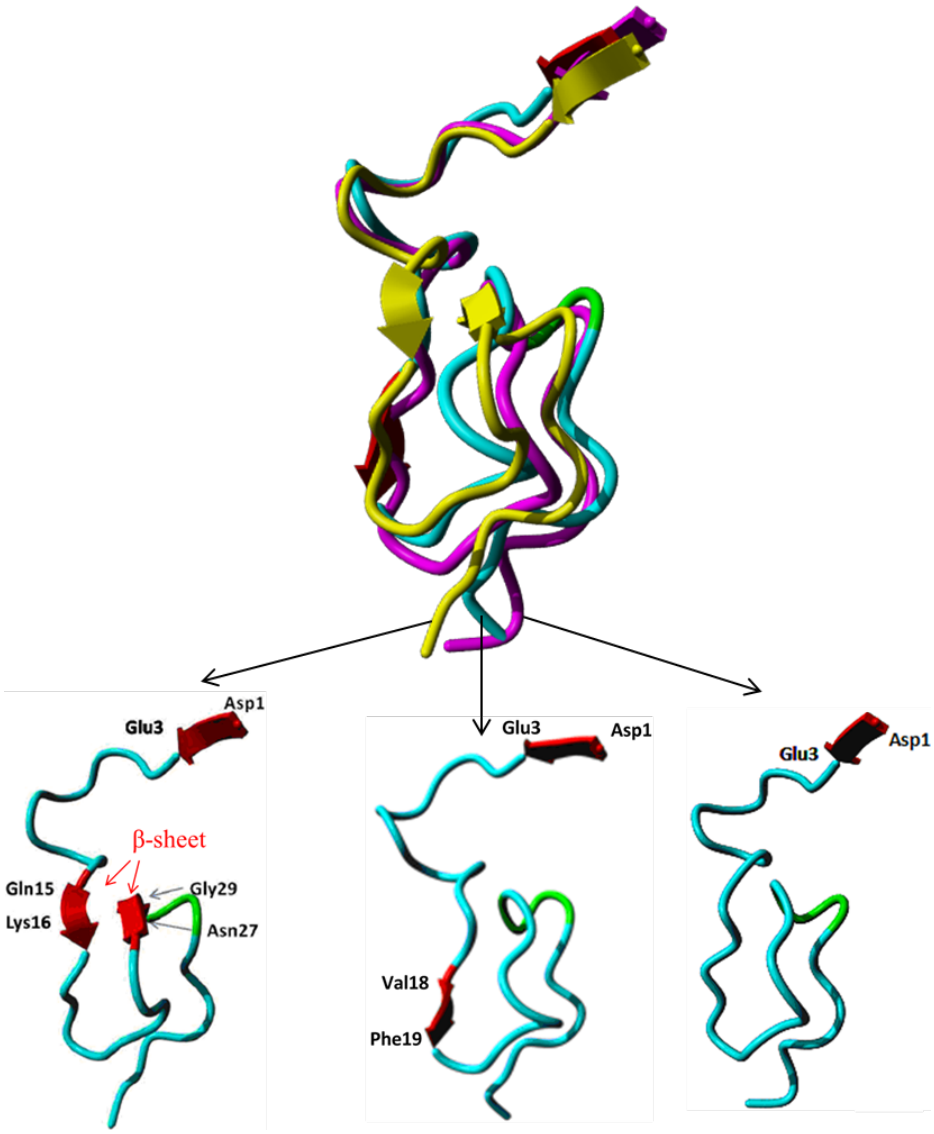

Figure 5. 3 Superposition of the conformation of Aβ40 derived from the most representative structures of the IDE^{WT}-Aβ40 (yellow), IDE^{R824A}-Aβ40 (cyan), and IDE^{Y831A}-Aβ40 (magenta). (a) Aβ40 derived from the most representative structure of the IDE^{WT}-Aβ40. (b) Aβ40 derived from the most representative structure of the IDE^{R824A}-Aβ40. (c) Aβ40 derived from the most representative structure of the IDE^{Y831A}-Aβ40.

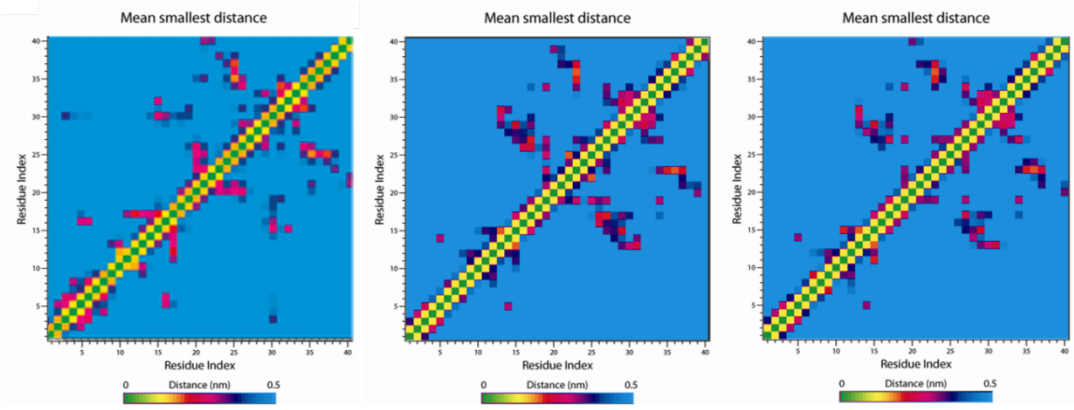

(a) (b) (c)

Figure 5. 4 (a) Contact map of Aβ40 inside the IDE^{WT} chamber. (b) Contact map of Aβ40 inside the IDE^{R824A} chamber. (c) Contact map of Aβ40 inside the IDE^{Y831A} chamber.

The contact maps also demonstrate the conformational changes in Aβ40. The contact map of Aβ40 from the most representative structure of the IDE^{WT}-Aβ40 simulation shows that it forms a large number of intramolecular interactions particularly in the Glu15-Phe19 and Ala21-Lys28 regions (Figure 5.4a). This means the backbone carbonyl (C=O) and amine (NH_2) groups of Gln15-Leu17 residues formed hydrogen bonds with the backbone carbonyl and amine groups of Asn27-Gly29 residues. In contrast to the Aβ40 from the IDE^{WT}-Aβ40, the contact maps of Aβ40 from the IDE^{R824A}-Aβ40 and IDE^{Y831A}-Aβ40 show fewer interactions. Especially in the regions of Glu15-Phe19 and Ala21-Lys28, where it doesn't form intramolecular interactions (Figure 5.4b, c). These

interactions might be responsible for the transformation of the Gln15-Leu17 and Asn27-Gly29 fragments from β-sheet to random coil conformation.

As mentioned above, during the simulations, both the Aβ40 substrates derived from the most representative structure of the IDE^{R824A}-Aβ40 and IDE^{Y831A}-Aβ40 lose their β-sheet characters. Since experiments suggested that Aβ40 adopted β-sheet character can facilitated their degradation by the enzyme, which might be responsible for the decreasing of the catalytic rate [285].

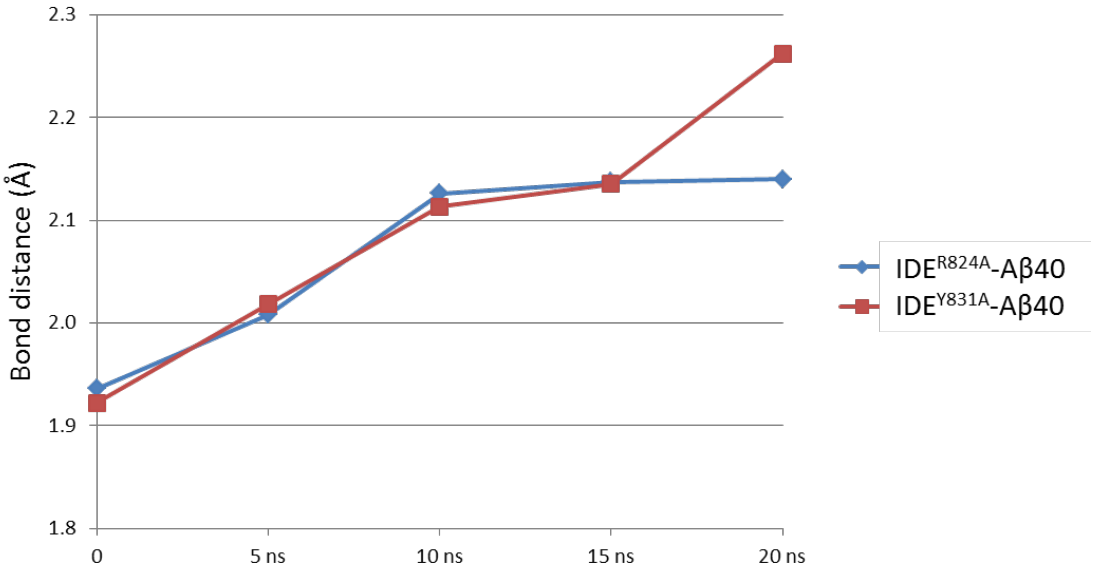

Figure 5. 5 Bond distance between Zn^{2+} ion and carbonyl oxygen (C=O) of Phe19.

In addition, in Aβ40 derived from the most representative structure of the IDE^{WT}-Aβ40, the carbonyl oxygen (C=O) of Phe19 was found to coordinate to the Zn^{2+} ion (Zn^{2+} -O distance of 1.92 Å). This interaction has been proposed to activate the hydrolysis of

the Phe19-Phe20 peptide bond.[273] However, during the simulation, the Zn^{2+}-O distance increases in Aβ40 of the IDE^{R824A}-Aβ40. It is similar to the Zn^{2+}-O distance in Aβ40 of the IDE^{Y831A}-Aβ40 (Figure 5.5).

Table 5. 2 List of Hydrogen Bonding Interactions between Aβ40 (C-terminal) and IDE

Aβ40 (residue)	IDE^{WT} (residue)	IDE^{R824A} (residue)	IDE^{Y831A} (residue)
Ile31	-	-	-
Ile32	Arg429	Arg429	-
	Arg429	-	-
Gly33	-	-	-
Leu34	Arg431	-	-
	Arg431	-	-
Met35	-	Arg429	-
Val36	Ser137	-	Arg431
Gly37	-	-	-
Gly38	Ser137	-	-
Val39	Ser128	Ser138	-
Val40	Ser128	Ser137	Ser128
	Asn821	Arg892	Thr822
	Thr825		Thr825

Secondly, we focus on the structural changes of IDE in mutants. The superposition of Aβ40 and truncated IDE domain 4 from IDE^{R824A}-Aβ40 and IDE^{WT}-Aβ40 is shown in Figure 5.6. This structure shows that around Arg824 and Tyr831 in WT IDE, Asn821-Lys826 fragment adopts α-helix conformation and Ile832-Arg839 residues form β-sheet structure. In contrast, around the mutated residue R824A, the α-helix conformation

transforms into a loop structure in IDE^{R824A}-Aβ40. Moreover, the β-sheet structure has been shortened around the Tyr831 residue. It can be seen that the C-terminal of Aβ40 has been pushed away from the mutated residue in IDE-C. That is due to the loss of hydrogen bonds between Aβ40 C-terminal and IDE^{R824A} (Table 5.2). Since IDE-C facilitate substrate binding, this change may affect the hydrolysis [286]. As it is shown in Table 5.3, the binding energy was found to be the lowest for IDE^{WT}-Aβ40 (-31.6 kcal/mol), which energies of the other two mutants are higher i.e. IDE^{R824A}-Aβ40 (-23.1 kcal/mol), IDE^{Y831A}-Aβ40 (-29.6 kcal/mol).

Table 5. 3 Solvation Free Energies of Six Enzyme-substrate Complexes

Enzyme-substrate Complex	E_{elec} (kcal/mol)	ΔG_{sol_A} (kcal/mol)	ΔG_{sol_B} (kcal/mol)	ΔG_{elec} (kcal/mol)	$\Delta G_{non\text{-}polar}$ (kcal/mol)	ΔG_{sol} (kcal/mol)
IDE^{WT}-Aβ40	-170.9	67.7	99.3	-3.9	-27.7	-31.6
IDE^{R824A}-Aβ40	-147.5	62.4	88.8	3.7	-26.8	-23.1
IDE^{Y831A}-Aβ40	-156.3	66.5	86.4	-3.4	-26.2	-29.6
IDE^{WT}-Aβ42	-147.0	62.3	84.9	0.2	-25.7	-25.5
IDE^{R824A}-Aβ42	-118.6	56.3	66.2	3.9	-24.4	-20.5
IDE^{Y831A}-Aβ42	-139.9	66.6	87.4	14.1	-27.9	-13.8

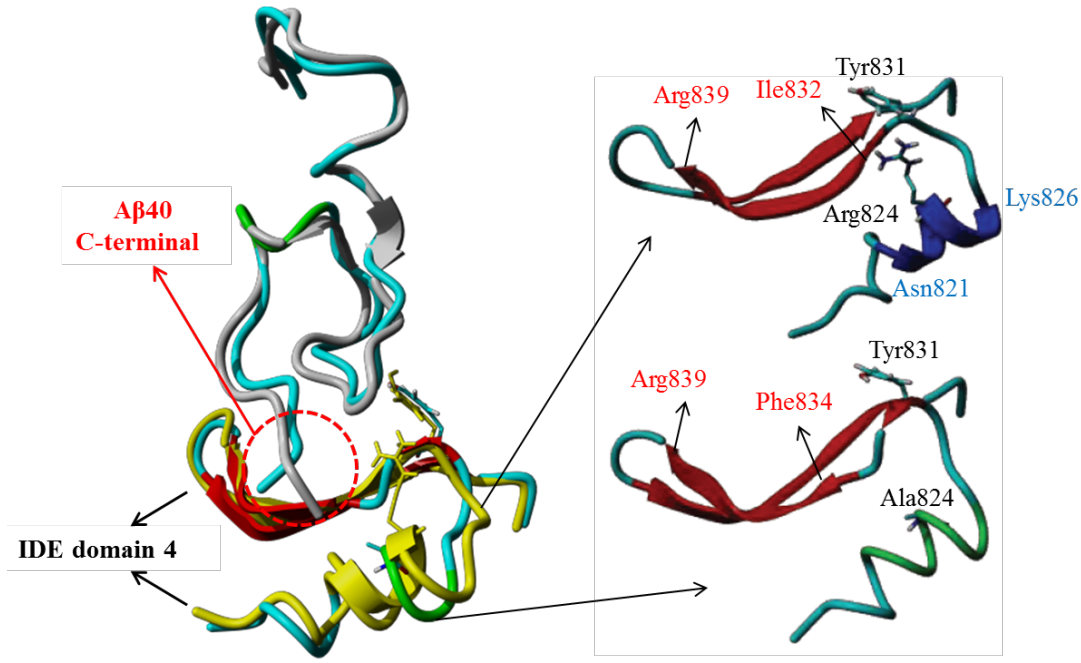

Figure 5. 6 Superposition of Aβ40 and truncated IDE domain 4 from IDE^{R824A}-Aβ40 and IDE^{WT}-Aβ40 (Aβ40 from IDE^{WT}-Aβ40: gray; IDE domain 4 from IDE^{WT}-Aβ40: yellow).

The superposition of Aβ40 and truncated IDE domain 4 from IDE^{Y831A}-Aβ40 and IDE^{WT}-Aβ40 is shown in Figure 5.7. Different from IDE^{WT}-Aβ40, there is no α-helix conformation around Arg824 in IDE^{Y831A}-Aβ40 domain 4. The β-sheet character around the mutated residue Y831A has been shortened to Ile832-Pro837 compared to Ile832-Arg839 in IDE-^{WT}-Aβ40. Moreover, the number of hydrogen bonds between Aβ40 C-terminal and IDE^{Y831A} decreases from 10 in WT to 4 (Table 5.2). This has been suggested to contribute to the movement of Aβ40 C-terminal away from the mutated domain 4 residue in IDE.

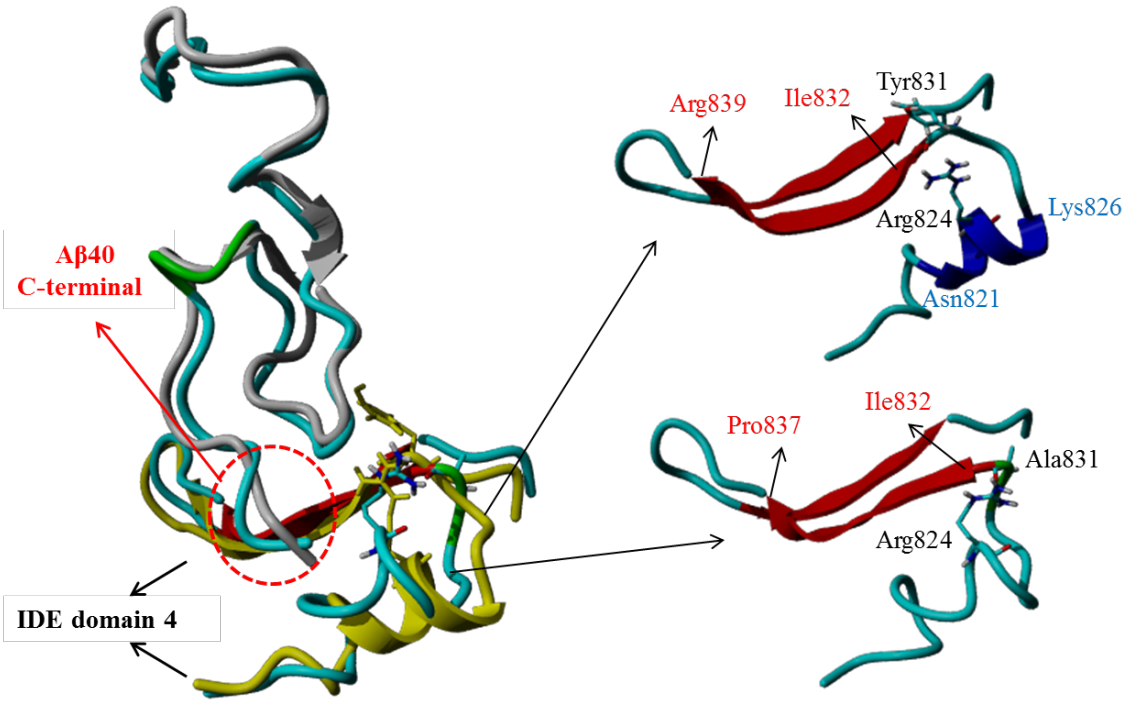

Figure 5. 7 Superposition of Aβ40 and truncated IDE domain 4 from IDE^{Y831A}-Aβ40 and IDE^{WT}-Aβ40 (Aβ40 from IDE^{WT}-Aβ40: gray; IDE domain 4 from IDE^{WT}-Aβ40: yellow).

In addition to the aforementioned structural changes, the MD simulations reveal intermolecular hydrogen bonding interactions change between the Aβ40 and IDE (Table 5.4 and 5.5). In IDE^{WT}-Aβ40, IDE and Aβ40 form 34 hydrogen bonds, but in IDE^{R824A}-Aβ40 and IDE^{Y831A}-Aβ40, this number decreases to 29 and 24, respectively (Figure 5.8). In particular, the cleavage site Phe19-Phe20 of Aβ40 interacts with Ala140, Arg824, Tyr831, and Phe141 (CH-π interaction) of IDE. These interactions have been experimentally reported to be responsible for the orientation and folding of the substrate inside IDE.[277] However, the cleavage site Phe19-Phe20 only interacts with Ala140,

Arg824 in IDE^{R824A}-Aβ40 and IDE^{Y831A}-Aβ40, respectively (Table 5.4 and 5.5). Moreover, in IDE^{WT}-Aβ40, the C-terminal Val36, Gly38, Val39, and Val40 residues of Aβ40 interact with the Ser137, Ser137, Ser128, Ser128, Asn821, and Thr825 residues of IDE, respectively. However, they lose many interactions between IDE and the C-terminal of Aβ40 in IDE^{R824A}-Aβ40 and IDE^{Y831A}-Aβ40 structures.

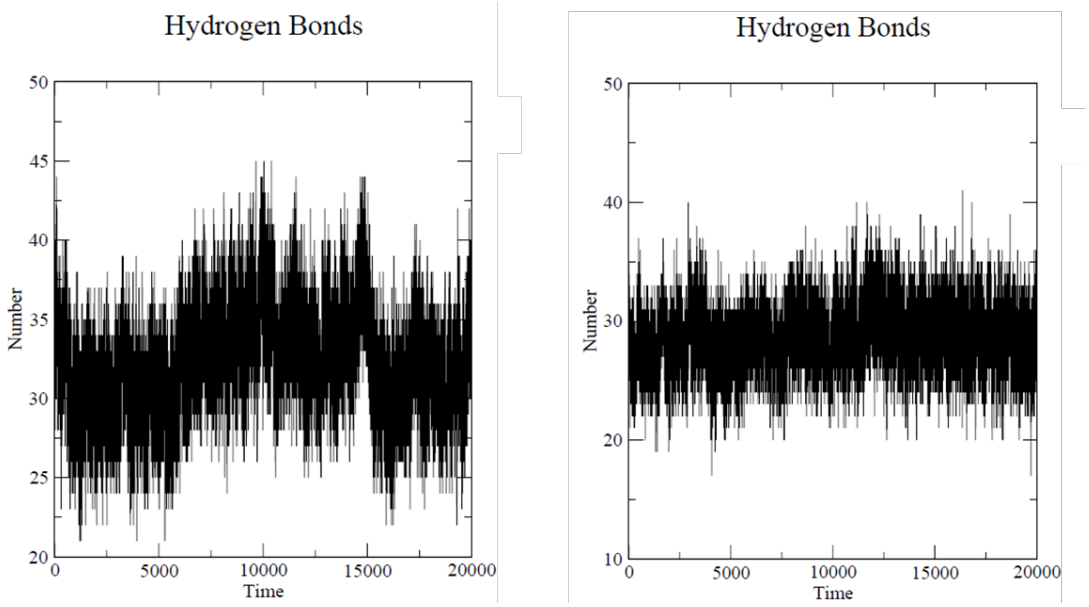

(a) (b)

Figure 5. 8 (a) Time-dependent variation of the number of hydrogen bonds between Aβ40 and IDE^{R824A}. (b) Time-dependent variation of the number of hydrogen bonds between Aβ40 and IDE^{Y831A}.

Table 5. 4 List of Hydrogen Bonding Interactions between Aβ40 and IDE (IDE^{WT} and IDE^{R824A})

Aβ40 (residue)	atom	IDE^{WT} (residue)	atom	Aβ40 (residue)	atom	IDE^{R824A} (residue)	atom
Asp1	N	Gly339	O	Asp1	N	Leu359	O
	N	Leu359	O		O	Gly361	N
	O	Gly361	N	Ala2	-	-	-
Ala2	-	-	-	Glu3	N	Gly361	O
Glu3	N	Gly361	O		O	Gln363	N
	O	Gln363	N	Phe4	-	-	-
Phe4	-	-	-	Arg5	NE	Lys364	O
Arg5	O	Gln363	NE2	His6	-	-	-
	NH2	Glu365	OE2	Asp7	OD1	Tyr444	OH
His6	NE2	Leu455	N		OD2	Gln322	NE2
Asp7	O	Gly366	N	Ser8	N	Gly322	O
	OD1	Tyr444	OH	Gly9	-	-	-
Ser8	O	Gln323	NE2	Tyr10	N	Glu145	OE2
Gly9	-	-	-	Glu11	OE2	Ser96	OG
Tyr10	-	-	-		O	Glu145	N
Glu11	O	Glu145	N	Val12	O	ser143	OG
	OE2	Lys206	NZ		N	Glu365	OE1
Val12	O	Ser143	OG	His13	N	Glu365	OE2
His13	-	-	-	His14	NE2	Lys436	NZ
His14	-	-	-	Gln15	-	-	-
Gln15	-	-	-	Lys16	NZ	Asn196	OD1
Lys16	O	Asn193	ND2	Leu17	-	-	-
	NZ	Asn196	OD1	Val18	N	Thr142	O
Leu17	-	-	-		O	Thr142	N
Val18	-	-	-	Phe19	-	-	-
Phe19	O	Tyr831	OH	Phe20	N	Ala140	O
Phe20	N	Ala140	O	Ala21	N	Asn139	OD1
	O	Arg824	NH2		O	Asn139	ND2
Ala21	N	Asn139	OD1	Glu22	OE2	Lys192	NZ
	O	Asn139	ND2		OE2	His679	ND1
Glu22	-	-	-	Asp23	-	-	-
Asp23	-	-	-	Val24	-	-	-
Val24	-	-	-	Gly25	-	-	-
Gly25	O	Lys192	NZ	Ser26	OG	Gln677	OE1
Ser26	-	-	-	Asn27	-	-	-
Asn27	-	-	-	Lys28	-	-	-
Lys28	-	-	-	Gly29	-	-	-
Gly29	-	-	-	Ala30	-	-	-
Ala30	-	-	-	Ile31	-	-	-
Ile31	-	-	-	Ile32	O	Arg429	NH2
Ile32	O	Arg429	NE	Gly33	-	-	-
	O	Arg429	NH2	Leu34	-	-	-
Gly33	-	-	-	Met35	SD	Arg429	NH1
Leu34	O	Arg431	NE	Val36	-	-	-
	O	Arg431	NH2	Gly37	-	-	-
Met35	-	-	-	Gly38	-	-	-
Val36	O	Ser137	OG	Val39	N	Ser138	O
Gly37	-	-	-	Val40	OT1	Ser137	OG
Gly38	N	Ser137	OG		OT2	Arg892	NH1
Val39	O	Ser128	OG				
Val40	OT1	Ser128	OG				
	OT1	Asn821	ND2				
	OT2	Thr825	OG1				

Table 5. 5 List of Hydrogen Bonding Interactions between Aβ40 and IDE (IDE^{WT} and IDE^{Y831A})

Aβ40 (residue)	atom	IDE^{WT} (residue)	atom	Aβ40 (residue)	atom	IDE^{Y831A} (residue)	atom
Asp1	N	Gly339	O	Asp1	N	Leu359	O
	N	Leu359	O		O	Gly361	N
	O	Gly361	N	Ala2	-	-	-
Ala2	-	-	-	Glu3	N	Gly361	O
Glu3	N	Gly361	O		O	Gln363	N
	O	Gln363	N	Phe4	-	-	-
Phe4	-	-	-	Arg5	O	Gln363	NE2
Arg5	O	Gln363	NE2	His6	-	-	-
	NH2	Glu365	OE2	Asp7	OD1	Tyr444	OH
His6	NE2	Leu455	N		OD1	Gln322	NE2
Asp7	O	Gly366	N		O	Gly366	N
	OD1	Tyr444	OH	Ser8	-	-	-
Ser8	O	Gln323	NE2	Gly9	-	-	-
Gly9	-	-	-	Tyr10	OH	Lys206	NZ
Tyr10	-	-	-	Glu11	OE2	Ser96	OG
Glu11	O	Glu145	N		O	Glu145	N
	OE2	Lys206	NZ	Val12	N	Glu365	OE1
Val12	O	Ser143	OG		O	Ser143	OG
His13	-	-	-	His13	-	-	-
His14	-	-	-	His14	N	Glu365	OE2
Gln15	-	-	-		ND1	Glu365	OE2
Lys16	O	Asn193	ND2	Gln15	-	-	-
	NZ	Asn196	OD1	Lys16	NZ	Gln677	OE1
Leu17	-	-	-	Leu17	-	-	-
Val18	-	-	-	Val18	-	-	-
Phe19	O	Tyr831	OH	Phe19	-	-	-
Phe20	N	Ala140	O	Phe20	N	Ala140	O
	O	Arg824	NH2		O	Arg824	NH2
Ala21	N	Asn139	OD1	Ala21	N	Asn139	OD1
	O	Asn139	ND2		O	Asn139	ND2
Glu22	-	-	-	Glu22	OE2	Lys192	NZ
Asp23	-	-	-	Asp23	-	-	-
Val24	-	-	-	Val24	-	-	-
Gly25	O	Lys192	NZ	Gly25	-	-	-
Ser26	-	-	-	Ser26	-	-	-
Asn27	-	-	-	Asn27	-	-	-
Lys28	-	-	-	Lys28	-	-	-
Gly29	-	-	-	Gly29	-	-	-
Ala30	-	-	-	Ala30	-	-	-
Ile31	-	-	-	Ile31	-	-	-
Ile32	O	Arg429	NE	Ile32	-	-	-
	O	Arg429	NH2	Gly33	-	-	-
Gly33	-	-	-	Leu34	-	-	-
Leu34	O	Arg431	NE	Met35	-	-	-
	O	Arg431	NH2	Val36	O	Arg431	NH1
Met35	-	-	-	Gly37	-	-	-
Val36	O	Ser137	OG	Gly38	-	-	-
Gly37	-	-	-	Val39	-	-	-
Gly38	N	Ser137	OG	Val40	OT1	Ser128	OG
Val39	O	Ser128	OG		OT1	Thr822	N
Val40	OT1	Ser128	OG		OT2	Thr825	N
	OT1	Asn821	ND2				
	OT2	Thr825	OG1				

Both the substrate and the enzyme change their secondary structures due to a decrease in the amount of intermolecular interactions. Aβ40 is more flexible in IDE mutants. These may be the factors that reduce the catalytic rate of IDE mutants.

5.3.2 IDE-Aβ42 Mutants

A superposition of Zn^{2+} metal center derived from IDE^{R824A}-Aβ42 and IDE^{WT}-Aβ42 is shown in Figure 5.9. In this structure, the residues in the first coordination shell (His108, His112, and Glu189) lie within bond forming distance of the Zn^{2+} ion (Figure 5.9a). It is similar to the superposition structure derived from IDE^{Y831A}-Aβ42 and IDE^{WT}-Aβ42 (Figure 5.9b). However, in the conformations of the most representative structure of IDE^{R824A}-Aβ42 and IDE^{WT}-Aβ42, it shows significant changes (rmsd value is 2.97 nm). For the substrate only, the rmsd value is 3.34 nm (Table 5.1). Phe20 remains the β-sheet conformation in Aβ42 derived from IDE^{R824A}-Aβ42 and IDE^{WT}-Aβ42. In Aβ42 of IDE^{WT}-Aβ42, the Tyr10-Gln15 region adopts α-helix character. However, the Tyr10-Gln15 segment loses its α-helix character in the IDE^{R824A}-Aβ42 mutant (Figure 5.10a, b). The missing intramolecular interactions might be responsible for the transformation of the Tyr10-Gln15 segment from α-helix conformation to loop.

The rmsd values of IDE^{Y831A}-Aβ42 and Aβ42 derived from IDE^{Y831A}-Aβ42 are 2.78 nm and 3.23 nm, respectively (Table 5.1). Phe20 retains its β-sheet character in Aβ42 derived from IDE^{Y831A}-Aβ42 and IDE^{WT}-Aβ42 (Figure 5.10a, c). Similar to the IDE^{R824A}-Aβ42 structure, the Tyr10-Gln15 also changes to loop structure.

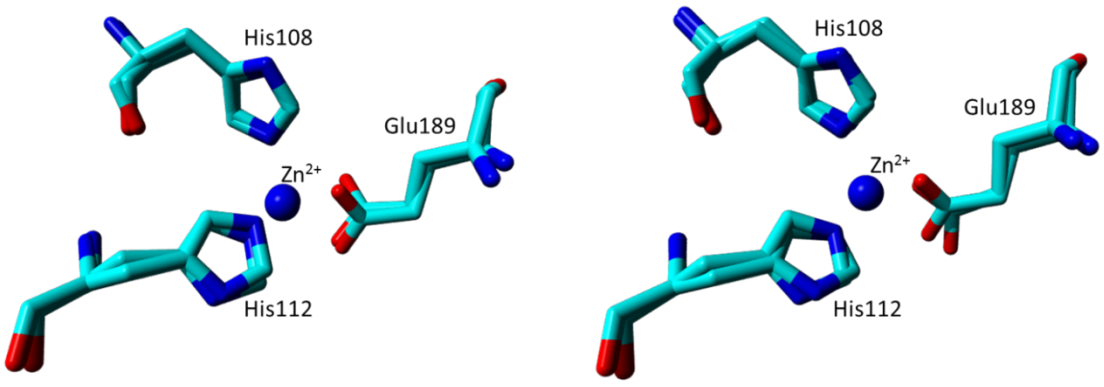

(a) (b)

Figure 5. 9 (a) Superposition of the conformation of the Zn^{2+} metal center derived from the most representative structure of the IDE^{R824A}-Aβ42 and IDE^{WT}-Aβ42 simulation. (b) Superposition of the conformation of the Zn^{2+} metal center derived from the most representative structure of the IDE^{Y831A}-Aβ42 and IDE^{WT}-Aβ42 simulation.

The contact maps also indicate the conformational changes in Aβ42. It shows that it forms a large number of intramolecular interactions particularly in the Tyr10-Gln15 region in Aβ42 derived from IDE^{WT}-Aβ42. It means the backbone carbonyl (C=O) and amine (NH_2) groups were formed hydrogen bonds inside the Tyr10-Gln15 region. The Aβ42 derived from IDE mutants generates fewer intramolecular interactions than Aβ42 derived from WT-IDE (Figure 5.11). Therefore, in both IDE^{R824A}-Aβ42 and IDE^{Y831A}-Aβ42, the substrates lose their α-helix conformations. These interactions might affect the catalytic rate due to losing interactions between Aβ42 and IDE domain 1.

In addition, in Aβ42 derived from the most representative structure of the IDE^{WT}-Aβ42, the carbonyl oxygen (C=O) of Phe19 was found to coordinate to the Zn^{2+} ion (Zn^{2+} -O distance of 1.97 Å). This interaction has been proposed to activate the hydrolysis of

the Phe19-Phe20 peptide bond.[273] However, during the simulation, the Zn^{2+}-O distance increases in Aβ42 of the IDE^{R824A}-Aβ42. It is similar to the Zn^{2+}-O distance in Aβ42 of the IDE^{Y831A}-Aβ42 (Figure 5.12).

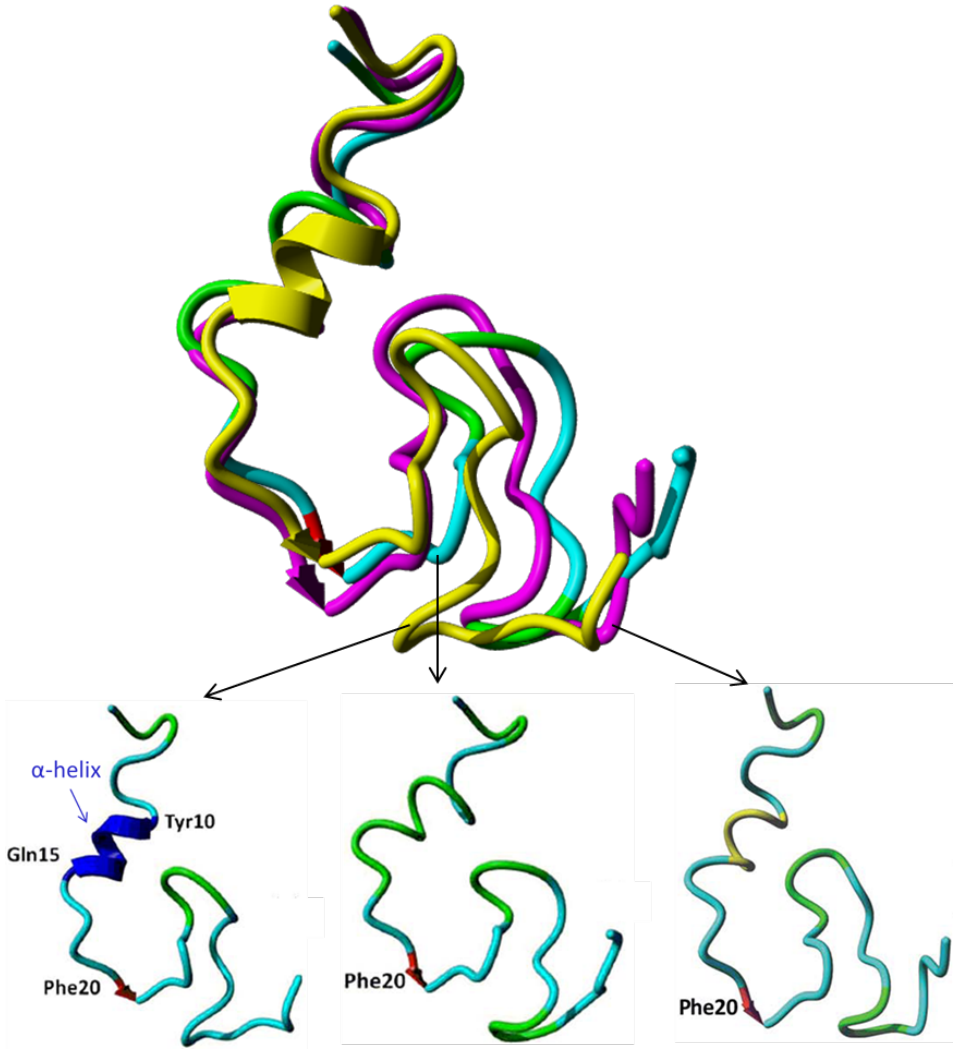

Figure 5. 10 Superposition of the conformation of Aβ42 derived from the most representative structures of the IDE^{WT}-Aβ42 (yellow), IDE^{R824A}-Aβ42 (cyan), and IDE^{Y831A}-Aβ42 (magenta). (a) Aβ42 derived from the most representative structure of the IDE^{WT}-Aβ42. (b) Aβ42 derived from the most representative structure of the IDE^{R824A}-Aβ42. (c) Aβ42 derived from the most representative structure of the IDE^{Y831A}-Aβ42.

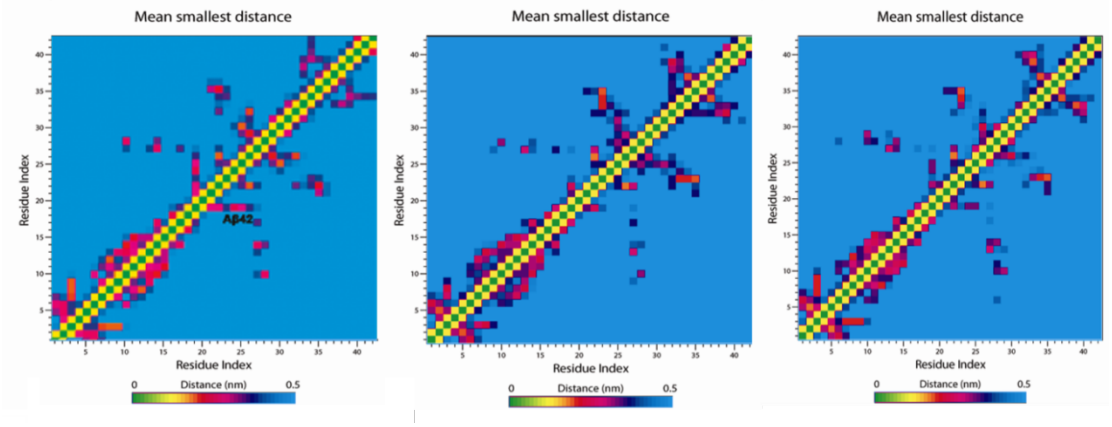

(a) (b) (c)

Figure 5. 11 (a) Contact map of Aβ42 inside the IDE^{WT} chamber. (b) Contact map of Aβ42 inside the IDE^{R824A} chamber. (c) Contact map of Aβ42 inside the IDE^{Y831A} chamber.

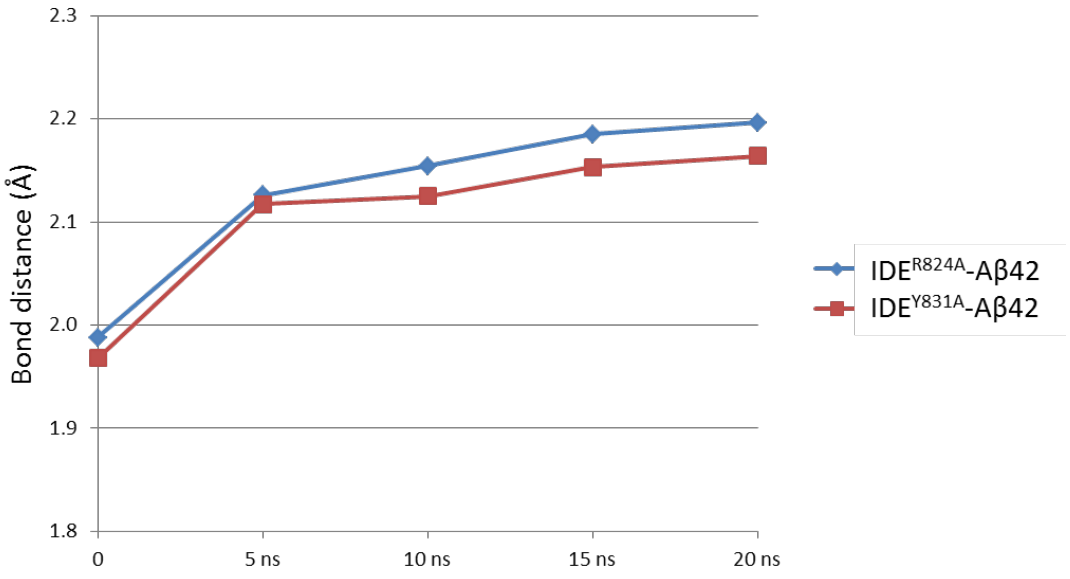

Figure 5. 12 Bond distance between Zn^{2+} ion and carbonyl oxygen (C=O) of Phe19.

These mutants also introduce substantial structural changes in the enzyme. The superposition of Aβ42 and truncated IDE domain 4 from IDE^{R824A}-Aβ42 and IDE^{WT}-Aβ42 is shown in Figure 5.13. This structure shows that around Arg824 and Tyr831 in WT-IDE, the Ile815-Asn821 fragment adopts α-helix conformation and Ile832-Ser835 forms the β-sheet structure. However, both the α-helix and β-sheet structures increase in IDE^{R824A}-Aβ42. Around the mutated residue R824A, the α-helix has been elongated to Ile815-Cys819 and Asn821-Thr825. The β-sheet structure increases to Ile832-Pro837 around residue Tyr831. Due to the loss of hydrogen bonds between Aβ42 C-terminal and IDE^{R824A} (Table 5.6), the C-terminal of Aβ42 has been pushed away from the mutated residue. This is similar to the IDE-Aβ40 complex (Table 5.3), the binding energy was found to be the lowest for IDE^{WT}-Aβ42 (-25.5 kcal/mol), and energies of the other two mutants are higher i.e. IDE^{R824A}-Aβ42 (-20.5 kcal/mol), IDE^{Y831A}-Aβ42 (-13.8 kcal/mol).

The superposition of Aβ42 and truncated IDE domain 4 from IDE^{Y831A}-Aβ42 and IDE^{WT}-Aβ42 is shown in Figure 5.14. Different from the former mutant IDE^{R824A}-Aβ42, the α-helix around the Arg824 in IDE^{Y831A}-Aβ40 domain 4 has been shortened to Ile815-Phe820. Whereas the β-sheet around mutated residue Y831A increases to Ile832-Arg838 compared to Ile832-Ser835 in IDE^{WT}-Aβ42. It is similar to IDE^{R824A}-Aβ42 that the C-terminal of Aβ42 moves away from the mutated domain 4 residue in IDE, since the number of hydrogen bonds between Aβ42 C-terminal and IDE^{Y831A} decreases from 7 in WT to 3 (Table 5.6).

Table 5. 6 List of Hydrogen Bonding Interactions between Aβ42 (C-terminal) and IDE

Aβ42 (residue)	IDE^{WT} (residue)	IDE^{R824A} (residue)	IDE^{Y831A} (residue)
Ile31	-	-	-
Ile32	-	-	-
Gly33	-	-	-
Leu34	Asn139	-	-
Met35	Arg824	-	Asn139
	Asn139	-	-
Val36	-	Ser137	Ser137
Gly37	Ser138	-	-
Gly38	Gln813	-	-
Val39	-	-	-
Val40	Gln813	-	-
Ile41	Arg839	Ser913	-
Ala42	-	-	Arg839

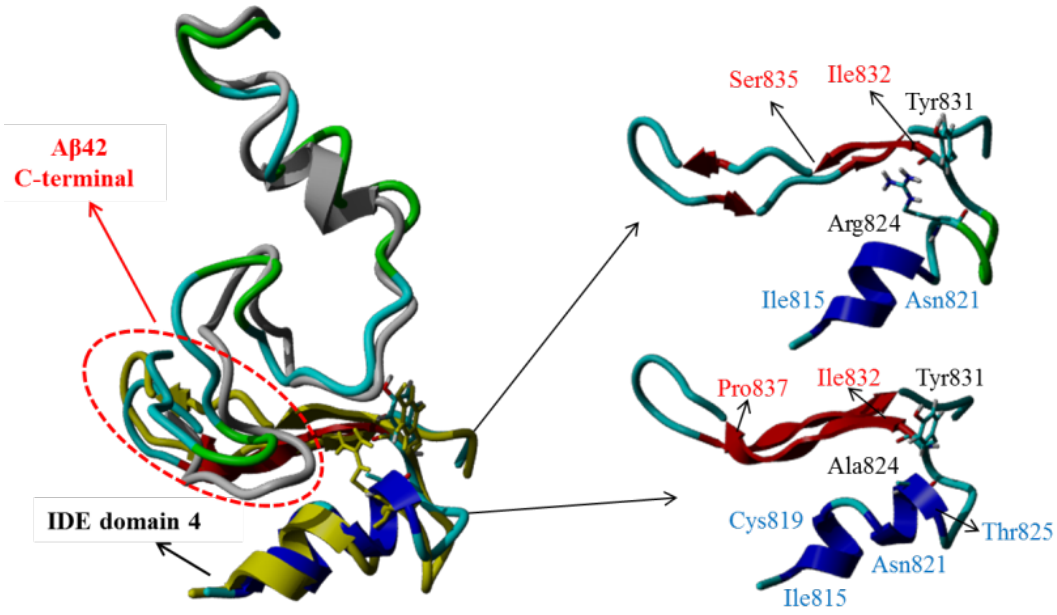

Figure 5. 13 Superposition of Aβ42 and truncated IDE domain 4 from IDE^{R824A}-Aβ42 and IDE^{WT}-Aβ42 (Aβ42 from IDE^{WT}-Aβ42: gray; IDE domain 4 from IDE^{WT}-Aβ42: yellow).

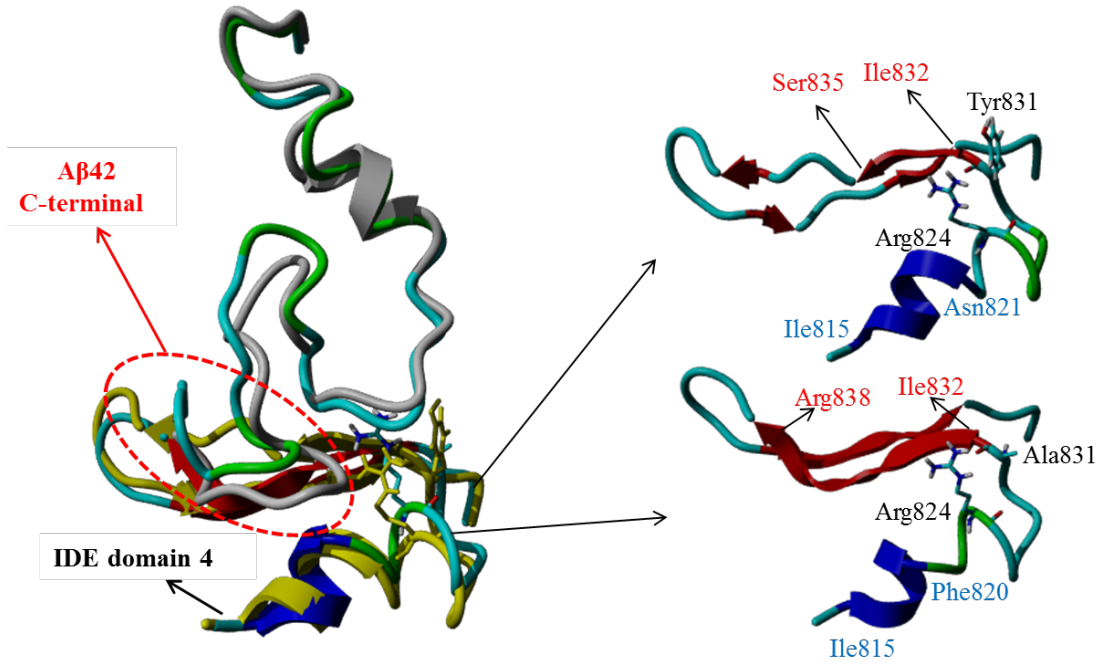

Figure 5. 14 Superposition of Aβ42 and truncated IDE domain 4 from IDE^{Y831A}-Aβ42 and IDE^{WT}-Aβ42 (Aβ42 from IDE^{WT}-Aβ42: gray; IDE domain 4 from IDE^{WT}-Aβ42: yellow).

In addition to the aforementioned structural changes, the MD simulations reveal the changes in intermolecular hydrogen bonding interactions between the Aβ42 and IDE (Table 5.7 and 5.8). In IDE^{WT}-Aβ42, IDE and Aβ42 form 24 hydrogen bonds, but in IDE^{R824A}-Aβ42 and IDE^{Y831A}-Aβ42, this number reduces to 19 (Figure 5.15). In particular, the cleavage site Phe19-Phe20 of Aβ42 interacts with Ala140, Tyr831, and Phe141 (CH-π interaction) of IDE. These interactions have been experimentally reported to be responsible for the orientation and folding of the substrate inside IDE.[277] However, the cleavage site Phe19-Phe20 only interacts with Ala140 in IDE^{R824A}-Aβ42 and

IDE^{Y831A}-Aβ42 (Table 5.7 and 5.8). Moreover, in IDE^{WT}-Aβ42, the C-terminal Met35, Gly37, Gly38, Val40, and Ile41 residues of Aβ42 interact with the Arg824, Asn139, Ser138, Gln813, Gln813, and Arg839 residues of IDE, respectively. However, they lose many interactions between IDE and the C-terminal of Aβ42 in IDE^{R824A}-Aβ42 and IDE^{Y831A}-Aβ42 structures (Table 5.7 and 5.8).

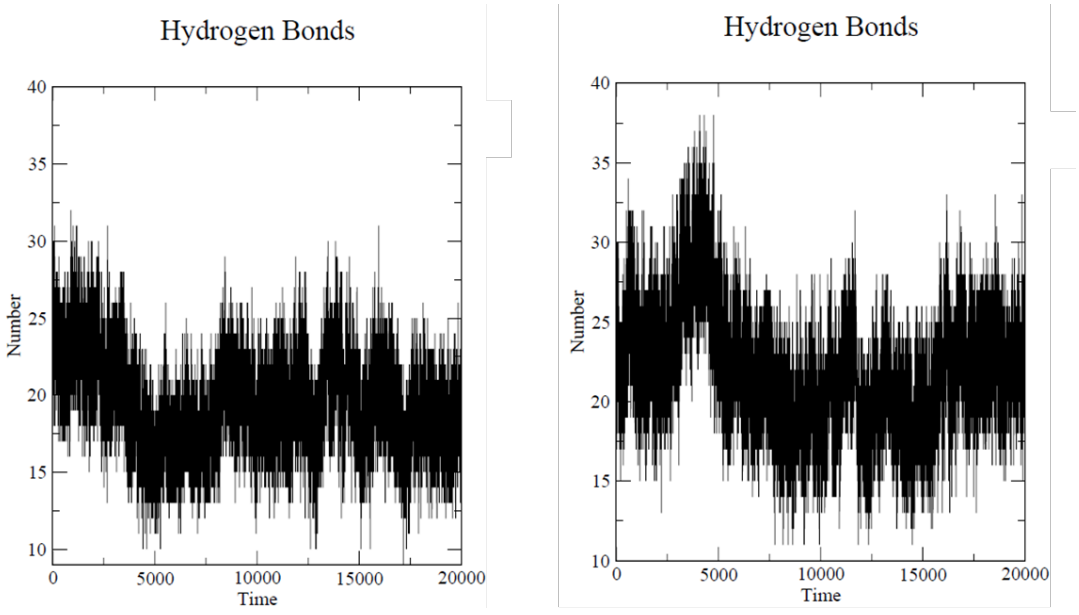

(a) (b)

Figure 5. 15 (a) Time-dependent variation of the number of hydrogen bonds between Aβ42 and IDE^{R824A}. (b) Time-dependent variation of the number of hydrogen bonds between Aβ42 and IDE^{Y831A}.

Table 5. 7 List of Hydrogen Bonding Interactions between Aβ42 and IDE (IDE^{WT} and IDE^{R824A})

Aβ42 (residue)	atom	IDE^{WT} (residue)	atom	Aβ42 (residue)	atom	IDE^{R824A} (residue)	atom
Asp1	OD2	Glu341	N	Asp1	OD2	Glu341	N
	OD1	Tyr609	OH		OD2	His340	ND1
	N	Leu359	O		OD1	Tyr609	OH
Ala2	-	-	-	Ala2	-	-	-
Glu3	-	-	-	Glu3	-	-	-
Phe4	-	-	-	Phe4	-	-	-
Arg5	N	Tyr609	OH	Arg5	NH1	Asn605	OD1
	NH2	Glu612	OE1	His6	-	-	-
	NH2	Tyr618	OH	Asp7	OD1	Gln363	N
	NH1	Asn605	OD1		OD2	Gln363	NE2
His6	-	-	-	Ser8	-	-	-
Asp7	-	-	-	Gly9	-	-	-
Ser8	OG	Lys436	NZ	Tyr10	-	-	-
Gly9	-	-	-	Glu11	OE1	Gly361	N
Tyr10	-	-	-	Val12	-	-	-
Glu11	-	-	-	His13	ND1	Ser143	OG
Val12	-	-	-	His14	O	Trp199	NE1
His13	-	-	-	Gln15	OE1	Lys364	NZ
His14	-	-	-	Lys16	N	Ser143	O
Gln15	OE1	Trp199	NE1		NZ	Ser143	O
Lys16	-	-	-	Leu17	-	-	-
Leu17	O	Asn193	ND2	Val18	N	Thr142	O
Val18	-	-	-	Phe19	-	-	-
Phe19	O	Tyr831	OH	Phe20	N	Ala140	O
Phe20	N	Ala140	O		O	Ala140	N
	O	Ala140	N	Ala21	-	-	-
Ala21	N	Asn139	OD1	Glu22	-	-	-
Glu22	-	-	-	Asp23	-	-	-
Asp23	OD1	Ser835	OG	Val24	-	-	-
	OD1	Ser835	N	Gly25	-	-	-
Val24	-	-	-	Ser26	OG	Arg431	NE
Gly25	-	-	-	Asn27	-	-	-
Ser26	-	-	-	Lys28	-	-	-
Asn27	-	-	-	Gly29	-	-	-
Lys28	-	-	-	Ala30	O	Arg429	NH1
Gly29	-	-	-	Ile31	-	-	-
Ala30	-	-	-	Ile32	-	-	-
Ile31	-	-	-	Gly33	-	-	-
Ile32	-	-	-	Leu34	-	-	-
Gly33	-	-	-	Met35	-	-	-
Leu34	O	Asn139	ND2	Val36	O	Ser137	OG
Met35	SD	Arg824	NH2	Gly37	-	-	-
	O	Asn139	ND2	Gly38	-	-	-
Val36	-	-	-	Val39	-	-	-
Gly37	O	Ser138	N	Val40	-	-	-
Gly38	O	Gln813	NE2	Ile41	O	Ser913	OG
Val39	-	-	-	Ala42	-	-	-
Val40	N	Gln813	OE1				
Ile41	O	Arg839	NH1				
Ala42	-	-	-				

Table 5. 8 List of Hydrogen Bonding Interactions between Aβ42 and IDE (IDE^{WT} and IDE^{Y831A})

Aβ42 (residue)	atom	IDE (residue)	atom	Aβ42 (residue)	atom	IDE (residue)	atom
Asp1	OD2	Glu341	N	Asp1	N	Leu359	O
	OD1	Tyr609	OH		OD1	Tyr609	OH
	N	Leu359	O	Ala2	-	-	-
Ala2	-	-	-	Glu3	-	-	-
Glu3	-	-	-	Phe4	O	Leu613	N
Phe4	-	-	-	Arg5	NH1	Asn605	OD1
Arg5	N	Tyr609	OH	His6	-	-	-
	NH2	Glu612	OE1	Asp7	OD1	Gln363	N
	NH2	Tyr618	OH	Ser8	OG	Lys364	NZ
	NH1	Asn605	OD1	Gly9	O	Lys436	NZ
His6	-	-	-	Tyr10	-	-	-
Asp7	-	-	-	Glu11	-	-	-
Ser8	OG	Lys436	NZ	Val12	-	-	-
Gly9	-	-	-	His13	O	Ser143	OG
Tyr10	-	-	-	His14	-	-	-
Glu11	-	-	-	Gln15	-	-	-
Val12	-	-	-	Lys16	-	-	-
His13	-	-	-	Leu17	-	-	-
His14	-	-	-	Val18	-	-	-
Gln15	OE1	Trp199	NE1	Phe19	-	-	-
Lys16	-	-	-	Phe20	N	Ala140	O
Leu17	O	Asn193	ND2		O	Ala140	N
Val18	-	-	-	Ala21	-	-	-
Phe19	O	Tyr831	OH	Glu22	OE2	Tyr150	OH
Phe20	N	Ala140	O		O	Arg824	NH1
	O	Ala140	N	Asp23	-	-	-
Ala21	N	Asn139	OD1	Val24	-	-	-
Glu22	-	-	-	Gly25	-	-	-
Asp23	OD1	Ser835	OG	Ser26	OG	Arg431	NH1
	OD1	Ser835	N	Asn27	-	-	-
Val24	-	-	-	Lys28	-	-	-
Gly25	-	-	-	Gly29	O	Arg429	NE
Ser26	-	-	-	Ala30	-	-	-
Asn27	-	-	-	Ile31	-	-	-
Lys28	-	-	-	Ile32	-	-	-
Gly29	-	-	-	Gly33	-	-	-
Ala30	-	-	-	Leu34	-	-	-
Ile31	-	-	-	Met35	O	Asn139	ND2
Ile32	-	-	-	Val36	N	Ser137	OG
Gly33	-	-	-		O	Arg892	NH1
Leu34	O	Asn139	ND2	Gly37	O	Gln813	NE2
Met35	SD	Arg824	NH2	Gly38	-	-	-
	O	Asn139	ND2	Val39	-	-	-
Val36	-	-	-	Val40	-	-	-
Gly37	O	Ser138	N	Ile41	-	-	-
Gly38	O	Gln813	NE2	Ala42	O1	Arg839	N
Val39	-	-	-				
Val40	N	Gln813	OE1				
Ile41	O	Arg839	NH1				
Ala42	-	-	-				

5.4 Summary

In this study, the interactions of two full-length Alzheimer amyloid β peptides (Aβ40 and Aβ42) with two IDE mutants (IDE^{R824A} and IDE^{Y831A}) through unrestrained, all-atom MD simulations in aqueous solution have been investigated. The structures of wild-type IDE bound with Aβ40/Aβ42 obtained from our previous 20ns MD simulations. The starting structures of the mutants (IDE^{R824A}-Aβ40, IDE^{Y831A}-Aβ40, IDE^{R824A}-Aβ42 and IDE^{Y831A}-Aβ42) were constructed from IDE^{WT}-Aβ40 and IDE^{WT}-Aβ42. The most representative structures derived from the MD simulations reproduced the spatial occupancies of the active site Zn^{2+} metal with His108, His112, and Glu189 residues. The carbonyl oxygen (C=O) of Phe19 in the Phe19-Phe20 cleavage site of the Aβ40 and Aβ42 substrates still coordinated to the Zn^{2+} ion, but the Zn^{2+}-O distance increased during the simulations. Moreover, the results showed the intramolecular interactions of Aβ peptides derived from IDE^{R824A}-Aβ40, IDE^{Y831A}-Aβ40, IDE^{R824A}-Aβ42 and IDE^{Y831A}-Aβ42 could be observed from the contact maps. Hence, both Aβ40 and Aβ42 substrates lost their α-helix or β-sheet structures. In WT IDE, the substrates adopted β-sheet conformations that facilitated their degradation by the enzyme. Therefore, the loss of α-helix or β-sheet structures in Aβ40 and Aβ42 might be responsible for the decrease in catalytic rate. On the other hand, the secondary structures around the mutated residues (R824A and Y831A) in IDE domain 4 also change. In comparison to the numbers of hydrogen bonds formed in IDE^{WT}-Aβ40 and IDE^{WT}-Aβ42, all mutants IDE^{R824A}-Aβ40, IDE^{Y831A}-Aβ40, IDE^{R824A}-Aβ42 and IDE^{Y831A}-Aβ42 were found to form fewer hydrogen bonds between the substrates and IDE mutants. In particular, the Phe19-Phe20 cleavage site and C-terminal of Aβ40 and Aβ42 interacted with IDE mutants via a small numbers

of hydrogen bonds. Hence, the Aβ peptides were observed to be more flexible. The aforementioned results reported in this study provided atomistic level details of conformational and interactional changes of full-length Aβ40 and Aβ42 inside the catalytic chamber of IDE mutants (IDE^{R824A} and IDE^{Y831A}) and will help to elucidate the factors that decrease the catalytic rate of these critical peptides by IDE.

References

(1) *Proteolytic Enzymes*; 2nd ed.; Beynon, R.; Bond, J. S., Eds.; Oxford University Press: New York, 2001.

(2) Thomas, J. J.; Bakhtiar, R.; Siuzdak, G. *Acc. Chem. Res.* **2000**, *33*, 179.

(3) Grant, K. B.; Kassai, M. *Current Organic Chemistry* **2006**, *10*, 1035.

(4) Radzicka, A.; Wolfenden, R. *J. Am. Chem. Soc.* **1996**, *118*, 6105.

(5) Sigel, H.; Martin, R. B. *Chem. Rev.* **1982**, *82*, 385.

(6) Wilcox, D. E. *Chemical Reviews* **1996**, *96*, 2435.

(7) Fersht., A. *Enzyme structure and mechanism (second edition), by Alan Fersht. W H Freeman, New York. 1985.* **1985**.

(8) Jencks., W. P. *Catalysis in Chemistry and Enzymology. William P. Jencks. McGraw-Hill, New York, 1969.* **1969**.

(9) Walsh., C. *Enzymatic reaction mechanisms: By C Walsh. WH Freeman & Co, Oxford. 1979.* **1979**.

(10) Milović, N. M., and Kostić, N. M. *J. Am. Chem. Soc.* **2003**, *125*, 781.

(11) Walker, J. M. *The proteins protocols handbook*; Humana Press: Totowa, NJ, 2002.

(12) Milović, N. M.; Kostić, N. M. *Inorg. Chem.* **2002**, *41*, 7053.

(13) *Handbook of protein sequence analysis*; Croft, L. R., Ed.; Wiley Chichester, 1980.

(14) Milović, N. M., Kostić, N. M. *Inorg. Chem.* **2002.**, *41*, 7053.

(15) Kirby, A. J. Effective Molarities for Intramolecular Reactions. In *Advances in Physical Organic Chemistry*; Gold, V., Bethell, D., Eds.; Academic Press, 1981; Vol. Volume 17; pp 183.

(16) Suh, J.; Hah, S. S. *Journal of the American Chemical Society* **1998**, *120*, 10088.

(17) Sutton, P. A.; Buckingham, D. A. *Acc. Chem. Res.* **1987**, *20*, 357.

(18) Suh, J.; Park, T. H.; Hwang, B. K. *Journal of the American Chemical Society* **1992**, *114*, 5141.

(19) Suh, J. *Acc. Chem. Res.* **1992**, *25*, 273.

(20) Rana, T. M., and Meares, C. F. *J. Am. Chem. Soc.* **1990**, *112*, 2457.

(21) Kassai, M.; Ravi, R. G.; Shealy, S. J.; Grant, K. B. *Inorg. Chem.* **2004**, *43*, 6130.

(22) Manka, S.; Becker, F.; Hohage, O.; Sheldrick, W. S. *J. Inorg. Biochem.* **2004**, *98*, 1947.

(23) Rivas, J. C. M., Salvagni, E., Prabaharan, R., Rosales, R. T. M., and Parsons, S. *Dalton Trans.* **2004**, 172.

(24) Murthy, N. N., Mahroof-Tahir, M., and Karlin, K. D. *J. Am. Chem. Soc.* **1993**, *115*, 10404.

(25) Krężel, A.; Kopera, E.; Protas, A. M.; Poznański, J.; Wysłouch-Cieszyńska, A.; Bal, W. *J. Am. Chem. Soc.* **2010**, *132*, 3355.

(26) Grant, K., and Kassai, M. *Curr. Org. Chem.* **2006**, *10*, 1035.

(27) Szajna-Fuller, E.; Ingle, G. K.; Watkins, R. W.; Arif, A. M.; Berreau, L. M. *Inorg. Chem.* **2007**, *46*, 2353.

(28) Lowther, W. T.; Matthews, B. W. *Chem. Rev.* **2002**, *102*, 4581.

(29) Suh, J. *Accounts of Chemical Research* **1992**, *25*, 273.

(30) Marcinkeviciene, J.; Luo, Y.; Graciani, N. R.; Combs, A. P.; Copeland, R. A. *J. Biol. Chem.* **2001**, *276*, 23790.

(31) Liu, C.; Sawaya, M. R.; Eisenberg, D. *Nat Struct Mol Biol* **2011**, *18*, 49.

(32) Yip, C. C.; Ottensmeyer, P. *J.Biol. Chem.* **2003**, *278*, 27329.

(33) Zako, T.; Sakono, M.; Hashimoto, N.; Ihara, M.; Maeda, M. *Biophys. J.* **2009**, *96*, 3331.

(34) Pillot, T.; Drouet, B.; Queillé, S.; Labeur, C.; Vandekerckhove, J.; Rosseneu, M.; Pinçon-Raymond, M.; Chambaz, J. *J. Neurochem.* **1999**, *73*, 1626.

(35) Suo, Z.; Humphrey, J.; Kundtz, A.; Sethi, F.; Placzek, A.; Crawford, F.; Mullan, M. *Neurosci. Lett.* **1998**, *257*, 77.

(36) Yan, R., Bienkowski, M. E., Shuck, M. E., Miao, H., Tory, M. C., Pauley, A. M., Brashler, J. R., Stratman, N. C., Mathews, W. R., Buhl, A. E., Carter, D. B., Tomasselli, A. G., Parodi, L. A., Heinrikson, R. L., and Gurney, M. E. *Nature* **1999**, *402*, 533.

(37) Haass, C., Schlossmacher, M., and Hung, A. Y. *Nature* **1992**, *359*, 322.

(38) Haass, C., Hung, A. Y., Schlossmacher, M. G., Teplow, D. B., and Selkoe D. J. *J. Biol. Chem.* **1993**, *268*, 3021.

(39) Seubert, P., Vigo-Pelfrey C., and Esch, F. *Nature* **1992**, *359*, 325.

(40) Shoji, M., Golde, T. E., and Ghiso, J. *Science* **1992**, *258*, 126.

(41) Weidemann, A., Eggert, S., Reinhard, F., Vogel, M., Paliga, K., Baier, G., Masters, C. L., Beyreuther, K., and Evin, G. *Biochemistry* **2002**, *41*, 2825.

(42) Bentahir, M., Nyabi, O., Verhamme, J., Tolia, A., Horre, K., Wiltfang, J., Esselmann, H. and De Strooper, B. . *J. Neurochem* **2006**, *96*, 732.

(43) Corder, E.; Saunders, A.; Strittmatter, W.; Schmechel, D.; Gaskell, P.; Small, G.; Roses, A.; Haines, J.; Pericak-Vance, M. *Science* **1993**, *261*, 921.

(44) Hsia, A. Y.; Masliah, E.; McConlogue, L.; Yu, G.-Q.; Tatsuno, G.; Hu, K.; Kholodenko, D.; Malenka, R. C.; Nicoll, R. A.; Mucke, L. *Proc. Natl. Acad. Sci. USA* **1999**, *96*, 3228.

(45) Levy, E., Carman, M. D., Fernandez-Madrid, I. J., Power, M. D., Lieberburg, I., van, Duinen, S. G., Bots, G. T. A. M., Luyendijk, W. and Frangione, B. . *Science* **1990**, *248*, 1124.

(46) Pike, C. J., Walencewicz, A. J., Glabe, C. G. and Cotman, C. W. *Brain. Res.* **1991**, *563*, 311.

(47) Rovelet-Lecrux, A., Hannequin, D., Raux, G. . *Nat. Genet.* **2006**, *38*, 24.

(48) Walsh, D. M., Lomakin, A., Benedek, G. B., Maggio, J. E., Condron, M. M. and Teplow, D. B. *J. Biol. Chem* **1997**, *272*, 22364.

(49) Huang, Y.; Mucke, L. *Cell* **2012**, *148*, 1204.

(50) Nalivaeva, N. N.; Beckett, C.; Belyaev, N. D.; Turner, A. J. *J. Neurochem.* **2012**, *120*, 167.

(51) Landau, L. D.; Lifshit□s□, E. M. *Quantum mechanics : non-relativistic theory*, 3d ed.; Pergamon Press: Oxford ; New York, 1977.

(52) Zhang, T. T.; Zhu, X. X.; Prabhakar, R. *Organometallics* **2014**, *33*, 1925.

(53) Zhang, T. T.; Zhu, X. X.; Prabhakar, R. *J. Phys. Chem. B* **2014**, *118*, 4106.

(54) Born, M., and Oppenheimer, R. . *Ann. der Physik* **1927**, *389*, 457.

(55) MacDonald, J. K. L. *Phys. Rev.* **1933**, *43*, 830.

(56) Hall, G. G. *Proc. R. Soc. Lond. A* **1951**, *205*, 541.

(57) Ditchfield, R., Hehre, W.J., and Pople, J.A. . *J. Chem. Phys.* **1971**, *54*, 724.

(58) Hohenberg, P., and Kohn, W. . *Phys. Rev.* **1964**, *136*, B864.

(59) Kohn, W. a. S., L.J. . *Phys. Rev.* **1965**, *140*, A1133.

(60) Jensen, F. *Computational Chemistry*; Wiley: Chichister, 1999.

(61) Becke, A. D. *Phys. Rev. A* **1988**, *38*, 3098.

(62) Becke, A. D. *J. Chem. Phys.* **1993**, *98*, 5648.

(63) Lee, C., Yang, W., and Parr, R. G. *Phys. Rev. B* **1988**, *37*, 785.

(64) Curtiss, L. A., Redfern, P.C., Raghavachari, K., Pople, J.A. *J. Chem. Phys.* **1998**, *109*, 7764.

(65) Bauschlicher, C. W. *Chemical Physics Letters* **1995**, *246*, 40.

(66) Curtiss, L. A., Raghavachari, K., Trucks, G.W., Pople, J.A. *J. Chem. Phys.* **1991**, *94*, 7221.

(67) Blomberg, M. R. A.; Siegbahn, P. E. M.; Svensson, M. *J. Chem. Phys.* **1996**, *104*, 9546.

(68) Ricca, A.; Bauschlicher, C. W. *J. Phys. Chem. A.* **1997**, *101*, 8949.

(69) Siegbahn, P. E. M. *J. Comput. Chem.* **2001**, *22*, 1634.

(70) Cossi, M. a. B., V. . Solvent effect on vertical electronic transitions by the polarizable continuum model. In *J. Chem. Phys.* , 2000; Vol. 112; pp 2427.

(71) Dapprich, S.; Komáromi, I.; Byun, K. S.; Morokuma, K.; Frisch, M. J. *J. Mol. Struc.: THEOCHEM* **1999**, *461–462*, 1.

(72) Humbel, S.; Sieber, S.; Morokuma, K. *J. Chem. Phys.* **1996**, *105*, 1959.

(73) Maseras, F., and Morokuma, K. *J. Comp. Chem.* **1995**, *16*, 1170.

(74) Matsubara, T.; Sieber, S.; Morokuma, K. *Int. J. Quantum Chem.* **1996**, *60*, 1101.

(75) Svensson, M.; Humbel, S.; Froese, R. D. J.; Matsubara, T.; Sieber, S.; Morokuma, K. *J. Phys. Chem.* **1996**, *100*, 19357.

(76) Svensson, M.; Humbel, S.; Morokuma, K. *J. Chem. Phys.* **1996**, *105*, 3654.

(77) Vreven, T.; Morokuma, K. *J. Comput. Chem.* **2000**, *21*, 1419.

(78) Frisch, M. J. e. a. Gaussian 09, Revision D.01, M.; Gaussian Inc.: Wallingford, CT, 2009; Vol. Revision A.1 ed.

(79) Frisch, M. J.; Trucks, G. W.; Schlegel, H. B.; Scuseria, G. E.; Robb, M. A.; Cheeseman, J. R.; Montgomery, J., J. A. ; Vreven, T.; Kudin, K. N.; Burant, J. C.; Millam, J. M.; Iyengar, S. S.; Tomasi, J.; Barone, V.; Mennucci, B.; Cossi, M.; Scalmani, G.; Rega, N.; Petersson, G. A.; Nakatsuji, H.; Hada, M.; Ehara, M.; Toyota, K.; Fukuda, R.; Hasegawa, J.; Ishida, M.; Nakajima, T.; Honda, Y.; Kitao, O.; Nakai, H.; Klene, M.; Li, X.; Knox, J. E.; Hratchian, H. P.; Cross, J. B.; Bakken, V.; Adamo, C.; Jaramillo, J.; Gomperts, R.; Stratmann, R. E.; Yazyev, O.; Austin, A. J.; Cammi, R.; Pomelli, C.; Ochterski, J. W.; Ayala, P. Y.; Morokuma, K.; Voth, G. A.; Salvador, P.; Dannenberg, J. J.; Zakrzewski, V. G.; Dapprich, S.; Daniels, A. D.; Strain, M. C.; Farkas, O.; Malick, D. K.; Rabuck, A. D.; Raghavachari, K.; Foresman, J. B.; Ortiz, J. V.; Cui, Q.; Baboul, A. G.; Clifford, S.; Cioslowski, J.; Stefanov, B. B.; Liu, G.; Liashenko, A.; Piskorz, P.; Komaromi, I.; Martin, R. L.; Fox, D. J.; Keith, T.; Al-Laham, M. A.; Peng, C. Y.; Nanayakkara, A.; Challacombe, M.; Gill, P. M. W.; Johnson, B.; Chen, W.; Wong, M. W.; Gonzalez, C.; Pople, J. A. Gaussian 03 C.02 ed.; Gaussian, Inc.: Wallingford CT, 2004.

(80) Hay, P. J., and Wadt, W. R. *J. Chem. Phys.* **1985**, *82*, 270.

(81) Ponder, J. W. a. C., D. A. *Force Fields for Protein Simulations*; Academic Press, 2003; Vol. 66.

(82) Berendsen, H. J. C.; Postma, J. P. M.; van Gunsteren, W. F.; Hermans, J. *Interation Models for Water in Relation to Protein Hydration*; D, Reider Publishing Company, Dordrecht, 1981.

(83) Darden, T. A.; York, D.; Pedersen, L. *J. Chem. Phys.* **1993**, *98*, 10089.

(84) York, D. M.; Wlodawer, A.; Pedersen, L. G.; Darden, T. A. *Proc. Natl. Acad. Sci. USA* **1994**, *91*, 8715.

(85) Lindahl, E.; Hess, B.; van der Spoel, D. *J. Mol. Model.* **2001**, *7*, 306.

(86) Oosteinbrink, C., Villa, A. , Mark, A. E. and van Gunsteren, W. F. *J. Comput. Chem.* **2004**, *25*, 1656.

(87) Miyamoto, S.; Kollman, P. A. *J. Comput. Chem.* **1992**, *13*, 952.

(88) Hess, B.; Bekker, H.; Berendsen, H. J. C.; Fraaije, J. G. E. M. *J. Comput. Chem.* **1997**, *18*, 1463.

(89) Dismukes, G. C. *Chem. Rev.* **1996**, *96*, 2909.

(90) Holm, R. H.; Kennepohl, P.; Solomon, E. I. *Chem. Rev.* **1996**, *96*, 2239.

(91) Lipscomb, W. N.; Sträter, N. *Chem. Rev.* **1996**, *96*, 2375.

(92) Nigel M, H. *FEBS Lett.* **1994**, *354*, 1.

(93) Sträter, N.; Lipscomb, W. N.; Klabunde, T.; Krebs, B. *Angew. Chem. Int. Ed. Engl.* **1996**, *35*, 2024.

(94) Vallee, B. L.; Auld, D. S. *Biochemistry* **1990**, *29*, 5647.

(95) Vallee, B. L.; Auld, D. S. *Proc. Natl. Acad. Sci. USA* **1993**, *90*, 2715.

(96) Vallee, B. L.; Auld, D. S. *Biochemistry* **1993**, *32*, 6493.

(97) Weston, J. *Chem. Rev.* **2005**, *105*, 2151.

(98) Wilcox, D. E. *Chem. Rev.* **1996**, *96*, 2435.

(99) Hegg, E. L.; Burstyn, J. N. *Coord. Chem. Rev.* **1998**, *173*, 133.

(100) Bruice, T. C. *Chem. Rev.* **2006**, *106*, 3119.

(101) Christianson, D. W. *Adv. Protein Chem.* **1991**, *42*, 281.

(102) Coleman, J. E. *Annu. Rev. Biochem.* **1992**, *61*, 897.

(103) Auld, D. S. *Methods Enzymol.* **1995**, *248*, 228.

(104) Jang, S. W.; Suh, J. *Organic Letters* **2008**, *10*, 481.

(105) Kim, H.; Jang, B.; Cheon, Y.; Suh, M.; Suh, J. *Journal of Biological Inorganic Chemistry* **2009**, *14*, 151.

(106) Suh, J.; Yoo, S. H.; Kim, M. G.; Jeong, K.; Ahn, J. Y.; Kim, M.-s.; Chae, P. S.; Lee, T. Y.; Lee, J.; Lee, J.; Jang, Y. A.; Ko, E. H. *Angew. Chem., Int. Ed.* **2007**, *46*, 7064.

(107) Kim, M.-s.; Jeon, J.; Suh, J. *JBIC Journal of Biological Inorganic Chemistry* **2005**, *10*, 364.

(108) Chei, W.; Ju, H.; Suh, J. *JBIC Journal of Biological Inorganic Chemistry* **2011**, *16*, 511.

(109) Kim, M.; Yoo, S.; Chei, W.; Lee, T.; Kim, H.; Suh, J. *JBIC Journal of Biological Inorganic Chemistry* **2010**, *15*, 1023.

(110) Suh, J.; Chei, W.; Lee, T.; Kim, M.; Yoo, S.; Jeong, K.; Ahn, J. *JBIC Journal of Biological Inorganic Chemistry* **2008**, *13*, 693.

(111) Jeon, J. W.; Son, S. J.; Yoo, C. E.; Hong, I. S.; Suh, J. *Bioorganic & Medicinal Chemistry* **2003**, *11*, 2901.

(112) Jang, B.; Suh, J. *Bull. Korean Chem. Soc.* **2008**, *29*, 202.

(113) Chae, P. S.; Kim, M.-s.; Jeung, C.-S.; Lee, S. D.; Park, H.; Lee, S.; Suh, J. *Journal of the American Chemical Society* **2005**, *127*, 2396.

(114) Kassai, M.; Grant, K. B. *Inorg. Chem. Commun.* **2008**, *11*, 521.

(115) Bellia, F.; La Mendola, D.; Pedone, C.; Rizzarelli, E.; Saviano, M.; Vecchio, G. *Chem. Soc. Rev.* **2009**, *38*, 2756.

(116) Breslow, R. Artificial Enzymes. In *Artificial Enzymes*; Wiley-VCH Verlag GmbH & Co. KGaA, 2006; pp 1.

(117) Breslow, R.; Overman, L. E. *J. Am. Chem. Soc.* **1970**, *92*, 1075.

(118) Ingle, G. K.; Makowska-Grzyska, M. M.; Szajna-Fuller, E.; Sen, I.; Price, J. C.; Arif, A. M.; Berreau, L. M. *Inorg Chem* **2007**, *46*, 1471.

(119) Elton, E. S.; Zhang, T.; Prabhakar, R.; Arif, A. M.; Berreau, L. M. *Inorganic Chemistry* **2013**, *52*, 11480.

(120) Milovic, N. M.; Kostic, N. M. *Journal of the American Chemical Society* **2003**, *125*, 781.

(121) Hardy, J., and Selkoe, D. J. *Science* **2002**, *297*, 353.

(122) Hamley, I. W. *Chemical Reviews* **2012**.

(123) Kim, J. H.; Britten, J.; Chin, J. *Journal of the American Chemical Society* **1993**, *115*, 3618.

(124) Chin, J., and Zou, X. *J. Am. Chem. Soc.* **1984**, *106*, 3687.

(125) Christianson, D., W.; Lipscomb, W., N. *Acc. Chem. Res.* **1989**, *22*, 62.

(126) Kim, M. G.; Kim, H. M.; Suh, J. *Bull. Korean Chem. Soc.* **2011**, *32*, 3113.

(127) Hay, P. J.; Wadt, W. R. *Journal of Chemical Physics* **1985**, *82*, 270.

(128) Becke, A. D. *Physical Review A* **1988**, *38*, 3098.

(129) Blomberg, M. R. A.; Siegbahn, P. E. M.; Babcock, G. T. *Journal of the American Chemical Society* **1998**, *120*, 8812.

(130) Cances, E.; Mennucci, B.; Tomasi, J. *Journal of Chemical Physics* **1997**, *107*, 3032.

(131) Chin, J. *Acc. Chem. Res.* **1991**, *24*, 145.

(132) Zhao, Y.; Truhlar, D. G. *J. Chem. Phys.* **2006**, *125*, 194101.

(133) Castillo-Blum, S. E.; Sosa-Torres, M. E. *Polyhedron* **1995**, *14*, 223.

(134) Hay, R. W.; Norman, P. R. *Transition Metal Chemistry (London)* **1997**, *22*, 248.

(135) Sosa, M. E.; Tobe, M. L. *J. Chem. Soc. Dalton Trans.* **1985**, 475.

(136) Iitaka, Y.; Shina, M.; Kimura, E. *Inorganic Chemistry* **1974**, *13*, 2886.

(137) Clarkson, A. J.; Buckingham, D. A.; Rogers, A. J.; Blackman, A. G.; Clark, C. R. *Inorganic Chemistry* **2000**, *39*, 4769.

(138) Styka, M. C.; Smierciak, R. C.; Blinn, E. L.; DeSimone, R. E.; Passariello, J. V. *Inorganic Chemistry* **1978**, *17*, 82.

(139) Kumar, A., Zhu, X., Walsh, K., and Prabhakar, R. *Inorg. Chem.* **2010**, *49*, 38.

(140) Amorim, M. T. S.; Chaves, S.; Delgado, R.; da Silva, J. J. R. F. *Dalton Trans.* **1991**, 3065.

(141) Wilkinson, G.; Gillard, R. D.; McCleverty, J. A. *Comprehensive coordination chemistry : the synthesis, reactions, properties & applications of coordination compounds*, 1st ed.; Pergamon Press: Oxford, England ; New York, 1987.

(142) Ghosh, S.; Sharma, A.; Talukder, G. *Biological Trace Element Research* **1992**, *35*, 247.

(143) Singhal, A.; Toth, L. M.; Lin, J. S.; Affholter, K. *Journal of the American Chemical Society* **1996**, *118*, 11529.

(144) Takarada, T.; Yashiro, M.; Komiyama, M. *Chemistry* **2000**, *6*, 3906.

(145) Kassai, M.; Ravi, G.; Grant, K. "4,13-Diaza-18-crown-6-substantially accelerates zirconium(IV)-assisted hydrolysis of unactivated peptide amide bonds at neutral pH", 2003.

(146) Kassai, M.; Ravi, R. G.; Shealy, S. J.; Grant, K. B. *Inorganic Chemistry* **2004**, *43*, 6130.

(147) Sigel, H.; Martin, R. B. *Chemical Reviews* **1982**, *82*, 385.

(148) Burgess, J. *Metal ions in solution*; Ellis Horwood ; distributed by Halsted Press: Chichester, New York, 1978.

(149) Becke, A. D. *Phys. Rev. A* **1988**, *38*, 3098.

(150) Becke, A. D. *J. Chem. Phys.* **1993**, *98*, 5648.

(151) Hay, P. J.; Wadt, W. R. *J. Chem. Phys.* **1985**, *82*, 270.

(152) Cances, E.; Mennucci, B.; Tomasi, J. *J. Chem. Phys.* **1997**, *107*, 3032.

(153) Lee, L.; Berg, D. J.; Bushnell, G. W. *Organometallics* **1997**, *16*, 2556.

(154) Dantz, D. A.; Buschmann, H. J.; Schollmeyer, E. *Thermochimica Acta* **1997**, *294*, 133.

(155) Chin, J.; Kim, H.-J. Artificial Hydrolytic Metalloenzymes. In *Artificial Enzymes*; Wiley-VCH Verlag GmbH & Co. KGaA, 2006; pp 133.

(156) Kaminskaia, N. V.; Johnson, T. W.; Kostic, N. M. *Journal of the American Chemical Society* **1999**, *121*, 8663.

(157) Kaminskaia, N. V.; Kostic, N. M. *Inorganic Chemistry* **2001**, *40*, 2368.

(158) Milovic, N. M.; Kostic, N. M. *Metal Ions in Biological Systems* **2001**, *38*, 145.

(159) Parac, T. N.; Kostic, N. M. *Journal of the American Chemical Society* **1996**, *118*, 5946.

(160) Parac, T. N.; Kostic, N. M. *Journal of the American Chemical Society* **1996**, *118*, 51.

(161) Zhu, L. G.; Kostic, N. M. *Inorganic Chemistry* **1992**, *31*, 3994.

(162) Milovic, N. M.; Kostic, N. M. *Journal of the American Chemical Society* **2002**, *124*, 4759.

(163) Chen, W.; Chang, C.-E.; Gilson, M. K. *Biophys. J.* **2004**, *87*, 3035.

(164) Zhang, B.; Breslow, R. *J. Am. Chem. Soc.* **1997**, *119*, 1676.

(165) Milović, N. M.; Badjić, J. D.; Kostić, N. M. *J. Am. Chem. Soc.* **2004**, *126*, 696.

(166) Bora, R. P.; Barman, A.; Zhu, X.; Ozbil, M.; Prabhakar, R. *J. Phys. Chem. B* **2010**, *114*, 10860.

(167) Kumar, A.; Zhu, X.; Walsh, K.; Prabhakar, R. *Inorg. Chem.* **2010**, *49*, 38.

(168) Frisch, M. J.; Trucks, G. W.; Schlegel, H. B.; Scuseria, G. E.; Robb, M. A.; Cheeseman, J. R.; Scalmani, G.; Barone, V.; Mennucci, B.; Petersson, G. A.; Nakatsuji, H.; Caricato, M.; Li, X.; Hratchian, H. P.; Izmaylov, A. F.; Bloino, J.; Zheng, G.; Sonnenberg, J. L.; Hada, M.; Ehara, M.; Toyota, K.; Fukuda, R.; Hasegawa, J.; Ishida, M.; Nakajima, T.; Honda, Y.; Kitao, O.; Nakai, H.; Vreven, T.; Montgomery, J., J. A.; ; Peralta, J. E.; Ogliaro, F.; Bearpark, M.; Heyd, J. J.; Brothers, E.; Kudin, K. N.; Staroverov, V. N.; Kobayashi, R.; Normand, J.; Raghavachari, K.; Rendell, A.; Burant, J. C.; Iyengar, S. S.; Tomasi, J.; Cossi, M.; Rega, N.; Millam, N. J.; Klene, M.; Knox, J. E.; Cross, J. B.; Bakken, V.; Adamo, C.; Jaramillo, J.; Gomperts, R.; Stratmann, R. E.; Yazyev, O.; Austin, A. J.; Cammi, R.; Pomelli, C.; Ochterski, J. W.; Martin, R. L.; Morokuma, K.; Zakrzewski, V. G.; Voth, G. A.; Salvador, P.; Dannenberg, J. J.;

Dapprich, S.; Daniels, A. D.; Farkas, Ö.; Foresman, J. B.; Ortiz, J. V.; Cioslowski, J.; Fox, D. J. Gaussian 09 (Revision A.1); Gaussian, Inc.: Wallingford CT, 2009.

(169) Vreven, T.; Morokuma, K.; Farkas, Ö.; Schlegel, H. B.; Frisch, M. J. *J. Comp. Chem.* **2003**, *24*, 760.

(170) Adamo, C.; Barone, V. *Journal of Chemical Physics* **1998**, *108*, 664.

(171) Zhao, Y.; Truhlar, D. G. *Journal of Chemical Physics* **2006**, *125*, 194101.

(172) Lindner, K.; Saenger, W. *Carbohydr. Res.* **1982**, *99*, 103.

(173) Martin, R. B. *Metal Ions in Biological Systems* **2001**, *38*, 1.

(174) "Center for Disease Control and Prevention, Morbidity and Mortality Weekly Report," 2005.

(175) Aoki, S.; Kimura, E. In *Comprehensive Coordination Chemistry II*; Pergamon: Oxford, 2004; pp 601.

(176) Bridgewater, B. M.; Parkin, G. *J. Am. Chem. Soc.* **2000**, *122*, 7140.

(177) Magyar, J. S.; Weng, T.-C.; Stern, C. M.; Dye, D. F.; Rous, B. W.; Payne, J. C.; Bridgewater, B. M.; Mijovilovich, A.; Parkin, G.; Zaleski, J. M.; Penner-Hahn, J. M.; Godwin, H. A. *J. Am. Chem. Soc.* **2005**, *127*, 9495.

(178) Andersen, R. J.; diTargiani, R. C.; Hancock, R. D.; Stern, C. L.; Goldberg, D. P.; Godwin, H. A. *Inorg Chem* **2006**, *45*, 6574.

(179) Farrer, B. T.; Pecoraro, V. L. *Curr Opin Drug Discov Devel* **2002**, *5*, 937.

(180) Matzapetakis, M.; Ghosh, D.; Weng, T. C.; Penner-Hahn, J. E.; Pecoraro, V. L. *J Biol Inorg Chem* **2006**, *11*, 876.

(181) Neupane, K. P.; Pecoraro, V. L. *Angew. Chem. Int. Ed. Engl.* **2010**, *49*, 8177.

(182) Neupane, K. P.; Pecoraro, V. L. *J. Inorg. Biochem.* **2011**, *105*, 1030.

(183) Chakraborty, S.; Kravitz, J. Y.; Thulstrup, P. W.; Hemminsen, L.; DeGrado, W. F.; Pecoraro, V. L. *Angew. Chem. Int. Ed. Engl.* **2011**, *50*, 2049.

(184) Zampella, G.; Neupane, K. P.; De Gioia, L.; Pecoraro, V. L. *Chemistry* **2012**, *18*, 2040.

(185) Zitka, O.; Kukacka, J.; Krizkova, S.; Huska, D.; Adam, V.; Masarik, M.; Prusa, R.; Kizek, R. *Curr Med Chem* **2010**, *17*, 3751.

(186) Gantt, S. L.; Gattis, S. G.; Fierke, C. A. *Biochemistry* **2006**, *45*, 6170.

(187) Dowling, D. P.; Gattis, S. G.; Fierke, C. A.; Christianson, D. W. *Biochemistry* **2010**, *49*, 5048.

(188) Kita, Y.; Nishii, Y.; Higuchi, T.; Mashima, K. *Angew. Chem. Int. Ed. Engl.* **2012**, *51*, 5723.

(189) Yashiro, M.; Kawakami, Y.; Taya, J.; Arai, S.; Fujii, Y. *Chem Commun (Camb)* **2009**, 1544.

(190) Yashiro, M.; Sonobe, Y.; Yamamura, A.; Takarada, T.; Komiyama, M.; Fujii, Y. *Org Biomol Chem* **2003**, *1*, 629.

(191) Groves, J. T.; Chambers, R. R. *J. Am. Chem. Soc.* **1984**, *106*, 630.

(192) Szajna, E.; Makowska-Grzyska, M. M.; Wasden, C. C.; Arif, A. M.; Berreau, L. M. *Inorg Chem* **2005**, *44*, 7595.

(193) Berreau, L. M. *Adv. Phys. Org. Chem.* **2006**, *41*, 79.

(194) Battistuzzi, G.; Borsari, M.; Menabue, L.; Saladini, M.; Sola, M. *Inorg. Chem.* **1996**, *35*, 4239.

(195) Claudio, E. S.; ter Horst, M. A.; Forde, C. E.; Stern, C. L.; Zart, M. K.; Godwin, H. A. *Inorg. Chem.* **2000**, *39*, 1391.

(196) Clapp, L. A.; Siddons, C. J.; Whitehead, J. R.; VanDerveer, D. G.; Rogers, R. D.; Griffin, S. T.; Jones, S. B.; Hancock, R. D. *Inorg Chem* **2005**, *44*, 8495.

(197) Claudio, E. S.; Godwin, H. A.; Magyar, J. S. *Prog. Inorg. Chem.* **2003**, *51*, 1.

(198) Frisch, M. J., et al. . Gaussian Inc.; Gaussian 03 C.02 ed. Wallingford CT, 2004.

(199) Raycroft, M. A.; Maxwell, C. I.; Oldham, R. A.; Andrea, A. S.; Neverov, A. A.; Brown, R. S. *Inorg Chem* **2012**, *51*, 10325.

(200) Sayre, L. M. *J. Am. Chem. Soc.* **1986**, *108*, 1632.

(201) Hegg, E. L.; Burstyn, J. N. *Coord. Chem. Rev.* **1998**, *173*, 133.

(202) Harrowfield, J. *Helv. Chim. Acta* **2005**, *88*, 2430.

(203) Matsui, M.; Fowler, J. H.; Walling, L. L. *Biol. Chem.* **2006**, *387*, 1535.

(204) Sträter, N.; Sherratt, D. J.; Colloms, S. D. *EMBO J* **1999**, *18*, 4513.

(205) Taylor, A. *FASEB J.* **1993**, *7*, 290.

(206) Walling, L. L. *Curr. Opin. Plant Biol.* **2006**, *9*, 227.

(207) York, I. A.; Goldberg, A. L.; Mo, X. Y.; Rock, K. L. *Immunol. Rev.* **1999**, *172*, 49.

(208) Sträter, N.; Lipscomb, W. N. *Biochemistry* **1995**, *34*, 14792.

(209) Sträter, N.; Sun, L.; Kantrowitz, E. R.; Lipscomb, W. N. *Proc. Natl. Acad. Sci. U. S. A.* **1999**, *96*, 11151.

(210) Burley, S. K.; David, P. R.; Taylor, A.; Lipscomb, W. N. *Proc. Natl. Acad. Sci. U. S. A.* **1990**, *87*, 6878.

(211) Carpenter, F. H.; Harrington, K. T. *J. Biol. Chem.* **1972**, *247*, 5580.

(212) Carpenter, F. H.; Vahl, J. M. *J. Biol. Chem.* **1973**, *248*, 294.

(213) Himmelhoch, S. R. *Arch. Biochem. Biophys.* **1969**, *134*, 597.

(214) Melbye, S. W.; Carpenter, F. H. *J. Biol. Chem.* **1971**, *246*, 2459.

(215) Allen, M. P.; Yamada, A. H.; Carpenter, F. H. *Biochemistry* **1983**, *22*, 3778.

(216) Hasselgren, C.; Park, H.; Ming, L.-J. *J. Biol. Inorg. Chem.* **2001**, *6*, 120.

(217) Thompson, G. A.; Carpenter, F. H. *J. Biol. Chem.* **1976**, *251*, 1618.

(218) Pulido-Cejudo, G.; Conway, B.; Proulx, P.; Brown, R.; Izaguirre, C. A. *Antiviral Research* **1997**, *36*, 167.

(219) Sharma, K. K.; Elser, N. J.; Kester, K. *Current Eye Research* **1996**, *15*, 774.

(220) Taylor, A.; Daims, M.; Lee, J.; Surgenor, T. *Current Eye Research* **1982**, *2*, 47.

(221) Mathe, G. *Biomedicine & Pharmacotherapy* **1991**, *45*, 49.

(222) Pretlow, T. G.; Nagabhushan, M.; Sy, M.; Guo, Y.; Pretlow, T. P. *Journal of Cellular Biochemistry Supplement* **1994**, *19*, 224.

(223) Umezawa, H. *Recent Results in Cancer Research* **1980**, *75*, 115.

(224) Buffone, G. J., Spence, J. E., Fernbach, S. D., Curry, M. R., O'Brien, W. E., and Beaudet, A. L. *Clin. Chem.* **1988**, *34*, 933.

(225) Cheggour, A.; Fanuel, L.; Duez, C.; Joris, B.; Bouillenne, F.; Devreese, B.; Van Driessche, G.; Van Beeumen, J.; Frere, J. M.; Goffin, C. *Mol. Microbiol.* **2000**, *38*, 504.

(226) Goffin, C.; Ghuysen, J. M. *Microbiol. Mol. Biol. Rev.* **1998**, *62*, 1079.

(227) Remaut, H.; Bompard-Gilles, C.; Goffin, C.; Frere, J. M.; Van Beeumen, J. *Nature Structural Biology* **2001**, *8*, 674.

(228) Adachi, H.; Katayama, T.; Inuzuka, C.; Oikawa, S.; Tsujimoto, M.; Nakazato, H. *J. Biol. Chem.* **1990**, *265*, 15341.

(229) Campbell, B. J.; Lin, Y. C.; Davis, R. V.; Ballew, E. *Biochim. Biophys. Acta* **1966**, *118*, 371.

(230) Kahan, F. M.; Kropp, H.; Sundelof, J. G.; Birnbaum, J. *J. Antimicrob. Chemother.* **1983**, *12 Suppl D*, 1.

(231) Kim, H. S.; Campbell, B. J. *Biochem. Biophys. Res. Commun.* **1982**, *108*, 1638.

(232) Kropp, H.; Sundelof, J. G.; Hajdu, R.; Kahan, F. M. *Antimicrob. Agents Chemother.* **1982**, *22*, 62.

(233) Nitanai, Y.; Satow, Y.; Adachi, H.; Tsujimoto, M. *Journal of Molecular Biology* **2002**, *321*, 177.

(234) Zhu, X.; Barman, A.; Ozbil, M.; Zhang, T.; Li, S.; Prabhakar, R. *J. Biol. Inorg. Chem.* **2012**, *17*, 209.

(235) Sakiyama, H.; Mochizuki, R.; Sugawara, A.; Sakamoto, M.; Nishida, Y.; Yamasaki, M. *Journal of the Chemical Society-Dalton Transactions* **1999**, 997.

(236) Sakiyama, H.; Igarashi, Y.; Nakayama, Y.; Hossain, M. J.; Unoura, K.; Nishida, Y. *Inorganica Chimica Acta* **2003**, *351*, 256.

(237) Becke, A. D. *J. Chem. Phys.* **1993**, *98*, 5648.

(238) Burley, S. K.; David, P. R.; Sweet, R. M.; Taylor, A.; Lipscomb, W. N. *J. Mol. Biol.* **1992**, *224*, 113.

(239) Kim, H.; Lipscomb, W. N. *Biochemistry* **1993**, *32*, 8465.

(240) Sträter, N.; Lipscomb, W. N. *Biochemistry* **1995**, *34*, 9200.

(241) Groves, J. T.; Olson, J. R. *Inorg. Chem.* **1985**, *24*, 2715.

(242) Prince, R. H.; Woolley, P. R. *Angew. Chem., Int. Ed.* **1972**, *11*, 408.

(243) Klein, W. L.; Krafft, G. A.; Finch, C. E. *Trends Neurosci.* **2001**, *24*, 219.

(244) Mattson, M. P. *Nature* **2004**, *430*, 631.

(245) Hardy, J. *Ann. Neurol.* **2003**, *54*, 143.

(246) Kirkitadze, M. D.; Bitan, G.; Teplow, D. B. *J. Neurosci. Res.* **2002**, *69*, 567.

(247) Klein, W. L. *Neurobiol. Aging.* **2002**, *23*, 231.

(248) Klein, W. L.; Stine Jr, W. B.; Teplow, D. B. *Neurobiol. Aging* **2004**, *25*, 569.

(249) Selkoe, D. J. *Nat. Cell. Biol.* **2004**, *6*, 1054.

(250) Hass C., H., A. Y., Schlossmacher, M.G., Teplow, D. B., and Selkoe D. J. . *J. Biol. Chem.* **1993**, *268*, 3021.

(251) Seubert, P.; Vigo-Pelfrey, C.; Esch, F.; Lee, M.; Dovey, H.; Davis, D.; Sinha, S.; Schlossmacher, M.; Whaley, J.; Swindlehurst, C. *Nature* **1992**, *359*, 325.

(252) *Amyloid Proteins. The Beta Sheet Conformation and Disease*; Sipe, J. D., Ed.; WILWY-VCK: USA, 2005; Vol. 2.

(253) Hardy, J. *Trends Neurosci.* **1997**, *20*, 154.

(254) Iwatsubo, T., Odaka, A., Suzuki, N., Mizusawa, H., Nukina, H., and Ihara, Y. *Neuron* **1994**, *13*, 45.

(255) Lamb, B. T. *Nature Med.* **1997**, *3*, 28.

(256) Roher, A. E., Lowenson, J. D., Clarke, S., Wolkow, C., Wang, R., Cotter, R. J., Reardon, I., Zurcher-Neely, H. A., Heinrikson, R. L., Ball, M. J., and Greenberg, B. D. *J. Biol. Chem.* **1993**, *268*, 3072.

(257) Selkoe, D. J. *Science* **1997**, *275*, 630

(258) Farris, W.; Mansourian, S.; Chang, Y.; Lindsley, L.; Eckman, E. A.; Frosch, M. P.; Eckman, C. B.; Tanzi, R. E.; Selkoe, D. J.; Guénette, S. *Proc. Natl. Acad. Sci. USA* **2003**, *100*, 4162.

(259) Kim, M., Hersh, L. B., Leissring, M. A., Ingelsson, M., Matsui, T., Farris, W., Lu, A., Hyman, B. T., Selkoe, D. J., Bertram, L., and Tanzi, R. E. *J. Biol. Chem.* **2007**, *282*, 7825.

(260) Leissring, M. A.; Farris, W.; Chang, A. Y.; Walsh, D. M.; Wu, X.; Sun, X.; Frosch, M. P.; Selkoe, D. J. *Neuron* **2003**, *40*, 1087.

(261) Miller, B. C.; Eckman, E. A.; Sambamurti, K.; Dobbs, N.; Chow, K. M.; Eckman, C. B.; Hersh, L. B.; Thiele, D. L. *Proc. Natl. Acad. Sci. U.S.A.* **2003**, *100*, 6221.

(262) Duckworth, W. C.; Bennett, R. G.; Hamel, F. G. *Endocr. Rev.* **1998**, *19*, 608.

(263) Kurochkin, I. *Trends Biochem. Sci.* **2001**, *26*, 421.

(264) Neant-Fery, M.; Garcia-Ordoñez, R. D.; Logan, T. P.; Selkoe, D. J.; Li, L.; Reinstatler, L.; Leissring, M. A. *Proc. Natl. Acad. Sci. U. S. A.* **2008**, *105*, 9582.

(265) Tseng, B. P.; Esler, W. P.; Clish, C. B.; Stimson, E. R.; Ghilardi, J. R.; Vinters, H. V.; Mantyh, P. W.; Lee, J. P.; Maggio, J. E. *Biochemistry* **1999**, *38*, 10424.

(266) Shen, Y., Joachimiak, A., Rosner, M. R., and Tang, W. J. *Nature* **2006**, *443*, 870.

(267) Guo, Q., Manolopoulou, M., Bian, Y., Schilling, A. B., and Tang, W. J. *J. Mol. Biol.* **2010**, *395*, 430.

(268) Im, H.; Manolopoulou, M.; Malito, E.; Shen, Y.; Zhao, J.; Neant-Fery, M.; Sun, C.-Y.; Meredith, S. C.; Sisodia, S. S.; Leissring, M. A.; Tang, W.-J. *J. Biol. Chem.* **2007**, *282*, 25453.

(269) Malito, E., Hulse, R. E., and Tang, W. J. *Cell. Mol. Life Sci.* **2008**, *65*, 2574.

(270) Malito, E., Ralat, L. A., Manolopoulou, M., Tsay, J. L., Wadlington, N. L., and Tang, W. J. *Biochemistry* **2008**, *47*, 12822.

(271) Manolopoulou, M., Guo, Q., Malito, E., Schilling, A. B. and Tang, W. J. *J. Biol. Chem.* **2009**, *284*, 14177.

(272) Li, P.; Kuo, W.-L.; Yousef, M.; Rosner, M. R.; Tang, W.-J. *Biochem. Biophys. Res. Commun.* **2006**, *343*, 1032.

(273) Bora, R.; Ozbil, M.; Prabhakar, R. *J. Biol. Inorg. Chem.* **2010**, *15*, 485.

(274) Berendsen, H. J. C.; van der Spoel, D.; van Drunen, D. *Comput. Phys. Commun.* **1995**, *91*, 43.

(275) Oostenbrink, C.; Villa, A.; Mark, A. E.; van Gunsteren, W. F. *J. Comput. Chem.* **2004**, *25*, 1656.

(276) Krieger, E.; Vriend, G. *Bioinformatics* **2002**, *18*, 315.

(277) Bora, R. P.; Prabhakar, R. *Biochemistry* **2010**, *49*, 3947.

(278) Baker, N.; Holst, M.; Wang, F. *J. Comput. Chem.* **2000**, *21*, 1343.

(279) Baker, N. A.; Sept, D.; Joseph, S.; Holst, M. J.; McCammon, J. A. *Proc. Natl. Acad. Sci. USA* **2001**, *98*, 10037.

(280) Pérez, C.; Pastor, M.; Ortiz, A. R.; Gago, F. *J. Med. Chem.* **1998**, *41*, 836.

(281) Dolinsky, T. J.; Nielsen, J. E.; McCammon, J. A.; Baker, N. A. *Nucleic Acids Res.* **2004**, *32*, W665.

(282) Dolinsky, T. J.; Czodrowski, P.; Li, H.; Nielsen, J. E.; Jensen, J. H.; Klebe, G.; Baker, N. A. *Nucleic Acids Res.* **2007**, *35*, W522.

(283) Sharp, K.; Nicholls, A.; Fine, R.; Honig, B. *Science* **1991**, *252*, 106.

(284) Sitkoff, D.; Sharp, K. A.; Honig, B. *J. Phys. Chem.* **1994**, *98*, 1978.

(285) Bora, R. P. a. P., R. *Biochemistry* **2010**, *49*, 3947.

(286) Li, P., Kuo, W. L., Yousef, M., Rosner, M. R., and Tang, W. J. *Biochem. Biophys. Research Commun.* **2006**, *343*, 1032.